COKE RESISTANT COATING TECHNOLOGY FOR APPLICATIONS IN ETHYLENE PYROLYSIS HEATERS

A Dissertation Presented

by

Alok Pratap Singh Chauhan

to

The Graduate School

in Partial fulfillment of the

Requirements

for the Degree of

Doctor of Philosophy

in

Materials Science and Engineering

Stony Brook University

August 2007

Stony Brook University

The Graduate School

Alok Pratap Singh Chauhan

We, the dissertation committee for the above candidate for the Doctor of Philosophy degree, hereby recommend acceptance of this dissertation.

Professor Henry J. White - Dissertation Advisor
Department of Materials Science and Engineering

Professor Clive R. Clayton – Chairperson of Defense
Department of Materials Science and Engineering

Professor Jonathan Sokolov
Department of Materials Science and Engineering

Dr. Kandasamy M. Sundaram
ABB Lummus Global Inc., Bloomfield, NJ

Dr. Jianming Bai
National Synchrotron Light Source,
University of Tennessee-Oakridge National Laboratory,
Brookhaven National Laboratory, Upton, NY

This dissertation is accepted by the Graduate School

Lawrence Martin
Dean of the Graduate School

Abstract of the Dissertation

Coke Resistant Coating Technology
For Applications In Ethylene Pyrolysis Heaters

By

Alok Pratap Singh Chauhan

Doctor of Philosophy

in

Materials Science and Engineering

Stony Brook University

2007

This dissertation begins with a description of the history of the events leading to ethylene pyrolysis tube failure. During service, hydrocarbons pass through the radiant heater coils at temperatures up to ~ 1100 C. The catalytic activity between the feedstock and the tube wall leads to heterogeneous coke formation. The accumulation of coke, a homogeneous event, leads to localized temperature excursions, pressure variations, and potential tube plugging which all play a significant role in premature tube failure by creep and stress rupture.

During normal operation, the tube metal temperature is frequently reduced to pass high pressure steam or steam air mixtures through the tubing to eliminate coke, a process known as decoking. At ~ 1100 C, depending on the materials of construction, a variety of topologically close packed phases (η, $M_{23}C_6$, σ, M_7C_3, etc.) form which can lead to premature tube failure by embrittlement during the decoke cycles.

In this dissertation, two techniques are discussed which have the potential for overcoming premature tube failure: (1) upgrading the metallurgy to a material that forms a protective oxide coating at the service temperature and also shows resistance to the formation of topologically closed pack phases and (2) a novel technique which can deposit coke resisting coating on the inner diameter of pyrolysis tubing.

To

My Parents, Family, Relatives, Friends, and Well-wishers

Table of Contents

List of Figures

List of Tables

Acknowledgements

I would like to sincerely thank my advisor, Dr. Henry J. White, by whose example I have developed thoroughness, perseverance and an appreciation for creativity necessary for the conduction of successful research. I am grateful for his enlightening suggestions, zealous encouragement, and precious consultations throughout my research.

I would like to express my sincere gratitude to Dr. Jonathan Sokolov and Dr. Clive Clayton, of SUNY Stony Brook University; Dr. Jianming Bai of Brookhaven National Laboratory; and Dr. Kandasamy M. Sundaram of ABB Lummus Global, Inc for the invaluable advice, fruitful discussions and continuous encouragement throughout this investigation.

I am indebted to Dr. Weidong Si of Brookhaven National Laboratory for the constant support and investigation and also helping me with the Pulsed Laser Deposition experiments. I thank Dr. Marvin Vasquez of Army Research Laboratory (also, alumni of Department of Materials Science and Engineering) for helping me with the XPS studies. I thank Dr. Jim Quinn, of the Materials Science and Engineering Department for guiding me with using Electron Microscopy instruments and also discussions with regards to research. I would also like to thank Lester Orlick of the College of Engineering and Applied Sciences, Stony Brook University, Kenneth Baldwin of the Department of Geosciences and Frank Loeb of Brookhaven National Laboratory for assistance at various stages of research. I thank Dr. Shouren Ge and Dr. Xian-Zhong Guo for helping me with the AFM experiments and Sinctag X-ray Diffraction studies respectively.

I acknowledge the former and current students in the laboratory, Jack Burke, Jeffrey Asselta, Dan Wilcosz, Wilton Moran, Kelvin Montero, Benoit Facchetty and Mir Anwar, for all the help and support provided to me during this work.

I thank Seongchan Park, Dr. Clive Song Li, Jose Mawyin, Krithika Kalyanasundaram, Xiaoting Jia, Shanshan Lian and all the other students of the department for their help and support. I would also like to thank Dr. Vemula Mahesh of Department of Electrical Engineering, Stony Brook University for encouraging and motivating me through this research.

The financial support through the National Science Foundation DMII program under the Grant No. 0346947 is gratefully acknowledged. I wish to thank Dr. Peter Johnson of Department of Condensed Matter Physics and Materials Science for allowing me to do my research at Brookhaven National Laboratory.

I express my gratitude to the office staff Debbie Michienzi, Gertha and Lynn Allopena for taking care of the paper work. In fact, handling of paperwork and procedures (non-research) by Debbie has helped me divert all my attention to my research. Help from all unmentioned Materials Science and Engineering Department members and from all other individuals or organizations is appreciated.

I thank all my teachers (St. Pauls' School, Gwalior; Air Force Vidyabharati School, Gwalior; Bansal Classes, Kota; Department of Ceramic Engineering, Institute of Technology, Banaras Hindu University, Varanasi; Electron Microscopy Department, DRDE, Gwalior; Department of Metallurgy, Indian Institute of Sciences, Bangalore, INDIA; Alfred University, NY) for educating me. Specially, I am thankful to Drs. Om

Parkash, E. S. Dwarakadasa, S. P. Singh, R. S. Chauhan, Alexander Fluegel, Ravi Gundakaram, Carl Boehlert and Devendra Kumar for their efforts.

I thank my friends Mamta Agarwal, Dr. Pradyumna Gupta, Amit Shah, Prasanna Thogulu, Sridhar Madishetty, N Madhusudhan, Lucas Carrey, Eli Hoory, Frank Szalajda, Serkan, Roopesh Sharma, Narayanan Ramanujam, Badri Rangarajan and Gajendra Pratap for their support.

Finally, I am indebted to my family for their never-ending support. Besides being my guide, my grandfather has constantly motivated and encouraged me that I have needed at difficult times. My grandfather who is more like my friend for fruitful discussions and his motivation to think beyond. My sister, Anjali for her patience and understanding. My cousin brother, Kamlendra Singh to help me to think and achieve what I dreamed in my life. My other cousins Jitendra Singh, Lokendra Singh, Pratap Singh, Amrendra Singh, Deepika, Arun Singh, Sanyogita, Preeti, Nitin Sengar, Pawan Sengar, Roopa Sengar, Jyoti Sengar, and Kanchan Sengar also played a part in this endeavor. I also like to thank my uncles Shri Charan Singh Sengar, Sunil Singh Sengar, Dharamveer Singh Chauhan, and Late Sanjay Dogra who motivated me to go for higher education. And last but not the least my parents who have always been a source of braveness and perseverance and are the very reason for my constant motivation towards the fulfillment of this PhD degree.

Vita

Alok Pratap Singh Chauhan was born in Gwalior (Madhya Pradesh) India, to Shri. Vinod Kumar Singh Chauhan and Smt. Shashi Bala Chauhan. His father worked for Indian Central Government in Accountant General Office and his mother was a housewife. He was grandson of Shri. Rativaran Singh Chauhan and Smt. Ramadevi Chauhan. He grew up with his younger sister Anjali who later on graduated with an Engineering degree from Indian School of Mines, Dhanbad. Alok, after completing his schooling from St. Paul's School, Gwalior, was selected to Institute of Technology – Banaras Hindu University, Varanasi. At Varanasi, he formed many friendships and became enthralled with the heady intellectual atmosphere. There he was selected for two internships: one in summer of 2000 at the Indian Institute of Sciences (IISc), Bangalore, and the other in summer of 2001 at DRDE, Gwalior. After graduating in 2002 with a Baccalaureate degree in Ceramic Engineering, Alok was eager to pursue higher studies. He was initially admitted to graduate program at Alfred University, NY and later transferred to Stony Brook University, NY; in United States of America. His graduate studies research also involved experimentation at National Synchrotron Light Source and Department of Physics at Brookhaven National Laboratory (BNL), NY. He was selected for an internship at Sulzer Metco, Inc, NY in summer of 2004. In 2005, he received his Masters of Science degree in Materials Science and Engineering from Stony Brook University, NY. He is fluent in Sanskrit, Hindi and English.

Areas of Specialty

- Thermodynamic Studies - Thermo-Calc Software
- Diffusion Calculations - Dictra Software
- Electron Back Scattered Diffraction (EBSD)
- Rutherford Backscattering Spectrometry (RBS)
- Spectroscopic Ellipsometry
- Thermo-Mechanical Simulation - Gleeble
- Scanning Electron Microscope and X-ray Energy Dispersive Spectroscopy
- Finite Element Analysis – ANSYS Software
- Pulsed Laser Deposition (PLD)
- X-ray Diffraction and Synchrotron X-rays
- Thermogravimetric Analysis and Differential Scanning Calorimetry
- Atomic Force Microscopy (AFM) and Scanning Probe Microscopy (SPM)
- Thermo-Mechanical Analysis - Instron Materials Testing System
- Metallography
- Laboratory Pack Carburization
- Experimentation design for Aging of Alloys
- Glass melting and Annealing
- Sintering studies of ceramic powder pellets.

Publications

1. Joel A. Payne, Roumiana S. Petrova, Henry J. White, Alok Chauhan, and Jianming Bai, Residual Stress Analysis of the Iron Monoboride Layer and Substrate in Boronized AISI 1018 Steel by Synchrotron Radiation, *Surface and Coatings Technology*, 2007 – Communicated.

2. Alok Chauhan, Mir Anwar, Kelvin Montero, Henry J. White, Roumiana S. Petrova, and Joel A. Payne, Weidong Si, Jianming Bai, Slip Plane X-ray Residual Stress Analysis of Pulsed Laser Self Ablated Coatings*, Surface and Coatings Technology*, 2006 – Communicated.

3. Alok Chauhan, Mir Anwar, Kelvin Montero, Henry White, and Weidong Si, Internal Carburization and Carbide Precipitation in Fe-Ni-Cr Alloy Tubing Retired from Ethylene Pyrolysis Service, *Journal of Phase Equilibria & Diffusion*, December 27(6): 684-690, 2006.

4. Alok Chauhan, Mir Anwar, Kelvin Montero, Henry White, Weidong Si, and Jianming Bai, Scaled Up Pulsed Deposition Technology: Carburization Resistant Ablation Coatings for Ethylene Pyrolysis Coils, *Materials Research Society Proceedings*, 890: 147-152, 2006.

5. Alok Chauhan, Wilton Moran, Shouren Ge, Weidong Si, and Henry J. White, Pulsed Laser Deposition of Ceramic Silicon Carbide on Centrifugally Cast A609 Grade HK-40: Effect of Surface Characteristics, *Scripta Metallurgica et Materialia*, 52(8): 735-738, APR 2005 (CITED 1x).

6. Alok Chauhan, Wilton Moran, Elizabeth Casey, Weidong Si, Henry White, Limiting Catalytic Coke Formation by the Application of Adherent SiC Coatings via Pulsed Laser Deposition to the Inner Diameter of Tube Material Traditionally Used for Ethylene Pyrolysis Service, *Materials Research Society Proceedings, Surface Engineering 2004 - Fundamentals and Applications*, 843: 341-345, 2005.

7. M. Kumar, A. Uniyal, A. P. S. Chauhan, and S. P. Singh, Optical absorption and fluorescent behaviour of titanium ions in silicate glasses, *Bulletin of Materials Science*, 26 (3): 335-341, APR 2003.

Presentations

1. **Alok Chauhan, in *11th Annual Open House of Garcia MRSEC of Polymers at Engineered Surfaces*, Queens College, NY, 2007.**

2. Alok Chauhan, Mir Anwar, Kelvin Montero, Henry J. White, Weidong Si, and Jianming Bai, in *NSF Design, Service, and Manufacturing Grantees and Research Conference*, St. Louis, MO, 2006.

3. Alok Chauhan, Mir Anwar, Kelvin Montero, Henry J. White, Weidong Si, and Jianming Bai, in *Undergraduate Research and Creative Activities (URECA)*, Stony Brook University, NY, 2006.

4. Alok Chauhan, Mir Anwar, Kelvin Montero, Henry White, and Weidong Si, in Multicomponent-Multiphase Diffusion Symposium in Honor of Mysore A. Dayananda: Industrial Applications, *135th TMS Annual Meeting & Exhibition*, San Antonio, TX, 2006.

5. **Alok Chauhan, in *10th Annual Open House of Garcia MRSEC of Polymers at Engineered Surfaces*, Queens College, NY, 2006.**

6. Alok Chauhan, Mir Anwar, Kelvin Montero, Henry White, Weidong Si, and Jianming Bai, in Surface Interactions and Surface Engineering for Manufacturing Applications, *MRS Fall Meeting*, Boston, MA, Abstract Y4.5, 2005.

7. Alok Chauhan, Wilton Moran, Weidong Si, and Henry White, in *Society of Hispanic Professional Engineers, National Technical and Career Conference (NTCC)*, Dallas, TX, 2005.

8. Alok Chauhan, Wilton Moran, Weidong Si, and Henry White, in *National Science Foundation DMII Conference*, Scottsdale, AZ, 2005.

9. Alok Chauhan, Invited speaker *Defence Research and Development Establishment (DRDE)*, 2004.

10. Alok Chauhan, Wilton Moran, Weidong Si, Shouren Ge, and Henry White, in *International Symposium of Research Students on Materials Science and Engineering (ISRS)*, IIT Madras, India, Abstract OR-SE-4, 2004.

11. Alok Chauhan, Wilton Moran, Weidong Si, Henry White, in Surface Engineering: Fundamentals and Applications, *MRS Fall Meeting*, Boston, MA, Abstract T3.4, 2004.

12. Alok Chauhan, Wilton Moran, Weidong Si, and Henry White, in *Society of Hispanic Professional Engineers Easter Technical and Career Conference (ETCC)*, Philadelphia, PA, 2004.

13. Alok Chauhan, Wilton Moran, Weidong Si, and Henry White, in *Undergraduate Research and Creative Activities (URECA)*, Stony Brook University, NY, 2005.

Teaching Experience

Spring 2006:	**Instructor** CEN 575 - Modern Materials.
Spring 2004:	Teaching Assistant for ESG 333 - Materials Sciences II: Electronic Properties.
Fall 2003:	Teaching Assistant for ESG 312 - Engineering Laboratory.

Awards

April 2006:	Michael Ohr Memorial Award for Outstanding Performance as a Teaching Assistant in Materials Science & Engineering Department, Stony Brook University, USA.
July 2006:	MII-NSF Conference, NSF Student Award, University of Missouri–Rolla, USA.

Professional Affiliations:

- The Material Research Society
- The American Ceramic Society
- The ASM International
- TMS, The Mineral, Metals & Materials Society
- Association for Iron & Steel Technology

Outreach (High School / Undergraduate)

- ***Invited Chair*** to American Society for Engineering Education (ASEE) Mid-Atlantic Section Fall 2005 Conference, Stony Brook University, Stony Brook, NY, October 28-29, 2005.
- ***Invited Talk*** to ASM Teachers Training Workshop, August 2-6, 2005, Comsewogue School District, NY.
- Teachers Materials Camp, Sponsored by ASM International, Rutgers University and Princeton University, August 8-12, 2005, Princeton, NJ.

Extracurricular Activities

- Elected as President of the Students' Chapter, 'Metro New York-New Jersey ASM International' at Stony Brook University, 2004-2006.
- Elected as senator for Graduate Student Organization at Stony Brook University to represent Department of Materials Science & Engineering, 2004-2005.
- Executive Board Member of the Alladin Club at Stony Brook University, 2005-2006.
- Executive Board Member of the Minority in Engineering and Applied Sciences (MEAS) Group at Stony Brook University, 2004-2006.

1. Introduction

1.1. Coking

Ethylene is one of the largest, by volume, chemical commodities in the world with production in the United States estimated to exceed 136 million metric tons by the year 2010. [1] Used as the building block for the production of polyethylene, ethylene glycol, polyester, and styrene monomer; ethylene is produced by cracking a gaseous or liquid hydrocarbon feedstock, such as ethane, propane, naphtha, or gas oil in the presence of steam inside the coils of a pyrolysis furnace. [2-4] Hydrocarbon cracking is accomplished at low pressures and elevated temperatures in the range of 750-1000 C (1382- 1832 F). The feedstock is passed at high velocities through heated coils (Fe-Ni-Cr alloy). The residence time of the feedstock within the coils is extremely short.

The type of feedstock used in an ethylene plant generally depends on the availability and geographical location of the plant. In the United States, ethane and butane are mainly used with some plants using naphtha. In the Middle East, mainly ethane and to some extent propane is used. In Europe and Asia, mainly naphtha is used; whereas some locations use feedstocks ranging from ethane to vacuum gas oils. [5] The feedstock cracking reactions that occur during pyrolysis of ethylene are free radical in nature and are nonselective, a range of useful hydrocarbons and detrimental coke being produced as byproducts. Two types of free radical reactions have been described [6]:

chain interference and transfer type propagation reactions as in equation (I) and chain termination reactions as depicted in equation (II)

$$RH + H^* = R^* + H_2 \qquad (I)$$

$$2R^* + M = R\text{-}R + M \qquad (II)$$

When the feedstock consists of propane, for example, some of the free radical cracking reactions are shown below [7-9]:

a) Initiation Reaction

$$C_3H_8 \rightarrow CH_3^* + C_2H_5^* \qquad (III)$$

b) Propagation Reactions

$$CH_3^* + C_3H_8 \rightarrow C_3H_7^* + CH_4 \qquad (IV)$$

$$C_2H_5^* + C_3H_8 \rightarrow C_3H_7^* + C_2H_6 \qquad (V)$$

$$C_2H_5^* \rightarrow H^* + C_2H_4 \qquad (VI)$$

$$CH_3^* + H_2 \rightarrow H^* + CH_4 \qquad (VII)$$

$$H^* + CH_4 \rightarrow CH_3^* + H_2 \qquad (VIII)$$

$$C_2H_5^* + H_2 \rightarrow H^* + C_2H_6 \qquad (IX)$$

$$C_2H_5^* + C_2H_4 \rightarrow CH_3^* + C_3H_6 \qquad (X)$$

$$H^* + C_2H_4 \rightarrow C_2H_5^* \qquad (XI)$$

$$C_2H_6 \rightarrow 2CH_3^* \qquad (XII)$$

$$CH_3^* + C_2H_6 \rightarrow C_2H_5^* + CH_4 \qquad (XIII)$$

$$CH_3^* + C_2H_4 \rightarrow C_3H_7^* \qquad (XIV)$$

$C_3H_7^* + C_2H_6 \rightarrow C_2H_5^* + C_3H_8$ (XV)

$H^* + C_2H_6 \rightarrow C_2H_5^* + H_2$ (XVI)

$H^* + C_3H_6 \rightarrow C_3H_7^*$ (XVII)

$C_3H_7^* \rightarrow CH_3^* + C_2H_4$ (XVIII)

$C_3H_7^* \rightarrow H^* + C_3H_6$ (XIX)

$C_3H_7^* + H_2 \rightarrow H^* + C_3H_8$ (XX)

$C_3H_7^* + CH_4 \rightarrow CH_3^* + C_3H_8$ (XXI)

$H^* + C_3H_8 \rightarrow C_3H_7^* + H_2$ (XXII)

$CH_3^* + C_3H_6 \rightarrow C_4H_9^*$ (XXIII)

$C_2H_5^* + C_2H_4 \rightarrow C_4H_9^*$ (XXIV)

$C_4H_9^* \rightarrow H^* + C_4H_8$ (XXV)

$C_4H_9^* + H_2 \rightarrow H^* + C_4H_{10}$ (XXVI)

$C_4H_9^* \rightarrow CH_3^* + C_3H_6$ (XXVII)

$C_4H_9^* \rightarrow C_2H_5^* + C_2H_4$ (XXVIII)

$C_2H_5^* + C_4H_{10} \rightarrow C_4H_9^* + C_2H_6$ (XXIX)

$C_4H_{10} \rightarrow CH_3^* + C_3H_7^*$ (XXX)

$C_4H_{10} \rightarrow 2C_2H_5^*$ (XXXI)

$H^* + C_4H_{10} \rightarrow C_4H_9^* + H_2$ (XXXII)

$CH_3^* + C_4H_{10} \rightarrow C_4H_9^* + CH_4$ (XXXIII)

c) Termination Reactions

$2H^* \rightarrow H_2$ (XXXIV)

$H^{*} + CH_3^{*} \rightarrow CH_4$ (XXXV)

$H^{*} + C_2H_5^{*} \rightarrow C_2H_6$ (XXXVI)

$H^{*} + C_3H_7^{*} \rightarrow C_3H_8$ (XXXVII)

$2CH_3^{*} \rightarrow C_2H_6$ (XXXVIII)

$CH_3^{*} + C_2H_5^{*} \rightarrow C_3H_8$ (XXXIX)

$2C_2H_5^{*} \rightarrow C_2H_4 + C_2H_6$ (XL)

$2C_2H_5^{*} \rightarrow C_4H_{10}$ (XLI)

$CH_3^{*} + C_3H_7^{*} \rightarrow CH_4 + C_3H_6$ (XLII)

The assumption that the highest molecular weight product formed from C_3H_8 is C_4H_{10}, is not necessarily true. Also, it is incorrect to assume that the same type of tar is obtained from low and high molecular weight feedstocks. The free radical reactions also lead to a variety of low vapor pressure high molecular weight products even at the high processing temperatures which condense (i.e. form liquid droplets) in the pyrolysis reactor.

The interaction of feedstock and products with the tube wall leads to coke formation, the mechanism of which is summarized in the Figure 1.1 [10]. Homogeneous events such as gas phase coke formation and feedstock/ product interactions with carbon and tar deposits on the surface are excluded in this illustration. The thick layers that are formed when non-catalytic events occur are not our primary concern and are described elsewhere in the literature [6, 11].

The steam used during cracking helps to minimize coke formation by virtue of the water-gas reaction. The trend in recent years has been to use an increasing cracking temperature with the aim of increasing the ethylene yield. However, the environment within the radiant section cracking tubes is carburizing, while that on the outside or firebox side is oxidizing. As the tube skin and cracking temperatures are increased, the potential for premature tube failure is accentuated. [12-14] A detrimental product of the cracking reactions, coke, deposits on the inner walls of the coils leading to process inefficiencies and tube failure. Since cracking furnaces need to be regularly decoked by steam and steam-air mixtures, ethylene production tends to be one of the most energy intensive processes in the world. [13-15] The combination of cracking and decoking cycles reduces tube life by 2-4 years (design life expectancy is 10 years). [16] The hot outlet tubes have average lives of six months to seven years depending on severity, design, alloy, and operation. Mid-section and inlet tubes have longer lives due to lower operating temperatures.

In the next portion of this section, I will briefly describe four types of coke formation:

- Catalytic or Heterogeneous Coke Formation
- Pyrolytic or Homogeneous Coke Formation
- Deposition of mechanically transferred coke in downstream equipment
- Condensation of high boiling components

1.1.1. Catalytic Coke Formation

Catalytic coke formation is dependent on the abundance of catalytic sites (metal particles on the surface, metal particles on filaments, active coke (free radicals), grain boundaries, metal crystallites, metal oxides, metal carbides, surface disorders, etc.) on metal surfaces at temperature above which catalytic reactions become possible. There existence of a significant number of catalytic sites, where olefins can be preferentially adsorbed over paraffins due to the existence of π electrons will lead to filament formation [11, 17-21]. The absence of chromium (a coke formation deterrent) as well as high iron content in the low or unalloyed steels is the primary reason for rapid coke formation [20, 22, 23]. Furthermore like iron, the presence of nickel aids in the formation of the coke.

The catalytic coke formation mechanisms are [24]:

i) Long periods of steady state deposition.

ii) Carbon deposits contain metal particles (at the tip of carbon filaments).

iii) At low temperatures (500 – 650 C) the rate of deposition is dependent on the metal surface.

iv) At higher temperatures, surface reactions are the rate determining step (surface carbon films deactivate the catalyst).

v) At even higher temperatures coke formation occurs by gas phase pyrolysis of hydrocarbons.

vi) Catalytic coke formation is accelerated by the presence of hydrogen.

vii) Ease of formation of catalytic carbon: acetylenes > olefins > paraffins.

The formation of catalytic coke on metal surface starts with the adsorption of hydrocarbon gas on a metal surface. The hydrocarbon gas then undergoes a series of reactions to form intermediates that adsorb on the metal surface. This in turn leads to production of carbon atoms when adsorbed species undergo reactions. Carbon atoms diffuse into the metal or migrate across the surface to nucleation/ growth centers. Carbon diffusing in the bulk migrates to grain boundaries and precipitates out, whereas the carbon on the surface forms an encapsulated layer and prevents further deposition of carbon on the catalyst. If encapsulation does not occur, catalytic reactions continue because the metal surface is at the tips of the growing filaments. Coke formation on any surface is effected by [6]:

A) Nature of gas phase species which depend on the nature of the surface (entrained metal particles).

B) If gas phase contains steam or hydrogen, encapsulated carbon can be removed and the coking rate can increase (in situ decoking).

C) The rougher the surface, the more nucleation sites and the higher is the coking rate.

D) Controlled amounts of sulfur can limit catalytic coke formation.

E) Surface conditions differ from bulk conditions: HK40- preoxidized - similar to the bulk/ pre-reduced has only manganese (Mn) and chromium (Cr) at the surface.

F) Alumina or Silica limits catalytic coke formation.

The formation of coke on catalytic surfaces affects the nature of the reactants, intermediates, and products. It offers nucleation and growth sites on the catalyst and thus has an influence on the structure and composition of coke. Secondary reactions are also influenced. Catalytic surfaces promote the formation of carbon via dissolution – precipitation mechanism. Also these catalytic surfaces alter the nature of gases present in the reactor by catalyzing gas-phase reactions and the nature and amount of tars or carbon formed in the gas phase. During cracking, catalytic surfaces get covered by inactive layers either deliberately (alumina or silica from the alloy) or accidentally (encapsulated coke). During coke formation on non-catalytic surfaces there is a change in mass and heat transfer in the system, generation of nucleation and growth sites, and physical properties such as porosity have an effect on coking. Non-catalytic surfaces collect condensed tar and soot, and this concentration of tar and soot allows further non-catalytic reactions to occur. [25, 26]

There is an induction period for the production of tars and carbon and in a flow reactor the inlet never becomes covered with tar or carbon [27]. Tube materials from the inlet will however influence downstream coking unless the inlet is coated [28-30]. Filamentous carbons with active metal tips are especially active and continue to generate carbon until the tip itself is covered with a non-reactive carbon [6, 31-37]. Mechanically polishing surface results in a reduction of the number of disorders or, general roughness that have resulted from manufacturing [35, 38-40]. Active metal particles already existing on the surface [41] are removed or, reduced in size and number with polishing [38, 42]. Exception to this is that at high temperatures (> 900 C), polishing effect is less pronounced or, non-existent [40, 43]. Most significant effects of polishing are not changes in surface composition, but the decrease in active sites from mechanical defects and from metal particle removal [10]**.** Compared to as fabricated and/or rough surfaces, polished surfaces operate at 50 to 100 C below the gas temperature, thus at the lower operating temperatures, the free radical reactions occur more slowly [32, 38]. Radiation and temperature of the substrate are affected during heat transfer by radiation emittance. Polished surface have an emittance of 0.1, whereas the emittance of a plain/ carburized surface tend to be a lot higher ~ 0.9. [44]

1.1.2. Pyrolytic Coke Formation

Pyrolytic coke formation is also known as radical coke formation or, thermal coking and is a form of homogeneous coking. Pyrolytic coke in the gas phase is quickly formed by radicals as coke precursors deposit non-preferentially on the surface of process equipment. [45] Polymerization of aromatic compound towards coke formation starts with formation of multi-ring aromatic components of higher molecular mass from simple aromatics via dehydrogenation/ nucleation above 700 C and further leading to formation of coke particulates in the gas phase [46]. Diels-Alder reaction, or polycyclization, is responsible for gas-phase reactions in the early stage of coke formation at temperatures below 600 C [47, 48]. Here, the addition of fragmented alkyl radical with unsaturated hydrocarbons produce cyclic compounds. The formation of pyrolytic coke decreases with decreasing temperature [49, 50]. The absolute coke formation rates are in the order of paraffins < aromatics < olefins < acetylene. The formation rates of pyrolytic coke from paraffins is 2-4 orders lesser than olefins. It has been observed that the larger hydrocarbons have higher coke formation rates in the same group and the temperature dependencies are in the reverse order: acetylene < olefins < aromatics < paraffins. [26]

There are seven theories with regards to formation of carbon/ coke in the gas phase [6]:

a) Atomic Theory: Monoatomic carbon is a significant species in nucleation.
b) C2 Theory: Solid carbon results from polymerization of C2 species.
c) C3 Theory: Solid carbon in flames arises by condensation of carbon vapor (C3 is a major species).
d) Acetylene Theory: Carbon particles are formed from acetylene by simultaneous polymerization and dehydrogenation.
e) Hydrocarbon Polymerization Theory: Fuels undergo a polymerization process that ends in carbon (liquid polymers, polymers with high molecular weight, polycyclic aromatics, and polynuclear aromatics are formed as intermediates).
f) Surface Decomposition Theory: Carbon is formed through a surface chemical reaction of the original hydrocarbon on a carbon surface.
g) Condensation Theory: Initial hydrocarbon is transformed by a gas phase reaction into macromolecules and then into droplets (condensation) and lastly into solid carbon (pyrolyzed).

1.1.3. Droplet Condensation

In this mechanism, coke formation/ deposition occurs in the low temperature sections such as downstream of the cracking coils [26]. Because of condensation mechanism, the heavy feedstocks like gas oil coke more than lighter ones such as ethane [51]. The coke forms as tar or mist [46], and here as the temperature decreases the coking rate increases, an inverse relationship [45]. Condensation coke has spherical morphology with micro-droplets condensing on graphite surfaces and globules of coke forming by dehydrogenation [17, 18, 46].

1.2. Carburization

Over a period of time coking (a surface diffusion event) leads to carburization (a bulk diffusion event) which both are thought to be common causes leading to tube failure in case of ethylene cracking [52, 53]. Carburization occurs when the metal is exposed to carbon monoxide, methane, ethane or other hydrocarbons at high temperature [54]. Carburization has an adverse effect on room temperature ductility, toughness, and weldability. It increases tube wall thickness/ volume and greatly amplifies the outer fiber tensile stresses, which in turn leads to cracking, fissures, and reduced tube life. Materials that have embrittled due to carburization cannot readily yield or relax under bending loads so they tend to rupture prematurely. [12] Carburization usually is localized and tends to be oriented towards the firing side of the tubing [54].

During carburization, there is formation of two zones of carbides: an inner $M_{23}C_6$ phase and an outer M_7C_3 phase (where M= Fe, Cr, and/or Ni). M_7C_3 is formed by conversion from $M_{23}C_6$. The Fe and Ni expelled from the matrix during the process can be seen as metallic particles in the carbide [55-58]. The formation of carbides depletes the matrix of Cr and shifts the composition within the Fe-Ni system. At temperatures 800 -1200 C, the activity of carbon is defined w.r.t. (with respect to) graphite, $a_c = 1$ so carburization takes place when $a_c \leq 1$. [12] The equilibria for the carbon activity are as below:

$$CH_4 = C + 2\,H_2 \qquad \text{(XLIII)}$$

$$2\,CO = C + CO_2 \qquad \text{(XLIV)}$$

$$CO + H_2 = C + H_2O \qquad \text{(XLV)}$$

As $c_cD_c >> c_mD_m$, the solubility (c) and diffusivity (D) of carbon in Fe-Ni-Cr alloys are relatively high so the inward diffusion of carbon (C) is high and the outward diffusion of carbide forming elements (M) is much slower [59, 60].

Carburization increases volume which leads to internally induced stresses in the uncarburized parts of the material. It causes an increase in the thermal conductivity, which is not a negative effect and leads to a reduction in room temperature tensile, ductility, and impact strength. Catastrophic brittle failure in carburized components occurs when the temperature is lowered from the service temperature. Carburization in general has no detrimental affect on the high temperature properties of the material. [12]

In case of nickel (Ni) based alloys, the reduction in room temperature ductility due to carburization is much more. It is caused, firstly, by the lower carbon solubility and, secondly, due to the formation of M_7C_3 and $M_{23}C_6$ with high metal/carbon ratio. [61]

Chromium oxide is a protective oxide layer for Fe-Ni-Cr alloys. It gets converted to unprotected carbides under certain conditions. Cr_2O_3 scale is affected by increasing the temperature, or decreasing the oxygen activity and/or increasing the carbon activity. The formation of chromium carbides from Cr_2O_3 begins at 1050 C in the CO_2-CO atmospheres and in contact with carbon (a_c=1). CO pressure controls the temperature at which the carbide formation occurs. [12]

At temperatures greater than 1050 C, presence of ~2% Si aids in the formation of SiO_2 sub-layer which resists carburization [62]. Thus, the protection from carburization below 1050 C is controlled by Cr_2O_3 formation while that above 1050 C is controlled by SiO_2 formation or, in the case of sufficient Al content on Al_2O_3 formation [12].

The mechanisms involved during high temperature carburization are simply [12]:

i) Diffusion in the boundary layer and transport in the gas atmosphere by gas flow;

ii) Phase boundary reactions known as dissociations and reactions of the gas molecules on the surface producing carbon atoms, are responsible for transfer of carbon to the metal phase;

iii) Inbound carbon diffusion; and

iv) Carbide-forming alloy elements react with carbon in the alloy interior.

Thus, carbon is transferred from gas atmosphere by CO, CO_2, CH_4 or other hydrocarbons into the metal matrix at high temperatures in Fe-Ni-Cr alloys leading to carburization and formation of $M_{23}C_6$ and M_7C_3. Carburization will occur no matter whether coke is deposited catalytically or, non-catalytically. [12]

Carbide formers present during carburization are niobium, tungsten, molybdenum, titanium, etc. apart from chromium, which interacts with carbon during carburization and cause carbides to be more complex [54]. In nickel-based alloys, the density of electrons per atom is calculated [63] to determine if other alloy phase instabilities (precipitates) form. Topologically close-packed (TCP) precipitated phases tend to form after prolonged exposure at temperatures in the range from 704 C – 899 C (1300 F – 1650 F). The main phases are gamma prime, laves, mu (μ), and sigma. The equation for electron vacancy number N_v is expressed as:

$$N_v = \sum_{i=1}^{n} m_i \left(N_v\right)_i \qquad \text{(XLVI)}$$

where, N_v is the electron vacancy number for the alloy, m_i is the atomic mass fraction of the ith element in the alloy composition, and $(N_v)_i$ is the electron vacancy number of the ith element. The sequence of phases which form in the gamma matrix is carbide precipitation followed by gamma prime formation. The residual matrix is determined from the phase reactions and is thus used to calculate the electron vacancy number. Table 1.1 - Table 1.4 shows the electron vacancy number calculations for HK 40, HPM, 25Cr-

35Ni (HP-Nb) and 35Cr-45Ni, respectively. The calculated electron vacancy numbers for these alloys are 2.89, 2.68, 2.60 and 2.63, respectively.

Nickel and chromium are the most common element in controlling carburization. The relationship of carbon absorption with nickel content depicts the decrease of carbon absorption with increase in nickel content. Silicon along with 3.5-4 % aluminum has been effective. But the rupture strength and weldability of both cast and wrought heat resistant alloys are affected if the silicon exceeds 2 %. Also ductility and fabricability (necessary for piping, tubing, pressure vessels, etc.) change adversely when aluminum percentage is higher than 2-2.5%. [64] It has been tried unsuccessfully to control the carburization of heat resistant alloys for long periods of time using coatings and surface enrichment using chromium, aluminum and silicon, and their combinations. Aluminum vapor diffusion coatings (Alonizing^{TM}) were unable to sustain the extreme temperatures of 1010 – 1040 C (1850 – 1900 F). [54]

The petrochemical industries face the problem of carburization more frequently than refining. Carburization is problematic in the radiant section of ethylene cracking furnaces. It is less severe and less frequent in reforming operations and in processes handling certain ratios of $CO/CO_2/H_2$ gas mixtures and other hydrocarbons [54]. Carburization is a serious problem in ethylene cracking furnaces due to the high tube metal temperatures reaching 1149 C (2100 F) and high carbon potential associated with the cracking of mixtures of naphtha, ethane, propane, and other hydrocarbon feedstocks. [12, 54]

As temperature and carbon are the main variables affecting carburization rate in ethylene cracking tubes, increasing steam dilution will reduce the rate. Thus the rate of carburization is process driven. The type of feed is also a factor with heavier feeds generally being less aggressive than lighter feeds because of their lower carbon potential. [54]

The rate of carburization is influenced by the severity and form of decoking operations. Steam is less deleterious than steam/air mixtures during decoking. Carburization is accelerated by high temperature decoking with low quantities of steam. [65] Carburization cannot be eliminated totally but can be reduced using the appropriate metallurgy. The most important characteristic of a useful alloy is the ability to form and maintain a stable protective oxide film. Chromium oxide films do not possess such quality and are unable to be sufficiently stable at the higher operating temperatures, and low oxygen partial pressures. Silica and alumina are better alternative for full protection in the heat resistant alloys but the addition of silicon or aluminum leads to poor strength, aged ductility, and/or weldability. The best solution is to have an alloy with 2 % of either elements; keeping in mind that still it is not the best alternative. [54]

Carburization is totally unpredictable and is non-uniform in nature in ethylene furnace tubes. Numerical models [66-76] developed with some success in predicting the general rates of carburization are based on operating experience which undermines their acceptability. This is because of the non-uniform nature of occurrence of carburization. It can be deduced that the degree of carburization vary dramatically both around the circumference of tubes and over short distances along the length of the tube. Temperature along with surface condition was considered as a major determining factor yet cannot be considered effective as the tubes which were initially identical and saw the same service conditions for a long time behave quite differently [54]. Also, the degree of carburization cannot be properly quantified due to the problem of non-uniformity. Carburization patterns are useful in revealing uneven firing patterns which are unable to be detected otherwise. Moreover, the complex model calculations fail to consider carbide precipitation having varying size and composition; and transport and phase boundary reaction through a changing matrix with concentration gradients [12]. This in turn helps in the implementation of selective metallurgical alternatives for tube alloys. So, in case of multi-tube coils, the upstream tube could be made of the lower cost, lower nickel modified HP alloys and outlet tubes of the higher cost and more resistant 35Cr-45Ni alloys [54].

1.3. Creep in Carburized and Uncarburized Materials

In high temperature applications creep resistance and ductility are highly important to the service life of components. Blackburn [77] studied the importance of creep behavior of carburized materials at service temperature. The tolerance can be increased to the stresses caused by differences between carburized and uncarburized zones because of high creep ductility which plays an important part in extending the life of carburized tubes. One of the candidate materials having high ductility is an alloy having composition 35% Cr-25% Ni -3.5-4.0% W.

For alloy Incoloy 800 (UNS No. N08800: 21% Cr-31% Ni-45% Fe-0.06%C-0.2% Al-0.4% Ti) [12] and Incoloy 800 with 1% Nb, two creep mechanisms are observed from the stress dependence of the creep rate: dislocation creep at high stresses and diffusion creep at low stresses. And after carburization, the diffusion creep observed is faster for both alloys. But, the dislocation creep is faster only for alloy 800 with Nb addition after carburization. The carburized specimens have been observed to have a longer lifetime when the creep rate is 10^{-7} s^{-1}. Void and crack formation and poor reduction in area led to brittle fracture for alloy 800 under the uncarburized and the carburized conditions. Voids are vertical to the stress direction formed at grain boundary carbides. There is less void formation with the fracture being ductile in case of carburized alloy 800 with 1% Nb. [78]

The equation XLVII shows that ε (creep rate) is directly proportional to the n^{th} power of the subtraction of σ_o (a threshold stress which is inversely proportional to the distance of particles) from σ (the applied stress). A is a proportionality factor which decreases with increasing number of particles at the grain boundaries and n is an exponent greater than equal to 3.

$$\varepsilon = A\,(\sigma - \sigma_o)^n \qquad \text{(XLVII)}$$

The carburization, in agreement with metallographic micrographs, leads to decrease of the factor A and an increase of the threshold stress σ_o which can be proved by a plot of $\varepsilon^{1/3}$ v/s σ. The carburized alloy 800 having Nb shows a threshold stress twice as high as that for the carburized alloy 800 without Nb because of presence of considerable amount of fine carbides in the grains. There is an increased amount of grain boundary carbides and smaller distances for the particles in the grains for the alloy 800 without Nb. [12] So in summary, if the carbon content is not too high in alloy 800, creep behavior is not deteriorated by carburization [78].

1.4. Oxidation: Beneficial not Detrimental

One of the types of most commonly experienced high temperature corrosion is oxidation. In the case of ethylene pyrolysis tubing, oxidation is considered as being not detrimental; it serves as a source for the development of corrosion resistance oxide film in heat resistant Fe- Ni- Cr alloys. Cr_2O_3 (Chromium Oxide) is considered as a useful film. The rate of oxidation increases with the increase in temperature, which is harmful. To increase oxidation resistance, increasing chromium content is considered a viable option. In a typical low sulphur flue gas environment, the rate of oxidation for these alloys is lower. [54]

The amount of other elements such as aluminum, silicon, rare earths, etc. to enhance the oxidation resistance has a limit on account of fabrication difficulties, and resulting instabilities. Only a small percent of rare earth elements such as yttrium, cerium, etc. are generally added. In wrought alloys, aluminum added is not more than 4 % and silicon is limited to less than 2 %. There exist very few alloys having chromium more than 30 %. High percentage of nickel causes chromium oxide to be more resistant to spalling and increases the metallurgical stability of the composition. The modified HP heat resistant and centrifugally cast alloys are generally used in ethylene cracking furnaces [12]. The failure of ethylene cracking furnace tube is not due to excessive oxidation rates but is due to carburization and coking tendencies. [54]

Thus, the present research incorporates:

i) Determine what microstructural changes the Fe-Ni-Cr tubing undergoes during service.

ii) Strategies for limiting catalytic coke formation by adhering coatings via pulsed laser deposition (PLD) to material traditionally used for pyrolysis heaters.

References

[1] C. A. Sorrell, Industrial Materials for the Future, (U. S. Department of Energy, 2001).

[2] S. Field, "Ethylene profitability trends", Hydrocarbon Processing 69 (1990) 47.

[3] A. K. K. Lee and A. M. Aitani, "Saudi Ethylene Plants Move Toward More Feed Flexibility", Oil and Gas Journal 88 (1990) 60.

[4] K. W. Otto, "Olefin-Capacity Surge Will Tighten Feedstock Supplies", Oil and Gas Journal 87 (1989) 35.

[5] K. M. Sundaram, Feedstocks Used in Ethylene Pyrolysis Plants, edited by A. P. S. Chauhan (Stony Brook, 2006).

[6] D. L. Trimm, in "Pyrolysis: Theory and Industrial Practice", edited by L. F. Albright, B. L. Crynes and W. H. Corcoran (Academic Press, 1983).

[7] G. F. Froment, B. O. Van de Steene, P. S. Van Damme, S. Narayanan and A. G. Goossens, "Thermal Cracking of Ethane and Ethane-Propane Mixtures", Industrial & Engineering Chemistry, Product Research and Development 15 (1976) 495.

[8] E. Ranzi, M. Dente, A. Goldaniga, G. Bozzano and T. Faravelli, "Lumping Procedures in Detailed Kinetic Modeling of Gasification, Pyrolysis, Partial Oxidation and Combustion of Hydrocarbon Mixtures", Progress in Energy and Combustion Science 27 (2001) 99.

[9] D. L. Trimm and C. J. Turner, "Pyrolysis of Propane - Effect of Hyrdrogen Sulphide", Journal of Chemical Technology and Biotechnology 31 (1981) 285.

[10] L. L. Crynes and B. L. Crynes, "Coke Formation on Polished and Unpolished INCOLOY 800 Coupons during Pyrolysis of Light Hydrocarbons", Industrial & Engineering Chemistry Research 26 (1987) 2139.

[11] L. F. Albright and J. C. Marek, "Mechanistic Model for Formation of Coke in Pyrolysis Units Producing Ethylene", Industrial & Engineering Chemistry Research 27 (1988) 755.

[12] H. J. Grabke, Carburization - A High Temperature Corrosion Phenomenon (Materials Technology Institute of the Chemical Processing Industries, Inc., St. Louis, MO, 1998).

[13] G. E. Moller and C. W. Warren, "Survey of Tube Experience in Ethylene and Olefins Pyrolysis Furnaces. T-5B-6 Task Group Preliminary Report", Materials Performance 20 (1981) 27.

[14] K. M. Sundaram and G. F. Froment, "Kinetics of Coke Deposition in the Thermal Cracking of Propane", Chemical Engineering Science 34 (1979) 635.

[15] K. M. Sundaram, P. S. Van Damme and G. F. Froment, "Coke Deposition in the Thermal Cracking of Ethane", AIChE Journal 27 (1981) 946.

[16] S. Ibarra, in "Pyrolysis: Theory and Industrial Practice", edited by L. F. Albright, B. L. Crynes and W. H. Corcoran (Academic Press, 1983) p. 427.

[17] L. F. Albright and J. C. Marek, "Coke Formation During Pyrolysis: Roles of Residence Time, Reactor Geometry, and Time of Operation", Industrial & Engineering Chemistry Research 27 (1988) 743.

[18] L. F. Albright and J. C. Marek, "Analysis of Coke Produced in Ethylene Furnaces: Insights on Process Improvements", Industrial & Engineering Chemistry Research 27 (1988) 751.

[19] G. Bach, G. Zimmermann, F.-D. Kopinke, S. Barendregt, P. van den Oosterkamp and H. Woerde, "Transfer-line heat exchanger fouling during pyrolysis of hydrocarbons. 1. Deposits from dry cracked gases", Industrial & Engineering Chemistry Research 34 (1995) 1132.

[20] F. D. Kopinke, G. Zimmermann and S. Nowak, "On the Mechanism of Coke Formation in Steam Cracking - Conclusions from Results Obtained by Tracer Experiments", Carbon 26 (1988) 117.

[21] R. Zou, Q. Lou, H. Liu and F. Niu, "Investigation of Coke Deposition During the Pyrolysis of Hydrocarbon", Industrial & Engineering Chemistry Research 26 (1987) 2528.

[22] D. C. W. Blaikley and N. Jorgensen, "Studies of Catalytically Enhanced Carbon Deposition and Removal Using a Gas Plasma System", (Publ by Elsevier Science Publ BV (North-Holland), Amsterdam, Neth, Loughborough, Engl, 1990) p. 277.

[23] J. J. Jones and J. Huber, in Tenth Ethylene Producer's Conference (1998) p. 105.

[24] C. A. Bernardo, Carbon Formation and Removal in the Context of Nickel Catalysts, Dissertation: Thesis (Doctoral), (University of London, London, 1977).

[25] M. J. Bennett, "Carbon Deposition: A Major Technological Problem", Materials and Corrosion-Werkstoffe Und Korrosion 49 (1998) 345.

[26] H. Cai, A. Krzywicki and M. C. Oballa, "Coke Formation in Steam Crackers for Ethylene Production", Chemical Engineering and Processing 41 (2002) 199.

[27] A. LaCava, Dissertation: Thesis (Doctoral), (University of London, London, 1977).

[28] H. W. Slotboom and J. M. L. Penninger, "Reactions of n-ButylBenzene in Thermal HydroCracking", Erdoel & Kohle, Erdgas, Petrochemie 27 (1974) 410.

[29] H. W. Slotboom and J. M. L. Penninger, "Role of the Reactor Wall in the Thermal Hydrocracking of Polyaromatic Compounds", Industrial & Engineering Chemistry, Process Design and Development 13 (1974) 296.

[30] D. L. Trimm, "Formation and Removal of Coke from Nickel Catalyst", Catalysis Reviews 16 (1977) 155.

[31] L. F. Albright and J. C. Marek, "Mechanistic Model for Formation of Coke in Pyrolysis Units Producing Ethylene" (Unpublished Paper), (Pudue University, 1986).

[32] L. F. Albright and W. A. McGill, "Metallurgical Control of Coke Formation in Olefin Furnaces Through Alonizing", (AIChE, New York, NY, USA, New Orleans, LA, USA, 1986) p. 34.

[33] R. T. K. Baker, M. A. Barber, R. J. Waite, P. S. Harris and F. S. Feates, "Nucleation and Growth of Carbon Deposits from Nickel Catalyzed Decomposition of Acetylene", Journal of Catalysis 26 (1972) 51.

[34] R. T. K. Baker, P. S. Harris, R. B. Thomas and R. J. Waite, "Formation of Filamentous Carbon from Iron, Cobalt and Chromium Catalyzed Decomposition of Acetylene", Journal of Catalysis 30 (1973) 86.

[35] A. M. Brown and M. P. Hill, "Characterization of Carbon Deposit Morphologies using In-Situ Scanning Electron Microscopy", in American Chemical Society Symposium Series 202, edited by L. F. Albright and R. T. K. Baker (ACS, Washington, DC, USA, New York, NY, USA, 1982) p. 193.

[36] A. I. LaCava, E. D. Fernandez-Raone, L. L. Isaacs and M. Caraballo, "Effect of Hydrogen on the Iron- and Nickel- Catalyzed Formation of Carbon from Benzene", in American Chemical Society Symposium Series 202, edited by L. F. Albright and R. T. K. Baker (ACS, Washington, DC, USA, New York, NY, USA, 1982) p. 89.

[37] J. G. McCarty, P. Y. Hou, D. Sheridan and H. Wise, "Reactivity of Surface Carbon on Nickel Catalysts: Temperature-Programmed Surface Reaction with Hydrogen and Water", in American Chemical Society Symposium Series 202, edited by L. F. Albright and R. T. K. Baker (ACS, Washington, DC, USA, New York, NY, USA, 1982) p. 253.

[38] C.-T. Chen, Surface Effects During Pyrolysis of Normal and Iso-Butanes Using a Continuous Flow Thermal Gravimetric Reactor, Dissertation: Thesis (Doctoral), (Oklahoma State University, Stillwater, 1987) p. 178 leaves.

[39] S. J. Gregg and H. F. Leach, "Reaction of Nickel with Carbon Monoxide at Elevated Temperatures", Journal of Catalysis 6 (1966) 308.

[40] J. C. Marek and L. F. Albright, "Surface Phenomena During Pyrolysis: The Effects of Treatments with Various Inorganic Gases", in American Chemical Society Symposium Series 202, edited by L. F. Albright and R. T. K. Baker (ACS, Washington, DC, USA, New York, NY, USA, 1982) p. 151.

[41] J. C. Marek and L. F. Albright, "Formation and Removal of Coke Deposited on Stainless Steel and Vycor Surfaces from Acetylene and Ethylene", in American Chemical Society Symposium Series 202, edited by L. F. Albright and R. T. K. Baker (ACS, Washington, DC, USA, New York, NY, USA, 1982) p. 123.

[42] M. Audier, P. Bowen and W. Jones, "Transmission Electron-Microscopic Study of Single-Crystals of Fe_7C_3", Journal of Crystal Growth 63 (1983) 125.

[43] L. F. Albright and J. C. Marek, "Coke Formation During Pyrolysis as a Function of Time of Operation" (Unpublished Paper), (Pudue University, 1986).

[44] R. Siegel and J. R. Howell, Thermal Radiation Heat Transfer (Hemisphere Pub. Corp., McGraw-Hill, Washington, 1981).

[45] B. Lohr, H. Dittman and A. G. Linde, "Steam-Cracker Economy Keyed to Quenching", Oil and Gas Journal 76 (1978) 63.

[46] J. Lahaye, P. Badie and J. Ducret, "Mechanism of Carbon Formation During SteamCracking of Hydrocarbons", Carbon 15 (1977) 87.

[47] D. Nohara and T. Sakai, "Kinetic Study of Model Reactions in the Gas Phase at the Early Stage of Coke Formation", Industrial & Engineering Chemistry Research 31 (1992) 14.

[48] D. Nohara and T. Sakai, in American Institute of Chemical Engineers, National Meeting (San Diego, CA, USA, 1990).

[49] G. F. Froment, "Coke Formation in the Thermal Cracking of Hydrocarbons", Reviews in Chemical Engineering 6 (1990) 293.

[50] P. A. Tesner, (Marcel Dekker Inc, New York, NY, USA, 1984) p. 1.

[51] M. Dente, E. Ranzi, S. Barendregt and F. W. Tsai, "Ethylene Cracker Transferline Exchanger Fouling: (A Study Towards the Mechanisms Involved and Mathematical Modelling of the Exchanger Performance)", (AIChE, New York, NY, USA, Houston, TX, USA, 1983) p. 45.

[52] M. W. Clark, "Materials Barrier in Pyrolysis Tubing for Ethylene Production", in Annual Conference, National Association of Corrosion Engineers (Philadelphia, PA, USA, 1970).

[53] R. Hubert and J. Thuillier, Carburization in Heat Resisting Alloys Used in Pyrolysis Furnaces, in "Acieres du Manoir Pompey" (1971).

[54] D. J. Tillack and J. E. Guthrie, "Wrought and Cast Heat-Resistant Stainless Steels and Nickely Alloys for the Refining and Petrochemical Industries", Nickel Institute Technical Series 10 (1998).

[55] H. E. Buhler, A. Rahmel and H. J. Schuller, "Observations Made with Carburization and Irreversible Transformation of Iron-Chromium-Nickel-Carbon Alloys", ARCHIV FUR DAS EISENHUTTENWESEN 38 (1967) 223.

[56] H. J. Grabke and A. Schnaas, "Review on High Temperature Gaseous Corrosion and Mechanical Performance \of Alloy 800\ in Carburizing and Oxidizing Environments", in Petten International Conference on Alloy 800 (North Holland Pub., Amsterdam, The Netherlands, 1978) p. 195.

[57] A. Schnaas and H. J. Grabke, "High- Temperature Corrosion and Creep of Ni-Cr-Fe Alloys in Carburizing and Oxidizing Environments", Oxidation of Metals 12 (1978) 387.

[58] A. Schnaas and H. J. Grabke, "VERAENDERUNG DER WERKSTOFFEIGENSCHAFTEN AUSTENITISCHER CeNiFe-LEGIERUNGEN DURCH AUFKOHLUNG. (Changes in Material Properties of Austenitic CrNiFe-Alloys by Carburization)", Werkstoffe und Korrosion 29 (1978) 635.

[59] R. A. Rapp, "Kinetics Microstructures and Mechanism of Internal Oxidation - Its Effect and Prevention in High Temperature Alloy Oxidation", Corrosion 21 (1965) 382.

[60] C. Wagner, "REAKTIONSTYPEN BEI DER OXYDATION VON LEGIERUNGEN", Zeitschrift Fur Elektrochemie 63 (1959) 772.

[61] D. F. Lupton and P. J. Ennis, "Influence of Carburisation on the Ductility of Four High Temperature Alloys", Res Mechanica Letters 1 (1981) 245.

[62] W. Steinkusch, "DAS AUFKOHLUNGSVERHALTEN VERSCHIEDENER WERKSTOFFE FUER PYROLYSEROHRE. (Carburizing Behavior of Various Alloys for Tubular Pyrolysis Furnace)", Werkstoffe und Korrosion 30 (1979) 837.

[63] Control of Electron Vacancy Number in Superalloys [SAE AS5491], in "SAE Aerospace Standards" (Society of Automotive Engineers, Inc., USA, 2002) p. 6.

[64] C. M. Schillmoller, "HP-Modified Furnace Tubes for Steam Reformer and Steam Crackers", Nickel Institute Technical Series.

[65] D. J. Hall, M. K. Hossain and R. F. Atkinson, "Carburisation Behaviour HK40 Steel in Furnaces used for Ethylene Production", High Temperatures - High Pressures 14 (1981) 527.

[66] K. Bongartz, D. F. Lupton and H. Schuster, "Model to Predict Carburization Profiles in High Temperature Alloys", Metallurgical Transactions A (Physical Metallurgy and Materials Science) 11A (1980) 1883.

[67] K. Bongartz, W. J. Quadakkers, R. Schulten and H. Nickel, "Mathematical Model Describing Carburization in Multielement Alloy Systems", Metallurgical Transactions A (Physical Metallurgy and Materials Science) 20A (1989) 1021.

[68] K. Bongartz, R. Schulten, W. J. Quadakkers and H. Nickel, "Finite Difference Model Describing Carburization in High-Temperature Alloys", Corrosion (Houston) 42 (1986) 390.

[69] H. J. Christ, W. Christl and H. G. Sockel, "AUFKOHLUNG VON HOCHTEMPERATURWERKSTOFFEN - TEIL L: MODELLMAESSIGE MATHEMATISCHE BESCHREIBUNG DES VORGANGES DER EINDIFFUSION MIT GLEICHZEITIGER AUSSCHEIDUNG EINER VERBINDUNG DES EINDRINGENDEN ELEMENTES

Carburization of High-Temperature Materials - Part 1: Mathematical Model Description of the Penetration and Simultaneous Precipitation of a Compound of the Diffusing Element", Werkstoffe und Korrosion 37 (1986) 385.

[70] D. Farkas and K. Ohla, "Modelling of Diffusion Processes During Carburization of Alloys", Oxidation of Metals 19 (1983) 99.

[71] H. J. Grabke, K. Ohla, J. Peters and I. Wolf, "Radiotracer Studies of Carbon Permeation Through Oxide Scales on Commercial High Temperature Alloys and Model Alloys", Werkstoffe und Korrosion 34 (1983) 495.

[72] S. Ling, T. A. Ramanarayanan and R. Petkovic-Luton, "Computational Modeling of Mixed Oxidation-Carburization Processes: Part 1", Oxidation of Metals 40 (1993) 179.

[73] H. G. McMath, Modelling Metallurgical Reactions in Steam Cracker Tubes 1995).

[74] J. A. Nesbitt, "Numerical Modeling of High-Temperature Corrosion Processes", Oxidation of Metals 44 (1995) 309.

[75] R. Petkovic-Luton and T. A. Ramanarayanan, "Mixed-Oxidant Attack of High-Temperature Alloys in Carbon- and Oxygen-Containing Environments", Oxidation of Metals 34 (1990) 381.

[76] H. G. Sockel, H. J. Christ and W. Christl, "Penetration of Foreign Elements Connected with Internal Precipitation: A Computer- Based Description and First Experimental Verification", Materials Science and Engineering 87 (1986) 119.

[77] J. Blackburn, "Current Status of Carburization Testing and Assessment", Materials Performance 16 (1977) 24.

[78] J. Hemptenmacher, G. Sauthoff and H. J. Grabke, "Einfluss der Aufkohlung auf das Kriechverhal ten Einer FeNiCr-HochTemperaturlegierung

Effects of Carburization of the Creep Behavior of a FeNiCr-High Temperature Alloy", Werkstoffe und Korrosion 35 (1984) 247.

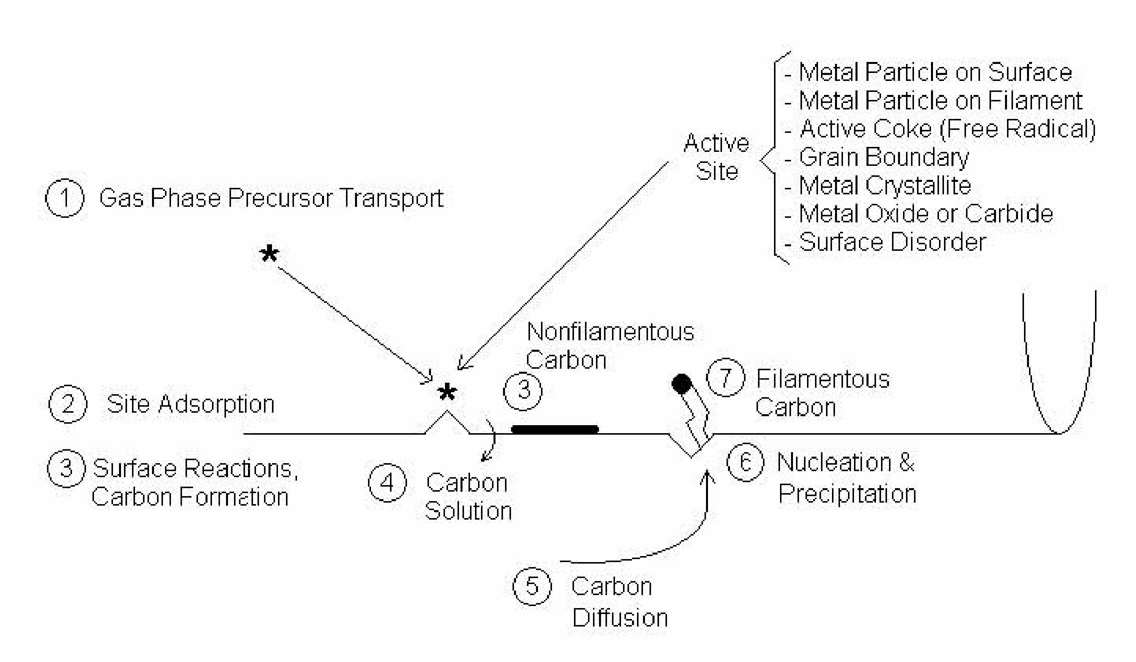

Figure 1.1. Coking Mechanism for Ethylene Pyrolysis Service [10].

Table 1.1. Matrix for Calculation of Nv (Electron Vacancy Number) for HK40 Alloy.

	Element	Wt %	Atomic Weight	Wt % / At. Wt.	Atomic Fraction	Precip. Adj.	Matrix Atomic Fraction	Nv	Nv Product
		A	B	C	D	E	F	G	H
ROW 1	**Cr**	25.00	52.00	0.48	0.26	0.22	0.23	4.66	1.08
ROW 2	**Ti**	0.00	47.90	0.00	0.00	0.00	0.00	6.66	0.00
ROW 3	**Mo**	0.00	95.94	0.00	0.00	0.00	0.00	4.66	0.00
ROW 4	**Al**	0.00	26.98	0.00	0.00	0.00	0.00	7.66	0.00
ROW 5	**Co**	0.00	58.93	0.00	0.00	0.00	0.00	1.71	0.00
ROW 6	**B**	0.00	10.81	0.00	0.00	0.00	0.00	7.66	0.00
ROW 7	**Zr**	0.00	91.22	0.00	0.00	0.00	0.00	6.66	0.00
ROW 8	**C**	0.40	12.01	0.03	0.02	0.00	0.00		0.00
ROW 9	**Si**	2.00	28.09	0.07	0.04	0.04	0.04	6.66	0.27
ROW 10	**Mn**	1.50	54.94	0.03	0.01	0.01	0.02	3.66	0.06
ROW 11	**Fe**	50.60	55.85	0.91	0.49	0.49	0.51	2.66	1.36
ROW 12	**Cu**	0.00	63.54	0.00	0.00	0.00	0.00	0.00	0.00
ROW 13	**V**	0.00	50.94	0.00	0.00	0.00	0.00	5.66	0.00
ROW 14	**W**	0.00	183.85	0.00	0.00	0.00	0.00	4.66	0.00
ROW 15	**Ta**	0.00	180.95	0.00	0.00	0.00	0.00	5.66	0.00
ROW 16	**Cb**	0.00	92.91	0.00	0.00	0.00	0.00	5.66	0.00
ROW 17	**Hf**	0.00	178.49	0.00	0.00	0.00	0.00	6.66	0.00
ROW 18	**Re**	0.00	186.21	0.00	0.00	0.00	0.00	4.66	0.00
ROW 19	**Ni**	20.50	58.71	0.35	0.19	0.19	0.20	0.61	0.12
SUM		100.00		1.87		0.95			**2.89**

Table 1.2. Matrix for Calculation of Nv (Electron Vacancy Number) for HPM Alloy.

	Element	Wt %	Atomic Weight	Wt % / At. Wt.	Atomic Fraction	Precip. Adj.	Matrix Atomic Fraction	Nv	Nv Product
		A	B	C	D	E	F	G	H
ROW 1	Cr	25.00	52.00	0.48	0.25	0.23	0.26	4.66	1.23
ROW 2	Ti	0.00	47.90	0.00	0.00	0.00	0.00	6.66	0.00
ROW 3	Mo	1.50	95.94	0.02	0.01	0.00	0.00	4.66	0.00
ROW 4	Al	0.00	26.98	0.00	0.00	0.00	0.00	7.66	0.00
ROW 5	Co	0.00	58.93	0.00	0.00	0.00	0.00	1.71	0.00
ROW 6	B	0.00	10.81	0.00	0.00	0.00	0.00	7.66	0.00
ROW 7	Zr	0.00	91.22	0.00	0.00	0.00	0.00	6.66	0.00
ROW 8	C	0.17	12.01	0.01	0.01	0.00	0.00		0.00
ROW 9	Si	1.80	28.09	0.06	0.03	0.03	0.04	6.66	0.25
ROW 10	Mn	1.00	54.94	0.02	0.01	0.01	0.01	3.66	0.04
ROW 11	Fe	32.53	55.85	0.58	0.31	0.31	0.35	2.66	0.93
ROW 12	Cu	0.00	63.54	0.00	0.00	0.00	0.00	0.00	0.00
ROW 13	V	0.00	50.94	0.00	0.00	0.00	0.00	5.66	0.00
ROW 14	W	0.00	183.85	0.00	0.00	0.00	0.00	4.66	0.00
ROW 15	Ta	0.00	180.95	0.00	0.00	0.00	0.00	5.66	0.00
ROW 16	Cb	0.00	92.91	0.00	0.00	0.00	0.00	5.66	0.00
ROW 17	Hf	0.00	178.49	0.00	0.00	0.00	0.00	6.66	0.00
ROW 18	Re	0.00	186.21	0.00	0.00	0.00	0.00	4.66	0.00
ROW 19	Ni	38.00	58.71	0.65	0.34	0.33	0.37	0.61	0.23
SUM		100.00		1.82		0.91			**2.68**

Table 1.3. Matrix for Calculation of Nv (Electron Vacancy Number) for 25Cr-35Ni (HP-Nb) Alloy.

	Element	Wt %	Atomic Weight	Wt % / At. Wt.	Atomic Fraction	Precip. Adj.	Matrix Atomic Fraction	Nv	Nv Product
		A	B	C	D	E	F	G	H
ROW 1	**Cr**	25.00	52.00	0.48	0.26	0.22	0.23	4.66	1.06
ROW 2	**Ti**	0.00	47.90	0.00	0.00	0.00	0.00	6.66	0.00
ROW 3	**Mo**	0.00	95.94	0.00	0.00	0.00	0.00	4.66	0.00
ROW 4	**Al**	0.00	26.98	0.00	0.00	0.00	0.00	7.66	0.00
ROW 5	**Co**	0.00	58.93	0.00	0.00	0.00	0.00	1.71	0.00
ROW 6	**B**	0.00	10.81	0.00	0.00	0.00	0.00	7.66	0.00
ROW 7	**Zr**	0.00	91.22	0.00	0.00	0.00	0.00	6.66	0.00
ROW 8	**C**	0.45	12.01	0.04	0.02	0.00	0.00		0.00
ROW 9	**Si**	2.20	28.09	0.08	0.04	0.04	0.04	6.66	0.30
ROW 10	**Mn**	1.50	54.94	0.03	0.01	0.01	0.02	3.66	0.06
ROW 11	**Fe**	35.85	55.85	0.64	0.34	0.34	0.37	2.66	0.97
ROW 12	**Cu**	0.00	63.54	0.00	0.00	0.00	0.00	0.00	0.00
ROW 13	**V**	0.00	50.94	0.00	0.00	0.00	0.00	5.66	0.00
ROW 14	**W**	0.00	183.85	0.00	0.00	0.00	0.00	4.66	0.00
ROW 15	**Ta**	0.00	180.95	0.00	0.00	0.00	0.00	5.66	0.00
ROW 16	**Cb**	0.00	92.91	0.00	0.00	0.00	0.00	5.66	0.00
ROW 17	**Hf**	0.00	178.49	0.00	0.00	0.00	0.00	6.66	0.00
ROW 18	**Re**	0.00	186.21	0.00	0.00	0.00	0.00	4.66	0.00
ROW 19	**Ni**	35.00	58.71	0.60	0.32	0.33	0.35	0.61	0.21
SUM		100.00		1.86		0.94			**2.60**

Table 1.4. Matrix for Calculation of Nv (Electron Vacancy Number) for 35Cr-45Ni Alloy.

	Element	Wt %	Atomic Weight	Wt % / At. Wt.	Atomic Fraction	Precip. Adj.	Matrix Atomic Fraction	Nv	Nv Product
		A	B	C	D	E	F	G	H
ROW 1	Cr	35.00	52.00	0.67	0.36	0.31	0.34	4.66	1.57
ROW 2	Ti	0.00	47.90	0.00	0.00	0.00	0.00	6.66	0.00
ROW 3	Mo	0.00	95.94	0.00	0.00	0.00	0.00	4.66	0.00
ROW 4	Al	0.00	26.98	0.00	0.00	0.00	0.00	7.66	0.00
ROW 5	Co	0.00	58.93	0.00	0.00	0.00	0.00	1.71	0.00
ROW 6	B	0.00	10.81	0.00	0.00	0.00	0.00	7.66	0.00
ROW 7	Zr	0.00	91.22	0.00	0.00	0.00	0.00	6.66	0.00
ROW 8	C	0.45	12.01	0.04	0.02	0.00	0.00		0.00
ROW 9	Si	2.20	28.09	0.08	0.04	0.04	0.05	6.66	0.30
ROW 10	Mn	1.50	54.94	0.03	0.01	0.01	0.02	3.66	0.06
ROW 11	Fe	15.85	55.85	0.28	0.15	0.15	0.16	2.66	0.43
ROW 12	Cu	0.00	63.54	0.00	0.00	0.00	0.00	0.00	0.00
ROW 13	V	0.00	50.94	0.00	0.00	0.00	0.00	5.66	0.00
ROW 14	W	0.00	183.85	0.00	0.00	0.00	0.00	4.66	0.00
ROW 15	Ta	0.00	180.95	0.00	0.00	0.00	0.00	5.66	0.00
ROW 16	Cb	0.00	92.91	0.00	0.00	0.00	0.00	5.66	0.00
ROW 17	Hf	0.00	178.49	0.00	0.00	0.00	0.00	6.66	0.00
ROW 18	Re	0.00	186.21	0.00	0.00	0.00	0.00	4.66	0.00
ROW 19	Ni	45.00	58.71	0.77	0.41	0.41	0.44	0.61	0.27
SUM		100.00		1.87		0.93			**2.63**

2. Pyrolysis Heater Radiant Coil Materials of Construction

2.1. Introduction

Generally in pressure vessels, pipings, fittings, valves and other equipment in refineries and petrochemical plants a wide variety of iron and nickel-based materials are used. Plain carbon steel is the most common. It loses strength and is susceptible to oxidation at 316-343 C. On addition of Cr (0.5-9%) and Mo (0.5-1%) the working temperature can be increased to 650 C. As these alloys have inadequate corrosion resistance at high temperature, more specialized Ni-Cr-Fe alloys are required. The aggressive environments in petrochemical and refining applications require cast and wrought heat-resistant alloys which have high Cr and Ni. Earlier HK40 material replaced commonly used wrought, heat resistant alloys and was used solely in the reformer tubes for 20-25 years. Slowly, HK40 was displaced by HP-Nb and most recently, 35Cr-45Ni is employed. There have also been developments in wrought alloys which have started displacing the cast alloys in crucial applications, such as, short residence time ethylene cracking furnaces. [1]

In petrochemical and refining industries, the main selection criteria to materials are:

i) Mechanical Properties

ii) Corrosion Resistance

iii) Fabricability
iv) Availability
v) Cost

The challenge has been developing material with (i) sufficient ductility at 1100 C to withstand in-service stresses, (ii) sufficient high temperature (~1100 C) creep strength; and (iii) sufficient ductility below 700 C after service aging to withstand startup and shutdown stresses. The materials normally used in ethylene pyrolysis service are listed in Table 2.1.

2.2. Materials Used for Radiant Coils in Pyrolysis Heaters

2.2.1. Cast: HK40, HP Type, 35Cr-45Ni, 36X Alloys

(A) HK40 Alloy

Research was done in the mid 1970s for improving the service temperatures by 100 degree C over HK 40 alloy as well as making it weldable and easy to cast by varying composition of iron, nickel and chromium [2], and with the addition of Ti and Nb [3-6]. Also addition of Nb, Ti and/or Zr showed improvement in the low cycle fatigue (LCF) life and fatigue crack propagation (FCP) resistance under creep conditions [7, 8]. Cerium was added (i.e. to form CeO_2 coatings) to improve hot corrosion cracking due to formation of Cr_2O_3 scale and other alloys were developed for greater resistance to thermal fatigue [9, 10]. Pack aluminization of HK40 alloy showed increased carburization resistance by 60 % [11-13]. Even deposition of SiC using pulsed lasers was looked into with regards to improving the HK40 alloy [14, 15]. The addition of semi-refractory and refractory elements of Group IVA – VIA such as vanadium (V), niobium (Nb), Molybdenum (Mo) or, Tungsten (W) assisted high temperature (HT) materials such as HK40 to withstand sulphidation [16]. Even laser remelting seems to improve the oxidation resistance of HK40 alloy at high temperature(s) [17].

Earlier mid-wall creep fissuring was detected using ultrasonic testing methods in order to predict the tube life and to forecast future tube replacements [18]. High quality crack-free welds were obtained by spray-arc transfer using Ar – 1% CO_2 as the shielding gas [19, 20]. Weldability was improved by the use of low heat inputs (630-950 kJm^{-1}) and low interpass temperatures (below 150 C). Buttering technique, use of high heat inputs 1100-1400 kJm^{-1}) and continuous welding led to fissures and cracks [21]. The weldability of aged parts is affected by transformation of primary carbides, precipitation of secondary carbides, and formation of sigma phase and nickel silicides [22]. An experimental technique, which uses optical gage having optical fiber, to measure local creep strain on the weld of HK40 with 15CrMo at 850 C has been reported [23, 24]. Mathematical modeling using finite element analyses was done to study the effect of temperature, carburization, internal pressure and creep on the life of HK40 tubing [25, 26]. Eddy current non-destructive techniques for carburization measurements using ANSYS finite element model (FEM) has also been reported [27]. Diffusion of carbon into the HK40 alloy matrix during carburization leading to precipitation of $M_{23}C_6$ and transformation to M_7C_3 was verified experimentally as well [28]. The correlation between rupture behavior and the elemental segregation of chromium, manganese, carbon, and silicon at the inner and middle regions was observed by line profiles and elemental mapping [29].

Initial cell structure of centrifugally cast tubes obtained by employing graphite, cast iron, and copper molds for solidification showed coarsening and continuous growth of the columnar grains [30, 31]. At higher temperature the dendrite structure obtained showed inverse relation with the square of creep rupture strength [31]. The main reasons for damage of HK40 steam reforming furnace tube are coalescence of carbides in higher temperature range and formation of the sigma phase in lower temperature range [32]. On incorporating electromagnetic field as in the case of electromagnetic centrifugal casting (ECC), development of equiaxed grains take place as well as refinement of both the columnar and equiaxed grains. Primarily, it is grain refining and increase of eutectic carbides [33]. This delays the coalescing and coarsening of the secondary carbides in the aging process and increases the tensile properties of casting at both room and higher temperatures [30, 34].

Generally the structure of HK40 alloys is characterized by a skeletal eutectic carbide network having finer secondary carbide precipitates for higher creep strength [35]. Additives such as zirconium (Zr), niobium (Nb) and titanium (Ti) increase dispersed secondary carbides in the matrix of material [7]. But at high temperatures, precipitation of sigma phase and carbides in HK40 alloys reduce strength [31, 36, 37]. Particularly, lamellar metallic carbide $M_{23}C_6$ precipitation is harmful to high temperature strength [38]. It is also observed that the number of secondary carbides precipitated in the HK40 alloy is larger than that of HP alloy [39]. Quantitative investigation of the change of microstructural parameters of the unstable carbide structure with time to understand the continuous decrease of the strain rate has been reported [40].

Carburization is found to be the main cause for the HK40 tube failures at high temperatures based on calculation and experiments [14, 15, 26 and 28]. From the synthesis gas mixtures (reaction products of methane with steam) in the laboratory to reproduce carburization in HK40 steel tubes used in ethylene production, it was found that the partial pressure of oxygen in the gas mixture, oxide scales and total carbide-forming element control carburization rate [41, 42]. Thus, carburization is preceded by oxidation on the inside of the tube; and fine precipitations of secondary carbides are the carburization products [43]. Carbide-denuded zones and complex oxide structures in both internal and external oxide scales are formed in subsurface regions due to oxidizing and carburizing conditions. [44] Also, composition and nature of the surface which is first exposed to the carburizing environment and oxides of iron on the surface can have a marked influence on the carburization behavior of HK40 [41]. On comparison of HK40 tubular material commissioned in service for approximately 25000 hours with that of virgin HK40, coarsening and transformation of the $M_{23}C_6$ eutectoid carbide phase of the as-cast condition into the M_7C_3 carbides with a heavily faulted structure is observed. The decreasing ratio of Cr/C necessitates transformation of higher Cr/C $M_{23}C_6$ carbides into M_7C_3 during the carburization. Precipitates of γ within M_7C_3 led to porosity in the material [45].

Some observations made during creep crack growth in HK40 alloy are:

a) The stress intensity factor increases the crack growth rate of the cast specimen faster than that of the creep damaged specimen. The fine secondary carbides play a vital role [46].

b) Creep crack growth rate and creep rupture life rely on both creep strength and creep ductility (elongation or reduction in area). Creep rupture life is a function of the primary, secondary and tertiary mechanisms. The longest creep rupture life is smaller than the creep ductility to reach the lowest creep crack growth [47].

c) Cracks propagate along the intensive sub-boundaries, on which coarse $M_{23}C_6$ carbides precipitate during the low cycle fatigue (LCF) test. The secondary carbides formed by addition of Zr, Nb and Ti additives lead to a uniform dislocation structure without intensive sub-boundaries and thus resulting in the dispersed precipitation of $M_{23}C_6$ carbides [7].

d) At the same aging temperature of 1250 C, creep crack growth rate of the specimens aged after the solution treatment is higher than that of the directly aged specimens, and which in turn is higher than the as-cast specimen. The blocky-shaped carbides produced by solution treatment have less resistance to crack growth than skeleton-shaped eutectic carbides on grain boundaries. The resistance to crack growth increases with the increase in size of secondary carbides, and decreases after reaching a critical size [48].

e) Creep crack growth process of HK40 steel is composed of the nucleation, growth and linkage of cavities in the front of the crack. The grain boundary strength cannot be neglected when considering the effect of the precipitate particles that mainly controls the grain strength [49].

f) 1% creep rupture strength of HK40 alloy in a carburizing environment is much less than in air for short and medium test times. But, on exposing the alloy for 4000 hours, the trend is opposite. [50, 51] The mechanisms responsible for creep rate irregularities are the process of particle ripening, the early formation of creep damage, and environment metal interactions [52].

g) There is existence of three regions of differing grain structures observed in cross-section of a centrifugally cast HK40 tube, such as, columnar grains in the middle region which occupies more than half of the cross-section, coarse equiaxed grains in the inner wall layer, and fine equiaxed grains near the outer tube wall [48, 53, 54]. The creep crack growth resistance of equiaxed grain material is superior to that of the columnar grain, when the load line is perpendicular to the columnar grain axis [53, 55]. The columnar grain boundaries assist in the propagation of the creep cracks in cast HK40 tubes. The higher creep crack propagation resistance is illustrated by an inclined columnar grain structure. The relation between creep crack propagation rate (da/dt) and grain inclination angle (θ) is in:

$$da/dt = A\left(K_I \cos^2(\theta/2) \right)^m \tag{1}$$

where, A and m are constants and K_I is the stress intensity factor [54].

h) In an in-service HK40 alloy for 25000 hours, silicon having high oxygen affinity is rejected to the matrix due to carburization and not able to dissolve in carbides. This happens to be an important precursor to crack propagation [44].

Konosu et al. [56-58] studied the creep-fatigue damage interactions at 800 C, 900 C and 1000 C for HK40 alloy for establishing design criteria. It was mentioned that the life fraction rule (LFR) assumes that fracture occurs when the sum of fatigue damage (ϕ_f) and creep damage (ϕ_c) equals a certain value (D), when damage is divided into fatigue damage and creep damage. The fracture criterion is given by the equation:

$$\phi_f + \phi_c = D \tag{2}$$

Fatigue damage ϕ_f and creep damage ϕ_c are given by:

$$\phi_f = n/N_f \tag{3}$$

$$\phi_c = \sum(t/t_r) \tag{4}$$

where, n and N_f are the number of cycles in a given strain range and corresponding fatigue life in this strain gauge, respectively; t is the working time at a given stress whereas t_r is stress rupture life under this stress. So, for the HK40 alloy creep-fatigue damage criteria based on the LFR were derived as:

$$5.67\phi_f + \phi_c = 1 \; ; \; \phi_c \geq 0.15 \tag{5}$$

$$\phi_f + 5.67\phi_c = D \; ; \; \phi_c < 0.15 \tag{6}$$

The LFR was applicable in estimating the creep-fatigue lives when materials were subjected to a cyclic strain pattern having tension hold periods at elevated temperatures, as the creep damage effect during the strain hold period could be sufficiently incorporated by such evaluation. Kihara, et al. [59] showed that the life lost before temporarily overheating the HK40 alloy beyond the design temperature cannot be recovered by any heat treating during the creep test. Also, the long-term creep strength cannot be improved.

HK40 was pack aluminized (also known as alonization), chromized and thermal sprayed with aluminum to improve the life time of bed heat-transfer tubes in an atmospheric fluidized bed combustor [60]. Results were promising with regard to use in syngas coolers operated at 500 C for long-time service on high-sulfur medium-btu gas [13, 61]. In alonization which is a specific variety of chemical vapor deposition (CVD), there is diffusion of aluminum; and the activity of the aluminum controls the phase composition of the diffusion layer. The desired phase, NiAl and Ni_3Al present in the aluminized layer obtained by two-process has better carburization resistance than that of the traditional process [11, 62].

Another interesting observation in HK40 alloy used in petrochemical plants is metal dusting, known as deleterious high temperature (350 – 900 C) corrosion phenomenon leading to pitting and metal wastage and thus disintegration of Fe, Ni and Co based materials into fine metal particles and carbon. It is different from carburization and occurs at activity $a_c > 1$. Uniform metal dusting, oxidation or sulfidation causes thinning. Pitting usually occurs with localized carburization followed by oxidation of the chromium carbides. It occurs on the inner diameter (ID) of the tubing [63, 64]. During metal dusting nickel directly disintegrates whereas the iron forms metastable carbide (cementite). Microstructural chromium dependent features seem to protect against metal dusting. The common starting mechanism on the atomic scale shows basal graphite lattice planes arranged in perpendicular orientation to the metal or, carbide surface and serving as active sites in the disintegration process. The reactions involved in metal dusting are:

$$CO + H_2 \rightarrow C_{(dissolved)} + H_2O \qquad (7)$$

$$3Fe + C_{(dissolved)} \rightarrow Fe_3C \qquad (8)$$

$$CO + H_2 \rightarrow C_{(graphite)} + H_2O \qquad (9)$$

$$Fe_3C \rightarrow 3Fe + C_{(graphite)} \qquad (10)$$

Equation 7 shows the dissolution of carbon in the metal delivered from the gas atmosphere. The formation of cementite from the carbon supersaturated metal is depicted by equation 8. After the graphite deposition on the metal occurs as shown in equation 9, cementite phase becomes unstable and starts disintegrating (when carbon activity $a_c = 1$) in equation 10. [65]

(B) HP Type Alloy

HP type centrifugally cast alloys are chemistry and vendor specific and are not governed by any national or international specification. The HP-BST reformer tube alloy has a better relaxation than HK40 alloy which leads to lesser effect of cyclic thermal stress on the creep damage at higher design temperature [66]. The creep-fatigue properties of conventional HK40 and HP-Nb alloys at both 800 and 1000 C is lower than HP-BST-M (Nb- and Ti-containing 25Cr-35Ni steel). Besides, low carbon HP-Nb matches HP-BST-M in creep-fatigue properties. HP-Nb matches HK40 in creep rupture strength at 800 C, but had higher strength than HK40 at 1000 C. Excellent creep ductility of HP-BST-M and low carbon-HP-Nb alloy is the reason behind the superior creep-fatigue properties [8]. Also, the fatigue-limited plant lifetime for HP-45 alloy at 1144 K was investigated by the total plastic work-per-cycle approach [67].

The rupture time of HP steel is greater than HK40 steel at the same initial stress intensity. The increase in resistance to cracking is due to more-eutectic carbides generated because of decrease of the solubility of $M_{23}C_6$ carbide in matrix. Resistance to creep crack growth increases with increasing nickel content [68].

For short time exposures, the number of secondary carbides precipitated on dislocations in the HP steel is lower than the HK40 steel. After long time exposure at high temperatures: the number of secondary carbides in HP steel increases, the shape of eutectic carbides in the HP steel was complex, whereas those in HK40 steel were simply spherical [39]. HP-Nb-Ti catalytic reformer tube have more reliable and longer tube life; lower thermal stress level and higher creep rupture strength (during high temperature service after ageing) in comparison to HK40 catalytic reformer [69]. The number of catalyst tubes of HP-Nb-Ti material required is less and thus it is more economic [70].

The resistance to carburization and creep damage of HP 45 (HP + Nb) heat-resistant steel is less than that of HP + W grade. Generally, the mode of tube failure for

HP 45 alloy is a combination of high temperature carburization attack and creep damage leading to intergranular cracking. Overheating during decoking operation(s) needs to be controlled to avoid tube failure [71]. The HP 45 heat resistant alloy having Nb and Ti additives on treating with hydrogen induces coarsening of the chromium carbides [72].

(C) 35Cr-45Ni Alloy

Centrifugally cast 35Cr-45Ni alloy has better stress rupture, resistance to oxidation, corrosion and carburization than most available ethylene pyrolysis tubing [73]. This material shows local corrosion at 600 C but not at 650 C in coal gasification atmospheres [74]. On using the tubing for molten carbonates, Ni showed excellent corrosion resistance with increasing P_{CO2} as well as the fuel gas. The formation of protective films and cathodic reaction is increased by oxygen. Thus, the corrosion rate of steel at high Po_2 decreases and at low Po_2 increases [75].

(D) 36X Alloy

Manaurite 36X, as-cast alloy is also used in steam/hydrocarbon reformer furnace tube. Baer et al., Richter, Bruch et al. and Schubert et al. have published results pertaining to Manaurite 36X which have similar properties and behavior to the above mentioned alloys [76-79].

2.2.2. Wrought: HPM Alloy

Tubes having similar or better elevated temperature strength and carburization resistance, but with higher ductility, better toughness, and ability to be produced in smaller and longer tubing in comparison to HP grade centrifugally cast tubes were developed. HPM, a wrought alloy, has the composition: 25Cr38Ni-Mo-Ti [80-82]. The application of specially shaped (i.e. straight and twist internally finned) and/or smaller tubings is effective for shortening the reaction time and raising the efficiency of the product ratio in the ethylene plant cracking tubings. HPM based tubes are a better choice on account of no dimensional limitations in diameter, wall thickness and length [83]. The chromium content lowered by the precipitation of eutectic carbides in HP centrifugal casting steel makes it less resistant to carbon deposition than HPM wrought steel [84]. Magnetic force microscopy (MFM) used to study the change in magnetic behavior of a HPM alloy carburized by exposure in an ethylene production furnace shows transition from paramagnetic to ferromagnetic material. The chromium depleted region around carbides is the origin for ferromagnetism, and the ferromagnetic material links up to form an increasing domain structure [85]. Eddy current carburization measurements for HPM tubes used in ethylene production have been mentioned elsewhere [27].

2.3. Coatings Used for Radiant Coils in Pyrolysis Heaters

2.3.1. Silicon Carbide

Silicon based ceramics such as silicon carbide (SiC) have been identified by the Department of Energy as attractive materials for ethylene pyrolysis heater tubing due to their higher temperature capabilities relative to metals and alloys; high thermal conductivity; retention of mechanical properties at operating temperatures; and excellent thermal shock resistance. Long length prototype SiC tubes have been constructed by FM Technologies Inc. (Fairfax, VA) with the intent that: the service temperature could be increased from 1000 to ~1400 C; 6.39 trillion BTU/ year (based on 10% increase in efficiency) could be potentially saved by converting ethane to ethylene at higher temperatures; and the reduction in catalytic coke formation would result in fewer productivity losses resulting from shutdowns for coil cleaning. [86] Although this seems viable, it is important to note that the high temperatures and pressures experienced during operation (i.e. in- service and during decoking) leads to catastrophic failures of metallic tubing making it impractical to use “brittle ceramic tubing”. [87] Thus deposition of SiC coatings via pulsed laser deposition (PLD) to the inner diameter of tube material was investigated. [14, 15]

2.3.2. Other Coating Considerations

As mentioned by Grabke [63], Cr_2O_3 and SiO_2 oxide layers prevent diffusion of carbon from coke into the matrix of the tubings made of Cr-Ni-Fe based alloys and acts as an initial deterrent to catalytic coke formation. If the concentration of oxides such as Cr_2O_3 is increased on the inner diameter of tube material, then it will subdue the initial catalytic coke formation. Pulsed laser deposition of Fe- Ni- Cr alloys in oxidizing atmospheres onto similar materials used in ethylene pyrolysis service has been reported. [88]

References:

[1] D. J. Tillack and J. E. Guthrie, "Wrought and Cast Heat-Resistant Stainless Steels and Nickely Alloys for the Refining and Petrochemical Industries", Nickel Institute Technical Series 10 (1998).

[2] P. I. Fontaine and P. J. Penrice, "Development of a Weldable, Cast Ni-Cr-Base Alloy IN-643 for Use in High-Temperature Tube Applications", Journal of the Institute of Metals (London) 101 (1973) 15.

[3] M. Bahaa Zaghloul, T. Shinoda and R. Tanaka, "On the Strengthening of the Centrifugally Cast HK40 Tube", in Institution of Chemical Engineers Symposium Series (Claitor's Publ Div, Baton Rouge, La, 1976) p. 265.

[4] Y. Fukui, R. Sasaki, F. Hataya and H. Ishizuka, "High-Temperature Strength and Ductility of HK40 and HP Centrifugal Casting Tube after Long-Term High-Temperature Heating", in Tetsu-To-Hagane/Journal of the Iron and Steel Institute of Japan (1982) p. 444.

[5] Y. Fukui, R. Sasaki, F. Hataya and S. Takahasi, "Effect of Alloying Elements on Creep Rupture Strength of 25Cr-20Ni Casting Steel", Tetsu-To-Hagane/Journal of the Iron and Steel Institute of Japan 64 (1978) 478.

[6] T. Shinoda, M. B. Zaghloul, Y. Kondo and R. Tanaka, "Effect of Single and Combined Additions of Ti and Nb on the Structure and Strength of the Centrifugally Cast HK40 Steel", Transactions of the Iron and Steel Institute of Japan 18 (1978) 139.

[7] T. Yokomaku and M. Saori, "Microstructural and Mechanical Factors Affecting Creep-Fatigue Properties of Heat Resisting Cast Steels", Zairyo/Journal of the Society of Materials Science, Japan 39 (1990) 181.

[8] T. Yokomaku, M. Saori, T. Okuda and A. Nohara, "Creep-Fatigue Properties of Various Reformer-Tube Materials and their Life-Prediction Methods", Zairyo/Journal of the Society of Materials Science, Japan 37 (1988) 308.

[9] A. R. Ward, "Newer Alloys Widen the Scope for Castings in Heat Treatment Furnaces", Heat Treatment of Metals 4 (1977) 89.

[10] C. Zeng, J. Zhang and W. Wu, "The Effects of Ce on Hot Corrosion of Iron-Based Alloys", Journal of Rare Earths 12 (1994) 225.

[11] Z.-R. Huang, L.-B. Ma and P.-N. Li, "Pack Aluminization of HK40 Steel and Evaluation of Carburization Resistance", Cailiao Gongcheng/Journal of Materials Engineering (2005) 25.

[12] Z.-R. Huang, L.-B. Ma, P.-N. Li and H. Xu, "Controlled New Process of Pack Aluminization", Cailiao Rechuli Xuebao/Transactions of Materials and Heat Treatment 25 (2004) 692.

[13] R. A. Perkins, "Materials for Syngas Coolers of Entrained Slagging Gasifiers", in Corrosion Resistant Materials for Coal Conversion Systems (Applied Science Publ, London, Engl, London, Engl, 1983) p. 219.

[14] A. Chauhan, W. Moran, E. Casey, W. Si and H. White, "Limiting Catalytic Coke Formation by the Application of Adherent SiC Coatings via Pulsed Laser Deposition to the Inner Diameter of Tube Material Traditionally Used for Ethylene Pyrolysis Service", (Materials Research Society, Warrendale, PA 15086, United States, Boston, MA, United States, 2005) p. 341.

[15] A. Chauhan, W. Moran, S. Ge, W. Si and H. J. White, "Pulsed Laser Deposition of Silicon Carbide on Heat Resistant Materials", Scripta Materialia 52 (2005) 735.

[16] K. N. Strafford, P. K. Datta, A. F. Hampton, F. Starr and W. Y. Chan, "Influence of Additions of Refractory Elements on the Sulphidation Behaviour of Cobalt-Based Alloys", Corrosion Science 29 (1989) 775.

[17] G. Fu, W. Wu, M. Wang and S. Zhu, "Oxidation Behavior of Laser Remelted Cr-Containing Steels", Journal of Materials Science and Technology 9 (1993) 258.

[18] R. E. Marlow, "Ultrasonics as a Detection Tool", in Saf in Ammonia Plants and Relat Facil, Symp, 17th Annu, Proc, AIChE Natl Meet, 78th (AIChE (Ammonia Plant Safety), New York, NY, Salt Lake City, UT, USA, 1975) p. 65.

[19] P. C. Loh, C. R. Loper, Jr. and J. T. Gregory, "Gas Metal-Arc Welding of HK40 Steel", Welding Journal (Miami, Fla) 60 (1981) 31.

[20] P. C. Loh, C. R. Loper, Jr. and J. T. Gregory, "Welding of HK40 Steel Using Gas Metal-Arc Welding", (AFS, Des Plaines, Ill, USA, Cincinnati, OH, Engl, 1982) p. 506.

[21] H. W. Ebert, "Fabrication of HK-40 in Field", Welding Journal 55 (1976) 939.

[22] S. Haro, R. Colas, A. Velasco and D. Lopez, "Study of Weldability of a Cr-Si Modified Heat-Resisting Alloy", Materials Chemistry and Physics 77 (2003) 831.

[23] X. Y. He, J. Xia, C. Quan, C. J. Tay and S. D. Tu, "Creep Deformation Measurement Using Quartz Optical Fiber", Optics Communications 190 (2001) 79.

[24] J. Xia, C. F. Wang, X. Y. He, S. D. Tu and J. M. Gong, "An Optical Gage for High Temperature Strain Measurement by Using Quartz Optical Fiber", in 2nd International Conference on Experimental Mechanics (Society of Photo-Optical Instrumentation Engineers, Singapore, 2001) p. 229.

[25] X. Su, S. Zhu, L. Wang and F. Wang, "Study on Structure Integrity of HK40 Reformer Tube", Kang T'ieh/Iron and Steel (Peking) 30 (1995) 52.

[26] M. L. Zhu, Y. Yin, T. Wang, S. T. Liu and J. S. Zhang, "Numerical Simulation on Stress and Creep Damage Fraction in Ethylene Cracking Tube", Dalian Ligong Daxue Xuebao/Journal of Dalian University of Technology 41 (2001) 192.

[27] K. J. Stevens and W. J. Trompetter, "Calibration Eddy Current Carburization Measurements in Ethylene Production Tubes Using Ion Beam Analysis", Journal of Physics D: Applied Physics 37 (2004) 501.

[28] M. Zhu, Q. Xu and J. Zhang, "Numerical Simulation of Reaction-Diffusion During Carburization of HK40 Steel", Journal of Materials Science and Technology 19 (2003) 327.

[29] P. G. Caceres-Valencia and I. J. Baiges, "Effect of Elemental Redistribution on the Failure of Centrifugally Cast HK40 Alloy", Journal of Failure Analysis and Prevention 6 (2006) 67.

[30] X.-Q. Wu, Y.-S. Yang, X.-D. Hui and Z.-Q. Hu, "Relationships Between the Initial Solidification Conditions and the Structure Characteristics of Centrifugally-Cast HK40 Steel", Scandinavian Journal of Metallurgy 28 (1999) 59.

[31] M. B. Zaghloul, T. Shinoda and R. Tanaka, "Relation between Structure and Creep-Rupture Strength of Centrifugally Cast HK40 Steel", Transactions of the Iron and Steel Institute of Japan 17 (1977) 28.

[32] M. Saori, T. Yoshida and S. Ohta, "Analysis and Prevention of Failures in Steam Reforming Furnace Tube", R&D, Research and Development (Kobe Steel, Ltd) 33 (1983) 65.

[33] X. Q. Wu, H. M. Jing, Y. G. Zheng, W. Ke, Y. S. Yang and Z. Q. Hu, "Mechanical Properties of the Industrial HK40 Reforming Tubes Produced by an Improved Centrifugal Processing", Zeitschrift fuer Metallkunde/Materials Research and Advanced Techniques 92 (2001) 179.

[34] Y. Yang and Z. Hu, "Solidification of Alloys in Electromagnetic Field", Zeitschrift fuer Metallkunde/Materials Research and Advanced Techniques 91 (2000) 280.

[35] W. Hou, "Structure of Austenitic Stainless Steel Tubes Cast Centrifugally", Kang T'ieh/Iron and Steel (Peking) 22 (1987) 21.

[36] K. Narita, K. Yamamoto, K. Kanamono and C. Hayashi, "Behavior of Precipitates in High Carbon Austenitic Heat-Resisting Steels During Creep Rupture Test at 1050 Degree C", Tetsu-To-Hagane/Journal of the Iron and Steel Institute of Japan 69 (1983) 117.

[37] D. Yamasaki, I. Hirata, T. Morimoto and K. Ono, "Characteristics of Sigma Phase Precipitated in HK40-Alloy", Tetsu-To-Hagane/Journal of the Iron and Steel Institute of Japan 65 (1979) 969.

[38] Z. Shi, Y. Yu, Z. Cao and H. Wang, "Influence of Lamellar Carbides on the High Temperature Endurance Strength of HK40 Alloy", Jinshu Rechuli/Heat Treatment of Metals (1986) 33.

[39] Y. Kondo, Y. Sakurai, J. Namekata, M. Tanaka and F. Hangai, "Effect of High Temperature Aging on Eutectic Carbide Morphology of Centrifugally Cast HK40 and HP Steels", Tetsu-To-Hagane/Journal of the Iron and Steel Institute of Japan 76 (1990) 1195.

[40] G. Luxenburger and M. Schuetze, "Einfluss der Carbidstruktur auf das Kriechverhalten der hitzebestaendigen Edelstahl-Gusslegierung HK 40. [Influence of the Carbide Structure on Creep Behaviour of HK 40]", Zeitschrift fuer Metallkunde 82 (1991) 430.

[41] D. J. Hall, M. K. Hossain and R. F. Atkinson, "Carburisation Behaviour of HK40 Steel in Furnaces Used for Ethylene Producition", in IUPAC Conf on the Chem of Mater at High Temp (Harwell, Engl, 1981) p. 527.

[42] R. H. Kane and J. C. Hosier, "Carburization Resistance of Some Wrought Nickel-Containing Alloys in Simulated Industrial Environments", in High Temperature Corrosion in Energy Systems. (AIME, Metallurgical Soc, New York, NY, USA, Detroit, MI, Engl, 1985) p. 581.

[43] A. Czyrska-Filemonowicz, F. Ciura, A. Zychal and S. Gorczyca, "ANALIZA ZMIAN STRUKTURALNYCH STALIWA HK40 WYWOLANYCH EKSPLOATACJA RUR W INSTALACJI DO PAROWEGO REFORMINGU METANU. [Analysis of the Structural Changes in HK40 Cast Steel Tubes Resulting from Their Use in a Methane Steam Reforming Plant]", Hutnik 48 (1981) 469.

[44] A. A. Kaya, P. Krauklis and D. J. Young, "Microstructure of HK40 Alloy after High Temperature Service in Oxidizing / Carburizing Environment: I. Oxidation Phenomena and Propagation of a Crack", Materials Characterization 49 (2002) 11.

[45] A. A. Kaya, "Microstructure of HK40 Alloy after High-Temperature Service in Oxidizing / Carburizing Environment: II. Carburization and Carbide Transformations", Materials Characterization 49 (2002) 23.

[46] S. Zhu, P. Li, Y. Yu, J. Zhang and Z. Cao, "Effects of Temperature and Creep Damage on Creep Crack Growth in HK40 Steel", Jixie Gongcheng Xuebao/Chinese Journal of Mechanical Engineering 24 (1988) 59.

[47] S. J. Zhu, P. E. Li, J. Zhao and Z. B. Cao, "The Effect of Prior Aging on the Creep Crack-Growth Behaviour of Austenitic HK40 Steel", Materials Science & Engineering A: Structural Materials: Properties, Microstructure and Processing A114 (1989) 7.

[48] S. J. Zhu, J. Zhao and F. G. Wang, "Creep Crack Growth of HK40 Steel: Microstructural Effects", Metallurgical Transactions A (Physical Metallurgy and Materials Science) 21A (1990) 2237.

[49] S. J. Zhu, J. Zhao and F. G. Wang, "Effects of Grain and Grain Boundary-Strengths on the Creep Crack-Growth of HK40 Steel", Scripta Metallurgica et Materialia 24 (1990) 559.

[50] V. Guttman and R. Burgel, "Effect of a Carburizing Environment on the Creep Behaviour of Some Austenitic Steels", in Corrosion Resistant Materials for Coal Conversion Systems (Applied Science Publ, London, Engl, London, Engl, 1983) p. 423.

[51] V. Guttmann and H. Schoenherr, "Creep Properties of Two 25Cr-20Ni Cast Alloys in Air and Under Carburizing Conditions", High Temperature Technology 3 (1985) 79.

[52] V. Guttmann and R. Burgel, "Study on the Influence of Structural Instabilities on Creep of Austenitic Steels", in Deformation of Multi-Phase and Particle Containing Materials, Proceedings of the 4th Riso International Symposium on Metallurgy and Materials Science. (Riso Natl Lab, Roskilde, De, Roskilde, Den, 1983) p. 269.

[53] T. Kawai, K. Takemura, T. Shibasaki and T. Mohri, "Effect of Macrostructure on Catalyst Tube Damage and Creep Rupture Properties of HK40", in AIChE Annu Meet, 72nd (AIChE (CEP (Chem Eng Prog) Tech Man), New York, NY, San Francisco, CA, USA, 1980) p. 119.

[54] S. M. Zhu, S. J. Zhu, J. S. Zhang and S. C. Tjong, "Dependence of Creep Crack Propagation on Columnar Grain Orientation in Cast HK40 Tube", Materials Science and Technology 12 (1996) 513.

[55] S. Zhu, J. Zhao and F. Wang, "Influence of Grain Shape and Carbide on Creep Crack Growth in HK40", Jinshu Xuebao/Acta Metallurgica Sinica 26 (1990) 231.

[56] S. Konosu, "Elevated Eemperature Low-Cycle Fatigue Behavior of HK40 Alloy", Fatigue and Fracture of Engineering Materials & Structures 17 (1994) 683.

[57] S. Konosu, T. Koshimizu, T. Iijima and K. Maeda, "Evaluation of Creep-Fatigue Damage Interaction in HK40 Alloy", Journal of Mechanical Design, Transactions Of the ASME 115 (1993) 41.

[58] S. Konosu, T. Lijima, T. Koshimizu and K. Maeda, "Evaluation of Creep-Fatigue Damage Interaction in HK40 Alloy", in 9th Biennial Conference on Reliability, Stress Analysis, and Failure Prevention presented at the 1991 ASME Design Technical Conferences (Publ by ASME, New York, NY, USA, Miami, FL, USA, 1991) p. 145.

[59] S. Kihara, K. Asakawa, A. Ohtomo and Y. Saiga, "Effects of Overheating and Heat Treatment on Remaining Creep Life of HK40 Alloy", IHI Engineering Review (English Edition) 10 (1977) 12.

[60] J. B. Gilmoure, D. C. Briggs, A. W. Lui and H. Hindam, "Preliminary Results of the Canadian AFBC Materials Tests", in Technical Symposia - Corrosion 85. (NACE, Houston, TX, USA, Boston, MA, USA, 1985) p. 341. 1.

[61] R. A. Perkins, G. Morse and W. C. Coons, Materials for Syngas Coolers (Lockheed Palo Alto Research Laboratory.; Electric Power Research Institute, Palo Alto, CA, 1982).

[62] A. Kim, Y.-D. Jun, K.-B. Lee and S.-H. Nahm, "Particle Erosion of Aged HK40 Steel", in Proceedings of the 11th Asian Pacific Conference on Nondestructive Testing (Trans Tech Publications Ltd, Zurich-Ueticon, CH-8707, Switzerland, Jeju Island, South Korea, 2004) p. 1165.

[63] H. J. Grabke, Carburization - A High Temperature Corrosion Phenomenon (Materials Technology Institute of the Chemical Processing Industries, Inc., St. Louis, MO, 1998).

[64] Koswara, "Case of Metal Dusting on HK40 HyL III Radiant Pipe Heat Exchanger", in Proceedings of the Thirty First Annual Technical Meeting of the International Metallographic Society (ASM International, 9639 Kinsman Road, OH 44073-0002, United States, Ottawa, Ont., Canada, 1998) p. 123.

[65] E. Pippel, J. Woltersdorf and R. Schneider, "Micromechanisms of Metal Dusting on Fe-Base and Ni-Base Alloys", Materials and Corrosion-Werkstoffe Und Korrosion 49 (1998) 309.

[66] Y. Imoto and S. Terada, "Creep Damage Prediction of HP-BST Reformer Tube in View of Thermal Stress", R&D, Research and Development (Kobe Steel, Ltd) 35 (1985) 109.

[67] S. N. Singhal and R. A. Tait, "Evaluation of Low Cycle Creep-Fatigue Degradation for Notched Components", (ASTM, Philadelphia, PA, USA, Bolton Landing, NY, USA, 1987) p. 1096.

[68] S. J. Zhu, Y. Wang and F. G. Wang, "Comparison of the Creep Crack Growth Resistance of HK40 and HP40 Heat-Resistant Steels", Journal of Materials Science Letters 9 (1990) 520.

[69] T. Shibasaki, T. Mohri and I. Kojima, "Experiences of HP-Nb and Ti Catalyst Tubes After Using of Long Term at Elevated Temperature", in Safety in Ammonia Plants and Related Facilities Symposium 2004 (American Institute of Chemical Engineers, New York, NY 10016-5991, United States, Denver, CO, United States, 2004) p. 41.

[70] T. Mohri, K. Takemura and T. Shibasaki, "Proceedings of the 1992 Ammonia Safety Symposium", in Proceedings of the 1992 Ammonia Safety Symposium (Publ by AIChE, New York, NY, USA, San Antonio, TX, USA, 1993) p. 86.

[71] A. Ul-Hamid, H. M. Tawancy, A.-R. I. Mohammed and N. M. Abbas, "Failure Analysis of Furnace Radiant Tubes Exposed to Excessive Temperature", Engineering Failure Analysis 13 (2006) 1005.

[72] A. F. Ribeiro, L. H. De Almeida, D. S. Dos Santos, D. Fruchart and G. S. Bobrovnitchii, "Microstructural Modifications Induced by Hydrogen in a Heat Resistant Steel Type HP-45 with Nb and Ti Additions", (Elsevier Ltd, Annecy, France, 2003) p. 693.

[73] S. Haro, A. Velasco, R. Colas, D. Lopez and L. Martinez, "Weldability Aspects of a Cast Heat-Resistant Alloy", (ASM International, Indianapolis, IN, United States, 2001) p. 135.

[74] S. Kihara, K. Nakagawa, A. Ohtomo and M. Kato, "Corrosion Resistance of High-Chromium Steels in Coal Gasification Atmospheres", Materials Performance 26 (1987) 9.

[75] K. Nakagawa, S. Kihara and S. Ito, "Effect of Gas Composition of the Corrosion of Stainless Steels in Molten Carbonate", Boshoku Gijutsu/Corrosion Engineering 37 (1988) 473.

[76] C. A. Baer and S. P. Henson, "Catalyst Tube Failure Investigation and Inspection Following Furnace Fire", (Publ by AIChE, New York, NY, USA, Los Angeles, CA, USA, 1992) p. 26.

[77] U. Bruch, K. Doehle, J. Puetz, A. Rahmel, M. Schuetze and K. D. Schuhmacher, "Comparison of the Corrosion Behaviour of Different High Temperature Alloys With and Without Superimposed Creep Deformation in an Artificial Steam Reformer Atmosphere", (Natl Research Council of Canada, Ottawa, Ont, Can, Toronto, Ont, Can, 1984) p. 325.

[78] F. Richter, "Thermophysical Properties of Incoloy 800 and 5 Additional FeNiCr-Base High-Temperature Alloys in Comparision with the Nickel-Base Alloy Nimonic 86 between 20 and 1000-Degrees C", Metall 45 (1991) 467.

[79] F. Schubert, U. Bruch, R. Cook, H. Diehl, P. J. Ennis, W. Jakobeit, H. J. Penkalla, E. te Heesen and G. Ullrich, "Creep Rupture Behavior of Candidate Materials for Nuclear Process Heat Applications", Nuclear Technology 66 (1984) 227.

[80] Anon, "HPM, Ethylene Tube Alloy", Advanced Materials & Processes 154 (1998) 35.

[81] Y. Sawaragi, K. Ogawa, Y. Yano, M. Nishi and K. Yoshikawa, "Development of HPM Steel for Ethylene Plant Cracking Tubes", Sumitomo Metals 41 (1989) 11.

[82] K. Shibata and I. Morita, "Evaluation of Service Performance of Wrought and Centrifugal Cast Tubes for Cracking Heater", (ASME, New York, NY, USA, Honolulu, HI, USA, 1995) p. 155.

[83] Y. Sawaragi, H. Teranishi, A. Iseda and K. Yoshikawa, "Development of New Stainless Steel Tubes with High Elevated Temperature Strength for Fossil Fired Boilers and Chemical Plants", Sumitomo Metals 42 (1990) 260.

[84] S. Tokura and Y. Sawaragi, "Carbon Deposition of Cracking Tube Materials Used in Ethylene Plants", Sumitomo Metals 45 (1993) 1.

[85] K. J. Stevens, A. Parbhu, J. Soltis and D. Stewart, "Magnetic Force Microscopy of a Carburized Ethylene Pyrolysis Tube", Journal of Physics D: Applied Physics 36 (2003) 164.

[86] C. A. Sorrell, Industrial Materials for the Future, (U. S. Department of Energy, 2001).

[87] J. V. Albano, B. N. Greene and K. M. Sundaram, Personal Communication, edited by H. J. White (2003).

[88] A. Chauhan, M. Anwar, K. Montero, H. J. White, R. S. Petrova, J. A. Payne, W. Si and J. Bai, "Slip Plane X-ray Residual Stress Analysis of Pulsed Laser Self Ablated Coatings", Surface and Coatings Technology (2006 (Communicated)).

Table 2.1. Nominal Chemical Composition (wt. %) [Typical Ethylene Pyrolysis Tube Materials-of-Construction].

	HK40	HPM	25Cr-35Ni (HP-Nb)	35Cr-45Ni	36X
Carbon	0.40	0.17	0.45	0.45	0.35-0.40
Manganese	1.50	1.00	1.50	1.50	1.00-1.50
Silicon	2.00	1.80	2.20	2.20	1.00-2.00
Nickel	20.50	38.00	35.00	45.00	33.00-38.00
Chromium	25.00	25.00	25.00	35.00	23.00-28.00
Niobium	0.00	0.00	1.20	1.00	Additive
Molybdenum	0.00	1.50	0.00	0.00	0.00
Iron	Balance	Balance	Balance	Balance	Balance

3. Experimentation and Modeling of Coking Phenomena in Fe-Ni-Cr Alloys

3.1. Thermo-Calc

The Thermodynamic-Calculations software (Thermo- Calc) is used for CALculation of PHAse Diagrams (CALPHAD). [1] Calculations of thermodynamic quantities as well as equilibrium calculations are considered as broad classifications of CALPHAD. The modules for calculations within Thermo- Calc are divided as follows:

a) Scheil solidification simulation;
b) Tabulation of thermodynamic functions;
c) Potential diagrams;
d) Pourbaix diagrams (aqueous solutions);
e) Binary and ternary phase diagrams.

The basic thermodynamic principles combined with mathematical formulations to describe the various thermodynamic properties of phases define the history of CALPHAD. The strength of thermodynamics is that the underlying laws and principles are applicable to any type of system and therefore the CALPHAD approach can be used equally well in many disciplines, such as, geology, chemical and process engineering, materials science engineering and nuclear technology, etc. The brief chronology in the development of Thermo-Calc is:

- 1969 Formation of CALPHAD.
- 1971 Sublattice model for 2 compositions (Hillert and Staffansson, KTH: The Royal Institute of Technology, Sweden).
- 1977 Development of Thermo-Calc starts.
- 1977 KTH member of SGTE.
- 1981 First version of Thermo-Calc.
- 1981 Sublattice model for multi-component systems.
- 1984 First sale of TC and the Fe-data base.
- 1986 First version of TC for VAX/VMS.
- 1988 SGTE solution database (SSOL).
- 1990 First UNIX version of TC.
- 1992 TC 32-bit DOS/Windows version.
- 1994 First sale of DICTRA.
- 1997 The company Thermo-Calc Software is created.
- 2000 TCW, first real Windows version of TC.
- 2004 The subsidiary Thermo-Calc. Software Inc. is formed.

The first law of thermodynamics; the second law of thermodynamics; the third law of thermodynamics; chemical equilibrium and thermodynamics; and thermodynamics in solution phase form the basis of CALPHAD/ Thermo-Calc. The reason for preferring thermodynamic software like Thermo-Calc can be elucidated by considering the case of Cr-Fe system. Here, the Gibbs energy is described in liquid and solid states using the generalized formula as shown in equation 1. [1]

$$G = G_{ref} + G_{mix}^{ideal} + G_{mix}^{xs} \qquad (1)$$

$$G_{ref}^{b.c.c.} = x_{Cr} G_{Cr}^{b.c.c.} + x_{Fe} G_{Fe}^{b.c.c.} \qquad (2)$$

$$G_{ref}^{liq} = x_{Cr} G_{Cr}^{liq} + x_{Fe} G_{Fe}^{liq.} \qquad (3)$$

$$G_{ref} = \sum_i x_i G_i^0 \qquad (4)$$

In equations 2 and 3, Gibbs energies of the BCC and liquid phases in pure Cr and Fe are depicted by $G_{Cr,Fe}^{b.c.c}$ and $G_{Cr,Fe}^{liq}$ respectively. Equation 4 shows the same in generalized form, where G_i^0 and x_i are the Gibbs energy and mole fraction of component i. G_{mix}^{ideal} is the ideal Gibbs energy shown in equation 5 and 6 whereas G_{mix}^{xs} is the excess energy of mixing depicted in equation 7.

$$G_{mix}^{ideal} = RT\left(x_{Cr} \log_e x_{Fe} + x_{Fe} \log_e x_{Cr}\right) \qquad (5)$$

$$G_{mix}^{ideal} = RT \sum_i x_i \log_e x_i \qquad (6)$$

$$G_{mix}^{xs} = \sum_{i=1}^{n} \sum_{j=i+1}^{n+1} x_i x_j \left[\Omega_{ij}^0 + \Omega_{ij}^1 \left(x_i - x_j\right) + \Omega_{ij}^2 \left(x_i - x_j\right)^2 \ldots\ldots\ldots\ldots \right] (7)$$

Therefore to solve complicated equations such as equation 7 for thermodynamics system having only two components, a mathematical software tool, Thermo-Calc, is required. Ansara et al. [2] were able to determine the phase boundaries of the Cr-Ni-Fe-C system using CALPHAD. In line with study, here phase equilibria using Thermo-Calc and the TTNi Database [3] for 25Cr-35Ni (HP Nb), HK40, HPM, 35Cr-45Ni alloys were studied to determine what phases would be present during service temperatures.

3.1.1. 25Cr-35Ni (HP-Nb) Alloy

Isothermals (900 C, 1000 C, 1100 C, and 1200 C) of the 5 component C, Si, Ni, Cr, Fe system are shown in Figure 3.1. Here, the minor elements Mn and Nb were not considered to simplify the calculations. Since the inlet and midsection tube metal temperatures are typically between 900 - 1000 C, the outlet tube metal temperature is typically between 1000- 1100 C, and localized regions where coke deposits exist could reach temperatures ~ 1200 C; the selected isothermals for the multicomponent system can be used to predict internal carburization behavior of the tubing. Table 3.1 summarized these features.

At 900 and 1000 C, $M_{23}C_6$ initially exist in the FCC_A1 matrix. As internal carburization proceeds (green dotted line), $M_{23}C_6$ and M_7C_3 will initially co- exist (at 1% C) and eventually $M_{23}C_6$ will convert to M_7C_3. Bongartz [4], Zhang [5], and Christ [6] have proposed the following equations for the formation of $M_{23}C_6$ and M_7C_3 and transformation of $M_{23}C_6$ to M_7C_3.

$$16Cr + 7Fe + 6C = Cr_{16}Fe_7C_6 \qquad (8)$$

$$7Cr + 7Fe + 6C = 2Cr_{3.5}Fe_{3.5}C_3 \qquad (9)$$

$$54C + 7Cr_{16}Fe_7C_6 + 63Fe \rightarrow 32Cr_{3.5}Fe_{3.5}C_3 \qquad (10)$$

A similar situation exists at higher temperatures, the only difference being an increase in the amounts of carbon and chromium that exist in the FCC_A1 matrix (see tie line through 3% C on each phase diagram). The maximum amount of carbon/ chromium in the FCC_A1 matrix that can exist prior to graphite precipitation can also be determined from the phase diagrams (see location marked * on each of the phase diagrams and Table 3.1). Using these values and an expression which describes the depth of the internal carbide formation zone [7], a rough estimate can be made of the time required for through wall carburization (see equation 11).

$$t = \frac{x^2 * \nu * C_{Cr}}{2 * \varepsilon * D_C * C_C} \qquad (11)$$

In this equation υ is a stoichiometric factor; C_{Cr} is the chromium content in the FCC_A1 matrix; C_C is the carbon content in the FCC_A1 matrix; x is the tube wall thickness; D_C is the carbon diffusivity (~ 10^{-7} cm^2/ sec from [8]); and ε ranges from 0 to 1. For values of $\varepsilon < 1$, carbide formation slows the diffusion of carbon in the matrix. [9] Considering that carbides will impede carbon diffusion ($\varepsilon = 0.5$); $D_C = 10^{-7}$ cm^2/ sec; $\upsilon = 3$; x = 6 mm; and C_C and C_{Cr} values obtained from Table 3.1 (carbon/ chromium content in FCC_A1 before graphite precipitation). Figure 3.5(A) graphically shows the concentration of carbon and chromium at different temperatures. The estimated time for complete through wall carburization of HP-Nb tubing exposed to ethylene pyrolysis service at 1100 C was determined to be approximately 2 years, plotted in Figure 3.6. [10]

3.1.2. HK40, HPM, 35Cr-45Ni Alloys

Similar isothermals (900 C, 1000 C, 1100 C, and 1200 C) for the HK40, HPM, 35Cr-45Ni calculated for the 5 component C, Si, Ni, Cr, Fe system using Thermo-Calc are shown in Figures 3.2 - 3.4 respectively. Co, Mn, Nb and other minor elements were not considered to simplify the calculations. These figures likewise can be used to infer carbide precipitation and internal carburization behavior of the tubings made of HK40, HPM, and 35Cr-45Ni respectively at different temperatures, depicted in Table 3.2-3.4.

(i) **HK40 Alloy**:

In isothermals (900 C, 1000 C, 1100 C, and 1200 C) for HK40 alloy shown in Figure 3.2, $M_{23}C_6$ initially exist in the FCC_A1 matrix at 900 and 1000 C. $M_{23}C_6$ and M_7C_3 initially co- exist (at 1% C) and in the end, with the progress of internal carburization (green dotted lines), $M_{23}C_6$ transforms to M_7C_3. At higher temperatures, there is increase in amounts of carbon and chromium that exist in the FCC_A1 matrix (see tie line via 3% C on each phase diagram). The phase diagram also shows the maximum amount of carbon/ chromium (see location marked * on each of the phase diagrams and Table 3.2) in the FCC_A1 matrix existing prior to graphite precipitation at different temperatures shown in Figure 3.5(B). Using equation 11, the rough estimate for through wall carburization of

HK40 tubing exposed to ethylene pyrolysis service at 1100 C was determined to be approximately 1 year, outlined in Figure 3.6.[10]

(ii) **HPM Alloy**:

In Figure 3.3, illustrating isothermals (900 C, 1000 C, 1100 C, and 1200 C) for HPM alloy, $M_{23}C_6$ initially exist in the FCC_A1 matrix at 900 and 1000 C. Furthermore there is co- existence of $M_{23}C_6$ and M_7C_3 initially (at 0.75% C), and with the progress of internal carburization (green dotted lines), $M_{23}C_6$ converts to M_7C_3 in the end. At temperatures 1100 and 1200 C, the amount of chromium and carbon that exist in the matrix increases (tie line through 3% C on each phase diagram). In the FCC_A1 matrix, the maximum amount of carbon/ chromium (see location marked * on each of the phase diagrams and Table 3.3) that exists prior to graphite precipitation can be also be determined from the phase diagrams; also displayed in Figure 3.5(C).The rough estimate of time calculated using equation 11 for through wall carburization of HPM tubing subjected to ethylene pyrolysis service at 1100 C comes out to be approximately 2 years, similar to HP-Nb tubing; Figure 3.6. [10]

(iii) **35Cr-45Ni Alloy**:

Phase equilibria of 35Cr-45Ni at 900 C, 1000 C, 1100 C, and 1200 C are outlined in Figure 3.4. Here, $M_{23}C_6$ and sigma exist initially in the FCC_A1 matrix. Similar to the above mentioned HP-Nb, HK40 and HPM alloys, here too is initial co-existence of $M_{23}C_6$ and M_7C_3 initially (at 2% C) with advancement of internal carburization (green dotted lines), and later leading to the conversion of $M_{23}C_6$ to M_7C_3. Here, again a similar behavior at temperatures 900 C, 1000 C and 1100 C, but with a slight difference in increase in the quantities of chromium and carbon existing in the FCC_A1 matrix (see tie line through 3% C on each phase diagram). The maximum amount of carbon/ chromium (see location marked * on each of the phase diagrams and Table 3.4) that exists in the FCC_A1 matrix prior to graphite precipitation at separate temperatures can be obtained from the phase diagrams. The graphical plots of these values are shown in Figure 3.5(D). Equation 11 is again is used for calculating through wall carburization of 35Cr-45Ni tubing used in ethylene pyrolysis service at 1100 C, predicts tube life to be approximately 3 years, marked in Figure 3.6.[10]

Under the chosen conditions ($\varepsilon = 0.5$; $D_C = 10^{-7}$ cm^2/ sec; $\upsilon = 3$; $x = 6$ mm), it can be deduced that 35Cr-45Ni tubing is more resistant and HK40 tubing is least resistant to carburization at higher temperatures. The trend shown in Figure 3.6 is correct but it does not match with the tubings failed due to carburization in petrochemical plants. Carburization is less prevalent at lower temperature than at higher temperature; and does not follow the linear trend as shown in Figure 3.6. [10]

3.2. X-Ray Mapping

The mechanism of atomic number contrast used in scanning electron microscopy (SEM) prepared with the backscattered electron signal aids in providing information on compositional heterogeneity. It lacks in specific compositional information as its inability to identify the elements present or their concentration levels in spite of being able to recognize and classify the relative gray levels in the image by the knowledge of the sequence of the average atomic numbers of the phases present. [11]

The first imaging method showing the location of elements in a solid with a micrometer spatial resolution using x-ray signal(s) derived from a spectrometer(s) to prepare scanning images was developed by Duncumb and Cosslett in 1956. Due to the capability to show the presence or absence of each element within the field of view, led to the nomenclature “X-ray Mapping”. X-ray mapping finds applications in materials science, physics, chemistry, biology, environmental science, and geology. X-ray mapping can be incorporated in electron probe microanalyzer (EPMA), scanning electron microscope, and analytical electron microscope (AEM). [11, 12]

In x-ray mapping, the abundance of an element using the image intensity is generated as a two-dimensional image. X-ray mapping finds application in the cases where elements are marked and in the observance of element in different locations. Hence, the elements present are determined using survey analyses before doing x-ray mapping. The collection of characteristic x-rays from elements is done by rastering a focused electron beam over the specimen to excite atoms in the specimen. Generally, electrons are given preference in x-ray mapping of specimens because of their ability to excite atoms to produce characteristic x-rays, focusing to a small probe, and deflection to form scanned beam raster. [11, 12]

X-ray maps initially were determined with the wavelength-dispersive spectrometer (WDS) [13] and then later energy-dispersive x-ray spectrometer (EDS) was used [14]. The elemental detectability for WDS is 0.5-1 wt % and for EDS is 2-5 wt % and spatial resolution of 1 um is observed in x-ray maps of bulk specimens. X-ray maps are recorded both as analog dot maps and digital intensity maps. Digital intensity maps have displaced the analog dots maps in modern times due to their ability to be stored, processed and displayed using computers. [15, 16] The disadvantage with digital maps is that the data is collected sequentially, that is, the beam steps to the next pixel only after dwelling at the present pixel for a specified period of time while collecting x-ray counts. The full map is not available in real time but only after the scan is complete. This can disqualify the collected map because of contamination, electron beam damage and specimens drift. The survey scans in analog dot maps assist in verifying the appropriateness of collection of long-term maps. The survey-scan capability of analog maps is mimicked by rapid collection of digital maps by using various schemes. [17]

Diffusion, precipitation, and phase equilibria related phenomena of HP-Nb a centrifugally cast austenitic micro- alloyed nickel- chromium- iron alloy {0.45 wt% C/ ~1.5 wt% Mn/ ~2.2 wt% Si/ 35 wt% Ni/ 25 wt% Cr/ 1.2 wt% Nb/ bal Fe} [10] decommissioned from ethylene pyrolysis service as well as HPM, a wrought nickel-chromium- iron alloy {0.17 wt% C/ ~1.8 wt% Si/ 38 wt% Ni/ 25 wt% Cr/ 1.5 wt% Mo/ 1.0 wt% Mn/ bal Fe} were studied using SEM and X-ray mapping.

HP-Nb, HPM tubing removed from an ethylene pyrolysis plant during scheduled re- tubing; and HP-Nb tubing prior to service were supplied by ABB Lummus Global Incorporated. A 12 mm x 12 mm x 6 mm section of the tubing was removed and mounted in cross section in vacuum impregnated epoxy. The sample was prepared using standard metallographic specimen preparation techniques and examined (energy dispersive spectroscopy, x-ray mapping, and backscatter electron micrographs) using the LEO 1550 Schottky Field Emission Gun- Scanning Electron Microscope at Stony Brook University. [10]

In the present study, a complex oxide protective coating which formed on the HP-Nb alloy surface while in service prevented diffusion of carbon into the material from the process stream. Figure 3.7 shows a backscattered electron image and x-ray maps of the HP-Nb alloy prior to service. The x-ray maps indicate that all elements (C, Cr, Fe, Nb, Ni, Si, and O) are uniformly distributed in the matrix. The Fe- Si- Nb- Cr collage shows traces for chromium carbide that exist in the matrix. The large concentration of carbon at the surface is due to the sample preparation consumables. [10]

Figure 3.8 show backscattered electron images and x-ray maps of the diffusion and carbide precipitation behavior HP-Nb tubing which was decommissioned from ethylene pyrolysis service during a schedule re-tubing. While in service (1) chromium oxide forms at the surface; (2) silicon oxide forms beneath the chromium oxide surface layer; (3) metal carbides (mostly chromium) precipitate in the bulk; and (4) iron, nickel, and niobium remain uniformly distributed in the matrix. Figure 3.9 backscattered electron images and x-ray maps, higher magnification, again shows (1) the segregation of chromium and silicon to the surface to form a complex oxide coating which prevents diffusion of carbon; (2) beneath the protective layer, chromium is depleted from the FCC_A1 matrix; and (3) in the bulk metal carbides (mostly chromium) precipitate out of the FCC_A1 matrix. In Figure 3.10, the formation of precipitates of chromium carbide phases can be clearly seen in bulk. And, X-ray map of element C (carbon) is shown distinctly in Figure 3.11. Figure 3.12 shows backscattered electron images and x-ray maps of HPM alloy tubing decommissioned from ethylene pyrolysis service during a schedule re-tubing. Here, as can be seen all the elements (Cr, Fe, Ni, Si, and O) are uniformly distributed with negligible amount of Nb and C in the matrix. In the Fe-Si-Nb-Cr and C-Si-Cr collage, homogeneity of the elements can be seen. The large concentration of carbon at the surface is due to the sample preparation consumables. [10]

Several researchers have proposed models and have provided explanations for carburization of pyrolysis tubing.[18-29] Goldstein and Moren [18] studied the diffusion of carbon in the ternary Fe- C- M system (where M= Cr, Si, or Mn) utilizing Fick's second law for a ternary system to describe the diffusion process.

$$\frac{dC_C}{dt} = D_{CC}^{Fe}\frac{\partial^2 C_C}{\partial x^2} + D_{CM}^{Fe}\frac{\partial^2 C_M}{\partial x^2} \qquad (12)$$

$$\frac{dC_M}{dt} = D_{MM}^{Fe}\frac{\partial^2 C_M}{\partial x^2} + D_{MC}^{Fe}\frac{\partial^2 C_C}{\partial x^2} \qquad (13)$$

In these equations, C is the concentration of carbon and the metal M (Cr, Si, or Mn); self diffusion coefficient D_{MM} and D_{CC} measure the effects of the concentration gradient of a given component on its own flux, and D_{MC} and D_{CM} measure cross effects or ternary diffusional interactions. They further stated that D_{MM} is negligible since it diffuses via substitutional mechanisms (its value should be 10^4 to 10^6 time less than D_{CC} which diffuses via interstitial mechanisms); D_{MC} is small (= 0); and D_{CM} and D_{CC} can be estimated using an expression proposed by Brown and Kirkaldy [30]. This study did not include stainless steel compositions and did not consider the effect of carbide precipitation on carbon diffusion. Bongartz [4] and Zhang et al. [5] developed models for carbide precipitation events during the carburization process. These studies (1) coupled the effects of carbon diffusion and carbide precipitation; (2) considered as separate entities carbon in the matrix and that in the carbide; (3) only allowed the carbon in the matrix to diffuse; and (4) allowed carbide precipitates to serve as obstacles which slow down the carburization process. [10]

3.3. Magnetization Behavior Resulting from Carburization

B-H plot is conventionally used to present the behavior of magnetic materials during magnetization [31-33]. The magnetic materials at a temperature below T_c (Curie temperature) are composed of small-volume regions, called domains, in which there is a mutual alignment in the same direction of all magnetic dipole moments. Each domain is magnetized to its saturation magnetization and adjacent domains are separated by domain boundaries or walls, across which the direction of magnetization gradually changes. The large number of domains having different magnetization orientations is present in a macroscopic piece of material. The appropriately weighted vector sum of the magnetizations of all the domains is zero for an unmagnetized specimen. As depicted in the Figure 3.13(A) [31, 32]:

a) The unmagnetized condition of a ferromagnetic material is represented by the origin of coordinates O. On application of magnetizing force H, the domains change shape and size by the movement of domain boundaries until the macroscopic specimen becomes a single domain at point A, which is nearly aligned with the field. So, the line OA is known as magnetization curve.

b) From the saturation point A, when the applied field H is reduced by reversal of field direction, the curve does not retrace its original path. The B field lags behind the applied H field, or decreases at a lower rate giving rise to a hysteresis effect. When H field has been reduced to zero, there exists a residual positive B field known as remanence, a measure of its retentivity. The material remains magnetized in the absence of an external H field, as there is still some net volume fraction of domain oriented in the former direction.

c) To reduce the B field within the specimen to zero, the magnetizing force must be made negative, to a value indicated by point C, where H has a value known as the coercive force, a measure of coercivity. When the applied field is continued to be applied in the reverse direction, saturation is achieved in the opposite sense, corresponding to point D.

d) The closed contour formed when H is varied periodically about the origin is known as hysteresis loop.

The demagnetization curve is the portion of the loop lying in the second quadrant, and it is of interest in a discussion of permanent magnets. Generally, permanent magnets have a large remanence to retain a great portion of magnetization, and large coercive force in order that the magnet will not easily be demagnetized. Maximum value of the product BH (BH_{max}) corresponds to the area of the largest BH rectangle that can be constructed inside the second quadrant of the hysteresis curve. BH has the dimensions of energy density and is referred to as the energy product. The larger the BH_{max}, the harder is the material in terms of its magnetic characteristics. Figure 3.13(B) shows that hard magnetic material has a high remanence, coercivity, and saturation flux density, as well as a low initial permeability, and high hysteresis energy losses. [31-33]

In ethylene pyrolysis furnace tubing Mucek [34] mentioned that radiant coil furnace tubes are usually centrifugally cast Cr-Ni-Fe alloy. They are nonmagnetic in the as-cast state as they are austenitic (face centered cubic). Due to carburization in-service, Cr is withdrawn from the matrix as it combines with the diffusing carbon to form Cr carbides. A matrix progressively enriched in a magnetic Fe-Ni alloy is created due to this Cr depletion. Thus, as the carburization process continues, the tube becomes progressively more magnetic. Due to this reasoning, magnetization studies were conducted on coupons of the Cr-Ni-Fe alloy using the Vibrating Sample Magnetometer (VSM) at Stony Brook University, Figure 3.14. The coupon/ tubing section was adhered to the quartz rod and then placed between the two powerful magnets of the VSM. An external magnetic field H was applied and magnetic response B was calculated both for the unexposed and the exposed coupons, as depicted in Figure 3.15.

The BH curve in case of unexposed coupon showed linear response with no remanence leading to the conclusion that it is paramagnetic. Whereas, the BH curve in case of exposed coupon showed slight remanence a coercive force and hysteresis, meaning that the material is slightly ferromagnetic. In order to correlate the carburization phenomena with the magnetization behavior, X-ray Maps were collected on both the unexposed and exposed coupons. It can be clearly seen that the unexposed coupon has uniform distribution of elements C, Si and Cr. In the exposed coupon, there is depletion of Cr and segregation of Cr_2O_3 and SiO_2 towards the surface as can be seen in the Figure 3.15. Thus depletion of Cr results in the abundance of elements Ni and Fe towards the surface resulting in the magnetic response as shown in the BH plot. In short, magnetization studies as shown in the Figure 3.15 can be used as a non-destructive technique to confirm the effect of carburization on the magnetic behavior of the material. [34]

References

[1] N. Saunders and A. P. Miodownik, CALPHAD (Calculation of Phase Diagrams): A Comprehensive Guide (Elsevier Science Inc., New York, 1998).

[2] I. Ansara and M. H. Rand, in "The Industrial Use of Thermodynamical Data", edited by T. I. Barry (Chemical Society, London, 1980) p. 246.

[3] L. Hoglund, (Theromo-Calc, Foundation of Computational Thermodyanmics, Stockholm, Sweden: Royal Institute of Technology).

[4] K. Bongartz, D. F. Lupton and H. Schuster, "Model to Predict Carburization Profiles in High Temperature Alloys", Metallurgical Transactions A (Physical Metallurgy and Materials Science) 11A (1980) 1883.

[5] M. Zhu, Q. Xu and J. Zhang, "Numerical Simulation of Reaction-Diffusion during Carburization of HK40 Steel", Journal of Materials Science and Technology 19 (2003) 327.

[6] H. J. Christ, "Experimental Characterization and Computer-Based Description of the Carburization Behaviour of the Austenitic Stainless Steel AISI 304L", Materials and Corrosion-Werkstoffe Und Korrosion 49 (1998) 258.

[7] G. M. Smith, D. J. Young and D. L. Trimm, "Carburization Kinetics of Heat-Resistant Steels", Oxidation of Metals 18 (1982) 229.

[8] Y. Nishiyama, N. Otsuka and T. Nishizawa, "Carburization Resistance of Austenitic Alloys in CH_4-CO_2-H_2 Gas Mixtures at Elevated Temperatures", Corrosion 59 (2003) 688.

[9] H. J. Grabke, "Corrosion of Alloy 600 in a carburization furnace", Materials and Corrosion-Werkstoffe Und Korrosion 52 (2001) 546.

[10] A. Chauhan, M. Anwar, K. Montero, H. White and W. Si, "Internal Carburization and Carbide Precipitation in Fe- Ni- Cr Alloy Tubing Retired from Ethylene Pyrolysis Service", Journal of Phase Equilibria and Diffusion 27 (2006) 684.

[11] J. I. Goldstein, D. E. Newbury, P. Echlin, D. C. Joy, C. E. Lyman, E. Lifshin, L. Sawyer and J. R. Michael, Scanning Electron Microscopy and X-Ray Microanalysis (Springer, New York, 2003).

[12] C. E. Lyman, "Editorial: 50 years of X-ray mapping", Microscopy and Microanalysis 12 (2006) 1.

[13] D. A. Melford and P. Duncumb, "The Metallurgical Applications of X-ray Scanning Microanalysis", Metallugica 57 (1958) 159.

[14] Fitzgera.R, K. Keil and K. F. Heinrich, "Solid-State Energy-Dispersion Spectrometer for Electron-Microprobe X-Ray Analysis", Science 159 (1968) 528.

[15] J. I. Goldstein, D. E. Newbury, P. Echlin, D. C. Joy, A. D. Romig, Jr., C. E. Lyman, C. Fiori and E. Lifshin, Scanning Electron Microscopy and X-ray Microanalysis : A Text for Biologists, Materials Scientists, and Geologists (Plenum Press, New York, 1992).

[16] R. B. Marinenko, R. L. Myklebust, D. S. Bright and D. E. Newbury, "Digital X-Ray Compositional Mapping with Standard Map Corrections for Wavelength Dispersive Spectrometer Defocusing", Journal of Microscopy-Oxford 145 (1987) 207.

[17] J. J. Friel and C. E. Lyman, "X-ray Mapping in Electron-Beam Instruments", Microscopy and Microanalysis 12 (2006) 2.

[18] J. I. Goldstein and A. E. Moren, "Diffusion Modeling of the Carburization Process", Metallurgical Transactions A (Physical Metallurgy and Materials Science) 9A (1978) 1515.

[19] H. J. Grabke and D. Jakobi, "High Temperature Corrosion of Cracking Tubes", Materials and Corrosion-Werkstoffe Und Korrosion 53 (2002) 494.

[20] H. J. Grabke, K. Ohla, J. Peters and I. Wolf, "Radiotracer Studies of Carbon Permeation Through Oxide Scales on Commercial High Temperature Alloys and Model Alloys", Werkstoffe und Korrosion 34 (1983) 495.

[21] H. J. Grabke and A. Schnaas, in "Alloy 800: Proceedings of the Petten International Conference", edited by W. Betteridge (North-Holland Publication Company, Amsterdam, 1978) p. 195.

[22] H. J. Grabke and I. Wolf, "Carburization and Oxidation", Materials Science and Engineering 87 (1986) 23.

[23] J. Hemptenmacher and H. J. Grabke, "EINFLUESSE KLEINER ZUSAETZE VON NIOB ODER CER AUF KORROSION UND KRIECHEN VON INCOLOY 800 IN CO-H_2O-H_2-ATMOSPHAEREN
Effects of Small Alloying Additions of Niobium or Cerium on the Corrosion and Creep of Incoloy 800 in CO-H_2O-H_2-Atmospheres", Werkstoffe und Korrosion 34 (1983) 333.

[24] J. Hemptenmacher, G. Sauthoff and H. J. Grabke, "EINFLUSS DER AUFKOHLUNG AUF DAS KRIECHVERHALTEN EINER FeNiCr-HOCHTEMPERATURLEGIERUNG

Effects of Carburization of the Creep Behavior of a FeNiCr-High Temperature Alloy", Werkstoffe und Korrosion 35 (1984) 247.

[25] K. Ledjeff, A. Rahmel and M. Schorr, "Oxidation and Carburization of High Alloyed Materials for Cracking Tubes .1. Oxidation Behavior in Air", Werkstoffe Und Korrosion-Materials and Corrosion 30 (1979) 767.

[26] K. Ledjeff, A. Rahmel and M. Schorr, "Oxidation and Carburization of High Alloyed Materials for Cracking Tubes .2. Carburization Behavior in Oxygen and Carbon Containing Atmospheres with High-Carbon Activity", Werkstoffe Und Korrosion-Materials and Corrosion 31 (1980) 83.

[27] A. Schnaas and H. J. Grabke, "VERAENDERUNG DER WERKSTOFFEIGENSCHAFTEN AUSTENITISCHER CeNiFe-LEGIERUNGEN DURCH AUFKOHLUNG

Changes in Material Properties of Austenitic CrNiFe-Alloys by Carburization", Werkstoffe und Korrosion 29 (1978) 635.

[28] I. Wolf and H. J. Grabke, "Study on the Solubility and Distribution of Carbon in Oxides", Solid State Communications 54 (1985) 5.

[29] I. Wolf, H. J. Grabke and P. Schmidt, "Carbon Transport Through Oxide Scales on Fe-Cr Alloys", Oxidation of Metals 29 (1988) 289.

[30] L. C. Brown and J. S. Kirkaldy, "Carbon Diffusion in Dilute Ternary Austenites", Transactions of the Metallurgical Society of Aime 230 (1964) 223.

[31] D. R. Askeland, The Science and Engineering of Materials (PWS Pub., Boston, 1994) p. 812.

[32] D. R. Askeland and P. P. Phulé, The Science and Engineering of Materials (Thomson, Southbank, Victoria, Australia, 2006) p. 863.

[33] W. D. Callister, Materials Science and Engineering : An Introduction, (Wiley, 2000) p. 871.

[34] M. W. Mucek, "Laboratory Detection of Degree of Carburization in Ethylene Pyrolysis Furnace Tubing", Materials Performance 22 (1983) 25.

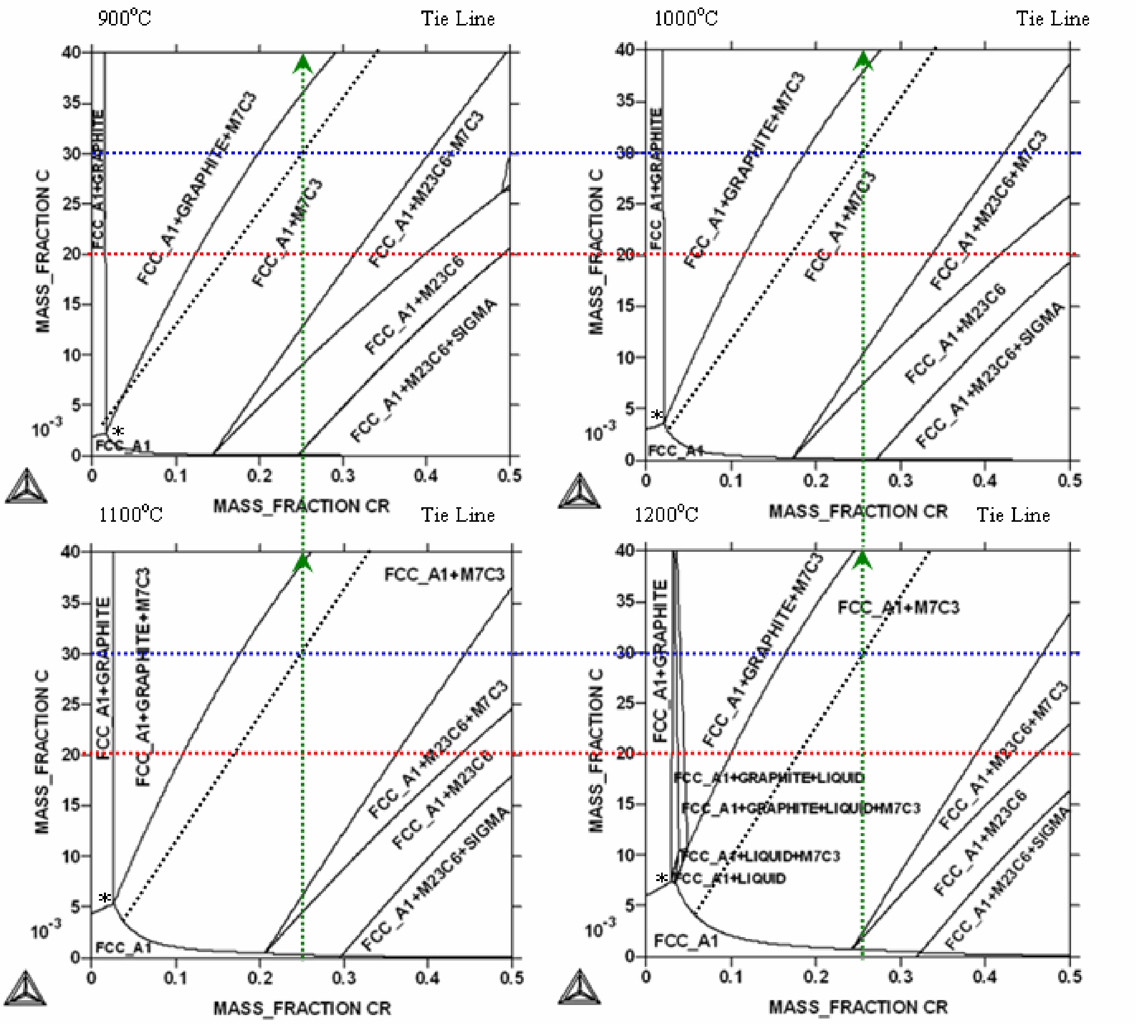

Figure 3.1. Phase equilibria of HP- Nb at 900, 1000, 1100, and 1200 C. In all cases, as the carbon content in the material increases (green lines), M23C6 will eventually transform into M7C3. * indicates carbon and chromium content in which graphite starts to precipitate. At 1200 C, melting may occur at the carbon/ chromium content where graphite starts to precipitate [10].

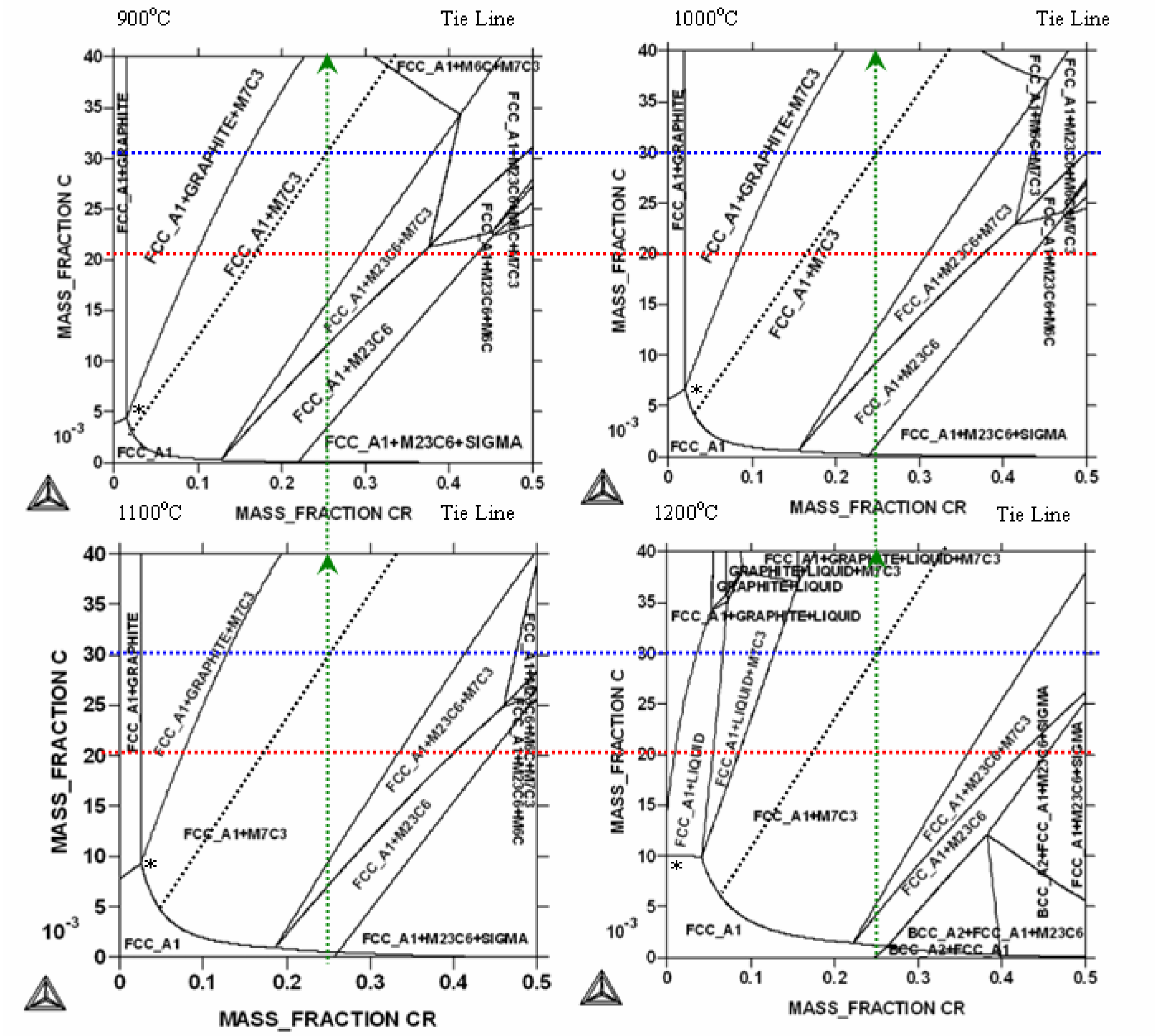

Figure 3.2. Phase equilibria of HK40 at 900, 1000, 1100, and 1200 C. In all cases, as the carbon content in the material increases (green lines), M23C6 will eventually transform into M7C3. * indicates carbon and chromium content in which graphite starts to precipitate. At 1200 C, melting may occur at the carbon/ chromium content where graphite starts to precipitate.

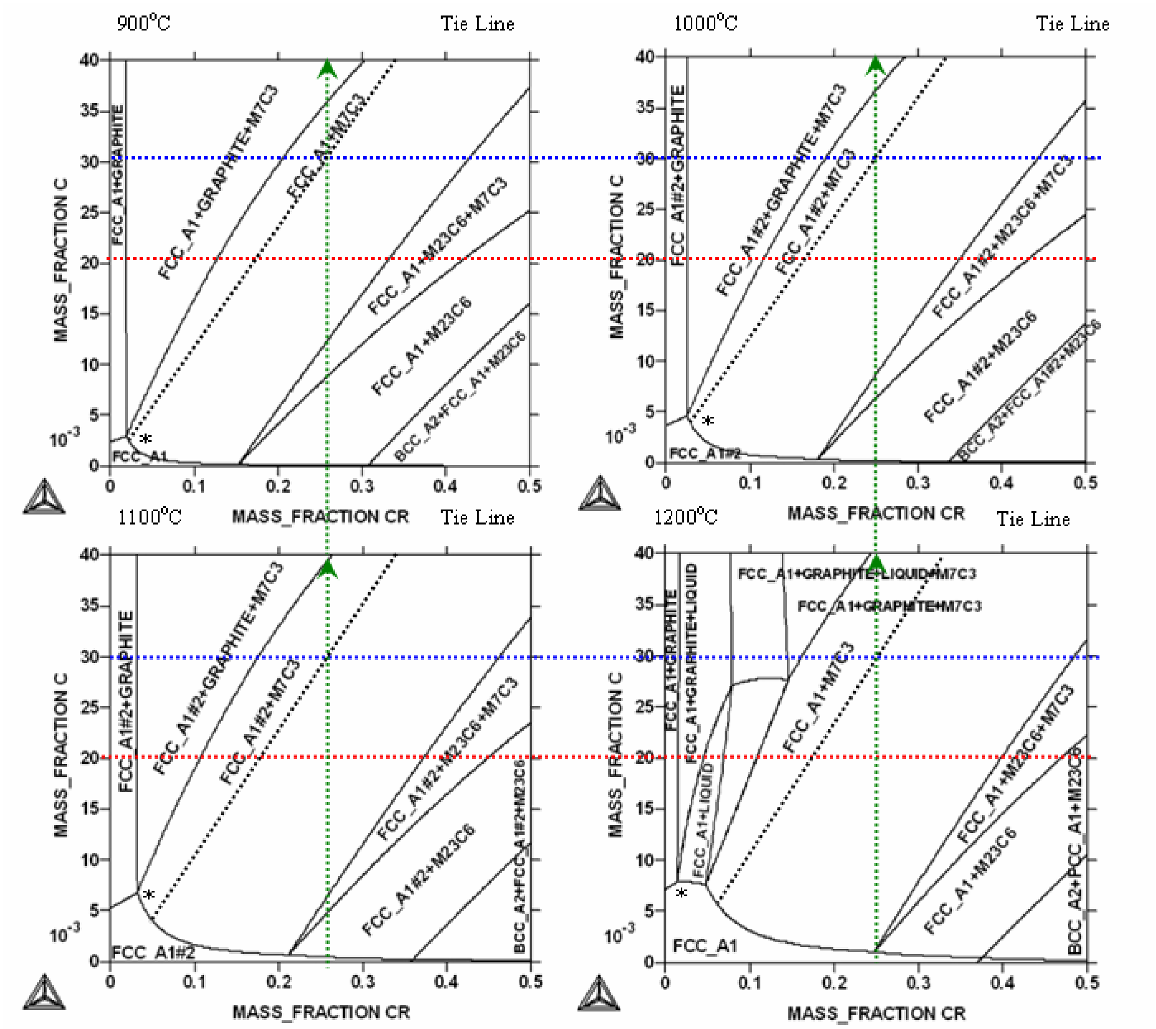

Figure 3.3. Phase equilibria of HPM at 900, 1000, 1100, and 1200 C. In all cases, as the carbon content in the material increases (green lines), M23C6 will eventually transform into M7C3. * indicates carbon and chromium content in which graphite starts to precipitate. At 1200 C, melting may occur at the carbon/ chromium content where graphite starts to precipitate.

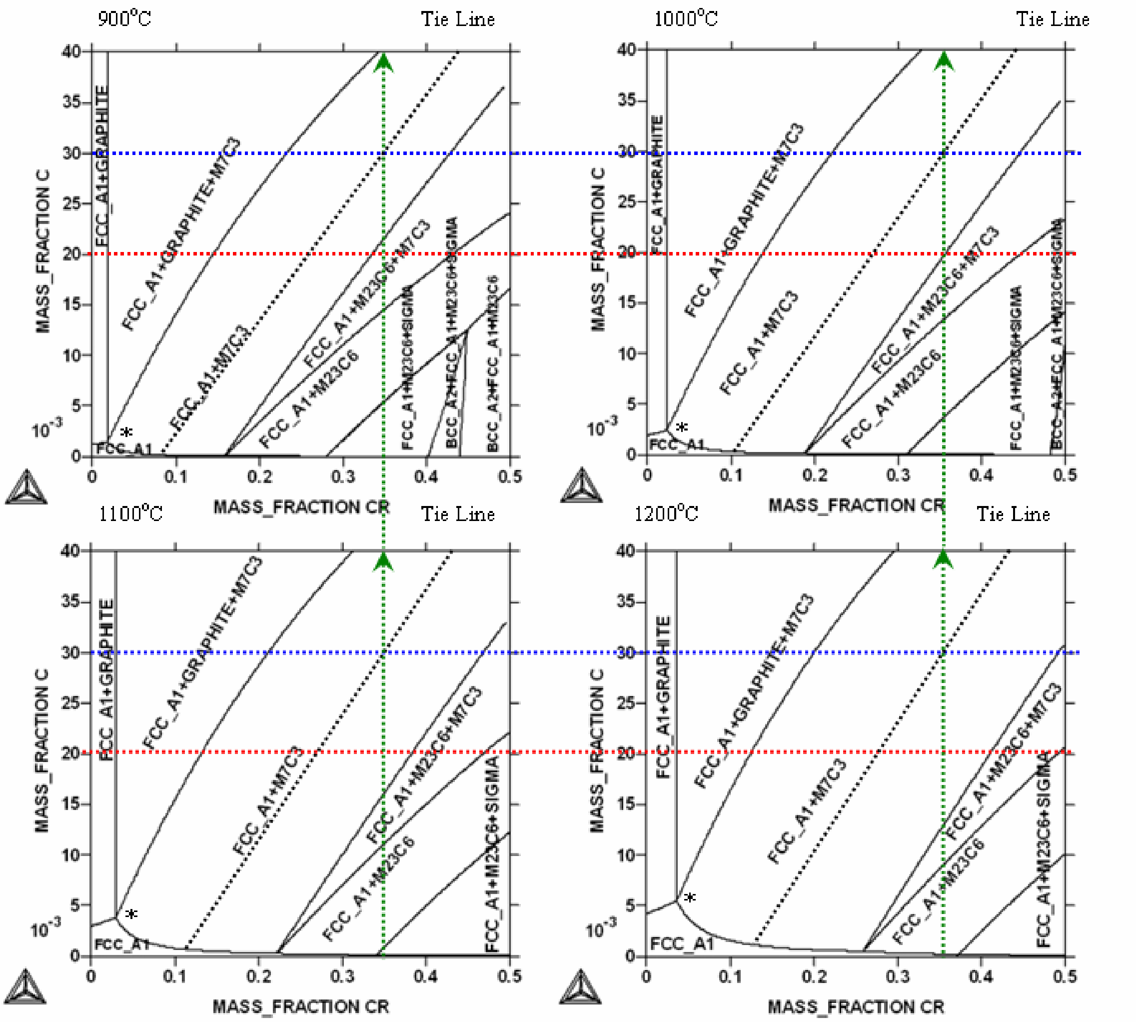

Figure 3.4. Phase equilibria of 35Cr-45Ni at 900, 1000, 1100, and 1200 C. In all cases, as the carbon content in the material increases (green lines), M23C6 will eventually transform into M7C3. * indicates carbon and chromium content in which graphite starts to precipitate.

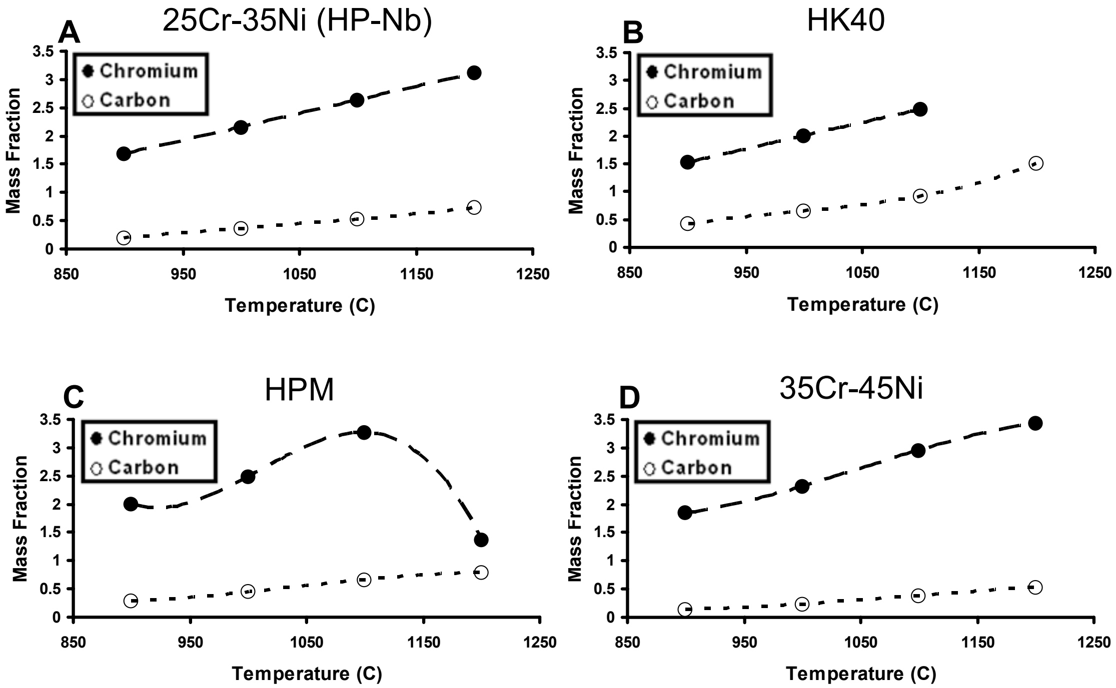

Figure 3.5. % of Chromium and Carbon in FCC_A1 Matrix Prior to Graphite Precipitation at 900 C, 1000 C, 1100 C, and 1200 C for (A) 25Cr-35Ni [HP-Nb] Alloy; (B) HK40 Alloy; (C) HPM Alloy; and (D) 35Cr-45Ni Alloy. There seems to be an anomaly in image (C) for the case of HPM alloy due to the decrease in Mass Fraction of Chromium at 1200 C.

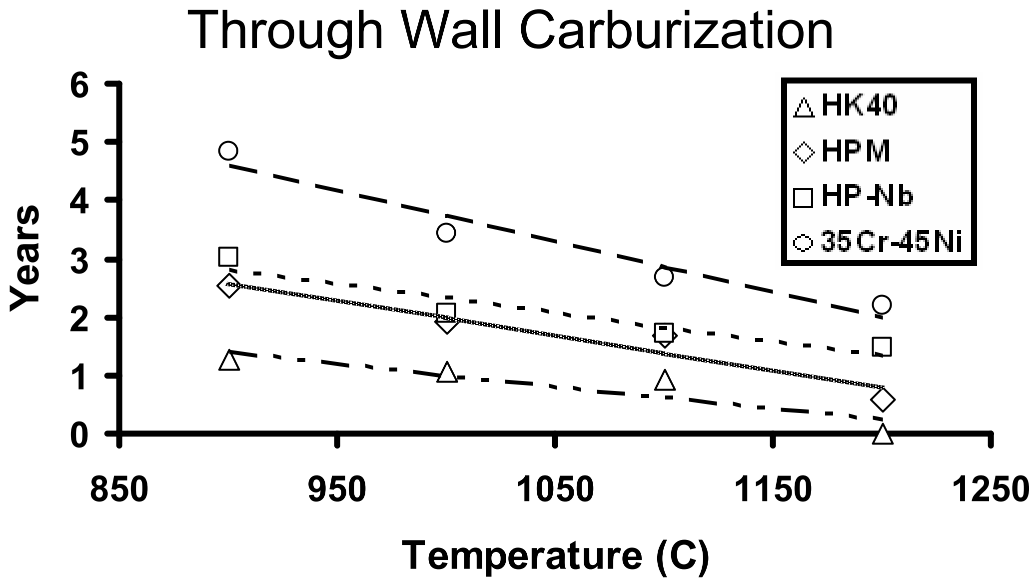

Figure 3.6. Through Wall Carburization for HK40, HPM, HP-Nb, and 35Cr-45Ni Alloys at 900 C, 1000 C, 1100 C, and 1200 C.

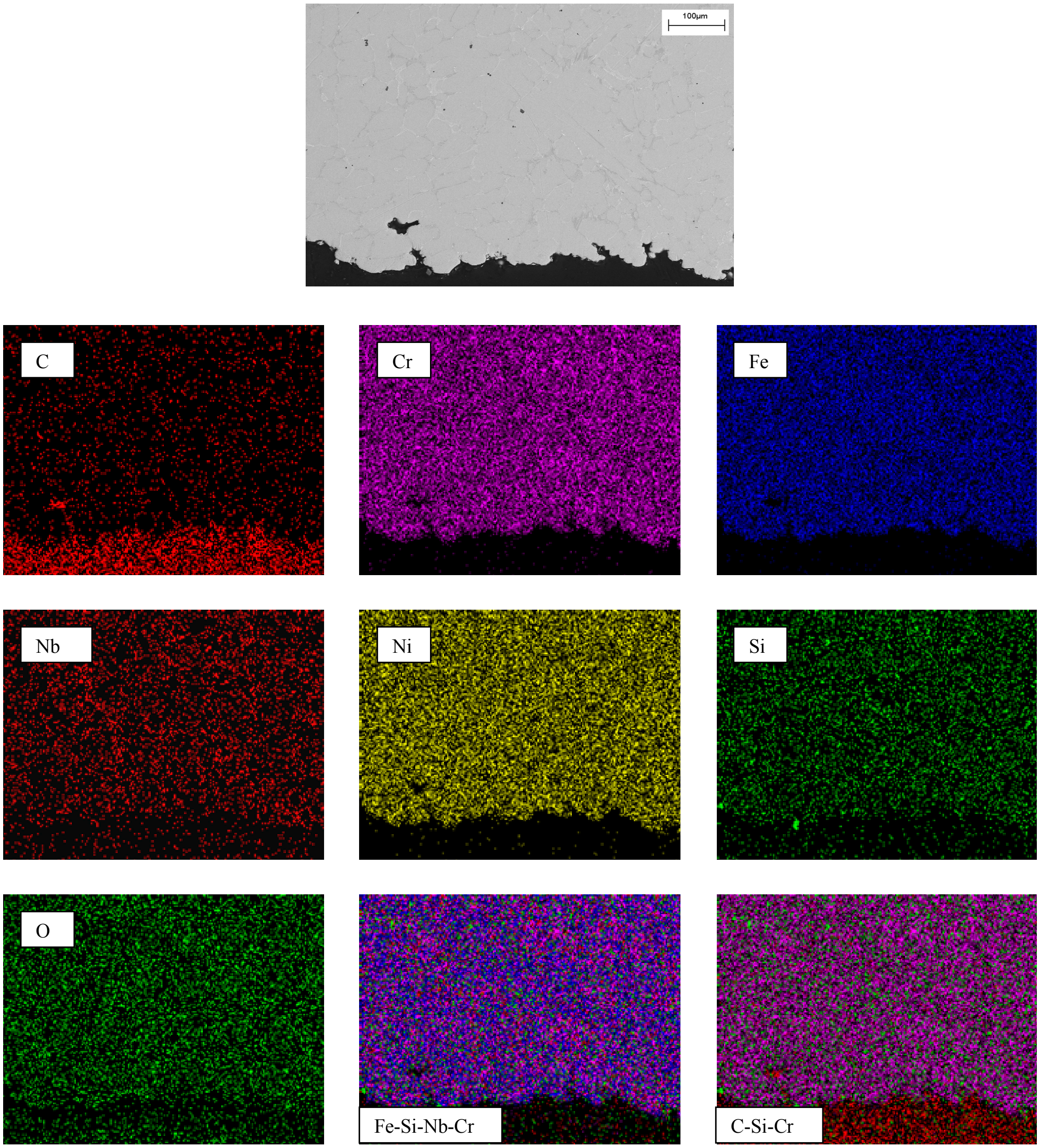

Figure 3.7. Backscatter electron image (top) and x-ray maps (C, Cr, Fe, Nb, Ni, Si, O, and collages) of HP- Nb tubing prior to service. All elements are uniformly distributed in the matrix. The large content of carbon at the surface is due to the sample preparation consumables [10].

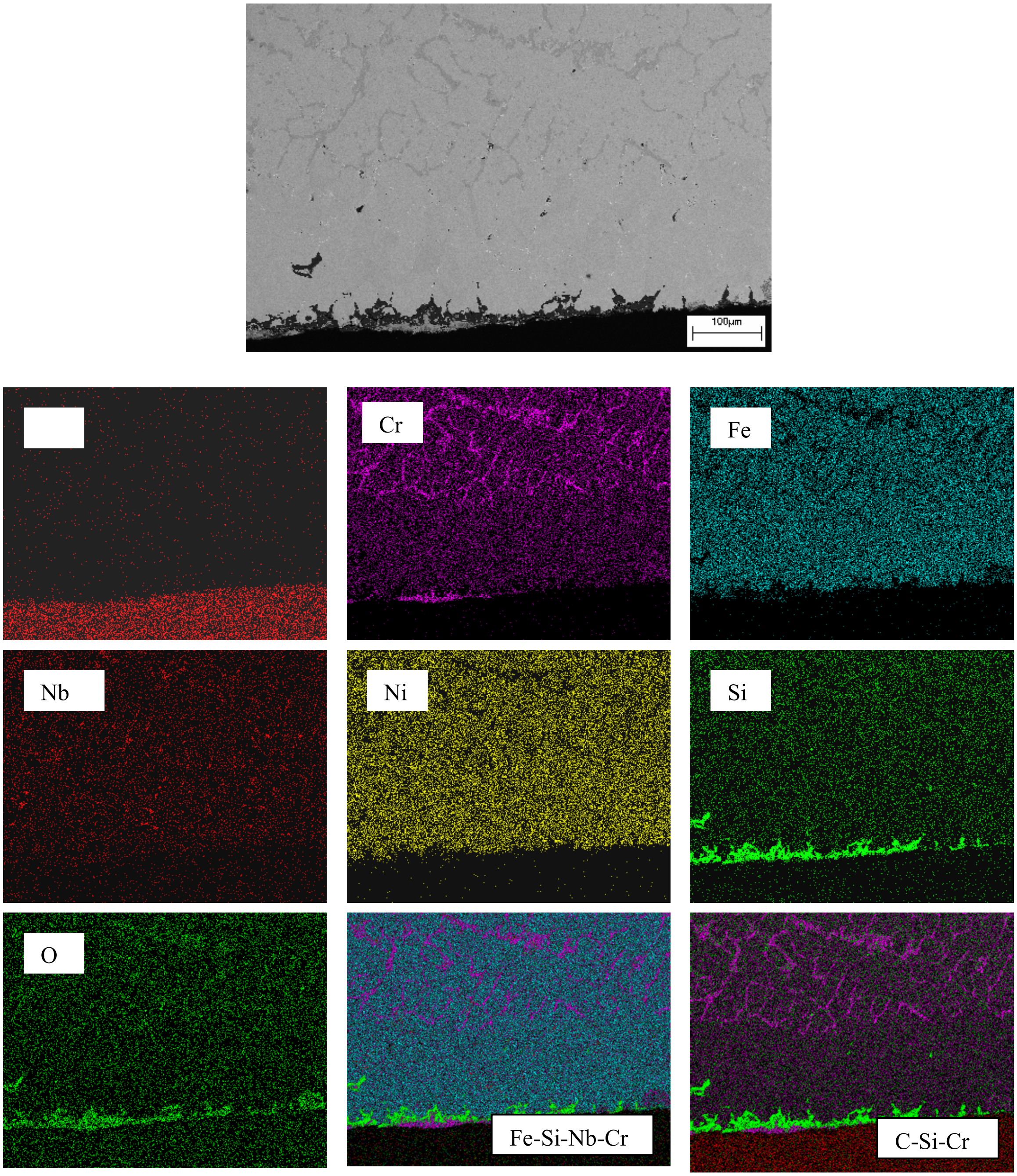

Figure 3.8. Backscatter electron image (top) and x-ray maps (C, Cr, Fe, Nb, Ni, Si, O, collages) of HP- Nb tubing removed from ethylene pyrolysis service during a scheduled re- tubing. The carbon is from the metallographic mount; chromium segregates to the bulk in the form of carbides and to the surface in the form of oxides; iron, niobium, and nickel are uniformly distributed in the matrix; and silicon and oxygen are found near the surface. Chromium oxide (Cr2O3) and silicon oxide (SiO2) protective layers effectively prevented process C diffusion [10].

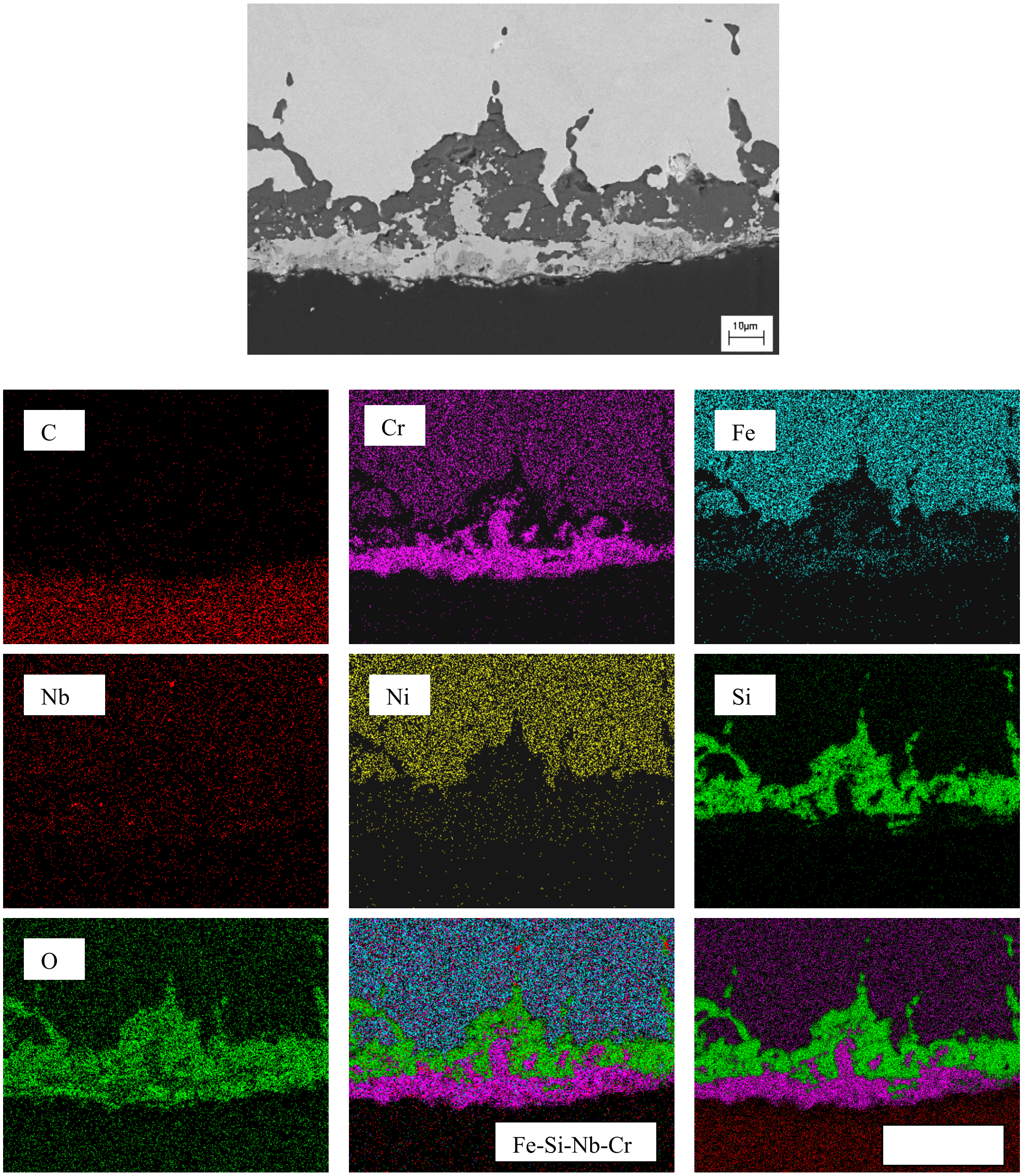

Figure 3.9. High magnification backscatter electron image (top) and x-ray maps (C, Cr, Fe, Nb, Ni, Si, O, collages) of surface area of the image shown in Figure 3.8. Here, chromium segregates to the surface in the form of oxides leading to the dominance of iron and nickel in the bulk. Silicon and oxygen are observed near the surface. The high concentration of carbon is from the metallographic mount.

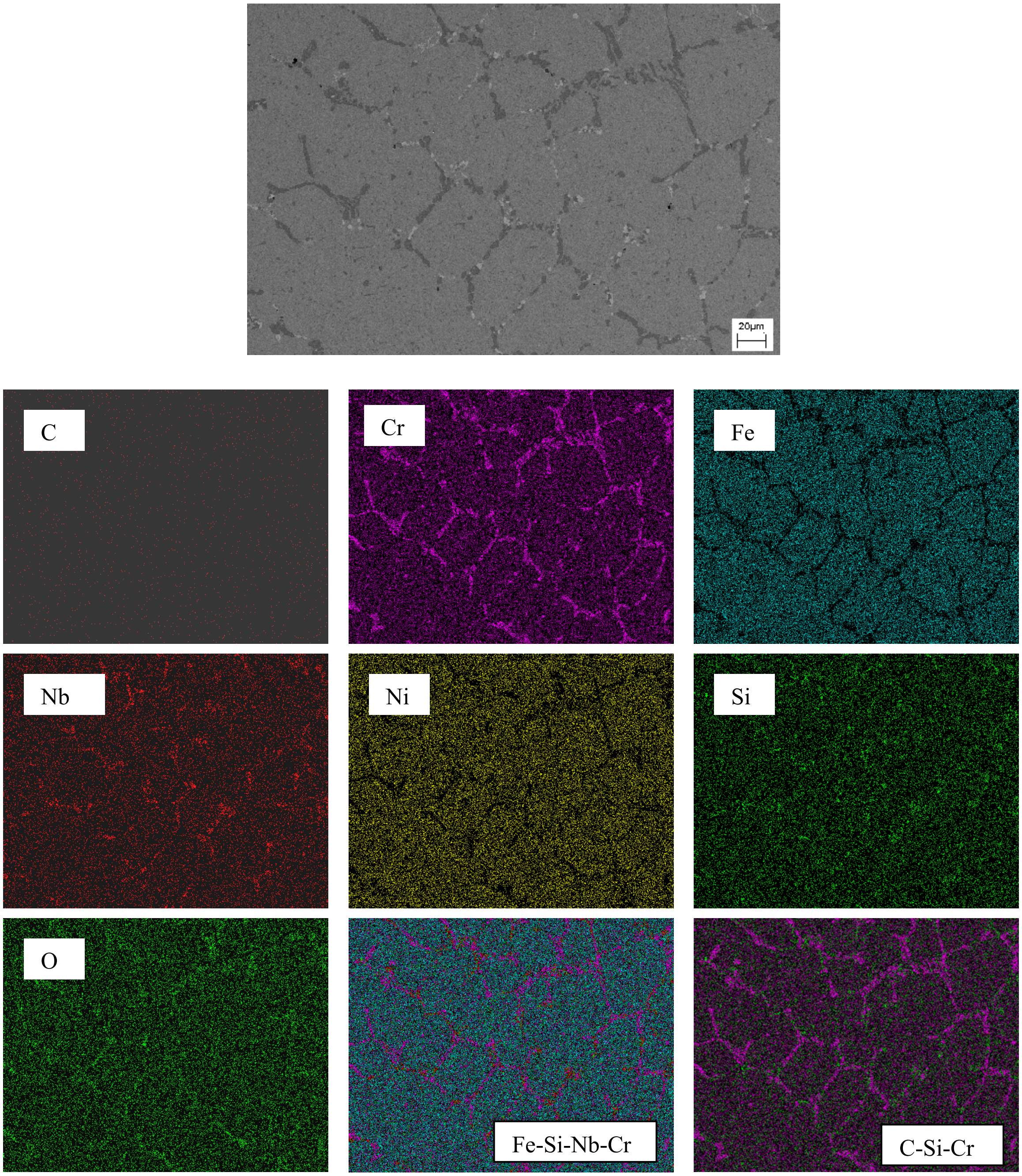

Figure 3.10. High magnification backscatter electron image (top) and x-ray maps (C, Cr, Fe, Nb, Ni, Si, O, collages) of bulk area of the image shown in Figure 3.8. There is uniform distribution of iron, niobium, and nickel in the matrix; and segregation of chromium in the bulk in the form of precipitates of chromium carbides.

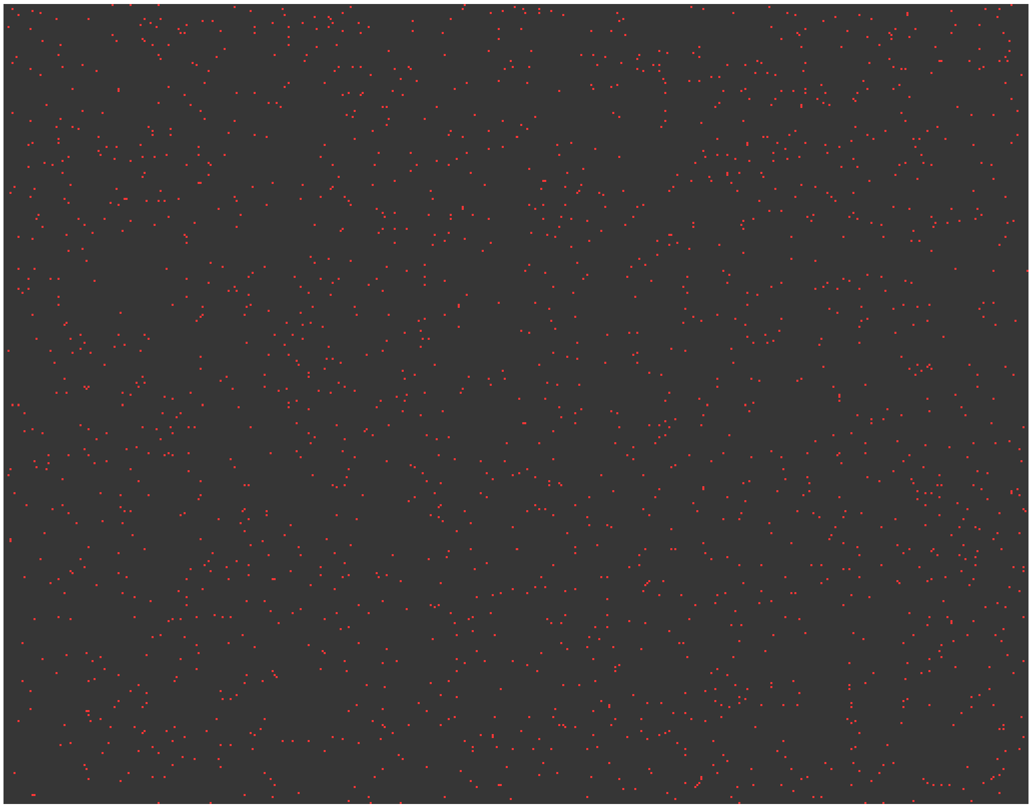

Figure 3.11. Enlarged x-ray map of element carbon of the image shown in Figure 3.10.

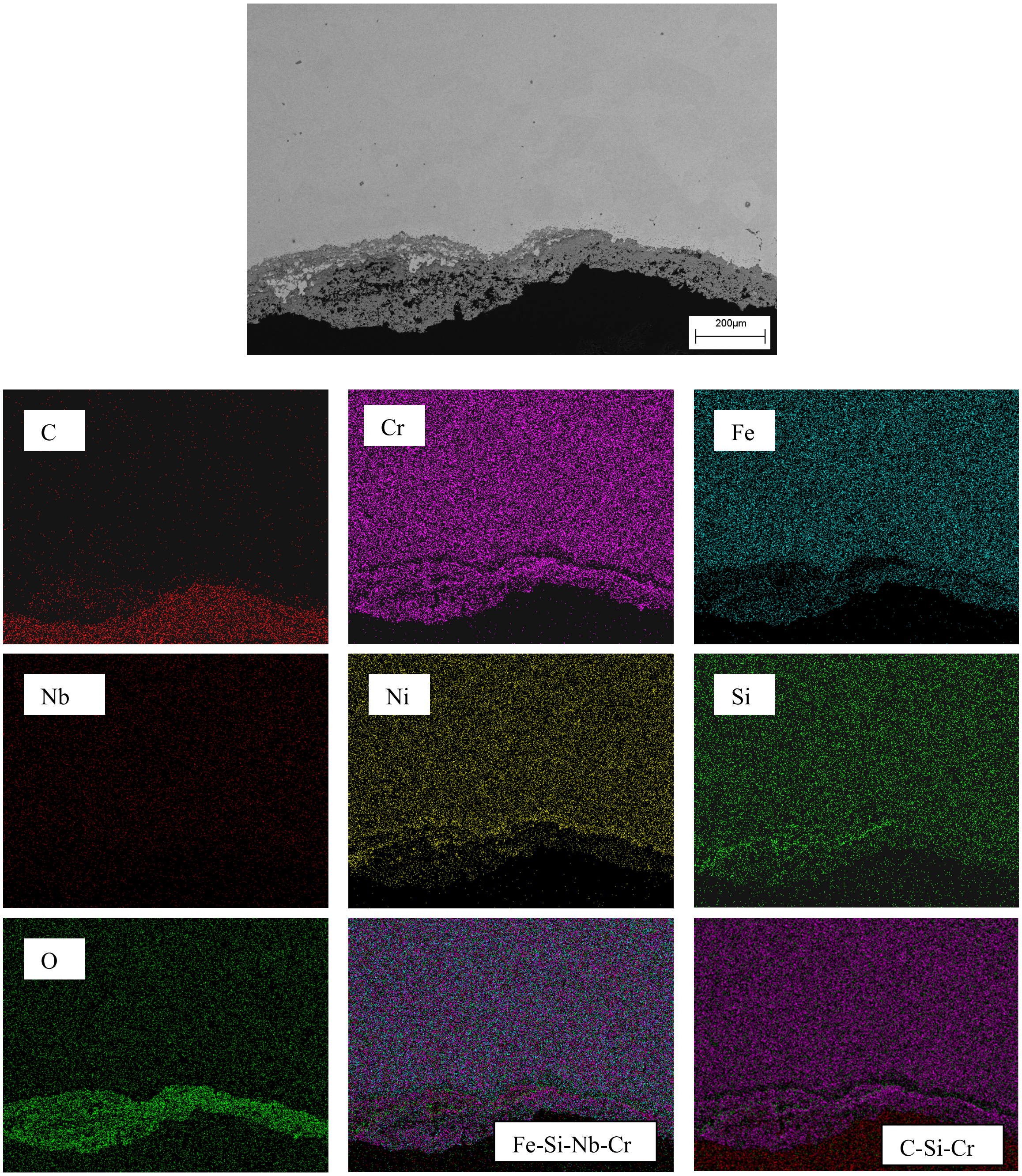

Figure 3.12. Backscatter electron image (top) and x-ray maps (C, Cr, Fe, Nb, Ni, Si, O, and collages) of HPM tubing removed from ethylene pyrolysis service during a scheduled re- tubing. All elements (Cr, Fe, Ni, Si, O) are uniformly distributed in the matrix; and there is presence of very small amounts of Nb and C. The large content of carbon at the surface is due to the sample preparation consumables.

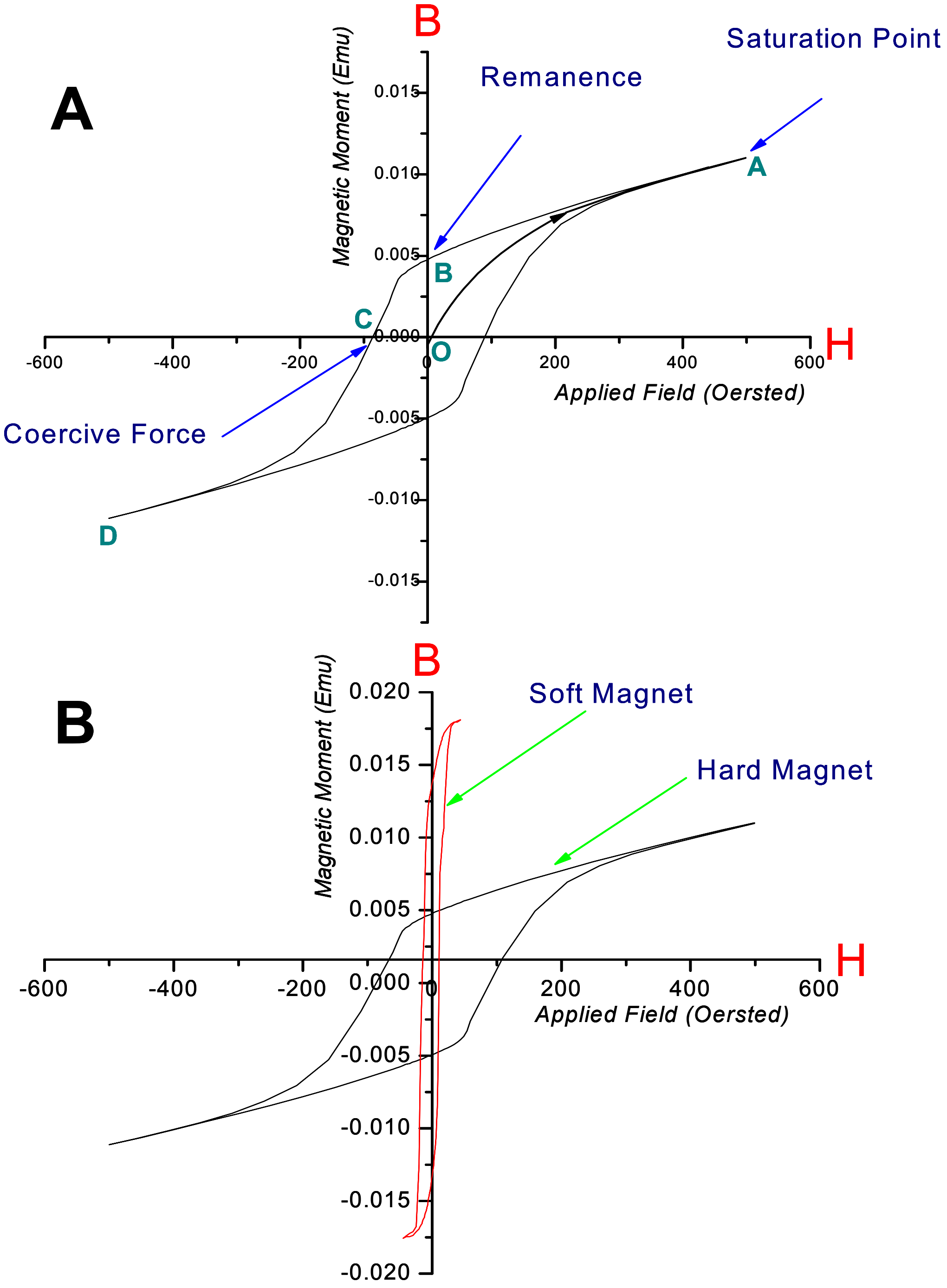

Figure 3.13. (A) BH Hysteresis Curve showing the effect of Applied Magnetic Field on Magnetic Moment for a Ferromagnetic Material. (B) BH Magnetization curves for Soft and Hard Magnetic Materials (Figures Reproduced from Askeland et. al. [32] and Callister et. al. [33]).

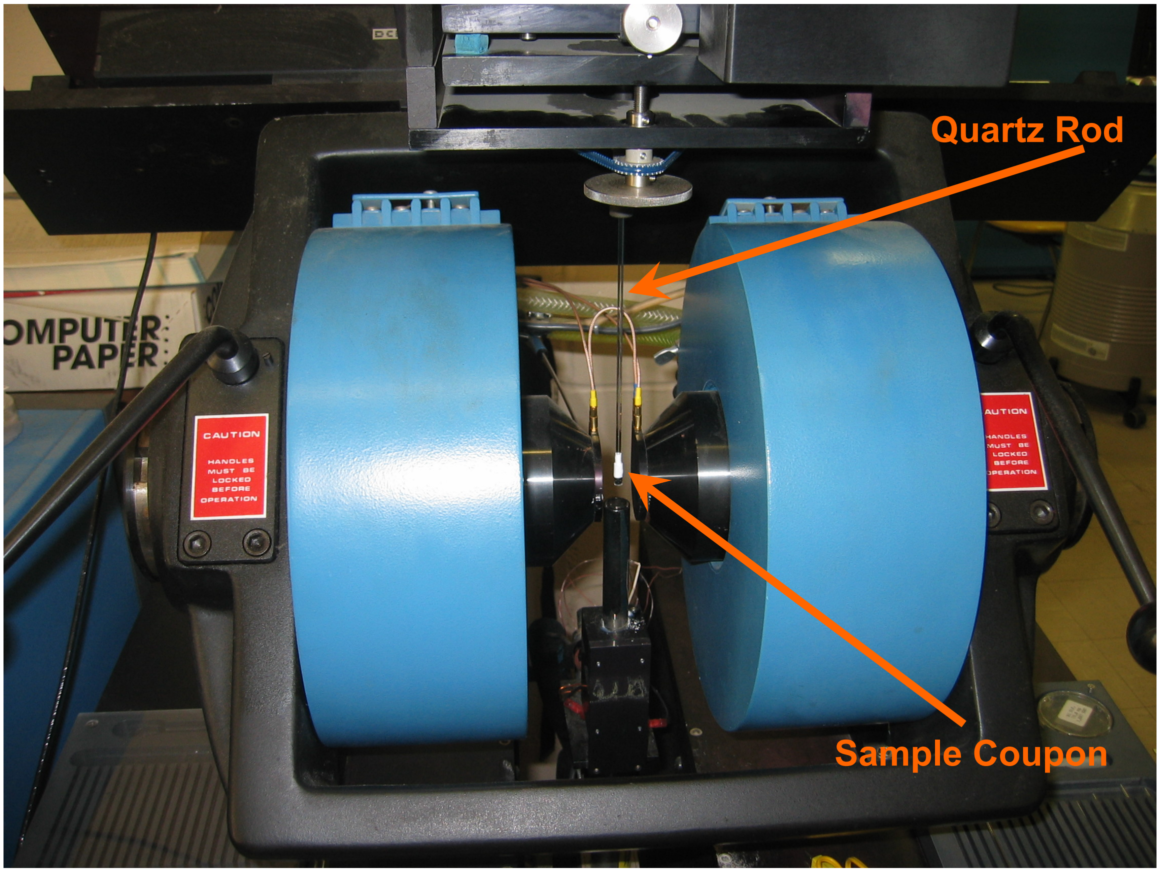

Figure 3.14. Vibrating Sample Magnetometer (VSM) at Stony Brook University.

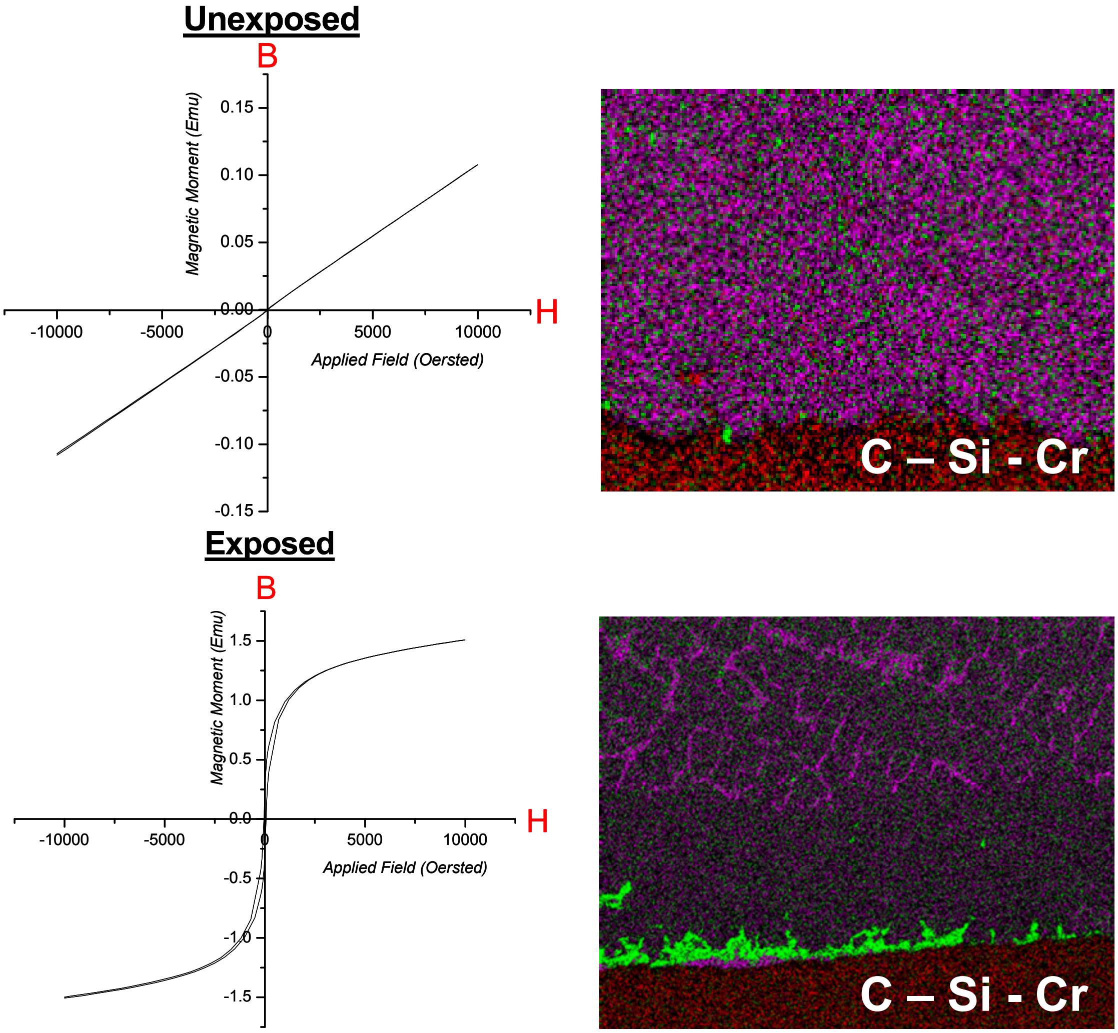

Figure 3.15. Magnetization Behavior of Unexposed and Exposed Alloy and Corresponding X-ray Maps.

Table 3.1. HP-Nb Phase Equilibria Data Predicted by Thermo-Calc.

	900 C	1000 C	1100 C	1200 C
Initial Phase Present 0.45% C	FCC_A1 + $M_{23}C_6$	FCC_A1 + $M_{23}C_6$	FCC_A1 + $M_{23}C_6$ + M_7C_3	FCC_A1 + M_7C_3
Phases Present at local 2%C	FCC_A1 + M_7C_3	FCC_A1 + M_7C_3	FCC_A1 + M_7C_3	FCC_A1 + M_7C_3
Phases Present at local 3%C	FCC_A1 + M_7C_3	FCC_A1 + M_7C_3	FCC_A1 + M_7C_3	FCC_A1 + M_7C_3
Carbon content in FCC_A1 at 3%C	~0.35%	~0.28%	~0.38%	~0.41%
Chromium content in FCC_A1 at 3%C	~1.7%	~2.63%	~3.74%	~5.79%
Carbon content in FCC_A1 before graphite precipitation	~0.19%	~0.36%	~0.52%	~0.72%
Chromium content in FCC_A1 before graphite precipitation	~1.68%	~2.15%	~2.63%	~3.1%

Table 3.2. HK40 Phase Equilibria Data Predicted by Thermo-Calc.

	900 C	**1000 C**	**1100 C**	**1200 C**
Initial Phase Present 0.45% C	FCC_A1 + $M_{23}C_6$	FCC_A1 + $M_{23}C_6$	FCC_A1 + $M_{23}C_6$	FCC_A1 + $M_{23}C_6$
Phases Present at local 2%C	FCC_A1 + M_7C_3	FCC_A1 + M_7C_3	FCC_A1 + M_7C_3	FCC_A1 + M_7C_3
Phases Present at local 3%C	FCC_A1 + M_7C_3	FCC_A1 + M_7C_3	FCC_A1 + M_7C_3	FCC_A1 + M_7C_3
Carbon content in FCC_A1 at 3%C	~0.3%	~0.4%	~0.5%	~0.6%
Chromium content in FCC_A1 at 3%C	~2.5%	~4%	~5%	~6%
Carbon content in FCC_A1 before graphite precipitation	~0.41%	~0.65%	~0.91%	~1.5%
Chromium content in FCC_A1 before graphite precipitation	~1.52%	~2%	~2.47%	--

Table 3.3. HPM Phase Equilibria Data Predicted by Thermo-Calc.

	900 C	**1000 C**	**1100 C**	**1200 C**
Initial Phase Present 0.45% C	FCC_A1 + $M_{23}C_6$	FCC_A1 + $M_{23}C_6$	FCC_A1 + $M_{23}C_6$ + M_7C_3	FCC_A1 + M_7C_3
Phases Present at local 2%C	FCC_A1 + M_7C_3	FCC_A1 + M_7C_3	FCC_A1 + M_7C_3	FCC_A1 + M_7C_3
Phases Present at local 3%C	FCC_A1 + M_7C_3	FCC_A1 + M_7C_3	FCC_A1 + M_7C_3	FCC_A1 + M_7C_3
Carbon content in FCC_A1 at 3%C	~0.3%	~0.4%	~0.42%	~0.6%
Chromium content in FCC_A1 at 3%C	~2%	~3%	~4.5%	~5.5%
Carbon content in FCC_A1 before graphite precipitation	~0.27%	~0.44%	~0.66%	~0.78%
Chromium content in FCC_A1 before graphite precipitation	~2%	~2.48%	~3.26%	~1.36%

Table 3.4. 35Cr-45Ni Phase Equilibria Data Predicted by Thermo-Calc.

	900 C	1000 C	1100 C	1200 C
Initial Phase Present 0.45% C	FCC_A1 + $M_{23}C_6$ + σ	FCC_A1 + $M_{23}C_6$ + σ	FCC_A1 + $M_{23}C_6$	FCC_A1 + $M_{23}C_6$
Phases Present at local 2%C	FCC_A1 + $M_{23}C_6$ + M_7C_3	FCC_A1 + $M_{23}C_6$ + M_7C_3	FCC_A1 + M_7C_3	FCC_A1 + M_7C_3
Phases Present at local 3%C	FCC_A1 + M_7C_3	FCC_A1 + M_7C_3	FCC_A1 + M_7C_3	FCC_A1 + M_7C_3
Carbon content in FCC_A1 at 3%C	~0.05%	~0.1%	~0.15%	~0.2%
Chromium content in FCC_A1 at 3%C	~8%	~11%	~12%	~13.5%
Carbon content in FCC_A1 before graphite precipitation	~0.13%	~0.23%	~0.38%	~0.53%
Chromium content in FCC_A1 before graphite precipitation	~1.84%	~2.31%	~2.95%	~3.42%

4. Pulsed Laser Deposition: Coking Resistant Coating Technology

4.1. Introduction

The origin of pulsed laser deposition technology can be traced back to Smith and Turner [1] who used a ruby laser to deposit thin films on a variety of materials. Currently, over 1000 Patents on pulsed laser deposition technology exist. The latest, combinatorial pulsed laser deposition has been found to produce high quality thin films [2].

Pulsed laser deposition (PLD) is predominantly used in the preparation of thin films and multilayer structures. The initial cost for setting up a PLD is around 10 times lower than that of the molecular beam epitaxy (MBE) with no loss in the quality of the films. In PLD, the independence of the laser source from the deposition system assists in the straightforward production of the multilayer films by the translation of the different targets as well as mirrors into and out of the beam focal point. [3]

200nm-400nm is the appropriate range of laser wavelengths for the growth of thin-films using PLD as majority of the materials utilized for the deposition demonstrates strong absorption in this spectrum. Variation of wavelength affects the penetration depths, the shorter the wavelength the higher the absorption coefficient and thus lower the penetration. This consequently aids in the ablation of thinner layers of the target surface. It is difficult to work with wavelengths below 200nm because Schumann-Runge bands of molecular oxygen hinder the process because of strong absorption. Furthermore, the optics required is also complex. [3]

The two types of lasers commonly used are excimer and Nd^{3+}: YAG lasers. In the Nd^{3+}:YAG lasers, the neodymium ions are present as impurities in the YAG (yttrium aluminum garnet) host and serve as the active medium. Originally Nd^{3+}: YAG laser emits at 1045nm, quite outside the requisite range mentioned above. Doubling the frequency by using a non-linear crystal and 50% power conversion efficiency yields an output of 532nm. The desired outputs of 355nm or 266nm lying in the UV range are produced by either mixing the 532nm output with the residual 1064nm light or frequency doubled as above. [3]

Excimer lasers, basically gas laser systems, emit radiation directly in the UV range contrary to the Nd^{3+}: YAG lasers. The commercially available excimers deliver high outputs in excess of 1 J/pulse. The energies near 500 mJ/pulse having high pulse repetition rates of several hundred hertz are easily achieved. PLD predominantly uses excimer because of the reasons mentioned above. [3] KrF and XeCl are mostly used excimers for the PLD applications. KrF has higher wavelength than XeCl, still KrF is preferred over XeCl for the PLD work as the former has the highest gain system for electrically discharged pumped excimer and it produces the requisite pulse energy suitable for PLD work as compared to XeCl. [3]

PLD is a rather simple film growing technique. Target holder and a substrate holder are housed in a vacuum chamber. In order to deposit thin films by vaporizing materials, a high-power laser is used as an external energy source. The laser beam is rastered and focused over the target surface by using a set of optical components. The topological, optical and thermodynamical properties of the target along with laser characteristics control the mechanism of material ablation. On absorption of laser radiation by solid surface, electromagnetic energy is converted to electronic excitation and subsequently into thermal, chemical and mechanical energy to cause ablation, plasma formation, excitation, exfoliation and evaporation. The “plume” is formed from evaporants having mixture of energetic species including electrons, atoms, ions, molecules, clusters, micron-sized solid particulates and molten globules. [3] There are more than one mechanism in a complex laser-target interaction. The three types of absorptions which are taken into account are:

i) Plume absorption.
ii) Volume absorption by the electrons and phonons in the lattice.
iii) Absorption at the surface by free carrier.

In the multi-step picture, due to laser beam impinging on the target, photons are absorbed by the surface and form a molten layer which is known as Knudsen layer. During the heating of metals using lasers, there are three methods: receiving of radiation energy by free electrons, interchange of energy between lattice and electrons, and free electron motion through media leading to the advancement of energy. [4, 5] The large local temperature differences arise between the lattice and electrons due to the heating of the free electrons to an effective temperature greater than that of the lattice. This happens in cases when metal is observed from the perspective of a two-temperature system during the high power laser heating. Therefore, there is consideration of a coefficient of heat transfer coupling between phonon and electron and subsequently the relaxation mechanism for the transfer of energy from the electrons to the lattice. [4, 6]

The advantages in PLD are: there is absence of heating elements and discharging electrodes, so any kind of reactive gas can be contained in deposition ambient. As there is fast and very directional plume, attenuation due to trajectory change as a result of collisions with the background gas is small. And also, pressure in all the other physical vapor deposition techniques is an order of magnitude less than the pressure of the reactive gas during the film growth in PLD (which can be as high as 1 torr). On comparison of PLD with ion implantation and chemical-vapor deposition techniques, it is observed that PLD is unusual because the laser source is outside the chamber where ablation takes place. Also the growth of epitaxial and adherent films happen at lower substrate temperatures in PLD as the layer formation is affected by the emission of energetic ions during laser-target-vapor interaction. This is very critical in microelectronics as the higher temperature can modify the physical properties and the depth composition of crystals during the deposition on doped semiconductor materials. In case of metallorganic vapor phase epitaxy and molecular beam epitaxy techniques, it is observed that PLD has the following unique characteristics: the laser plume has high kinetic energy which assists in surface mobility on the growing film, the source material transfer process restricts the heated material amount to that what is liberated; the source material is easily replaced, and the pulsed nature allows pulsed reactive gas sources to synchronize with short duration/ high flux pulses as well as helps in the precise regulation of the deposition thickness [4, 7].

The drawbacks observed in PLD are [3]:

i) In ceramic high-temperature superconductors there is problem of non-stoichiometric material transfer of multi-elemental targets.

ii) The laser intensity has pulse-to-pulse fluctuations.

iii) $\text{Cos}^n\theta$ profile of the ablation plume (where, $2 \leq n < 6$) cause in inhomogeneities of deposition rates.

iv) Splashing: There is production of droplets due to laser. It's an intrinsic problem and difficult to overcome.

v) Lack of uniformity over a large area due to narrow angular distribution of the plume. This can be overcome by engineering solutions like rastering the substrate or the laser substrate using rotation and translation.

The mechanisms by which origin of splashing can be explained are exfoliation, expulsion of the liquid layer by the shock wave recoil pressure, and subsurface boiling. Subsurface boiling is also called "True Splashing" and is present in ablation of metal targets under high power irradiation and doesn't occur in dielectric material. The former two mechanisms are the significant sources of splashing. The splashing can be avoided by [3]:

i) Plume Manipulation.

ii) Target Surface Improvement: High density and smooth surfaces to have desirable features.

iii) Off-axis PLD.

iv) Mechanical Particle Filter: a velocity selector placed between the target and the substrate to remove the slow-moving particulates.

v) Target Surface Improvement: The desirable features of a target material are high density and smooth surfaces.

The target morphology, laser power density, the target material, and the target density affect formation of particulates in PLD. The particles observed in laser deposited films are of two types: outgrowths or precipitates having composition different than the film matrix; and droplets, particulates and boulders have rounded shapes and same composition as the film matrix. The surfaces which are suitable to obtain good electrical and crystallographic properties give poor results because of growth of precipitates and surface roughness due to low laser densities that degrades the film stoichiometry. [3]

4.2. Depositing Thin Films Using PLD

In order to achieve a stationary ablation rate using PLD technology, a planar target is rotated or moved in the focal plane of the laser beam. Material ablation from the target is induced by a focused laser beam. The substrate located at a specified distance from the target and held stationary can be heated to get desired film growth. The desired chemical reactions are produced in the film growth process according to the selected gases. [4] The setup for PLD used in the experiments conducted for the present research is shown in Figure 4.1.

In our studies, centrifugally cast A609 Grade HK40 (19.0–22.0% Ni, 23.0–27.0% Cr, 0.35–0.45% C, 0.05–2.0% Si, 1.5% max. Mn) tubing was obtained from Ultra-cast Inc. The tubing was turned on a lathe with a carbide bit to an inside diameter of 2.3” and an outside diameter of 2.4”. A water-cooled silicon carbide cutting wheel was used to extract and flatten a 0.25” × 0.25” specimen from the tubing. The target material, SiC (0.009% Al, 0.020% B, 0.031% Fe, 0.015% O and 0.017% Mn, traces of Ni and Ti), was supplied by Kurt J. Lesker Company. A KrF excimer laser (λ = 248 nm) was used to ablate and deposit SiC on as machined and shot peened (170/ 325 mesh glass beads at 80 psi air pressure) HK40 substrates.

The films were deposited inside a stainless steel vacuum system pumped to a pressure in the range 10^{-4}–10^{-5} torr. The KrF laser was focused using mirrors and lenses to a rectangular spot 0.125 cm × 0.078 cm on a rotating SiC target. The target diameter was 25.4 mm and the rotation speed ranged from 10 to 20 revolutions/ minute. The pulse energy and frequency of the laser were ~500 mJ and 5–10 hertz, respectively. The laser/ target angle of incidence was 45° and the target to substrate distance was 40–50 mm. Depositions were performed at room temperature and at a substrate temperature of 500 C. The upper temperature limit was selected to limit sigma phase formation [8] during the deposition process. A schematic of the experimental setup is shown in Figure 4.2. [9]

4.3. Thin Film Characterization

4.3.1. Atomic Force Microcopy

Texture or, roughness is a surface property having a direct influence on the different types of analysis. Friction is a direct outcome of roughness in a material. Apart from smooth polished silicon wafers, ceramics and metals have roughness on a micron scale. These topological variations are measured by surface sensitive techniques such as atomic force microscopy. The two commonly used terms are shown in equations as below:

$$\mathrm{RA} = \frac{1}{N}\sum_{i=1}^{N}\left|z_i - \bar{z}\right| \qquad \text{(I)}$$

$$\mathrm{RMS} = \left[\frac{1}{N}\sum_{i=1}^{N}\left(z_i - \bar{z}\right)^2\right]^{1/2} \qquad \text{(II)}$$

where, RA is average roughness and RMS stands for root-mean-square roughness. N is the number of measurements, and if z is height then average height is $\bar{z}$. RA is the mean deviation of height measurements and RMS is the standard deviation. Atomic Force Microscope (AFM) is also termed as Scanning Force Microscope (SFM). It has a very sharp probe tip mounted on a cantilever beam with spring constant of approximately 0.1-1.0 N/m which measures the force between a sample surface. The typical spring constant between two atoms is higher by an order of magnitude than the cantilever beam of AFM. The piezoelectric tubes control the rastering motion during scanning. The surface topography is obtained by the determination of force as a function of the sample's position. Beam deflection and interferometry are the optical means to do measurements. AFM can help in analyses of insulating and conducting material without any sample preparation. The tip usually is in contact with the sample and the spatial resolution can be at the atomic scale for smaller ranges as well as few nanometers for scans up to 130 um. [10-12]

Here two coupons were prepared of HK40 alloy following the procedure mentioned in section 4.2. One coupon was as-machined while the other was shot-peened using glass beads. Contact mode atomic force microscopy (AFM) studies were performed on the target, substrate, and coating as shown in the setup Figure 4.3. All specimens were scanned at 50 um × 50 um × 2 um and no corrections were made during analysis. The local roughness on all surfaces was comparable and varied from 300 to 500 nm. The surface morphology of the coated and uncoated substrates did not change. Machining produced a common "scratch-like" appearance and surface tensile stresses. Shot peening introduced compressive stress on the HK40 surface and produced a "dimple-like" morphology. The surface morphology of the machined and shot peened surfaces is shown in Figure 4.4. [9]

4.3.2. Scanning Electron Microcopy

The deposited samples were observed using SFEG-SEM: Schottky Field-Emission Gun on a Scanning Electron Microscope (LEO-1550). Typical backscatter electron (BSE) microscopy image of as deposited SiC is shown in Figure 4.5. During room temperature deposition on as machined "scratch-like" surfaces, poor coverage and adhesion is apparent. Deposition at higher temperatures and on shot peened "dimple-like" surfaces showed significant coverage and improved adhesion. [9] The coating thickness of the ablated HK40 alloy was determined by SEM of the scratch tested specimen (refer section 4.3.6). The thickness was estimated to be ~ 1 um as shown in Figure 4.6.

The chemistry of the coating (Figure 4.5) and target was studied by qualitative energy dispersive spectroscopy (EDS) to determine if there was direct transfer of the target chemistry to the HK40 substrate. Similarities in the spectra for the target and coating were observed (see Figure 4.7). A strong aluminum peak, a residual element from the target material, existed in both spectra. A significant oxygen peak appeared in the spectrum for the coated substrate. Since oxygen was not detected in both spectra, it is believed that this can be diminished by using better vacuum conditions. Weak iron and chromium peaks appeared in the coating spectra from the HK40 substrate. Nickel, manganese, boron and titanium were not detected in either spectrum. [9]

4.3.3. X-Ray Diffraction

X-ray Diffraction is an inexpensive, non-destructive technique for characterization of the thin films and identification of phases. Here, when a collimated beam of X-rays having wavelength λ is focused on a specimen; their diffraction by the crystalline phases in the specimen follows Bragg's law:

$$\lambda = 2d \sin\theta \qquad \text{(III)}$$

where, spacing between atomic planes in the crystalline phase is denoted by *d*. The specimen's orientation and the diffraction angle 2θ are used to measure the intensity of the diffracted X-rays for yielding diffraction pattern. The obtained diffraction pattern is used in solving the atomic structure and calculating the specimen's structural properties such as, strain; epitaxy; and the orientation and size of crystallites apart from the crystalline phases. Film thicknesses; atomic arrangements in amorphous materials and multilayers; characterization of defects; and concentration profiles are also determined by XRD. Due to the small diffracting power of thin films, XRD techniques and instruments are designed in order to maximize the diffracted X-ray intensities. The angle between the incident and diffracted X-rays is 2θ. [10, 13]

Pulsed laser self ablation was done of 35Cr-45Ni-0.4C target onto coupon made of the same material following the procedure mentioned in section 4.2. XRD studies were performed using an automated X-ray powder diffractometer (Model Thermo ARL Scintag PAD-X) with Cu normal focus X-ray tube operated at 45 kV and 20 mA. Both the substrate and coated substrate were examined. As shown in Figure 4.8, there is direct transfer of stoichiometry of elements from the target to the substrate. When the XRD studies were done on the SiC target and the film of SiC formed by pulsed laser deposition, direct transfer of stoichiometry did not occur (see Figure 4.9). The silicon carbide film contained SiC, C, Si, and SiO_2. Bonnell et al [14] found similar results in their studies and determined that the covalently bonded SiC on ablation breaks down into a variety of atoms and molecules (i.e. Si, SiC, SiC_2, Si_2C, C, C_2, C_3, Si_2, Si_3) instead of ions. These differences in stoichiometry of the films of SiC and 35Cr-45Ni-0.4C targets deposited by pulsed laser ablation also lead to the preliminary investigation of the plume discussed in Appendix on Plume Analysis in the end.

Neocera Inc. in their patent [15] suggested that the laser beam which impinges on the target focused by the focusing element and housed inside the lead glass chamber as shown in Figure 4.10, controls the stoichiometry of the deposited film. To look into this suggestion, experiments were conducted using KrF laser (λ = 248 nm, pulse energy ~ 500 mJ, frequency = 10 Hz) by ablating the SiC target and depositing on the Si coupons. The target material, SiC (Hexoloy), was donated by Saint Gobain Ceramics Structural Ceramics Inc. The Si coupons were cleaned in HF before mounting as substrate inside the stainless steel vacuum chamber. The focusing lens was translated from A to B by a distance of 5 mm, and similarly from position B to C by 5 mm. The mounted SiC target having diameter of 25.4 mm was rotated at the speed of 10-20 rpm and the pressure inside the stainless steel vacuum chamber was around 10^{-4} - 10^{-5} Torr. The distance between target and substrate was 40 mm and angle of incidence of laser/ target was 45^{o}. Depositions were done at positions A, B and C of the focusing lens for 5 minutes.

The deposited SiC film on Si at positions A, B and C; along with the SiC target were analyzed by using an automated X-ray powder diffractometer (Model Thermo ARL Scintag PAD-X, Scintag Inc., Cupertino, CA) having Cu normal focus X-ray tube operated at 45 kV and 20 mA at the Department of Geosciences, Stony Brook University, NY. The scan was done in the range of 2θ, 10 to 90 degrees with a continuous scan mode of 1 degree per minute and scan size of 0.02 degree, by controlling the goniometer using the computer.

The XRD studies of SiC target, sample A, sample B and sample C are shown in the Figure 4.11 in red, black, blue and green color plots. It can be clearly seen that there is a variation in the stoichiometry of the deposited SiC film as the focusing lens is moved away from the stainless steel chamber.

Again, the reason for absence of direct transfer of stoichiometry from the SiC target to the SiC deposited film had been explained by Bonnell [14]; which stresses that the SiC has covalent bonds and the covalent SiC bond on ablation breaks down into atoms and molecules of Si, SiC, SiC_2, Si_2C, C, C_2, C_3, Si_2, Si_3 instead of ions. Here in our experiments the following "finger prints" were observed Si_5C_3 (PDF# 50-1349) [16], Si_5C_3 (PDF# 77-1084) [17], SiO_2 (PDF# 81-69) [18], Si (PDF# 47-1186) [19], Coesite (PDF# 12-711) [20], C (PDF# 26-1083) [21, 22], C (PDF# 43-1104) [23], C8 (PDF# 72-2091) [24], Graphite (PDF# 41-1487) [25] in the deposited SiC films. Film A has presence of Si_5C_3 (PDF# 50-1349), C (PDF# 26-1083) and C (PDF# 43-1104); film B has presence of Si_5C_3 (PDF# 50-1349), Si (PDF# 47-1186), Graphite (PDF# 41-1487) and Coesite (PDF# 12-711); and film **C** has Si_5C_3 (PDF# 77-1084), SiO_2 (PDF# 81-69), and C8 (PDF# 72-2091).

SiO_2/Coesite (PDF# 12-711) present in SiC target transfers with the same stoichiometry in sample B, and changes form for sample C as SiO_2 (PDF# 81-69) , whereas there is absence of SiO_2 for sample A. The stoichiometry of Si_5C_3 (PDF# 50-1349) is same for both film A and B, which is different from Si_5C_3 (PDF# 77-1084) of film C. Si_5C_3 (PDF# 50-1344) and Si_5C_3 (PDF# 77-1084) is a derivative of original SiC present in the SiC target. Signatures of Carbon C (PDF# 26-1083) and C (PDF# 43-1104) are seen in film A, graphite (PDF# 41-1487) in film B and C8 (PDF# 72-2091) in film C, which are not present in X-ray diffraction pattern of the original SiC target.

Figure 4.11 proves that the change in position of the lens can lead to variation in stoichiometry of the deposited SiC film. The high intensity peaks of Coesite (PDF# 12-711) and Graphite (PDF# 41-1487) are observed in the case of film B; whereas high intensity peaks of Si_5C_3 (PDF# 77-1084) are observed for film C. This leads to the conclusion that the Si_5C_3 (PDF# 77-1084) obtained for film C which is derivative of SiC (PDF# 74-1302) [26] present in the SiC target matches perfectly with the parent target material of SiC than that for the film A and film B. Due to instrumental limitation other positions of the focusing lens were not performed. Based on the present analysis of effect of position of focusing lens on the stoichiometry of the SiC deposited film, it leads to the conclusion that varying the position of focusing lens can lead to the film deposition of similar stoichiometry as the ceramic SiC target. Noticeably, in the present experimental observations the stoichiometry of the deposited film has a comparatively higher match with the SiC target when the focusing lens is farthest from the stainless steel vacuum chamber. Furthermore, this focusing lens is at largest distance from the SiC target on which it focuses the laser beam to ablate SiC and develop the films. Accordingly, the combination of the power of laser, the type of laser, the distance of the focusing lens from the target, the distance of the target from the substrate, the atmosphere inside the vacuum chamber, the type of target, etc. all play a role in affecting the transfer of stochiometry from the target to the substrate.

4.3.4. Synchrotron X-Ray Diffraction

Synchrotron X-ray diffraction experiments were performed at Beamline x14a National Synchrotron Light Source- Brookhaven National Laboratory, NY on self ablated 35Cr-45Ni-0.4C coupons. A KrF excimer laser (λ= 248 nm) was used for target ablation. The laser was directed and focused into the deposition chamber using mirrors and lenses. Prior to deposition, the substrate was heated to 500 C under 5 x 10^{-5} torr vacuum pressure. The deposition temperature was chosen to improve coating adhesion and limit the formation of detrimental phases during processing [9]. Pulsed laser deposition occurred under the following conditions: pulse rate- 10 hertz; pulse length- 25 nanoseconds; target rotation- 10 rpm; fluence- ~100 mj/ mm^2; oxygen pressure- 10 millitorr; target/ substrate distance- 40 mm; and deposition times- 0, 15, 30, and 45 minutes.

During our experiments, the wavelength was fixed at 0.177 nm. Figure 4.12 shows the diffraction geometry used during the x-ray experiments. [27] So as in this Figure 4.12, when the position of goniometer is varied to change:

i) Angle θ (not shown), structural information can be observed.
ii) Angle ψ and Φ, textural information is measured.
iii) Angle ψ, to calculate in plane stresses.

Figure 4.13 shows the full scan x-ray diffraction patterns collected with ψ = 0. Experimental peaks matched PDF #47-1405 [28] which were used to identify planes. The

(111), (200), (220), (311), and (222) planes existed in the experimental full scans at all deposition times (0, 15, 30, 45 minutes).

Figure 4.14 and Figure 4.15 show the slip plane analysis taken at ψ= 0, 5, 10, 15, 30, and 60 degrees from samples where the deposition times were (a) 30 minutes and (b) 45 minutes. The small side peak contribution in Figure 4.14 and Figure 4.15, which is not apparent at lower deposition times (t = 0 and 15 minutes), is due to the 35Cr- 45Ni film. The film side peak is a 111 peak with a larger interplanar spacing than the substrate. In general, the interplanar spacing tends to be smaller {not only for the (111) plane} for thicker films, but the (111) peaks split to double peaks with the side peak (film) interplanar spacing even larger than the substrate. The nanoparticulates that make up the film have a preferred orientation to the surface normal (i.e. at higher ψ angles, the side peak disappears). Also at higher ψ angles, the intensity decreases and the side peak appears to move closer to the main peak and eventually disappears at ψ > 30 (see Table 4.1). [27]

For stress measurements, different reflections can be brought into the diffraction condition at the suitable 2θ values for a polycrystalline specimen observed with a diffractometer using monochromatic radiation. Here for the present samples observed using synchrotron X-rays, the (222) plane was selected for residual stress analysis because the high angle peak displays a larger shift in 2θ [29]. On differentiating Bragg's law:

$$n\lambda = 2d \sin\theta \qquad \text{(IV)}$$

$$0 = 2d \cos\theta\Delta\theta + 2\Delta d \sin\theta \qquad \text{(V)}$$

$$\Delta\theta = - \varepsilon . \tan\theta \qquad \text{(VI)}$$

$$\varepsilon = \frac{\Delta d}{d} \qquad \text{(VII)}$$

For larger θ, tanθ is larger which results in larger Δθ for a given stress. Using equations (VI) and (VII), the peak shift Δθ of the (222) plane at 117^{o} 2θ was around 3.46 times the peak shift Δθ of (111) plane at 50.5^{o} 2θ, when calculations were done at room temperature of the deposited film. Thus, X-ray diffraction residual stress measurements should be carried out at high angles.

Residual stresses in a coating are caused by mismatch of thermophysical properties between the substrate and the coating during fabrication. It can affect the performance and constitutional properties of the coating. The measurement of in-plane residual stresses assist in the designing and understanding of the processes to create coatings with improved adhesion, durability and overall effectiveness. [30] Here, the studies were conducted on films prepared as discussed in the beginning of this section. Figures 4.16 and 4.17 show the results from the residual stress analysis experiments. In Figure 4.16, as the film thickness increases the (222) peak shifts to higher values of 2θ. This shift indicates that higher elastic macrostrains exist in thicker films. Figure 4.17 shows the d versus $\sin^2\psi$ (in plane stress measurements for $\phi = 0$) measured from the (222) reflection. Assuming a biaxial state of stress and assuming that equation (VIII) is valid;

$$\frac{d_{\phi\psi} - d_o}{d_o} = \frac{1+\upsilon}{E}\sigma_\phi \sin^2\psi - \frac{\upsilon}{E}(\sigma_{11} + \sigma_{22}) \qquad \text{(VIII)}$$

the in-plane stress can be determined from the slope of d versus $\sin^2\psi$ plot if Poisson's ratio (ν) and the Young's modulus (E) of the material are known. Typical values for the x-ray constant Ke = $E/(1+\nu)$ for nickel based alloys range from 20,000 to 40,000 ksi. [13] From Figure 4.17, there is a transition from compressive to tensile in plane stress as the film thickness increases.

4.3.5. Electron Spectroscopy for Chemical Analysis (ESCA)

During X-ray Photoelectron Spectroscopy (XPS) analysis electron are ejected when monoenergetic soft X-rays bombard a sample material. The kinetic energies *KE* of these ejected photoelectrons (or, electrons) help in the identification of the elements present in the sample because of the dependence on the energy of the photon $h\nu$. In the Einstein photoelectric law:

$$KE = h\nu - BE \qquad \text{(IX)}$$

where, the binding energy of the particular electron to the atom concerned is denoted by *BE*. The binding energy *BE* is determined by measurement of *KE* as $h\nu$ is already known.

The chemical state of the elements is identified on a smaller scale by small variations in the determined kinetic energies. The measured photoelectron intensities facilitate calculation of relative concentrations of elements. XPS finds use both for biological and metallurgical materials because of its ability to do chemical state analysis and semiquantitative elemental analysis of surfaces without standards. Depending on the material used, the angle of the measurement, and the energy of the required photoelectron, XPS can probe 2-20 atomic layers deep for a solid. [10]

On SiC deposited coatings, the full scan at 25 degree angle similar to Huang et al. [31] is shown in Figure 4.18. These studies were conducted at Army Research Laboratory, USA. The presence of Na peaks in the plot is due to inherent contaminants. The peaks of interest are C1s, Si2p and O1s. The narrow scan of C1s peak is shown in Figure 4.19. After doing background subtraction of the peak, the peak is resolved into three Gaussians:

i) H-C: due to presence of contaminants in vacuum chamber such as moisture/ hydrocarbons.

ii) C-C: due to free graphite.

iii) Si-C: of which the film is made out of.

Figure 4.20 shows the narrow scan of peak Si2p, it has been resolved into three Gaussians of SiO_2, SiC, and $Si_{0.4}C_{0.6}$ or C-Si-O. These results tally exactly with what Huang et al. found shown in Table 4.2. [31] The narrow scan of the O1s peak was not examined.

4.3.6. Adhesion Tests

The scratch-test method consists of the generation of scratches with a spherical stylus (generally Rockwell C diamond, tip radius 200µm) which is drawn at a constant speed across the coating-substrate system to be tested, under either constant or progressive loading at a fixed rate. For progressive loading, the critical load (L_c) is defined as the smallest load at which a recognizable failure occurs; for the constant loading mode, the critical load corresponds to the load at which a regular occurrence of such failure along the track is observed.

The driving forces for coating damage in the scratch test are a combination of elastic-plastic indentation stresses, frictional stresses and the residual internal stresses. In the lower load regime, these stresses generally result in conformal or tensile cracking of the coating which still remains fully adherent. The onset of these phenomena defines a first critical load. In the higher load regime, one defines another critical load which corresponds to the onset of coating detachment from the substrate by spalling, buckling or chipping.

The scratch test is basically a comparison test. The critical loads depend, of course, on the mechanical strength (adhesion, cohesion) of a coating-substrate composite but also on several other parameters: some of them are directly related to the test itself, while others are related to the coating-substrate system [32].

The test specific parameters include:

- Loading rate,
- Scratching speed,

- Indenter tip radius,
- Indenter material (and also indenter tip wear).

The coating-substrate specific parameters include:

- Substrate hardness and roughness,
- Coating hardness and roughness,
- Coating thickness,
- Friction coefficient between coating and indenter,
- Internal stresses in the coating.

The means for critical load determination are:

i) Microscopic observation: This is the most reliable method to detect coating damage. This technique is able to differentiate between cohesive failure within the coating and adhesive failure at the interface of the coating-substrate system.

ii) Acoustic emission (AE) detection: Detection of elastic waves generated as a result of the formation and propagation of microcracks. The AE sensor is insensitive to mechanical vibration frequencies of the instrument.

iii) Tangential force (Ft) recording: This enables the force fluctuations along the scratch to be followed.

iv) Pre-scan, post-scan and penetration depth recording: The pre-scan provides a profile of the proposed scratch path allowing any non-uniformity in the flatness of the samples to borne into consideration when the penetration depth of the indenter is measured during the scratch test.

> The post scan allows the elastic recovery of the coating-substrate system to be investigated by providing a profile of the residual scratch path.

For each measurement the acoustic emission signal (AE), the tangential force (Ft) and the penetration depth (Pd) are recorded versus the normal load. The AE-Ft-Pd graphs for these measurements are shown in Figure 4.21. The following information can be found on each recording:

Substrate	Substrate material
Coating	Coating material
AE Sensit.	Sensitivity of the AE detector
Ind.	Indentor number
dx/dt	Scratching speed
dL/dt	Loading rate
LcAE	Critical load, Lc determined on the AE graph
LcFt	Critical load, Lc determined on the Ft graph
LcPd	Critical load, Lc determined on the Pd graph
File	File name in which the data are stored.

The coupon made of HK40 alloy and having a film of SiC deposited via pulsed laser deposition was tested for adhesion by scratch tester shown in Figure 4.22. Here the scratches were generated using a Rockwell C type diamond indenter (tip radius 50μm) which was drawn at a constant speed (4 mm/min.) across the coating–substrate system. [32] Tests were performed using loads between 0 to 6 N, a loading rate of 6 N/min, and a scratch length of 4 mm (Table 4.3). A critical load (i.e. the smallest load at which a recognizable failure occurs, see Figure 4.23 a) was attained at 0.48 ± 0.06 N. Complete delamination (see Figure 4.23 b) occurred at higher loading, 4.37 ± 0.4 N. These modest values indicate poor adhesion between the coating and substrate.

4.4. Modeling of Coking/ Carburization Behavior of Coated Ethylene Pyrolysis Tubing

DICTRA is a software tool which utilizes the subroutines of Thermo-Calc software program [33], described in section 3.1, to solve numerically and simulate DIffusion Controlled TRAnsformations [34]. This package was primarily developed by collective effort of the Max Planck Institute (MPI) for Iron Research at Dusseldorf and the Royal Institute of Technology (KTH) in Sweden to solve concurrently thermodynamic equations and the appropriate diffusion controlling phase transformations in both the solid and liquid states [35]. Here, multi-component diffusion equations are solved numerically maintaining thermodynamic equilibrium at interfaces. The DICTRA program has four subdivisions:

i) Diffusion equations are solved,

ii) Thermodynamic equilibrium is solved (The subroutine used here is from Thermo-Calc,

iii) Flux-balance equations are computed, and

iv) Adjustment of grid points with the mobility of phase interface positions.

The DICTRA program has applications in:

- Diffusion in Single-phase systems.
- Diffusion with moving boundaries (dissolution of particles, growth, etc.).
- Cell calculations (immobile interfaces, particle distributions, etc.).
- Diffusion in dispersed systems.
- Oswald ripening or, Coarsening.
- Cooperative growth.
- Kinetic data.
- Deviation from local equilibrium.
- Diffusion in complex phases.

The present model used to simulate coking/ carburization behavior of coated ethylene pyrolysis tubing is based on diffusion of dispersed phases. Similar modeling of carburization profiles in Alloy 800H at high temperatures was done by Bongartz et al [36]. Here in the calculations, the U-fraction of a component *t* is defined as [35]:

$$U_t = \frac{x_t}{\sum x_t} \qquad \text{(X)}$$

where, $\sum x_t$ is taken over the substitutional elements only. The composition variable related to the volume is used for the choice of the volume fixed frame of reference. The assumption made in calculation of U-fraction is that a species may or may not contribute to the volume of a phase. The volume contribution by interstitial species is assumed to be negligible. The activity of carbon is defined by [37]:

$$a_c = (\text{wt\% C})\,\Gamma \qquad \text{(XI)}$$

where, Γ is the coefficient of activity which is selected in order to have $a_c = 1$ for an equilibrium between graphite and amount of carbon in the solution. Nickel increases the coefficient of activity and chromium decreases it. The surface reaction gets affected by the driving force of carbon diffusion due to the presence of alloying elements. Diffusion studies were performed using DICTRA [38]; and the TTNi [39] and MOBNi1 [40-45] Databases. Figure 4.24 (A) and Figure 4.24 (B) shows the diffusion model for the diffusion of carbon in the FCC matrix of Fe-Ni-Cr-Si-C alloys (HK40 and 35Cr-45Ni) system. The austenitic FCC matrix has presence of active austenitic stoichiometric spheroidal phases of $M_{23}C_6$ and M_7C_3. The activity of carbon with reference to graphite is considered variable in the range 0.5 to 1.0. For computing the diffusion equations, the region is considered to have gridpoints (or, node points) spread out geometrically in the grid. The geometrical series controlled by a geometric factor greater than one gives a higher number of grid points at the carburized surface, as shown in Figure 4.24 (B). The depth of diffusion considered for calculations is 1mm (surface effect only).

The tubes made of Fe-Ni-Cr-Si-C alloys used in ethylene pyrolysis petrochemical plants are decoked every 2-3 months (Refer Chapter 2, 3). In the present model, the time for calculating the diffusion of carbon is considered to be 60 days (5184000 seconds).

Based on the analysis from Thermo-Calc of the material mentioned in section 3.1, the two alloys which were considered for modeling of coking/ carburization behavior of coated ethylene pyrolysis tubing are HK40 and 35Cr-45Ni. It can be recalled from Figure 3.6 that HK40 showed the least resistance and 35Cr-45Ni showed most resistance to carburization at higher temperatures.

4.4.1. HK40 Alloy

i) Phases:

The Figures 4.25 and Figures 4.26 are plotted as mole-fraction of phase versus distance in meters. Figures 4.25 (A), (C) and Figures 4.26 (A), (C) are Dictra plots at 900 C and 1200 C, respectively when activity value of carbon is 1. Figures 4.25 (B), (D) and Figures 4.26 (B), (D) are Dictra plots at 900 C and 1200 C, respectively when activity value of carbon is 0.5. Figures 4.25 (C), (D) and Figures 4.26 (C), (D) depict the diffusion phenomena at the surface (depth = 0.1 mm); while Figures 4.25 (A), (B) and Figures 4.26 (A), (B) depict the diffusion phenomena in the bulk (depth = 1 mm).

It can be clearly interpreted from the Figures 4.25 (A), (C) that at 900 C, the mole-fraction of FCC_A1 phase is less than M_7C_3 phase at the surface. With the diffusion of carbon at unit activity, FCC_A1 phase increases while that of M_7C_3 decreases towards the bulk. On considering, behavior at 0.5 carbon activity and 900 C temperature {Figures 4.25 (B), (D)}, the mole-fraction of phase FCC_A1 is more than M_7C_3 at the surface; and FCC_A1 phase increases, M_7C_3 decreases with the diffusion of carbon in the bulk.

At 1200 C and unit carbon activity outlined in Figures 4.26 (A), (C), the mole-fraction of FCC_A1 phase is less than M_7C_3 phase at the surface and remains constant towards the bulk. When the carbon activity is 0.5 as shown in Figures 4.26 (C), (D) the mole fraction of FCC_A1 phase is greater than the mole fraction of M_7C_3 phase. Here, even though the mole-fraction of chromium carbide is higher at the surface it decreases when going into the bulk. This pattern is different than the behavior, mentioned above, of 0.5 carbon activity and 900 C, which inherently has less chromium carbide at the surface and keeps decreasing when going into the surface.

ii) U-fraction:

Figures 4.27-4.31 show plots for U-fractions of carbon, chromium, iron, nickel and silicon respectively at activities of carbon of 0.5 and 1.0. The U-fractions show descending order with respect to elements at both 0.5 and 1.0 carbon activities as: iron < chromium < carbon < nickel. In Figures 4.27-4.31, (A) and (C) are at temperature 900 C while (B) and (D) are 1200 C. Furthermore, in Figures 4.27-4.31, (C) and (D) are the plots at the surface (depth = 0.1 mm). U-fraction plot of carbon at 900 C and 1200 C (Figures 4.27) show similar behavior for both the activities. The U-fraction is higher at carbon activity of 1.0 than that of 0.5, at the surface and remains higher going towards the bulk. U-fraction is larger at 1200 C than 900 C temperatures both for activity of 0.5 and 1.0 at the surface.

Besides carbon, comparing U-fraction of other elements, it can be seen that U-fraction of iron, nickel and silicon increases while that of chromium decreases on moving towards the depth. There is a dip in U-fraction of chromium, Figure 4.28 (C), and corresponding increase in U-fraction of iron, nickel and silicon as shown in Figures 4.29 (C), 4.30 (C) and 4.31 (C) respectively at both 0.5 and 1.0 activity of carbon. Similar behavior is seen in Figures 4.28-4.31 (B) at 1200 C for both the activities. Also, at the surface it can be observed in Figures 4.28 that the mole-fraction of chromium is lower at 900 C than 1200 C temperatures; whereas in Figures 4.29-4.31, respectively for mole-fraction of iron, nickel and silicon, mole-fractions are higher at 900 C than 1200 C temperatures. These results apply to both unit carbon activity as well as 0.5 carbon activity. It is also observed in case of chromium, iron, nickel and silicon that when the distance from the surface increases; the mole-fractions become constant and at 1200 C having the same values as that of 900 C temperature.

The Dictra plots at 1000 C and 1100 C temperatures showed similar patterns as that of at 1200 C temperature, and therefore have not been documented in the present analysis.

4.4.2. 35Cr-45Ni Alloy

i) Phases:

The mole-fraction of phase versus distance in meters is plotted in Figures 4.32 and Figures 4.33. The Dictra plots at 900 C and 1200 C, respectively when activity value of carbon is 1 are shown in Figures 4.32 (A), (C) and Figures 4.33 (A), (C). When the activity of carbon is 0.5, the Dictra plots at 900 C and 1200 C, respectively are shown in Figures 4.32 (B), (D) and Figures 4.33 (B), (D). Figures 4.32 (A), (B) and Figures 4.33

(A), (B) depict the diffusion phenomena in the bulk (depth = 1 mm); while Figures 4.32 (C), (D) and Figures 4.33 (C), (D) depict the diffusion phenomena at the surface (depth = 0.1 mm).

Figures 4.32 (A), (C) shows that at 900 C and unit carbon activity, the mole-fraction of M_7C_3 phase is larger than FCC_A1 phase at the surface. Towards the bulk, M_7C_3 phase decreases while that of FCC_A1 phase increases. A similar profile is seen in Figures 4.32 (B), (D) at 0.5 carbon activity and 900 C of M_7C_3 and FCC_A1 phases. The presence of $M_{23}C_6$ phase for both carbon activities of 0.5 and 1.0 at 900 C can be noticed during the diffusion of carbon at a distance of around 0.5 mm from the surface.

At 1200 C and unit carbon activity see Figures 4.33 (A), (C), the mole-fraction of M_7C_3 phase is more than FCC_A1 phase at the surface. M_7C_3 phase decreases and FCC_A1 phase increases towards the bulk, and becomes constant at distance of around 0.2 mm from the surface. The profile M_7C_3 and FCC_A1 phases at 0.5 carbon activity, shown in Figure 4.33 (C), (D) reveal analogous behavior to that of unit carbon activity. The mole-fraction of chromium carbide remains higher at the surface and decreases on going more towards the bulk. This behavior can be seen at all temperatures and all carbon activities.

ii) U-fraction:

The U-fraction plots of carbon, chromium, iron, nickel and silicon having carbon activities of 0.5 and 1.0 are shown in Figures 4.34-4.38, respectively. The U-fractions show descending order with respect to elements at both 0.5 and 1.0 carbon activities as:

nickel < chromium < carbon < iron < silicon. In each Figure 4.34-4.38, (A) and (C) are at 900 C while (B) and (D) are at 1200 C. Furthermore, in Figures 4.34-4.38, (C) and (D) are the plots at the surface (depth = 0.1 mm). The U-fraction of carbon at 900 C is higher at carbon activity of 1.0 than that of 0.5, at the surface and remains higher going towards the bulk. There is an increase in the value of U-fraction at 1200 C compared to 900 C, both for activity of 0.5 and 1.0 at the surface (Figures 4.34).

It can be observed that U-fraction of chromium and iron decreases while that of nickel and silicon increases on moving towards the bulk. There is a decrease in U-fraction of chromium, Figure 4.35 (C); and corresponding increase in U-fraction of nickel and silicon as shown in Figures 4.37 (C) and 4.38 (C) respectively at both 0.5 and 1.0 activity of carbon at around 0.01 mm distance from the surface. The increase can be noticed in iron and nickel in Figures 4.36 (A) and 4.37 (A), respectively with a corresponding decrease in silicon {see Figure 4.38(A)} for 0.5 and 1.0 carbon activity at depth of 0.4-0.6 mm from the surface.

Also, at the surface it is observed in Figures 4.35 and 4.36 that the U-fraction of chromium and iron, respectively is higher at 1200 C than 900 C temperatures; whereas in Figures 4.37, 4.38 U-fractions of nickel and silicon, respectively are lower at 1200 C than 900 C. These results apply to both unit carbon activity as well as 0.5 carbon activity. Similar to that of HK40, it can also be observed for chromium, iron, nickel and silicon that when the distance from the surface increases; the U-fractions become constant and at 1200 C the values are same as that of 900 C.

Here again, the Dictra plots at 1000 C and 1100 C temperatures showed similar patterns as that of at 1200 C temperature, and therefore have not been documented in the present analysis.

References:

[1] H. M. Smith and A. F. Turner, "Vacuum Deposited Thin Films Using a Ruby Laser", Applied Optics 4 (1965) 147.

[2] Q. Wang, K. Itaka, H. Minami, H. Kawaji and H. Koinuma, "Combinatorial Pulsed Laser Deposition and Thermoelectricity of $(La_{1-x}Ca_x)VO_3$ Composition-Spread Films ", Science and Technology of Advanced Materials 5 (2004) 543.

[3] D. B. Chrisey and H. G. K., Pulsed Laser Deposition of Thin Films, (J. Wiley, 1994) p. 613 p. : ill. ; 25 cm.

[4] S. M. Kaczmarek, "Pulsed Laser Deposition: Today and Tomorrow", (SPIE, 1997) p. 129.

[5] K. Mitra, S. Kumar and A. Vedavarz, "Parametric Aspects of Electron-Phonon Temperature Model for Short Pulse Laser Interactions with Thin Metallic Films", Journal of Applied Physics 80 (1996) 675.

[6] S. A. Akhmanov, V. A. Vysloukh and A. S. Chirkin, Optics of Femtosecond Laser Pulses/ Uniform Title: Optika femtosekundnykh lazernykh impul'sov. English (American Institute of Physics, New York, 1992).

[7] R. Timm, P. R. Willmott and J. R. Huber, "Ablation and Blow-Off Characteristics at 248 nm of Al, Sn and Ti Targets Used for Thin Film Pulsed Laser Deposition", Journal of Applied Physics 80 (1996) 1794.

[8] L. Rimai, R. Ager, E. M. Logothetis, W. H. Weber and J. Hangas, "Preparation of Oriented Silicon-Carbide Films by Laser Ablation of Ceramic Silicon-Carbide Targets", Applied Physics Letters 59 (1991) 2266.

[9] A. Chauhan, W. Moran, S. Ge, W. Si and H. J. White, "Pulsed Laser Deposition of Silicon Carbide on Heat Resistant Materials", Scripta Materialia 52 (2005) 735.

[10] C. R. Brundle, C. A. Evans Jr and W. Shaun, Encyclopedia of Materials Characterization : Surfaces, Interfaces, Thin Films, in "Materials characterization series;" (Butterworth-Heinemann ;; Greenwich, CT :; Manning, 1992) p. 751 p. : ill. ; 25 cm.

[11] N. A. Burnham and R. J. Colton, "Measuring the Nanomechanical Properties and Surface Forces of Materials Using an Atomic Force Microscope", Journal of Vacuum Science & Technology a-Vacuum Surfaces and Films 7 (1989) 2906.

[12] N. A. Burnham and R. J. Colton, edited by D. A. Bonnell (VCH Publishers, New York, N.Y., 1993) p. 436 p.

[13] B. D. Cullity, S. R. Stock and S. Stock, Elements of X-ray Diffraction (Prentice Hall, 2001).

[14] D. W. Bonnell, P. K. Schenck, J. W. Hastie and M. Joseph, "Ultra-High Temperature Laser Vaporization Mass Spectrometry of SiC and HfO_2", in Symposium on High Temperature Chemistry (Electrochemical Society, NJ, 1990).

[15] H. M. Christen, Scanned Focus Feposition System in "US Patent and Trademark Office" (Neocera, Inc. (Beltsville, MD), USA, 2002) p. 11.

[16] B. V. Khaenko, E. V. Prilutskii, A. A. Mikhailik and M. V. Karpets, "Phase State and Crystal Structure of Products Obtained by Reaction of SiC with SiO_2", Inorganic Materials 31 (1995) 304.

[17] B. V. Khaenko, E. V. Prilutskii, A. A. Mikhailik, M. V. Karpets and A. V. Krainikov, "State and Crystal Structure of the Products of Raction between SiC and SiO_2", Izv. Akad. Nauk SSSR, Neorg. Mater. 31 (1995) 6.

[18] J. R. Chelikowsky, N. Troullier, J. L. Martins and H. E. King, "Pressure-Dependence of the Structural-Properties of Alpha-Quartz Near the Amorphous Transition", Physical Review B 44 (1991) 489.

[19] S. J. Duclos, Y. K. Vohra and A. L. Ruoff, "Experimental-Study of the Crystal Stability and Equation of State of Si to 248GPA", Physical Review B 41 (1990) 12021.

[20] F. Dachille and R. Roy, "High-Pressure Region of the Silica Isotopes", Z. Kristallogr. 111 (1959).

[21] J. A. Holcombe, Private Communication, (1974).

[22] J. A. Holcombe, Report Y1887, (U.S. AEC Oak Ridge Y-12 Plant, 1973).

[23] H. Hirai and K.-i. Kondo, "A New Crystalline Form of Carbon under Shock Compression", in Proceedings of the Japan Academy. Ser. B: Physical and Biological (The Japan Academy, 1991) p. 22.

[24] N. N. Matyushenko, V. E. Strelnitsky and V. A. Gusev, "Electron-Diffraction Study of the Crystalline Phase-Structure of Carbon C8", Kristallografiya 26 (1981) 484.

[25] I. Sanc, ICDD Grant-in-Aid, (Polytechna, Foreign Trade Corporation, Panska, Czechoslovakia, 1990).

[26] A. Taylor and D. S. Laidler, "The Formation and Crystal Structure of Silicon Carbide", British Journal of Applied Physics 1 (1950) 174.

[27] A. Chauhan, M. Anwar, K. Montero, H. J. White, R. S. Petrova, J. A. Payne, W. Si and J. Bai, "Slip Plane X-ray Residual Stress Analysis of Pulsed Laser Self Ablated Coatings", Surface and Coatings Technology (2006 (Communicated)).

[28] R. G. Samvelyan, E. S. Abovyan, S. G. Agbalyan, N. N. Manukyan and M. S. Sakanyan, "X-Ray-Diffraction Examination of the Process of Thermal Stabilization of Powder Thermal Bimetals", Soviet Powder Metallurgy and Metal Ceramics 30 (1991) 606.

[29] I. C. Noyan and J. B. Cohen, Residual Stress: Measurement by Diffraction and Interpretation (Springer- Verlag, 1987).

[30] M. Wenzelburger, D. Lopez and R. Gadow, "Methods and Application of Residual Stress Analysis on Thermally Sprayed Coatings and Layer Composites", Surface and Coatings Technology 201 (2006) 1995.

[31] N. K. Huang, D. Z. Wang, Q. Xiong and B. Yang, "XPS Study of Hydrogen Permeation Effect on SiC-C Films", Nuclear Instruments & Methods in Physics Research Section B-Beam Interactions with Materials and Atoms 207 (2003) 395.

[32] P. A. Steinmann, Y. Tardy and H. E. Hintermann, "Adhesion Testing by the Scratch Test Method - the Influence of Intrinsic and Extrinsic Parameters on the Critical Load", Thin Solid Films 154 (1987) 333.

[33] B. Sundman, in "User Aspects of Phase Diagrams", edited by F. H. Hayes (Institute of Metals, 1991) p. 303.

[34] N. Saunders and A. P. Miodownik, CALPHAD (Calculation of Phase Diagrams): A Comprehensive Guide (Elsevier Science Inc., New York, 1998).

[35] User's Guide, DICTRA, Version 24, (Thermo-Calc Software).

[36] K. Bongartz, D. F. Lupton and H. Schuster, "A Model to Predict Carburization Profiles in High Temperature Alloys", Metallurgical Transactions A (Physical Metallurgy and Materials Science) 11A (1980) 1883.

[37] Gas Carburizing, (Key to Metals Group AG, 2007).

[38] B. Sundman, M. Schalin and P. Shi, DICTRA, (Foundation of Computational Thermodynamics, Royal Institute of Technology, Stockholm, Sweden, 2006).

[39] N. Saunders, Ni-Data V.6, A Thermodynamic Database for Calculation of Phase Equilibria in Multi-Component Ni-Based Super Alloys, (Thermotech Ltd, Surrey Technology Centre, The Surrey Research Park Guildford, Surrey GU2 5YG, 2003).

[40] J. Agren, "A Revised Expression for the Diffusivity of Carbon in Binary Fe-C Austenite", Scripta Metallurgica 20 (1986) 1507.

[41] Engstrom, Diffusion of Si in FCC Ni.

[42] B. Jonsson, "Assessment of the Mobilities of Cr, Fe and Ni in Binary FCC Cr-Fe and Cr-Ni Alloys", Scandinavian Journal of Metallurgy 24 (1995) 21.

[43] B. Jonsson, "Assessment of the Mobilities of Cr, Fe, and Ni in FCC Cr-Fe-Ni Alloys", Zeitschrift fuer Metallkunde/Materials Research and Advanced Techniques 86 (1995) 686.

[44] B. Jonsson, "Mobilities in Fe-Ni Alloys Assessment of the Mobilities of Fe and Ni in FCC Fe-Ni Alloys", Scandinavian Journal of Metallurgy 23 (1994) 201.

[45] B. Jonsson, "Assessment of the Mobility of Carbon in FCC C-Cr-Fe-Ni Alloys", Zeitschrift Fur Metallkunde 85 (1994) 502.

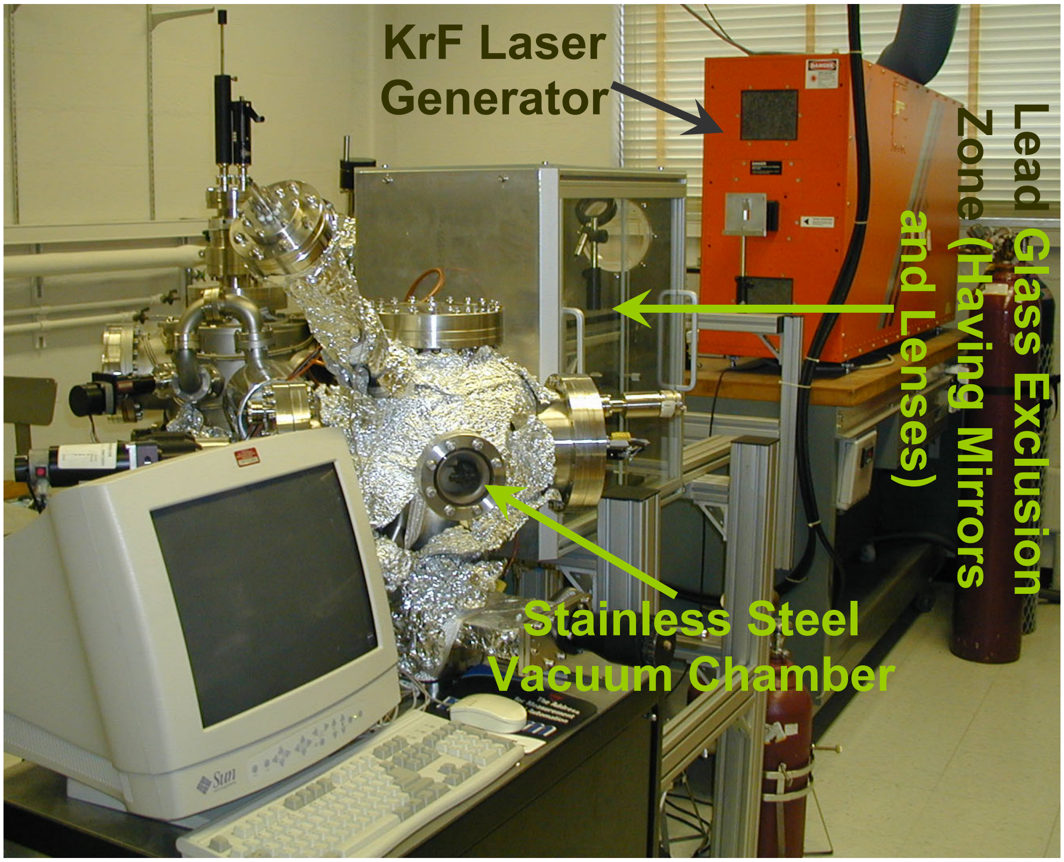

Figure 4.1. Setup of Pulsed Laser Deposition (PLD) unit at Brookhaven National Laboratories. The KrF laser of 248 nm is generated in the orange rectangular box and then it passes through lead glass exclusion zone having mirrors and lenses for proper deflection and direction. Ablation takes place in the stainless steel vacuum chamber.

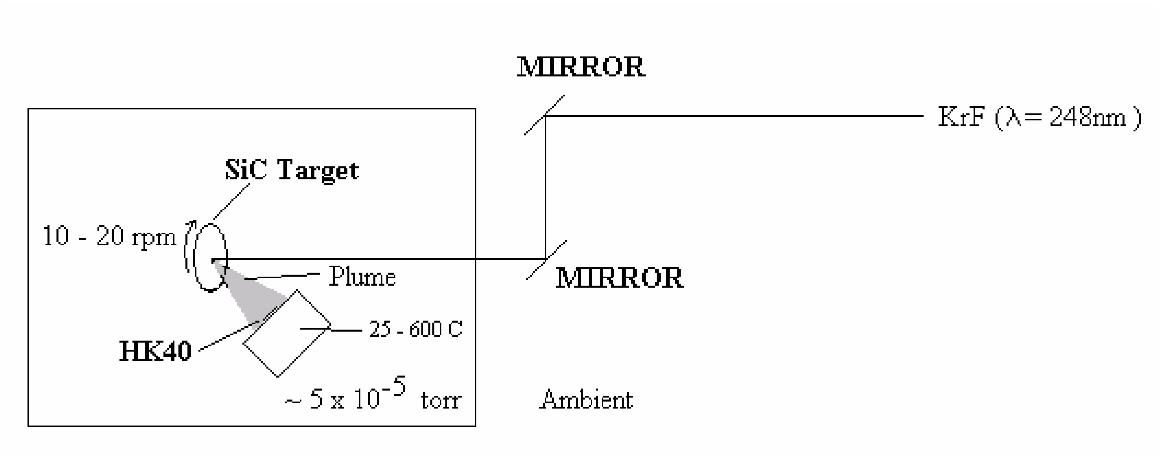

Figure 4.2. Pulsed Laser Deposition system equipped with rotating target and substrate heating stage [9].

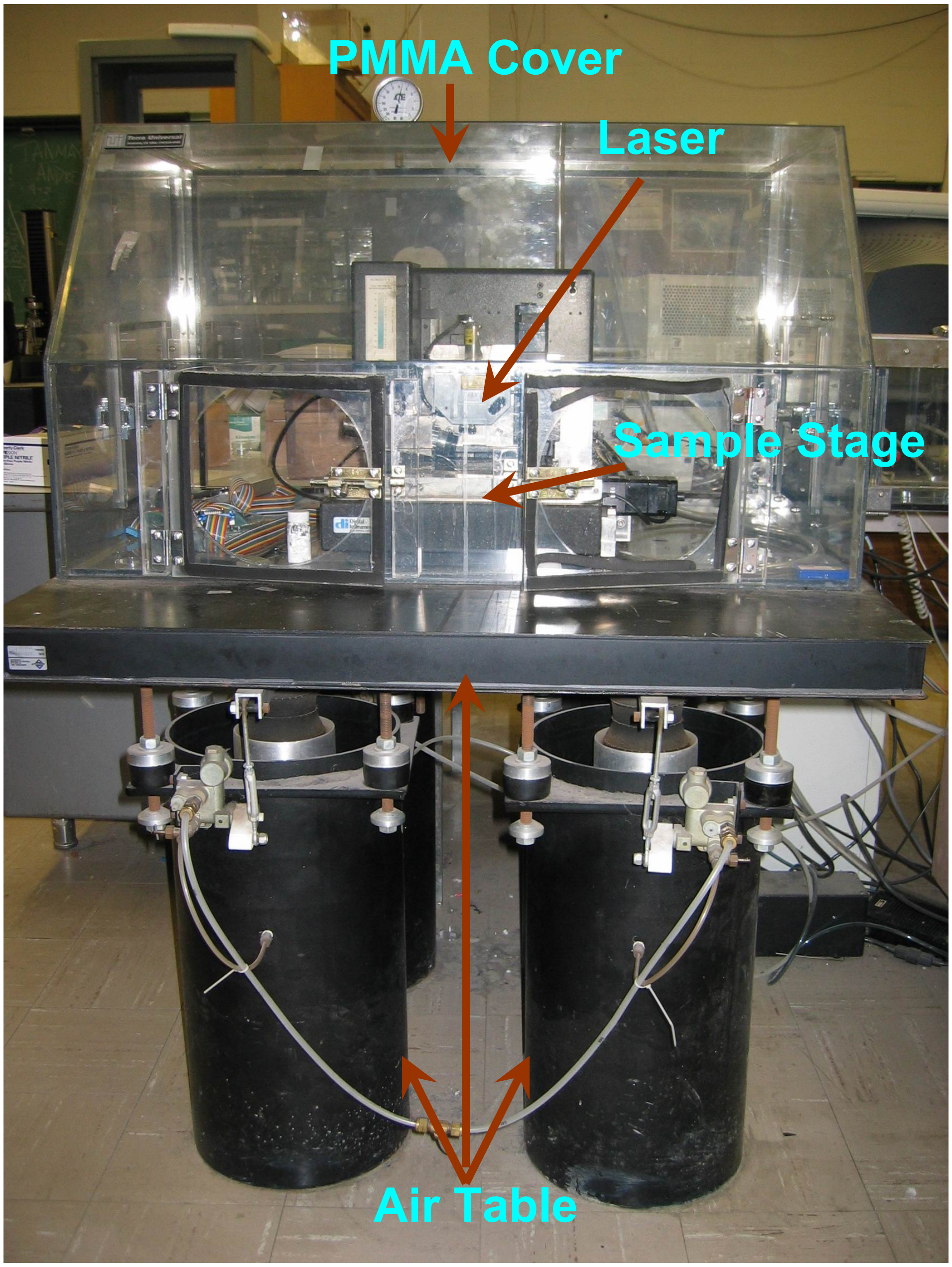

Figure 4.3. Atomic Force Microscope at Stony Brook University.

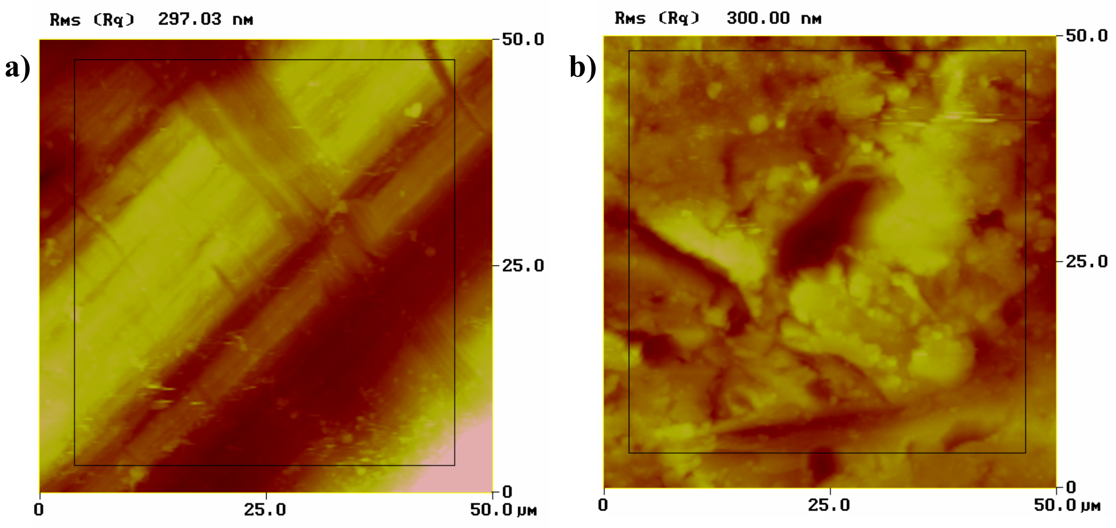

Figure 4.4. (a) Atomic Force Microscopy image showing "scratch-like" morphology on machined HK40 substrate; (b) "dimple-like" appearance of shot peened HK40 substrate [9].

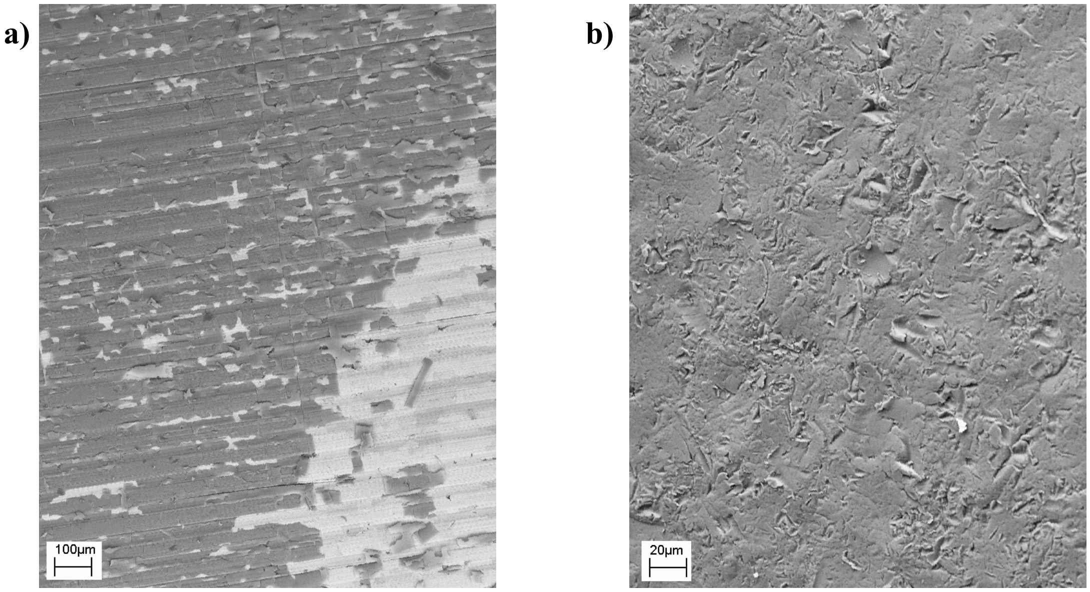

Figure 4.5. (a) BSE (Back Scattered Electron) micrograph of Pulsed Laser Deposition of SiC on machined HK40. Deposition was performed at room temperature. High z-contrast areas (white) represent HK-40 (Fe-Ni-Cr) and low z-contrast areas (dark) represent SiC coating. Poor adhesion and coverage are apparent. (b) BSE micrograph of Pulsed Laser Deposition of SiC on shot peened HK40. The substrate temperature was 500 C during deposition. Complete coverage of SiC on HK40 is shown [9].

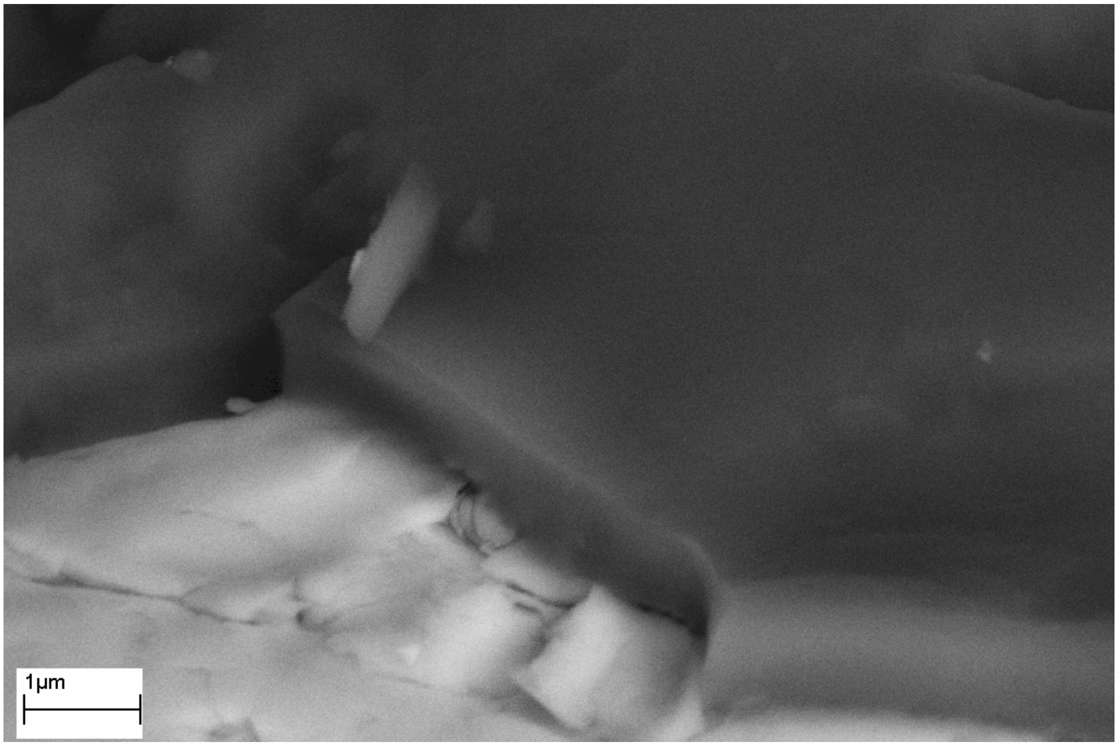

Figure 4.6. BSE of scratch tested specimen. The specimen was tilted 45 degrees. The dark region (low z-contrast) is the SiC film, the bright region (high z-contrast) is the HK40 substrate [9].

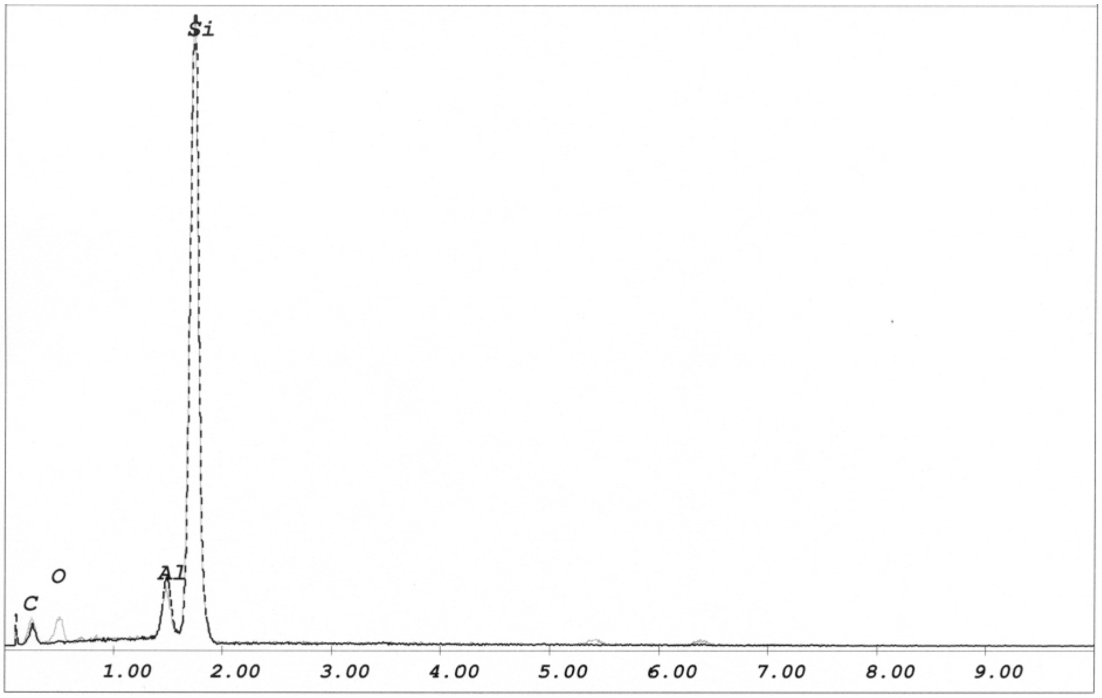

Figure 4.7. EDS (Energy Dispersive Spectroscopy) spectrum of coated HK40 (Fe-Ni-Cr) substrate (grey) superimposed on target spectrum (black-dotted lines). In the spectrum of the coated material (grey) note the presence of a strong oxygen peak at 0.5 Kev and weak Cr and Fe peaks at 5.4 Kev and 6.4 Kev, respectively [9].

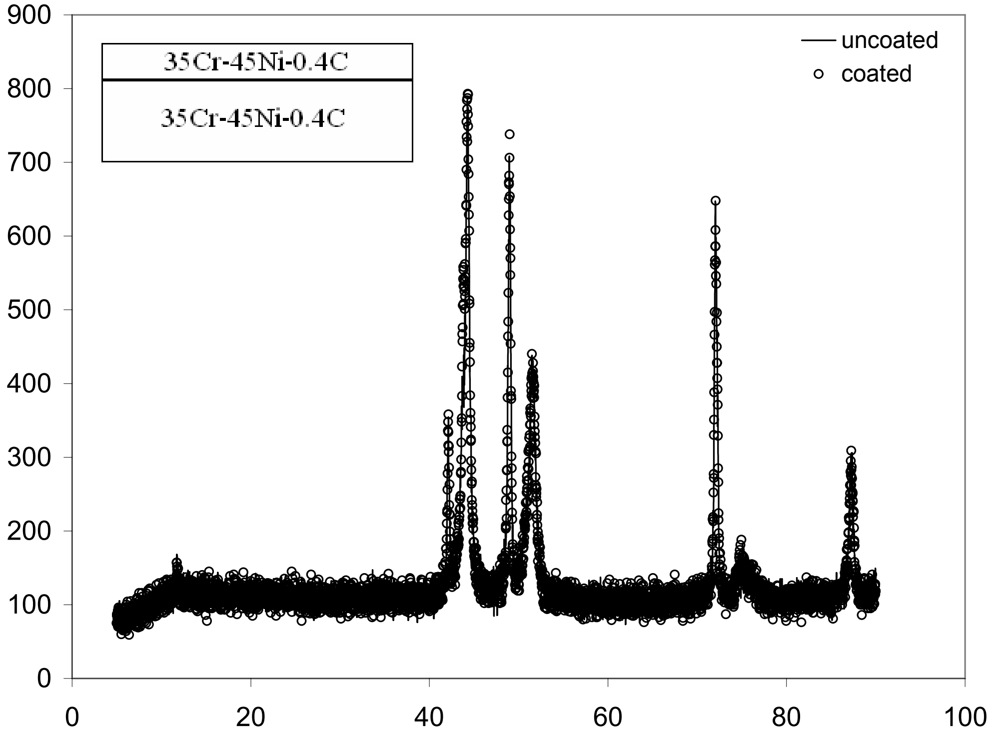

Figure 4.8. Comparison of X-ray Diffraction (XRD) pattern of 35Cr-45Ni-0.4C alloy with Pulsed Laser Self-Ablated film of 35Cr-45Ni-0.4C.

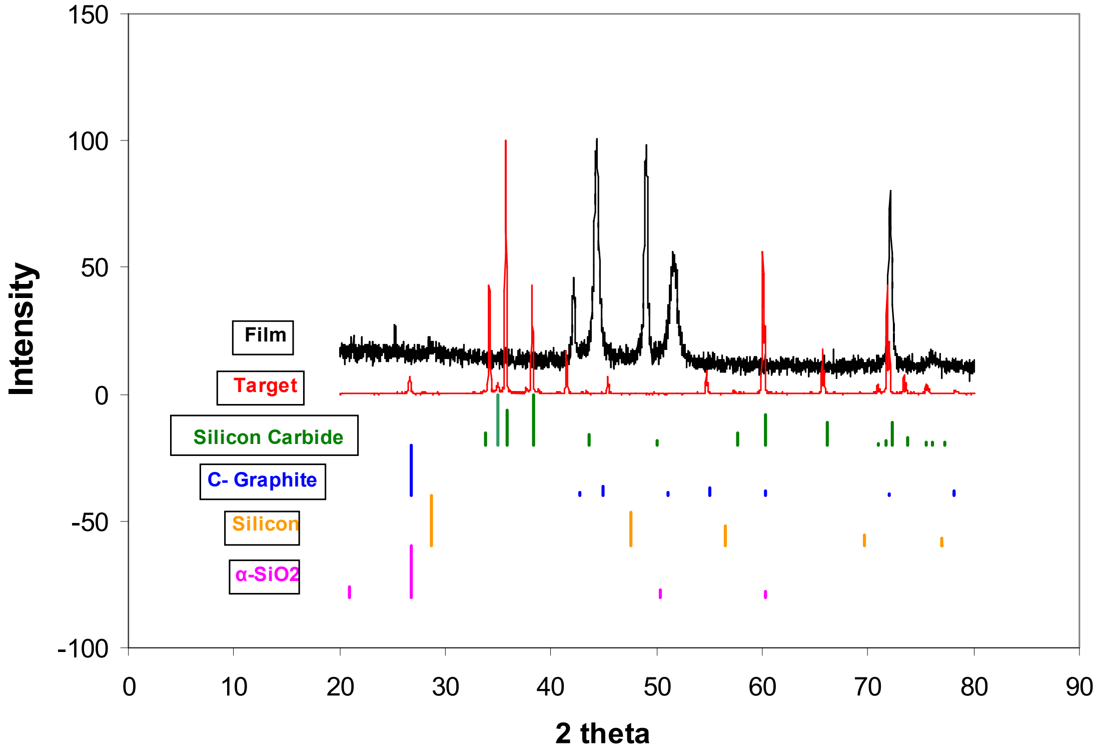

Figure 4.9. Comparison of X-ray Diffraction of SiC target with SiC film formed by Pulsed Laser Ablation of the SiC target.

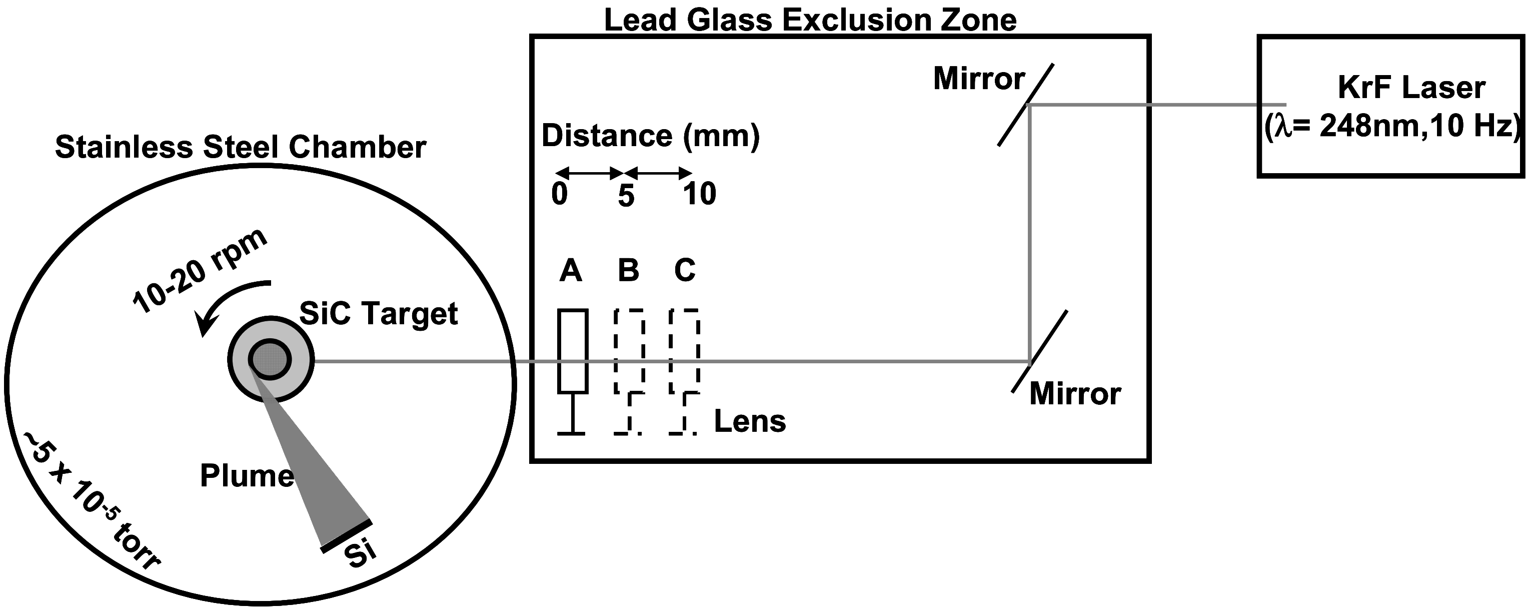

Figure 4.10. Schematic for showing the set-up to deposit thin-film using KrF laser in Pulsed Laser Deposition technique. Here the position of focusing lens inside the lead-glass exclusion zone is changed from position A to B and then B to C by displacing by a distance of 5 mm each. The effects on the stoichiometry of the deposited film of SiC are illustrated in Figure 4.11.

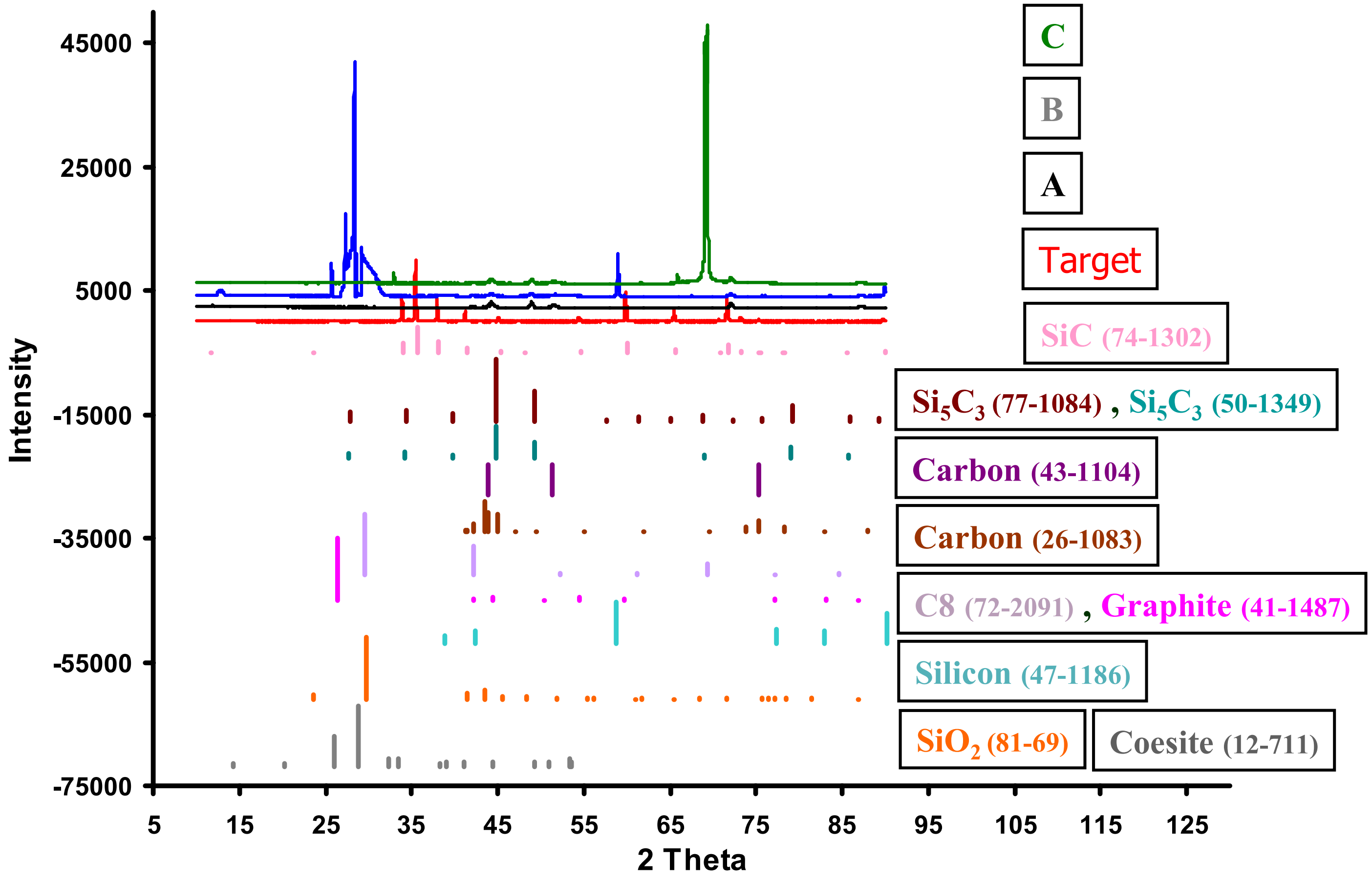

Figure 4.11. Comparison of X-ray Diffraction of SiC target with SiC films deposited by using Pulsed Laser Ablation technique of the SiC target; displacing the focusing lens in the lead glass exclusion zone by 5 mm from position A to B, and then again by 5 mm from position B to C as shown in Figure 4.10.

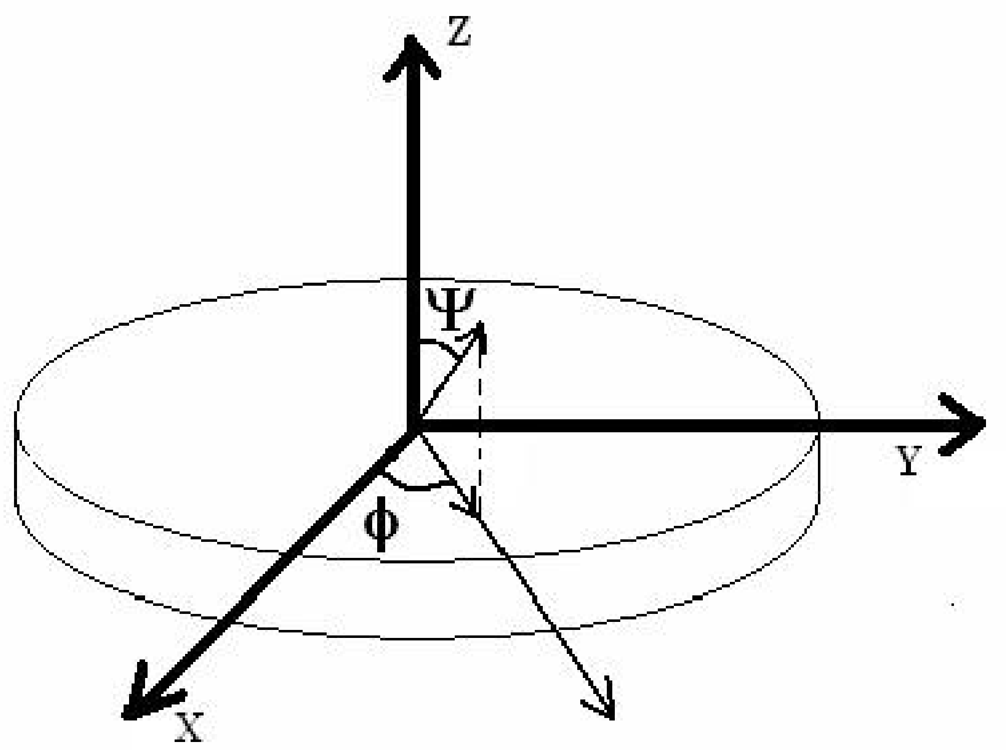

Figure 4.12. X-ray diffraction geometry. Diffraction patterns were collected at different ψ angles. Angle ψ is used to calculate in- plane stresses. Both ψ and ϕ are used to measure textural information [27].

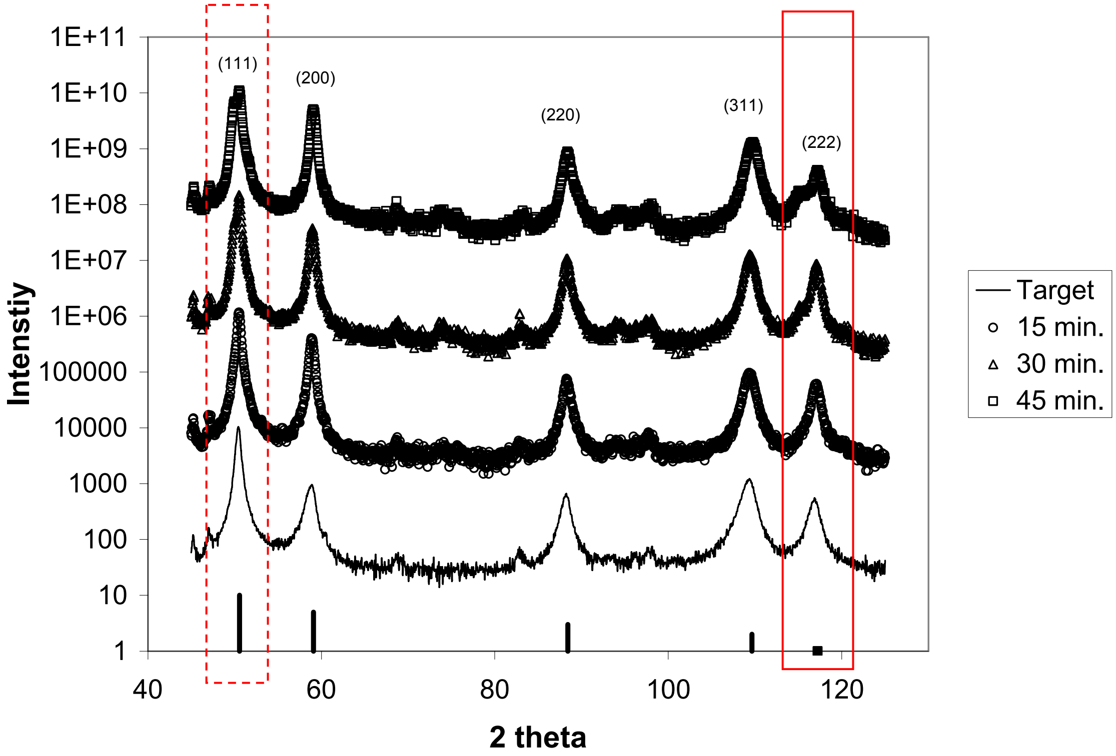

Figure 4.13. X-ray powder diffraction patterns collected with ψ = 0. Experimental peaks matched PDF #47-1405 which were used to identify planes. Marked red boxes show the peaks of interest [27].

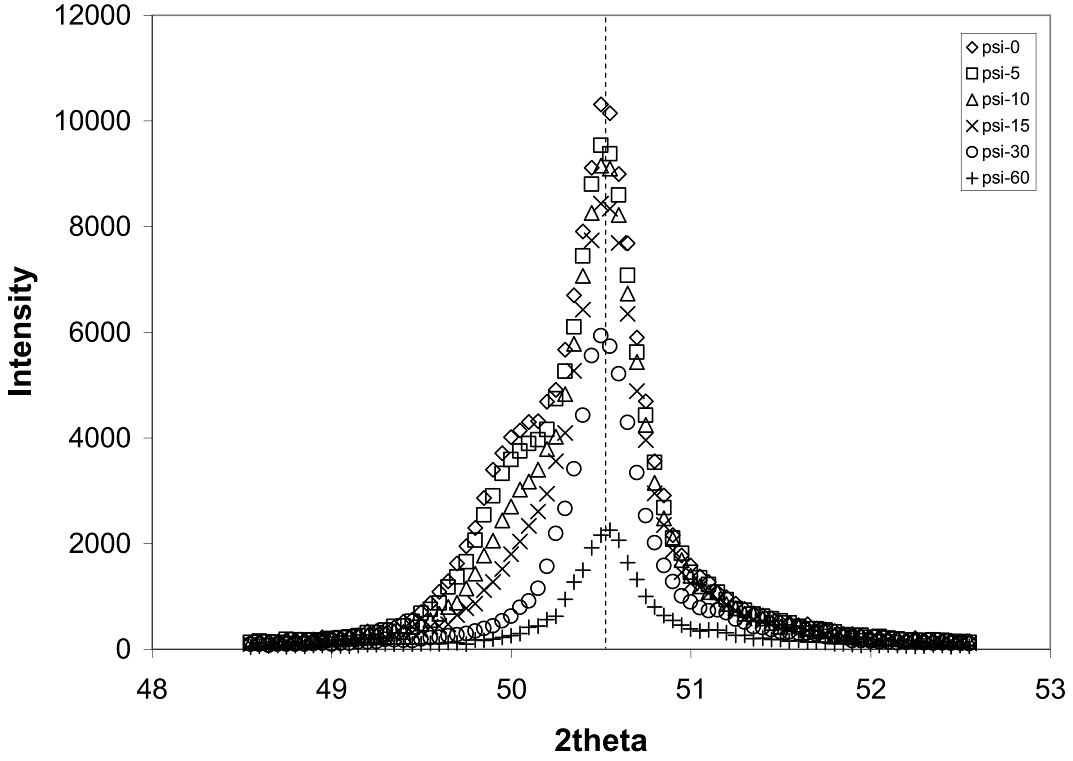

Figure 4.14. X-ray powder diffraction slip plane analysis at different ψ angles. Deposition time 30 minutes. Side peak from film moves closer to the main substrate peak and disappears at ψ ≥ 30 degrees [27].

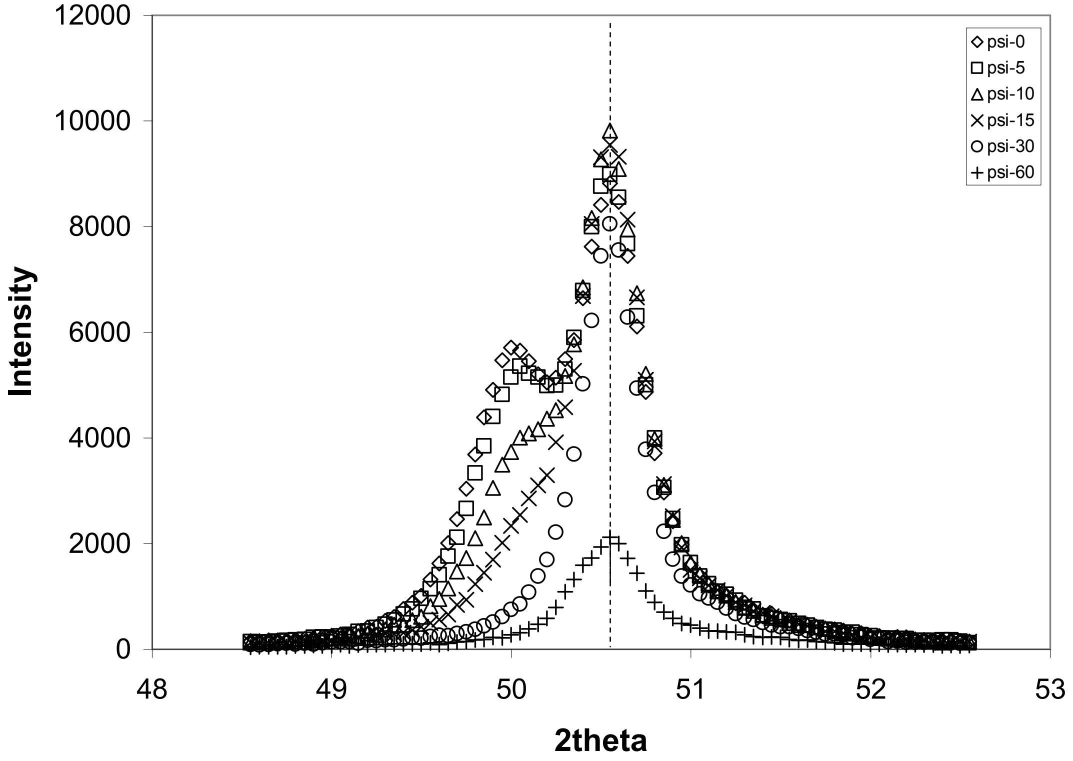

Figure 4.15. X-ray powder diffraction slip plane analysis at different ψ angles. Deposition time 45 minutes. Side peak from film moves closer to the main substrate peak and disappears at ψ ≥ 30 degrees [27].

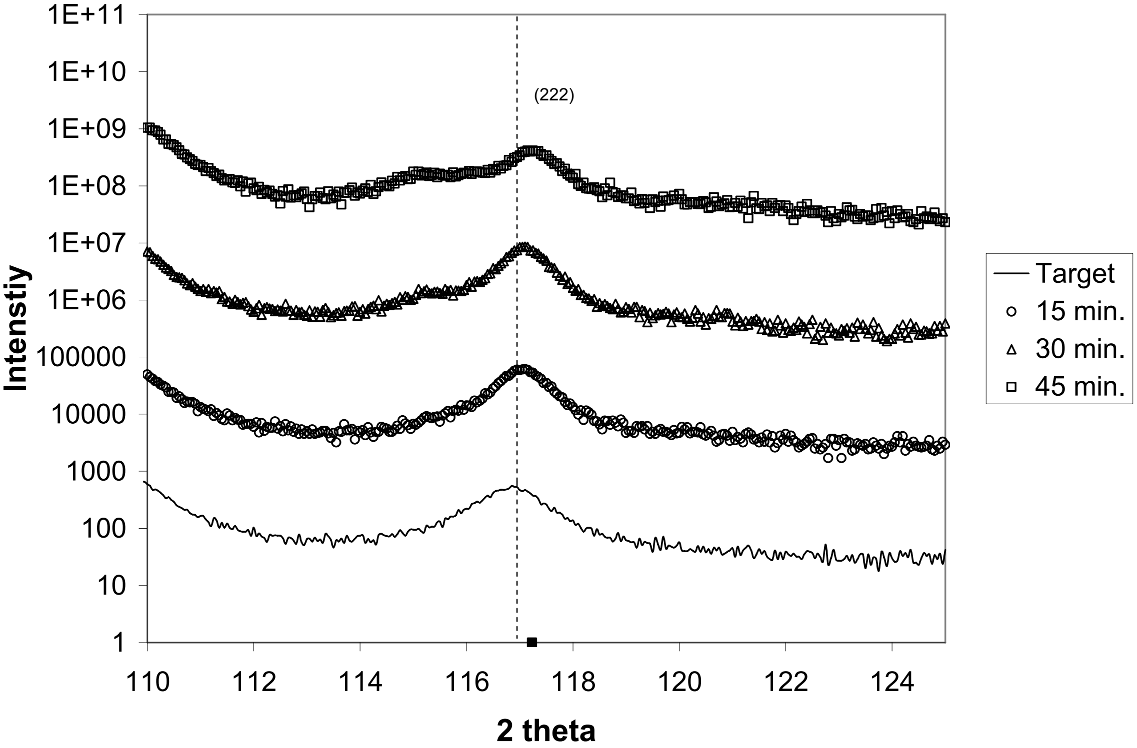

Figure 4.16. High angle peak (222) used for x-ray residual stress analysis. As film thickness increased, peak shifted to higher 2θ. Peak shift is indication of elastic macrostrains [27].

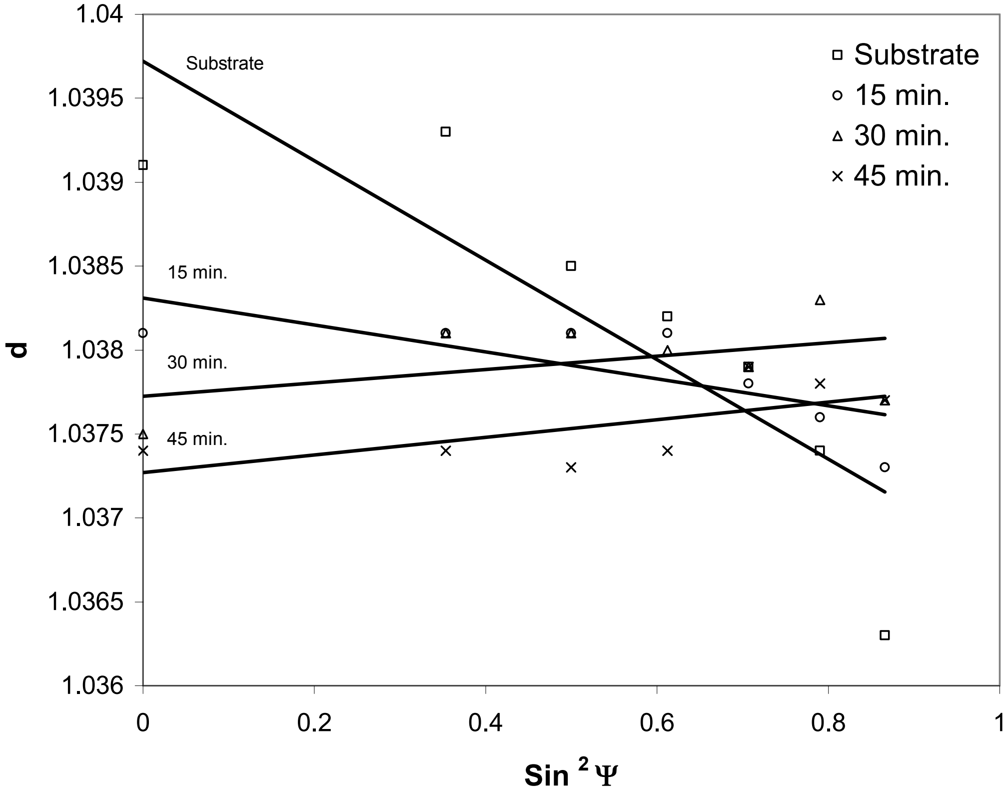

Figure 4.17. Interplanar spacing versus sin$^2\psi$ plot. As film thickness increases the state of in- plane stress changes from compressive to tensile [27].

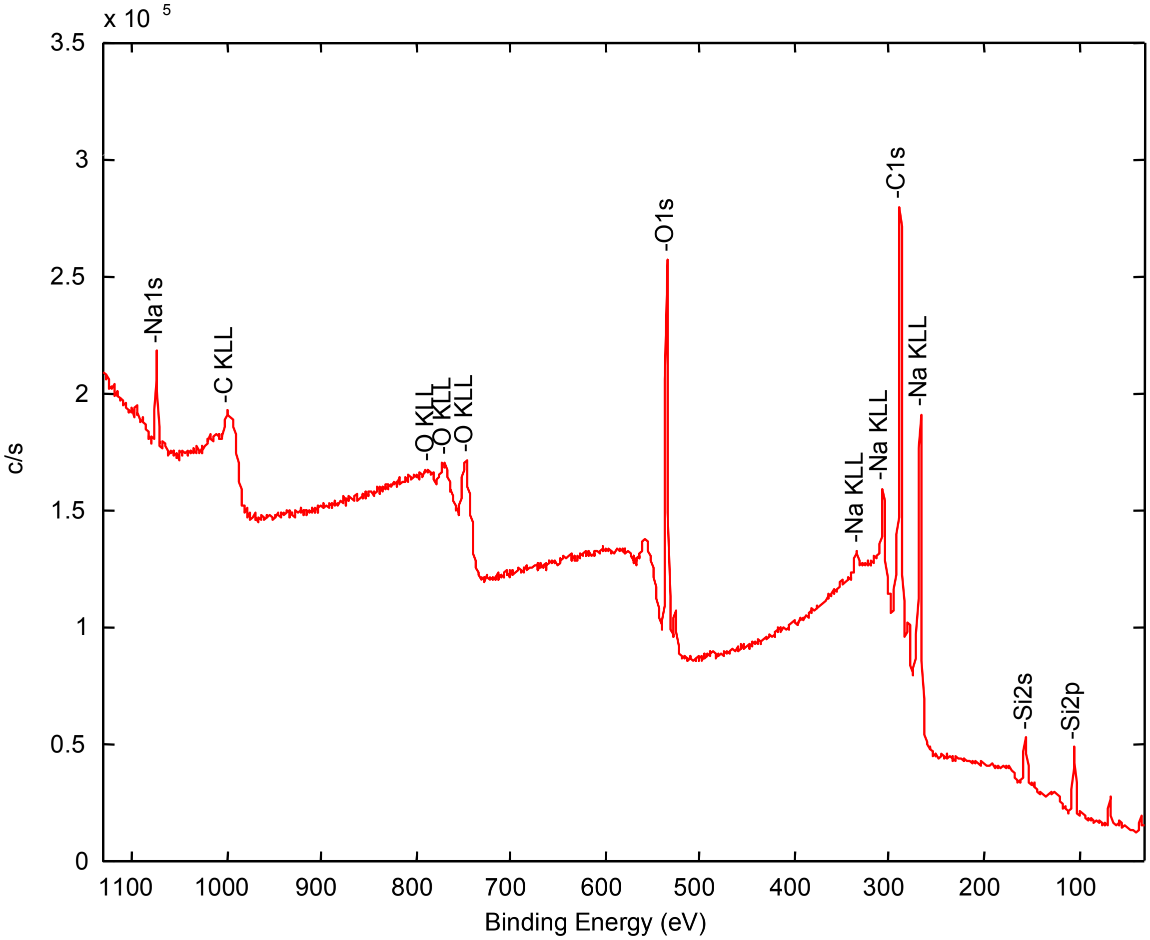

Figure 4.18. Full Scan Electron Spectroscopy Chemical Analysis (ESCA) of Ceramic SiC Film.

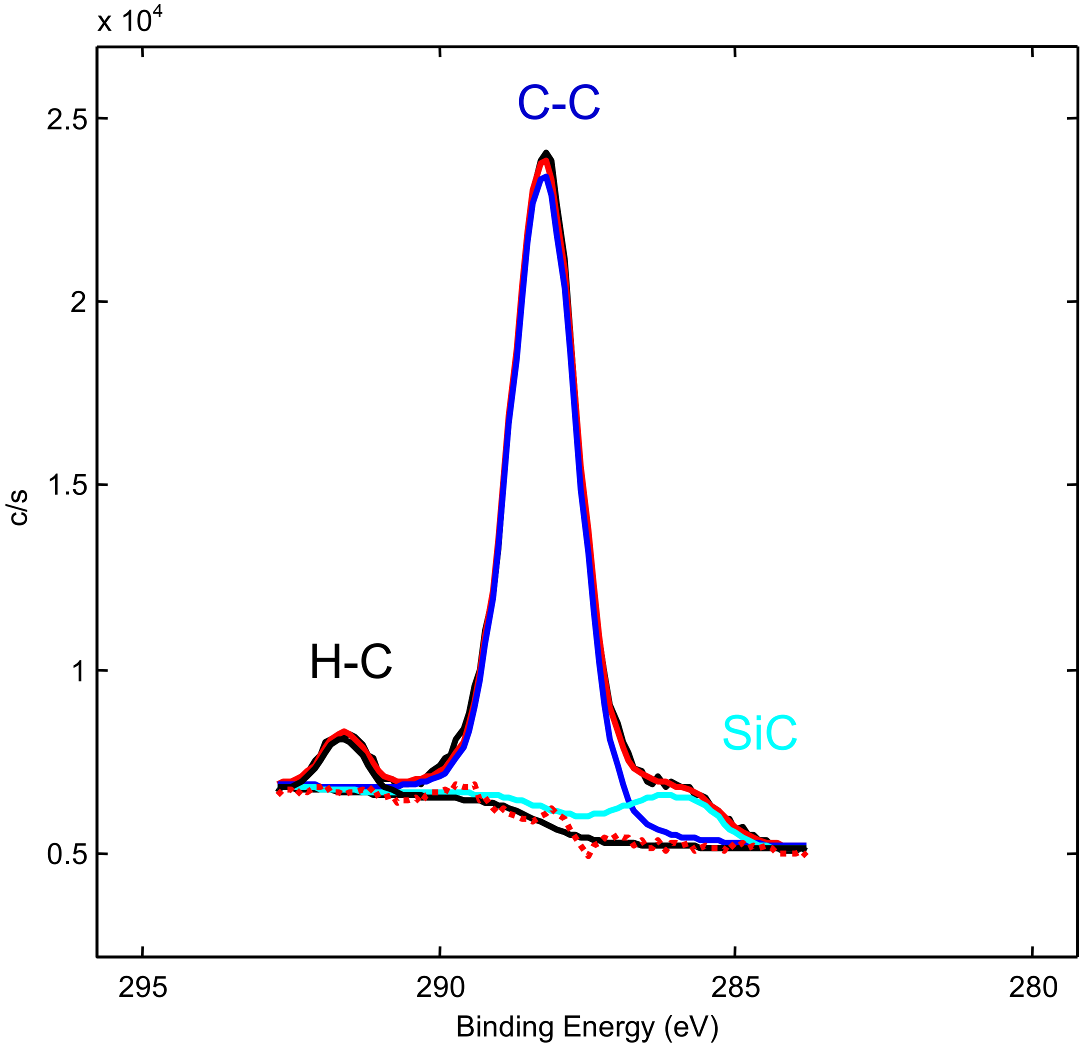

Figure 4.19. Narrow Scan Electron Spectroscopy Chemical Analysis (ESCA) of C1s peak.

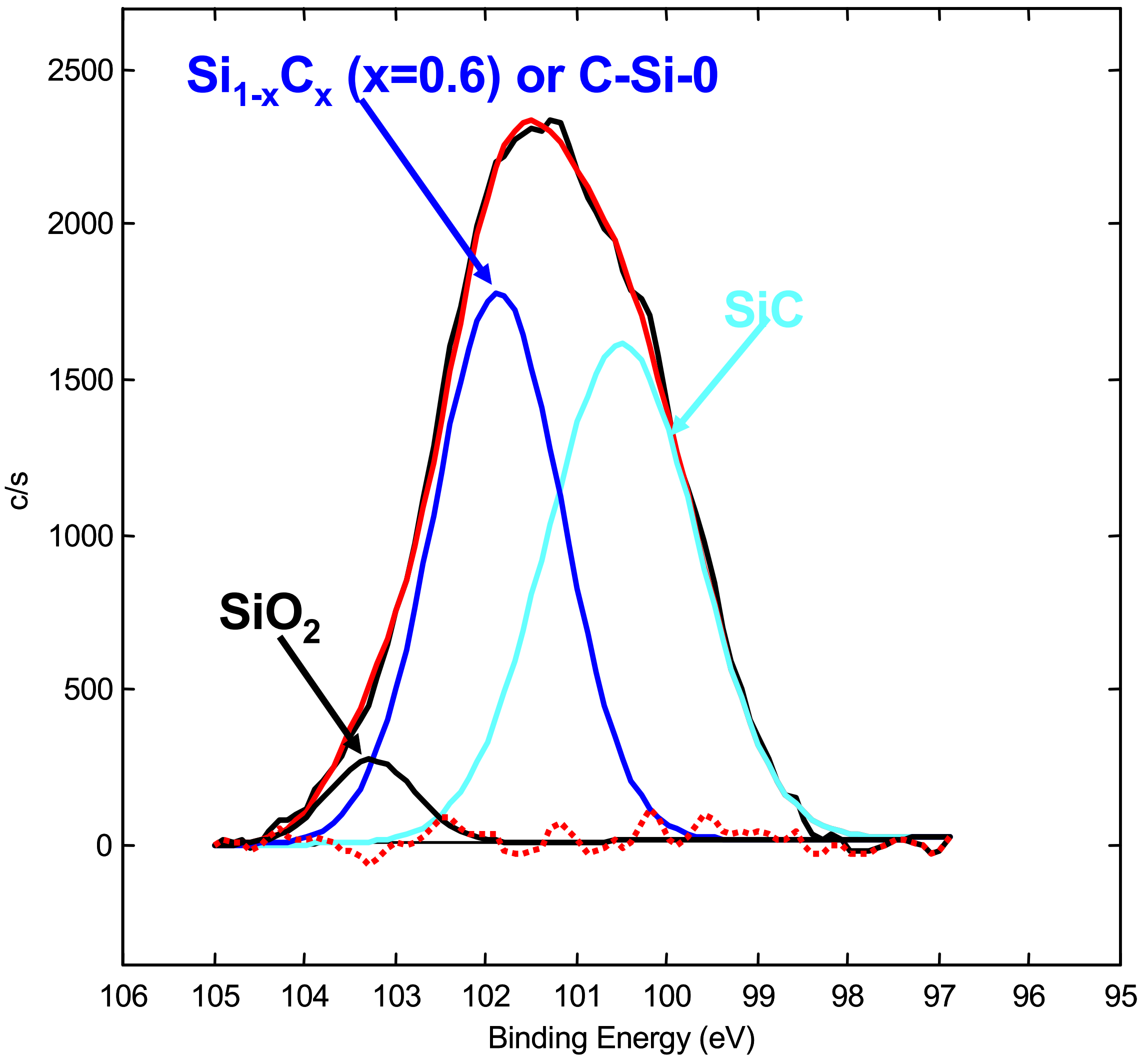

Figure 4.20. Narrow Scan Electron Spectroscopy Chemical Analysis (ESCA) of Si2p peak.

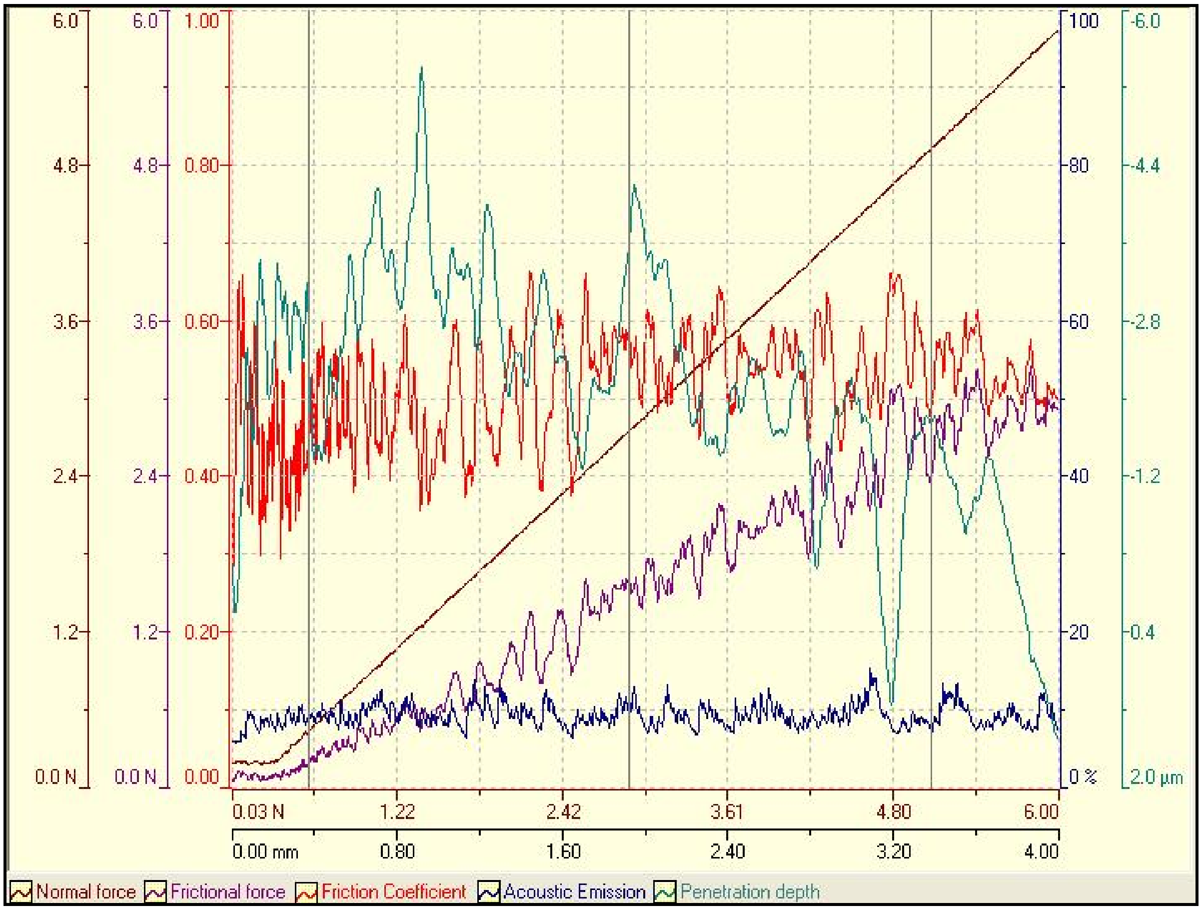

Figure 4.21. Example of acoustic emission signal (AE), the tangential force (Ft) and the penetration depth (Pd) plot recorded versus the normal load. Also known as MST (Micro Scratch Testing) plot.

Figure 4.22. Micro Scratch Tester (Micro Photonics, Inc., USA).

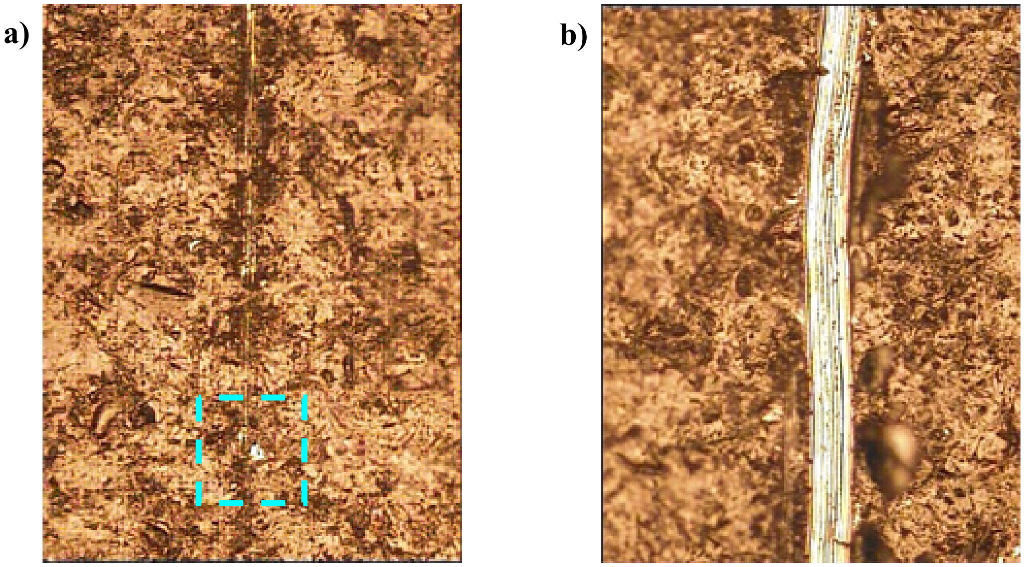

Figure 4.23. Adhesion test performed on specimen shown in Figure 4.5 b: (a) region of initial failure; (b) complete delamination [9].

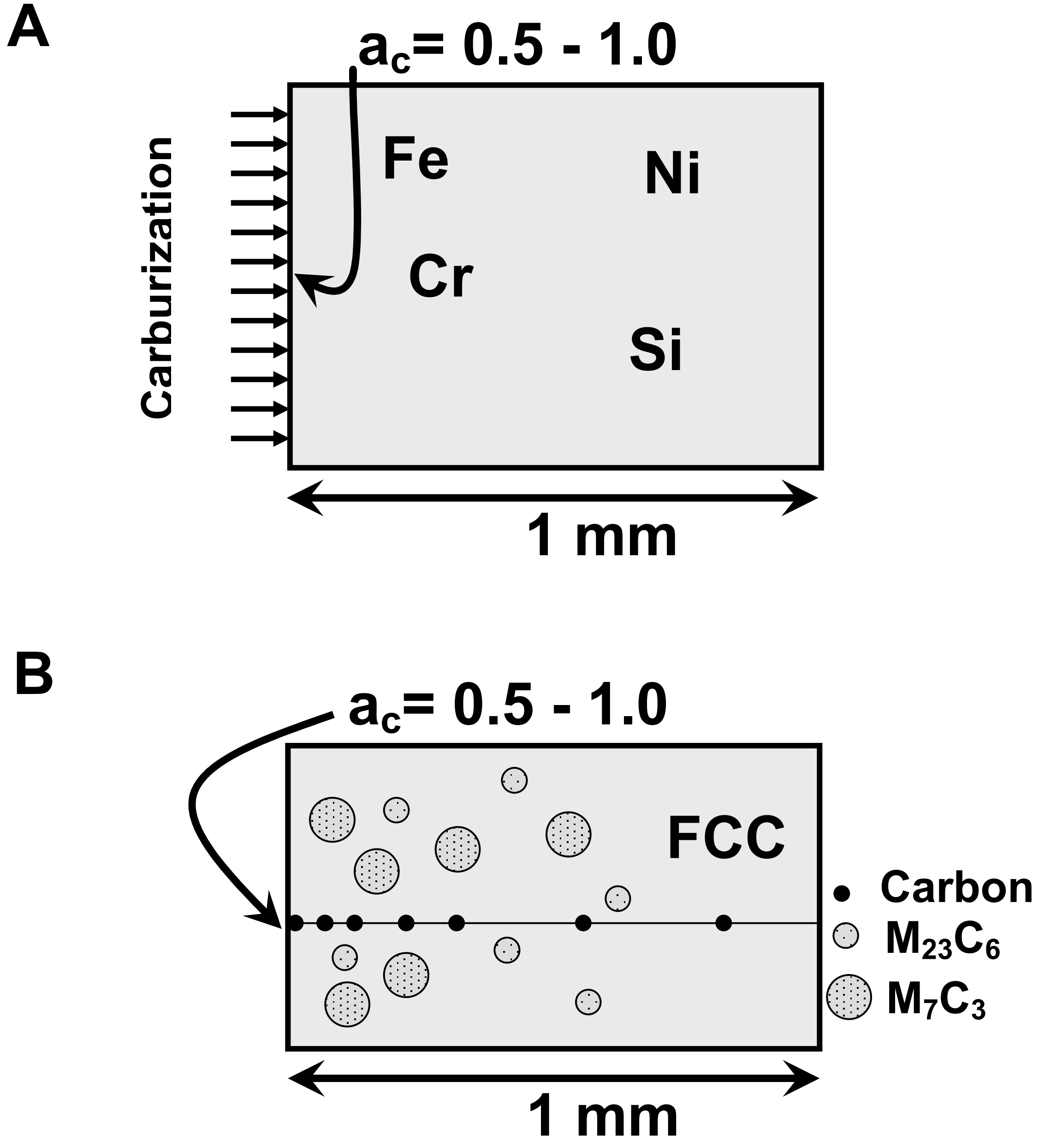

Figure 4.24. Diffusion model for understanding the diffusion phenomena in Fe-Cr-Ni-Si based alloy system. In the FCC matrix there is presence of M7C3 and M23C6 phases. The diffusion of carbon takes place from the surface. Activity of carbon varies from 0.5 to 1.0.

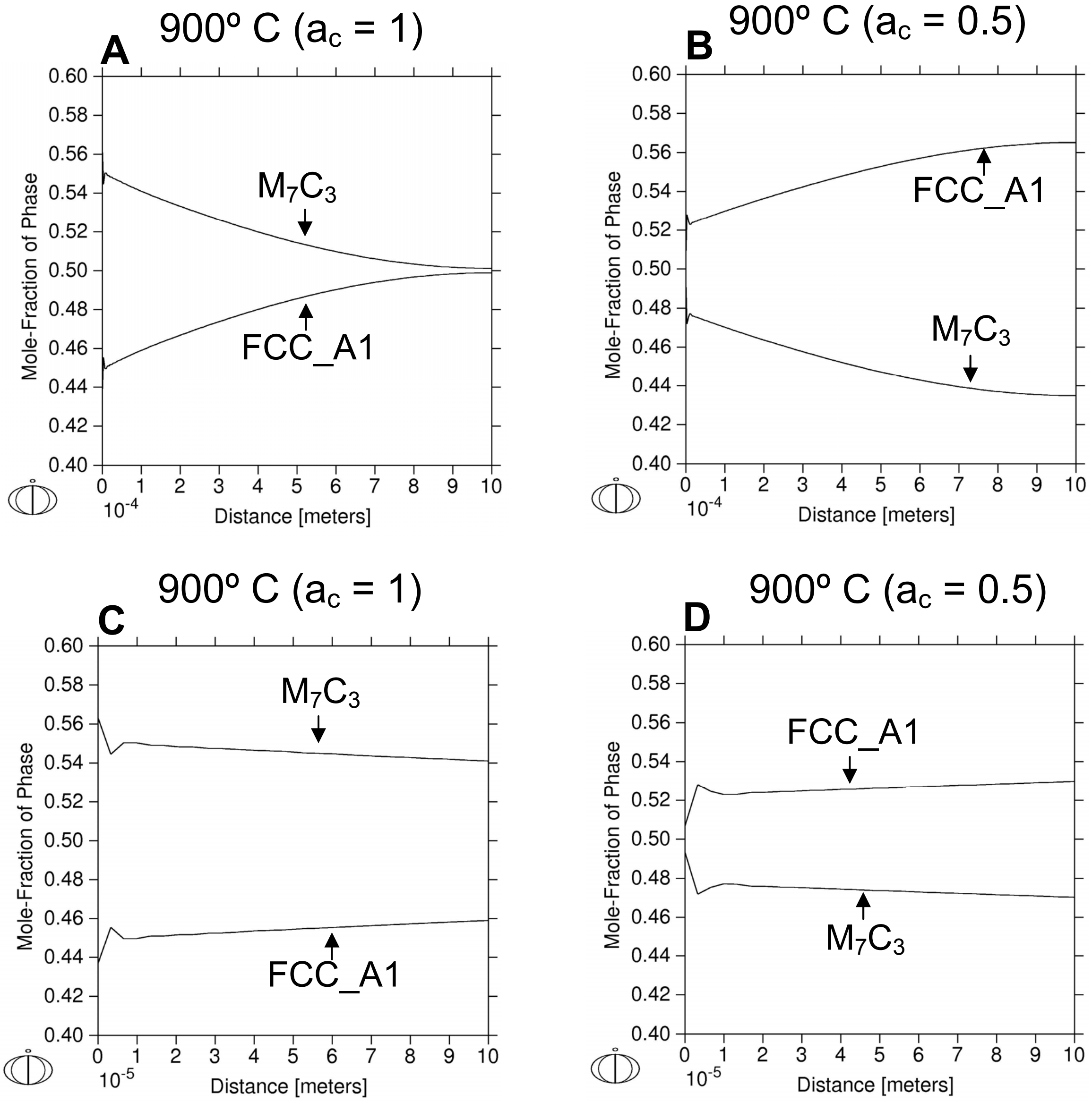

Figure 4.25. Plots of mole-fraction of phase versus distance in meters for HK40 alloy at 900 C temperature and at activities of 1.0 and 0.5. Figures A and B are plotted for a distance of 1 mm at activities of 1.0 and 0.5, respectively. Figures C and D are plotted for a distance of 0.1 mm at activities of 1.0 and 0.5, respectively.

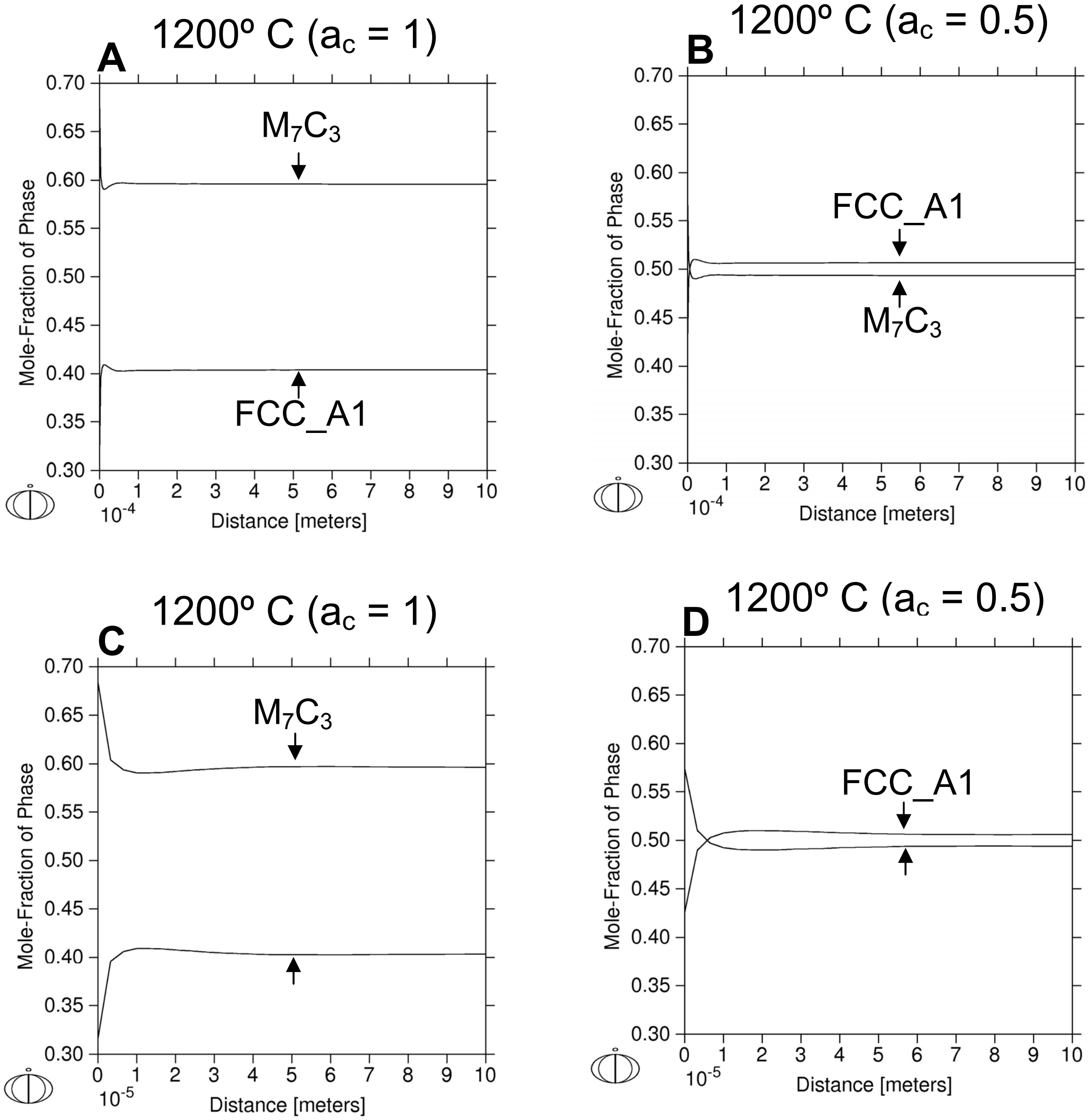

Figure 4.26. Plots of mole-fraction of phase versus distance in meters for HK40 alloy at 1200 C temperature and at activities of 1.0 and 0.5. Figures A and B are plotted for a distance of 1 mm at activities of 1.0 and 0.5, respectively. Figures C and D are plotted for a distance of 0.1 mm at activities of 1.0 and 0.5, respectively.

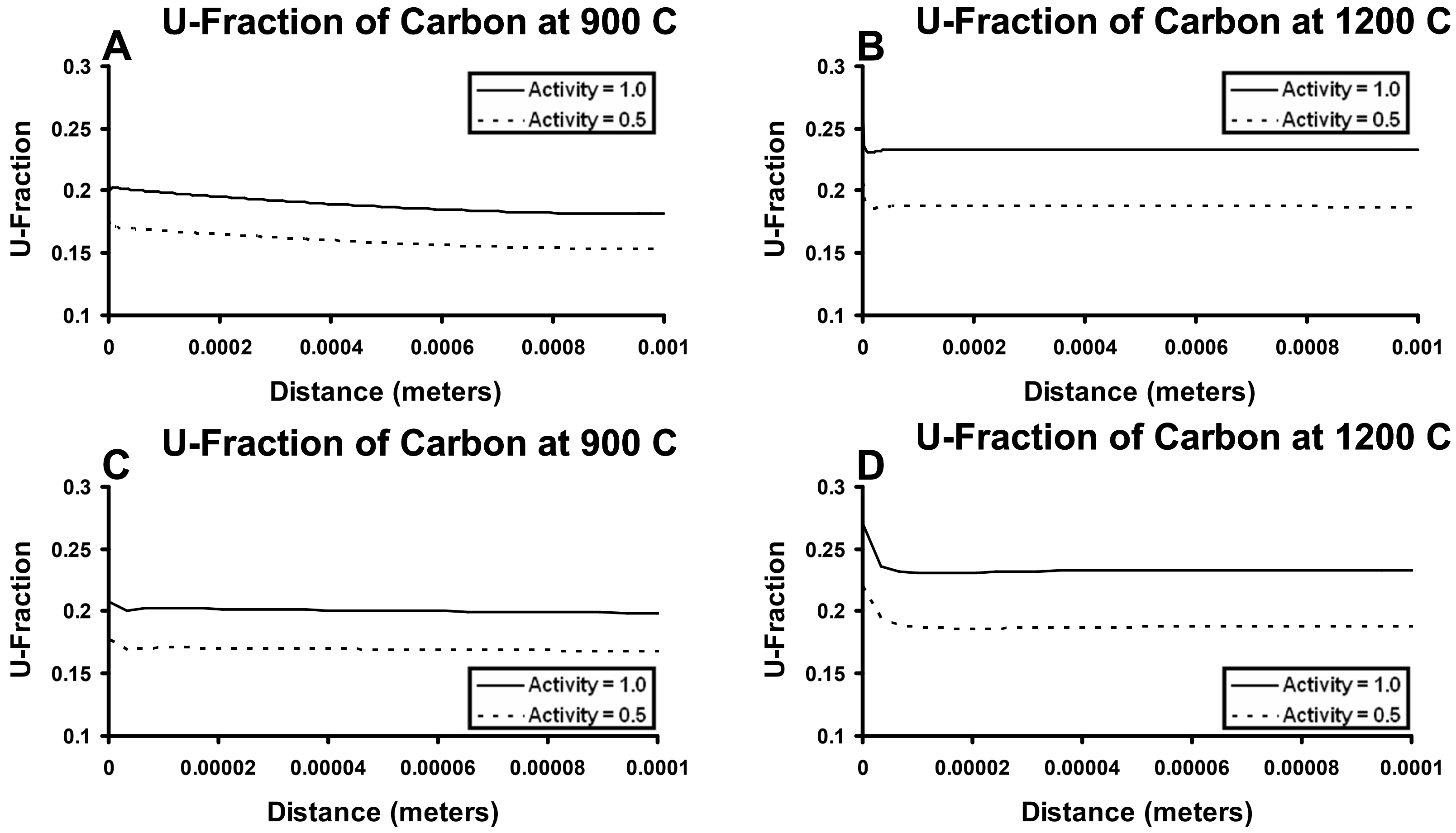

Figure 4.27. Graphs of U-fraction of carbon versus distance in meters at 900 C and 1200 C temperatures for both 0.5 and 1.0 carbon activities, for HK40 alloy. Figures A and B are plotted for a distance of 1 mm, whereas figures C and D are plotted for a distance of 0.1 mm.

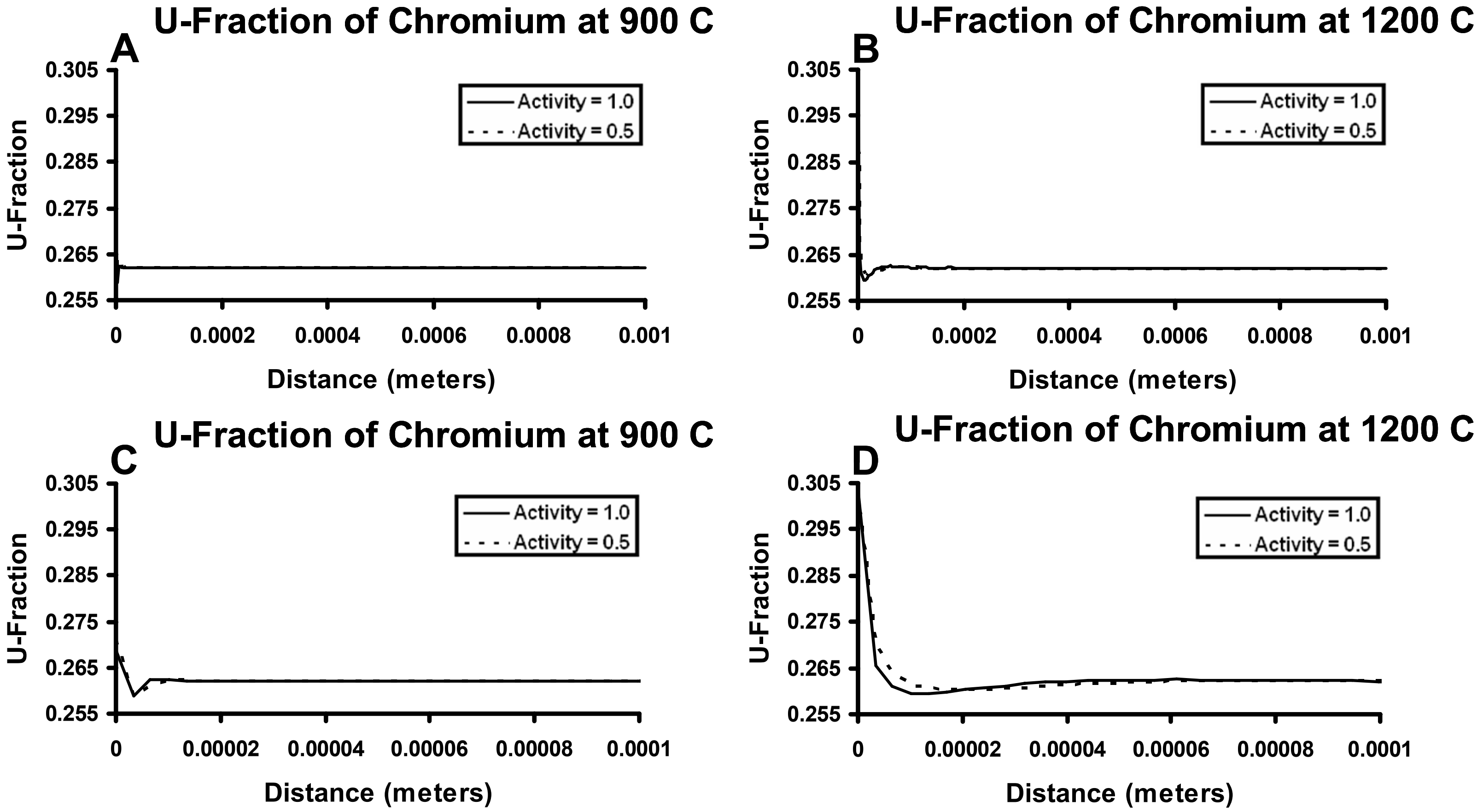

Figure 4.28. Graphs of U-fraction of chromium versus distance in meters at 900 C and 1200 C temperatures for both 0.5 and 1.0 carbon activities, for HK40 alloy. Figures A and B are plotted for a distance of 1 mm, whereas figures C and D are plotted for a distance of 0.1 mm.

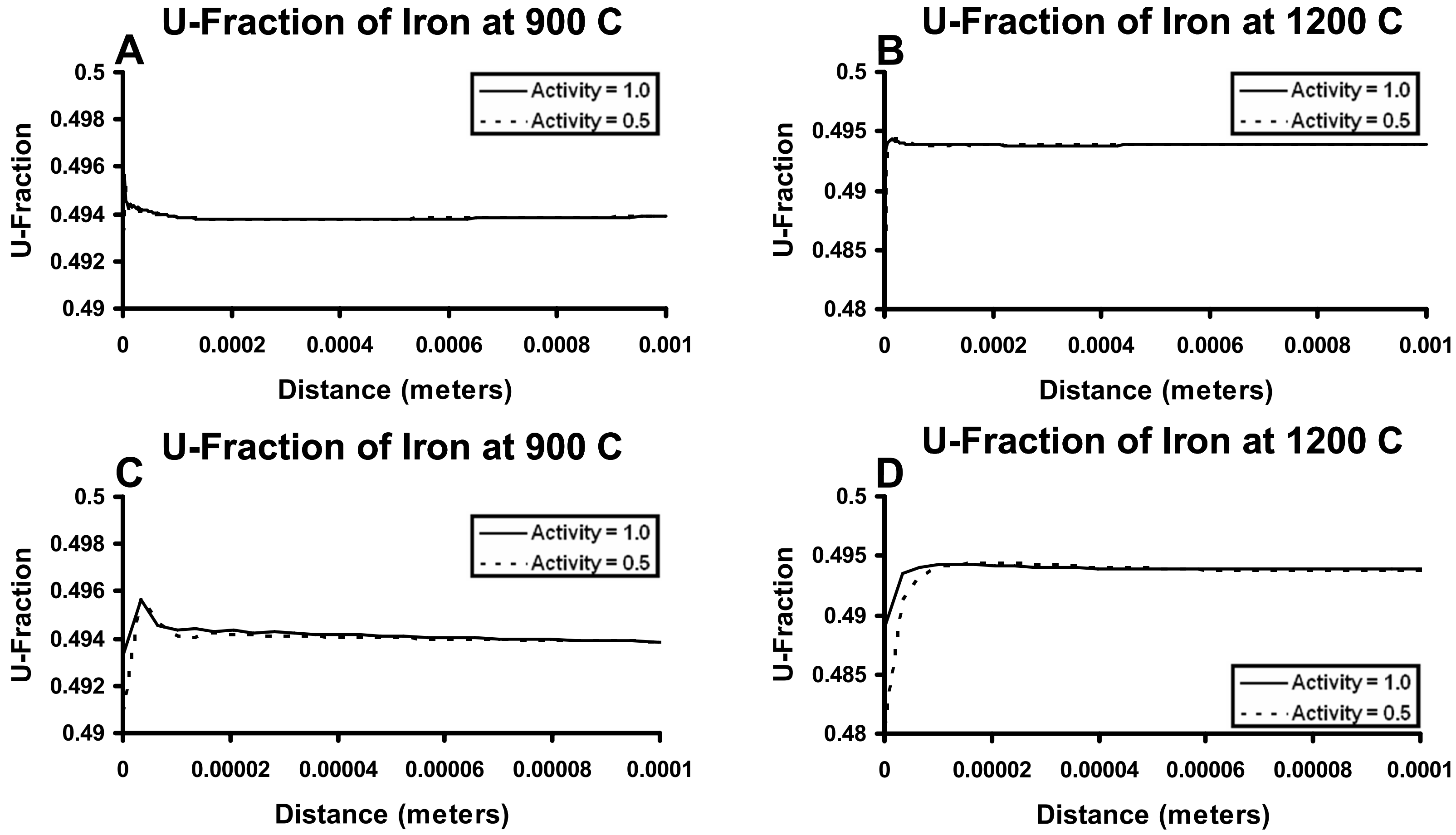

Figure 4.29. Graphs of U-fraction of iron versus distance in meters at 900 C and 1200 C temperatures for both 0.5 and 1.0 carbon activities, for HK40 alloy. Figures A and B are plotted for a distance of 1 mm, whereas figures C and D are plotted for a distance of 0.1 mm.

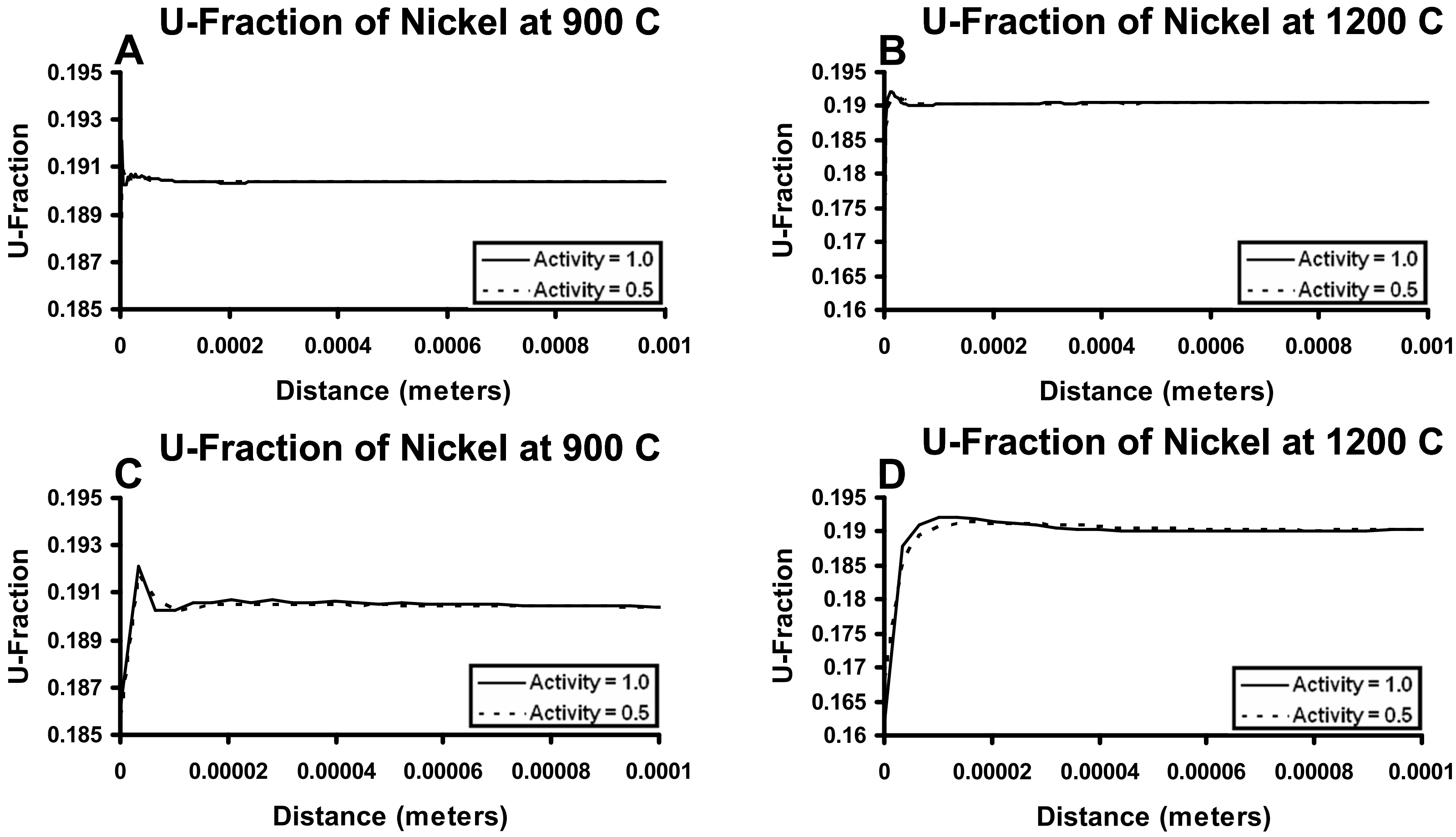

Figure 4.30. Graphs of U-fraction of nickel versus distance in meters at 900 C and 1200 C temperatures for both 0.5 and 1.0 carbon activities, for HK40 alloy. Figures A and B are plotted for a distance of 1 mm, whereas figures C and D are plotted for a distance of 0.1 mm.

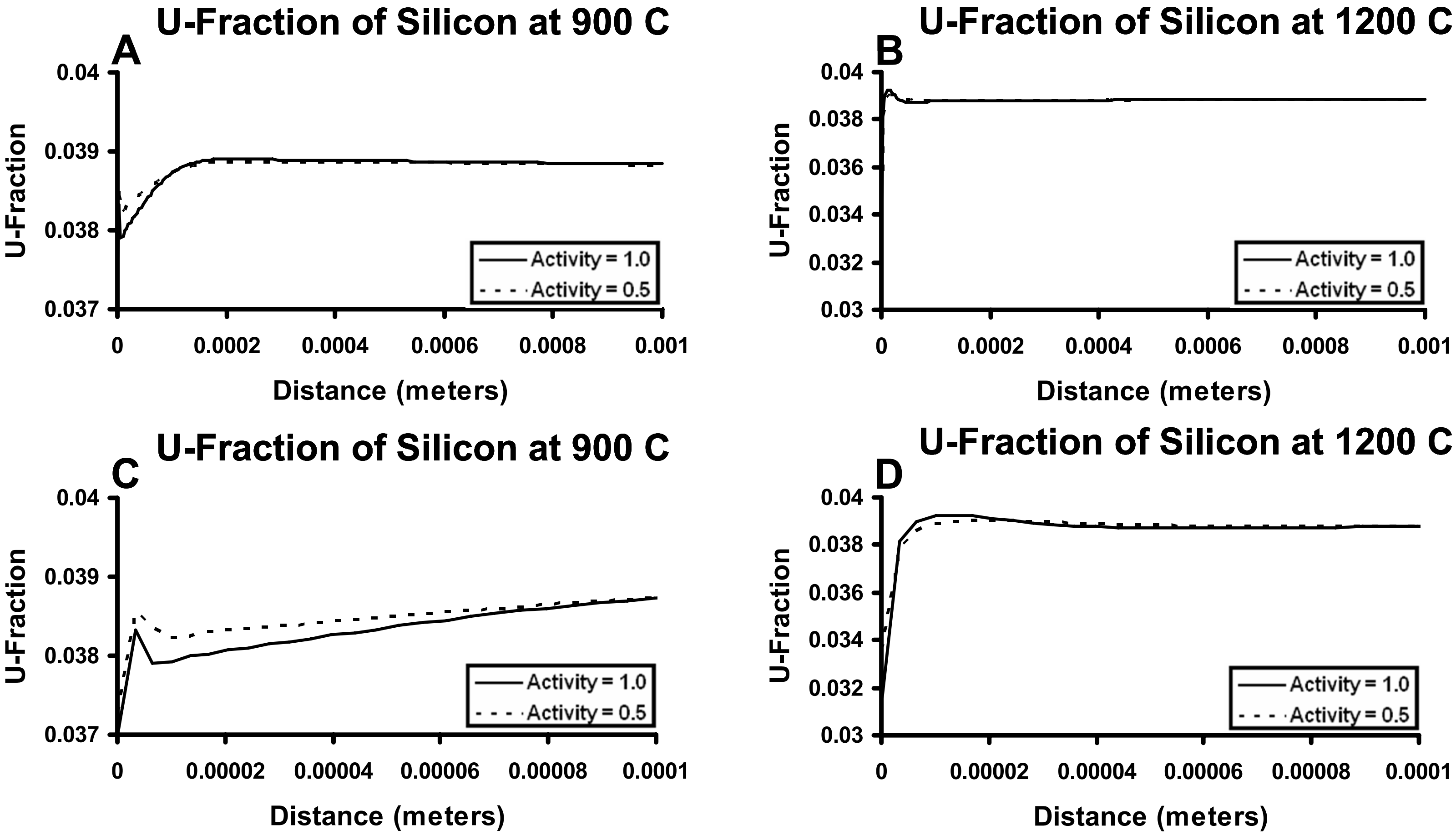

Figure 4.31. Graphs of U-fraction of silicon versus distance in meters at 900 C and 1200 C temperatures for both 0.5 and 1.0 carbon activities, for HK40 alloy. Figures A and B are plotted for a distance of 1 mm, whereas figures C and D are plotted for a distance of 0.1 mm.

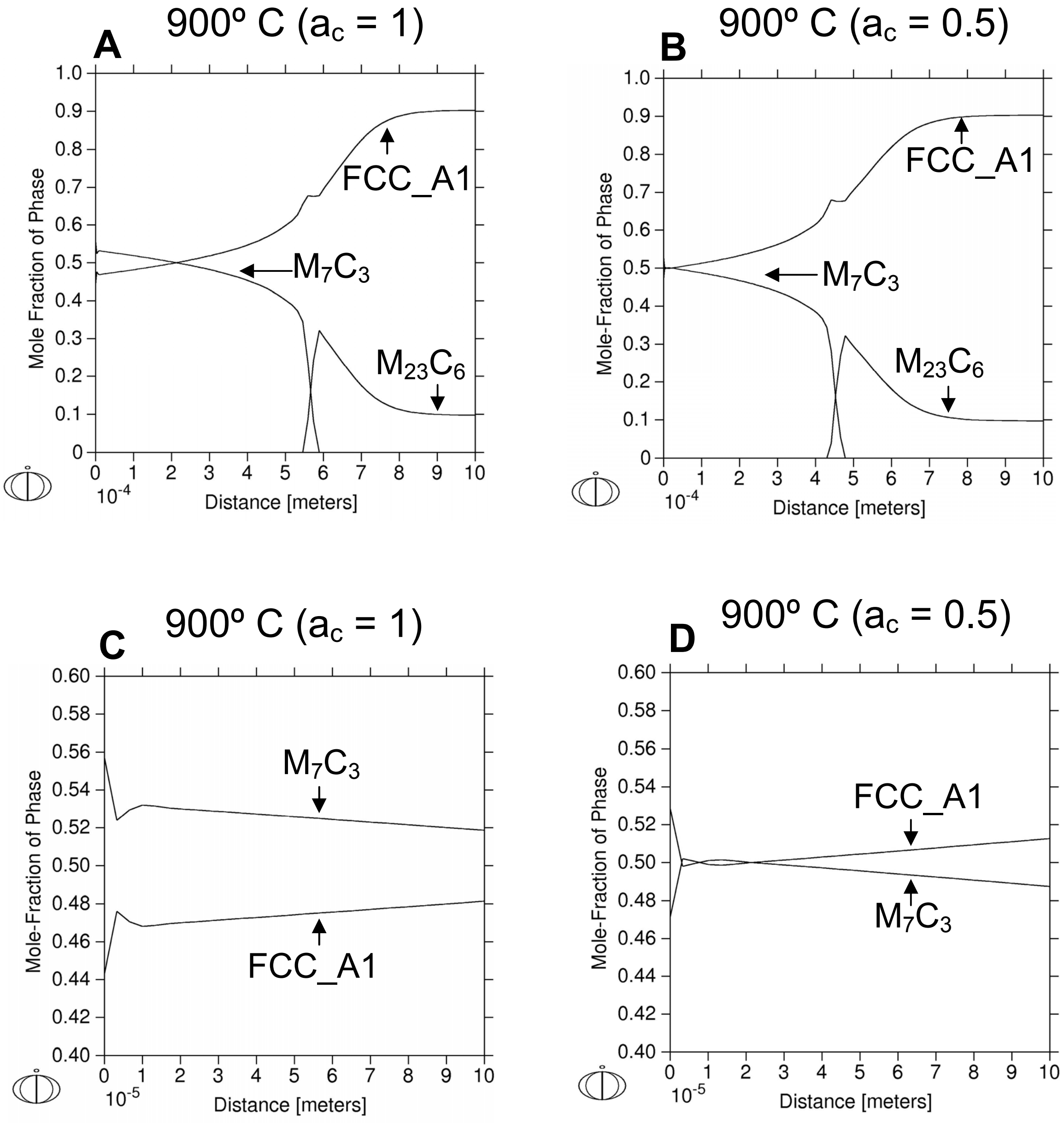

Figure 4.32. Plots of mole-fraction of phase versus distance in meters for 35Cr-45Ni alloy at 900 C temperature and at activities of 1.0 and 0.5. Figures A and B are plotted for a distance of 1 mm at activities of 1.0 and 0.5, respectively. Figures C and D are plotted for a distance of 0.1 mm at activities of 1.0 and 0.5, respectively.

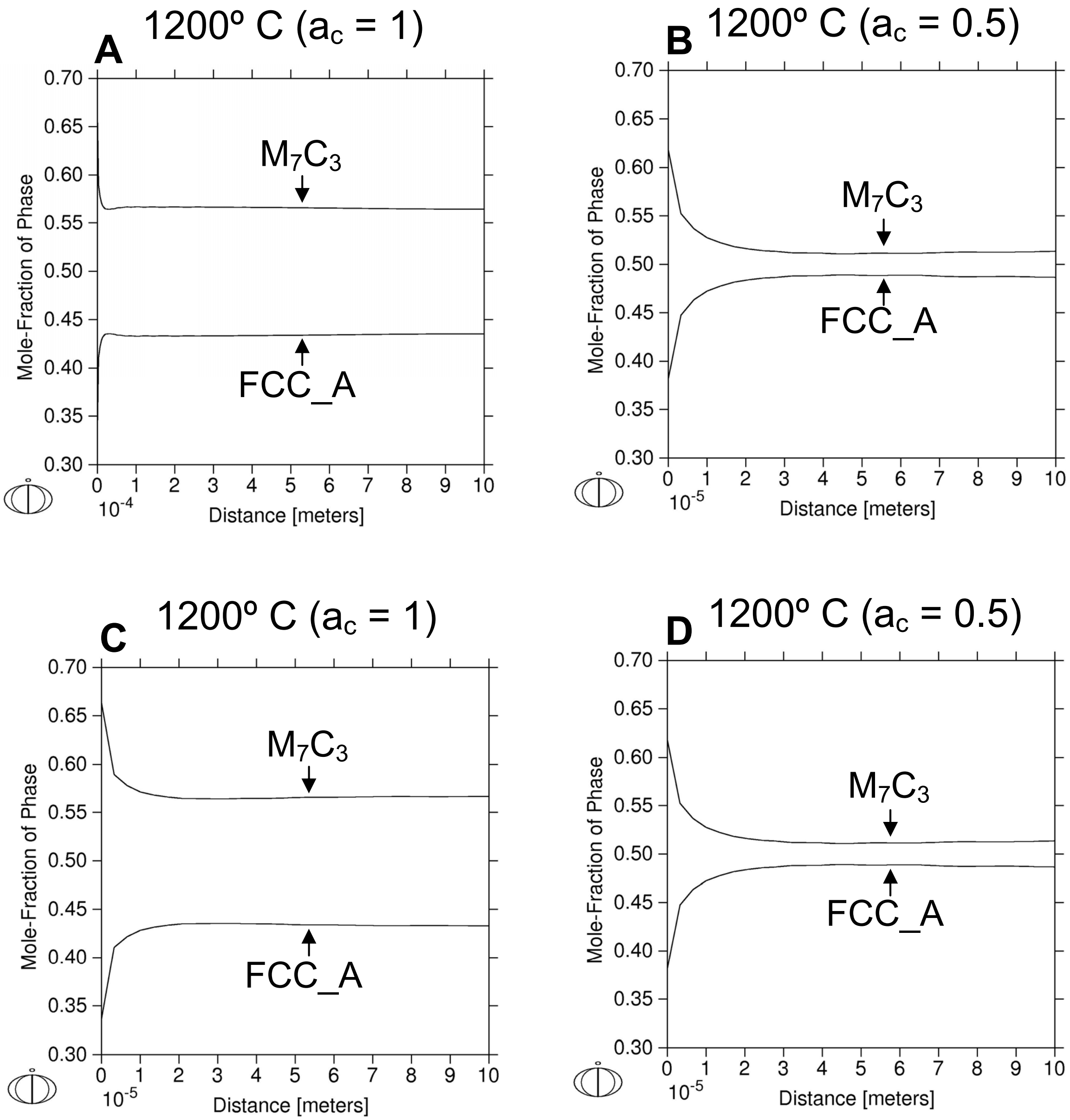

Figure 4.33. Plots of mole-fraction of phase versus distance in meters for 35Cr-45Ni alloy at 1200 C temperature and at activities of 1.0 and 0.5. Figures A and B are plotted for a distance of 1 mm at activities of 1.0 and 0.5, respectively. Figures C and D are plotted for a distance of 0.1 mm at activities of 1.0 and 0.5, respectively.

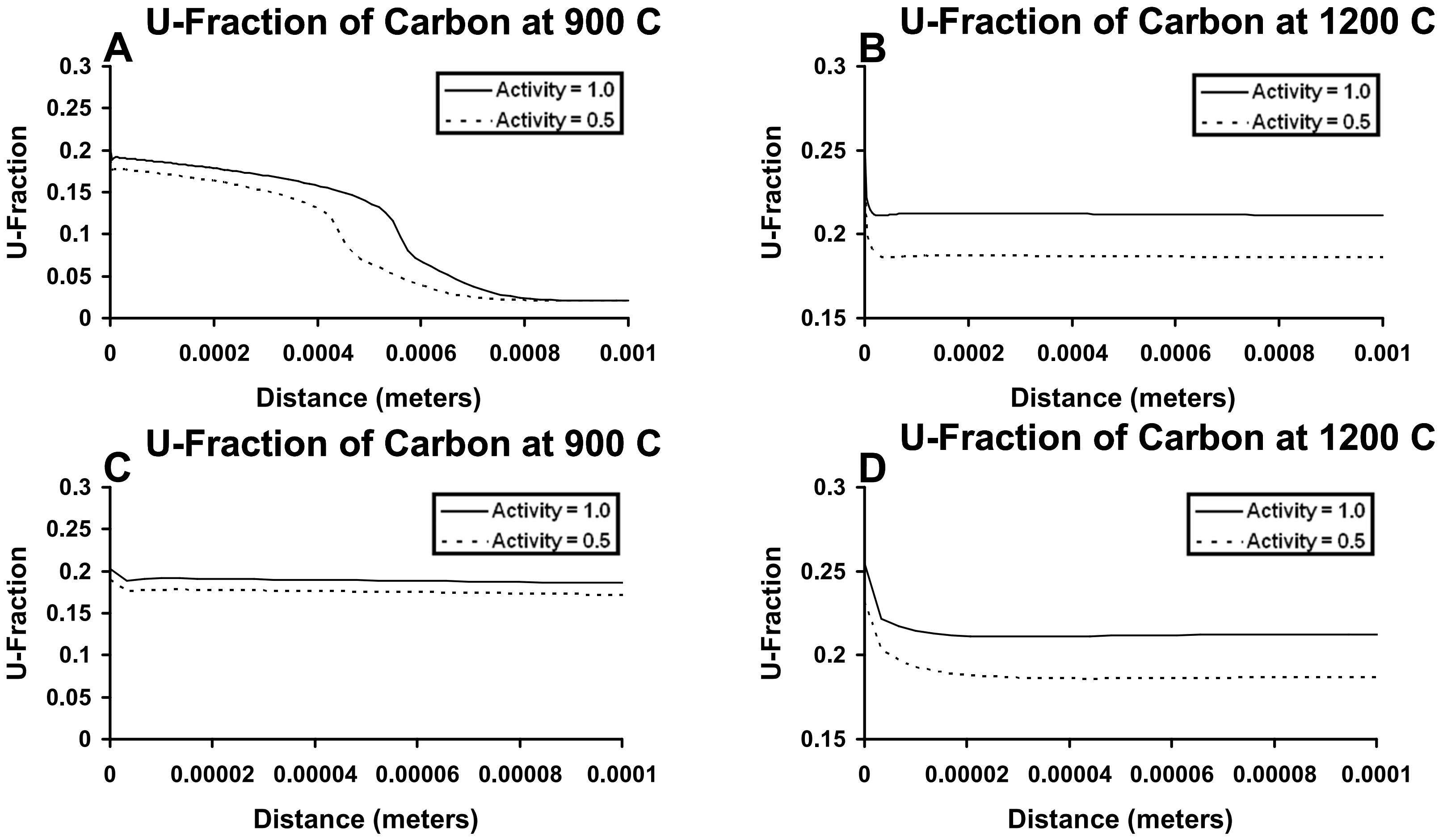

Figure 4.34. Graphs of U-fraction of carbon versus distance in meters at 900 C and 1200 C temperatures for both 0.5 and 1.0 carbon activities, for 35Cr-45Ni alloy. Figures A and B are plotted for a distance of 1 mm, whereas figures C and D are plotted for a distance of 0.1 mm.

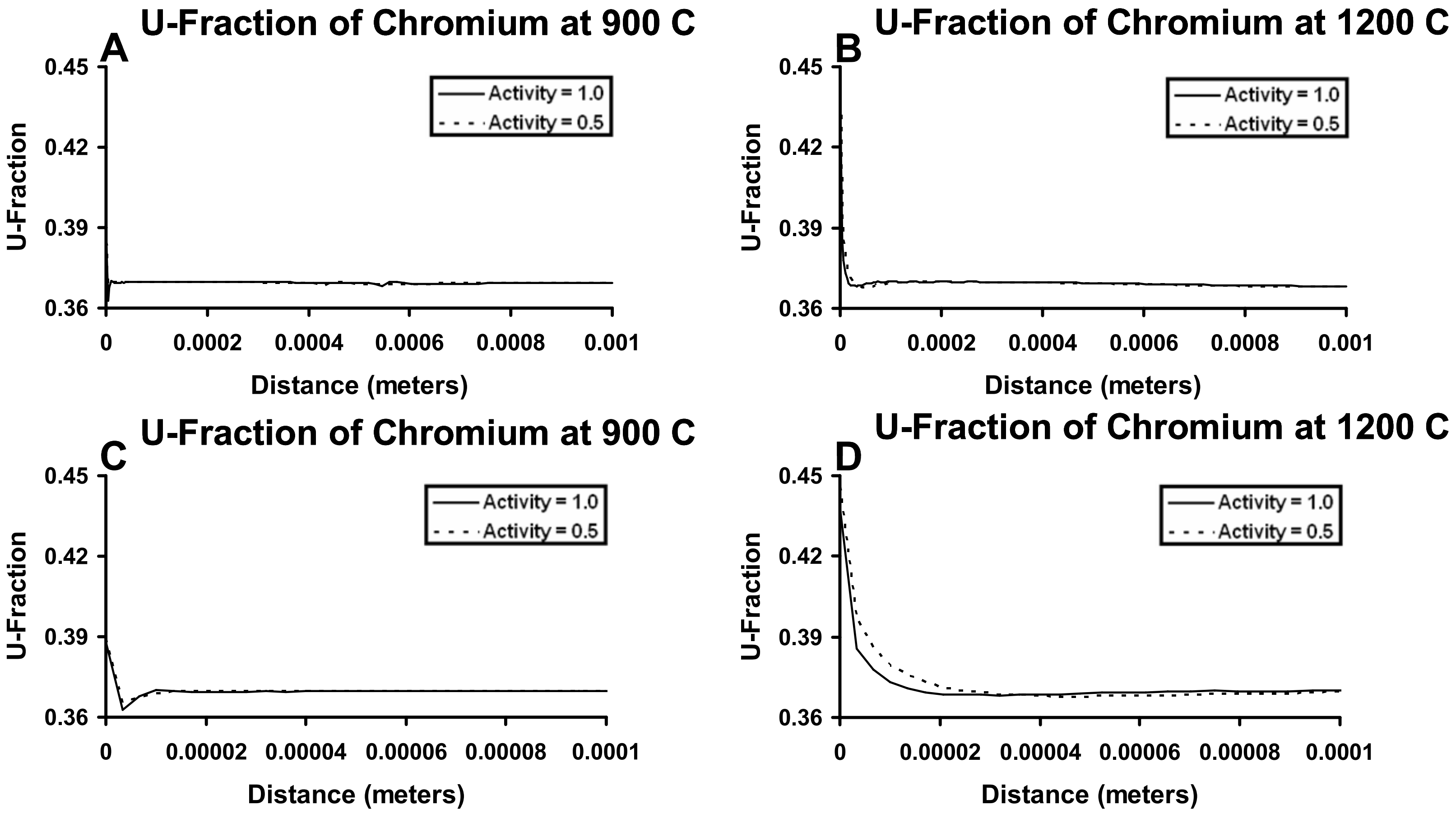

Figure 4.35. Graphs of U-fraction of chromium versus distance in meters at 900 C and 1200 C temperatures for both 0.5 and 1.0 carbon activities, for 35Cr-45Ni alloy. Figures A and B are plotted for a distance of 1 mm, whereas figures C and D are plotted for a distance of 0.1 mm.

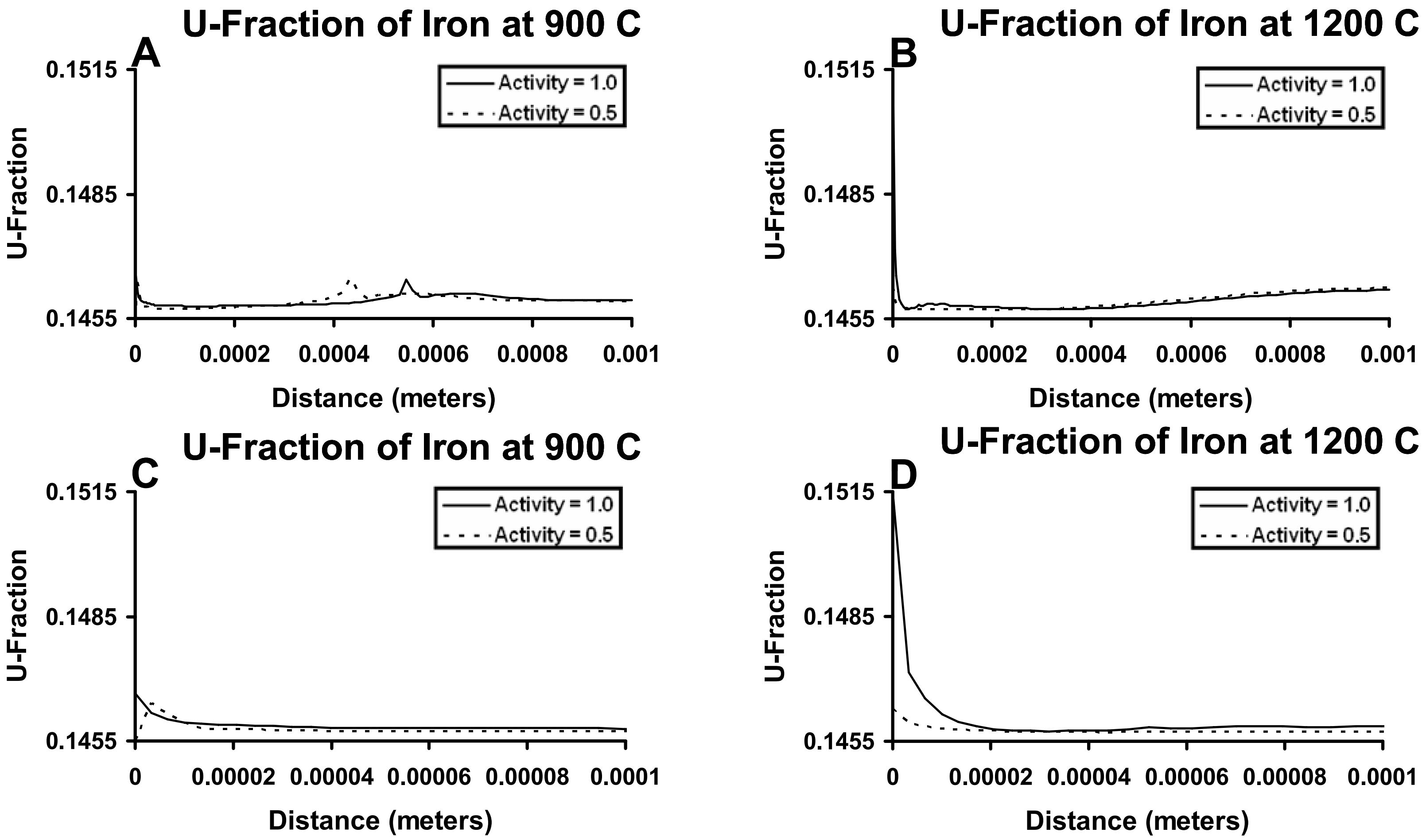

Figure 4.36. Graphs of U-fraction of iron versus distance in meters at 900 C and 1200 C temperatures for both 0.5 and 1.0 carbon activities, for 35Cr-45Ni alloy. Figures A and B are plotted for a distance of 1 mm, whereas figures C and D are plotted for a distance of 0.1 mm.

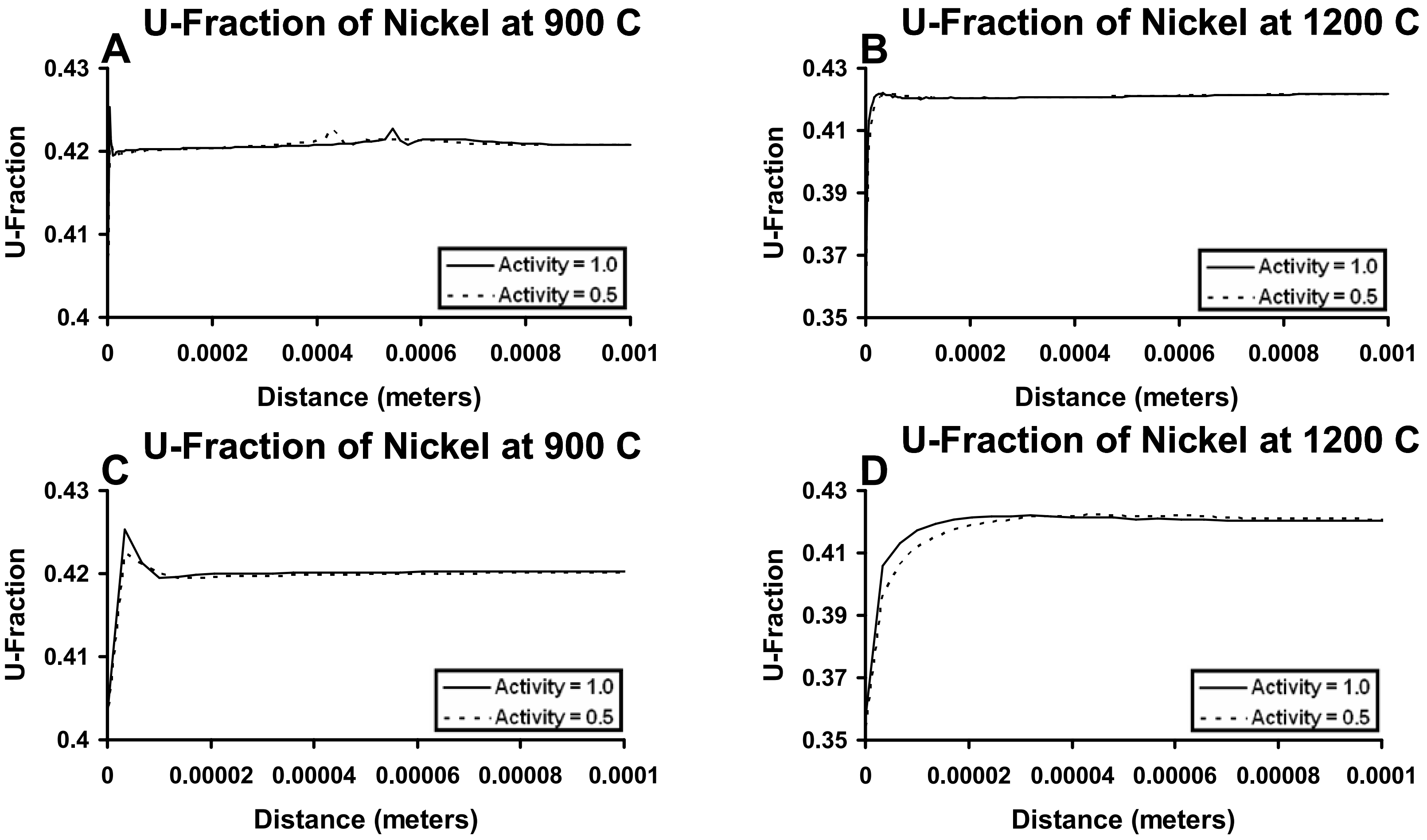

Figure 4.37. Graphs of U-fraction of nickel versus distance in meters at 900 C and 1200 C temperatures for both 0.5 and 1.0 carbon activities, for 35Cr-45Ni alloy. Figures A and B are plotted for a distance of 1 mm, whereas figures C and D are plotted for a distance of 0.1 mm.

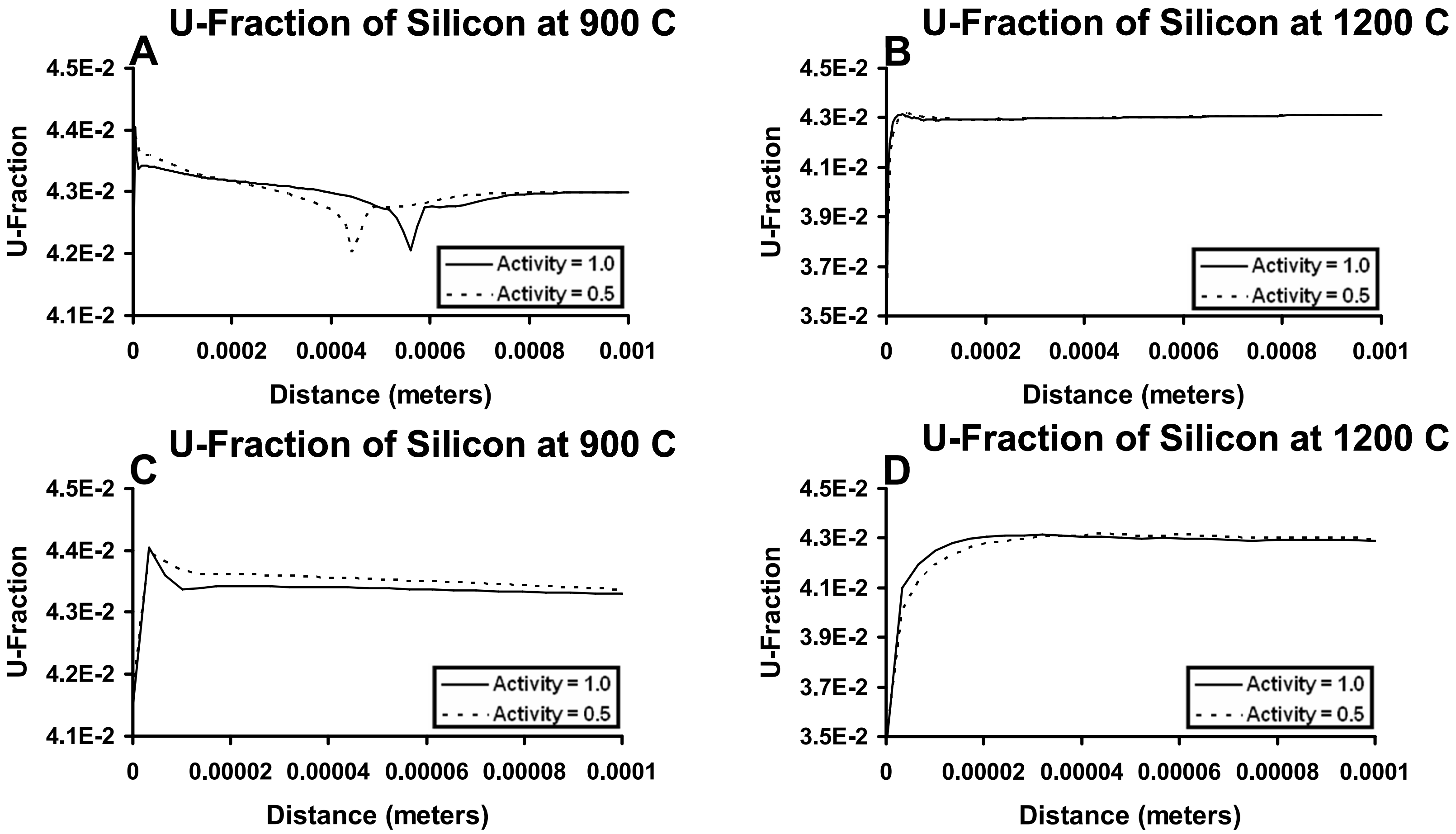

Figure 4.38. Graphs of U-fraction of silicon versus distance in meters at 900 C and 1200 C temperatures for both 0.5 and 1.0 carbon activities, for 35Cr-45Ni alloy. Figures A and B are plotted for a distance of 1 mm, whereas figures C and D are plotted for a distance of 0.1 mm.

Table 4.1. Interplanar Spacing of Slip Plane Main and Side Peak [27].

Ψ (degrees)	$d_{sidepeak}$	$d_{mainpeak}$
0	2.0909	2.0723
5	2.0867	2.0721
10	2.0790	2.0723
15	2.0775	2.0726

Table 4.2. Binding Energies (eV) of 70% SiC-C films [31].

Possible Products	C1s	Si2p	O1s
SiC	283.5	100.4	
C-Si-O		101.8	532.7
Adsorbed C			
Graphite	284.4		
Active C			
$C\text{-}H_x$	286.2		
SiO_2		103.4	531.6
$O\text{-}CH_2$			

Table 4.3. Settings used in the Micro Scratch Tester.

Loading range	0 to 6 N
Loading rate, dL/dt	6 N/min
Scratch length	4 mm
Scratching speed, dx/dt	4 mm/min
AE sensitivity, S_{AE}	9
Indenter	50 μm
Diamond reference number	E-050

Summary and Conclusion

The present studies begin with an introduction to tube failure mechanisms (coking, carburization, creep, and oxidation) in pyrolysis heater radiant coils. Coking which is the precursor for carburization can be catalytic, pyrolytic or in the form of droplet condensation. The different materials of construction used in the pyrolysis heaters: HK40, HP, HPM, 35Cr-45Ni and 36X alloys, were discussed. The important selection criteria for tube materials are cost, accessibility, resistance to corrosion, and manufacturability. In order to improve the life of the tubings used in the pyrolysis heaters, coatings (i.e. silicon based ceramics and chromium/ silicon oxides) were introduced and discussed.

The numerical analysis of the thermodynamical processes responsible for the radiant tube failure at high temperatures using a commercial software package called Thermo-Calc was presented. It can be clearly seen that as the process carbon diffuses into the chromium-nickel-iron matrix at temperatures above 900 C, $Cr_{23}C_6$ phase transforms to Cr_7C_3. Tie lines are drawn to calculate the percentage of chromium and carbon existing in the FCC matrix. At the interface of graphite and Cr_7C_3 phase, graphite precipitates out of the FCC matrix; using this composition and the Wagner equation, the predicted time for through wall carburization of 6 mm thick tubing was calculated to be 3 years, 2 years, 2 years and less than 1 year at 1100 C for 35Cr-45Ni, HP-Nb, HPM and HK40, respectively. Based on the assumption made in our calculations ($\varepsilon = 0.5$; $D_C = 10^{-7}$ cm^2/

sec; and $\upsilon = 3$) the time period for tube failures in petrochemical plants is different than predicted. Magnetization, a non-destructive technique used to study carburization, revealed that the service exposed centrifugally cast chromium-nickel-iron based material changed from austenitic to slightly ferromagnetic. Destructive techniques such as X-ray Mapping to understand the diffusion and precipitation phenomena indicated that there is a strong correlation between the magnetization response of the material and extent of carburization. It can be visually seen from the x-ray maps that depletion of chromium clearly aids in the dominance of magnetic nickel and iron responsible for the hysteresis in the carburized alloy.

One of the suggested solutions to handle coking is to deposit a coating either of silicon based ceramics or chromium/ silicon oxide using pulsed laser deposition (PLD). PLD is preferred over others coating techniques, as the source of laser is independent of the deposition system that supports production of smart films. The X-ray Diffraction patterns of the deposited SiC film did not match the target unlike the results from the self chromium-nickel-iron based alloys deposition. A unique correlation was observed with regards to the variation in the stoichiometry of SiC film as the position of the focusing lens in the lead glass exclusion zone had an affect on the resulting stoichiometry. Residual stresses studied on self-ablated chromium-nickel-iron based alloy onto itself using synchrotron x-ray radiation showed a variation from compressive to tensile stresses with the increasing film thickness. The (222) slip plane peak shift was found to be more dominant than (111) slip plane in the synchrotron x-ray diffraction studies. Supporting x-ray photoelectron spectroscopy (XPS) showed presence of Si-C, C-C, C-H; and SiO_2, SiC, and $Si_{0.4}C_{0.6}$ or C-Si-O bonds on resolving C1s and Si2p peaks respectively. The adhesion test, a destructive technique, conducted on SiC deposited films using scratch-tester showed marginal adhesion suggest future work in the area of methodology for adhesion improvement. The modeling of coking/ carburization behavior of coated ethylene pyrolysis tubing was done using commercially purchased software using TTNi and MOBNI2 databases. The mole-fraction of phases and U-fraction were calculated at carbon activity of 0.5 and 1.0; and at temperatures of 900 C and 1200 C. The U-fraction of silicon was the lowest for both in the case of HK40 and 35Cr-45Ni; but U-fractions of iron and nickel were observed to be higher in HK40 than 35Cr-45Ni, respectively. In all the U-fraction plots, except those of carbon, the U-fractions at higher temperature of Cr, Fe, Ni and Si attain similar values when moving away from the surface at both 900 C and 1200 C. Furthermore, from plots for mole-fraction, there is a tendency for M_7C_3 phase to decrease and FCC_A1 phase to increase on moving more towards the bulk at both activities and both temperatures.

5. Future Work

5.1. Scaled Up Pulsed Deposition Technology and Controlled Random Search

5.1.1. Introduction

A preliminary study of the near optimal settings of the processing parameters for pulsed laser deposition of ceramic SiC on heat resistant tubing traditionally used for ethylene service were investigated using a semi quantitative controlled random search methodology. Minimization of the objective function which was based on width, thickness and coverage of the thin film resulted in an optimal deposition time of 4.3 minutes and surface finish of 272 nm.

James Greer of Raytheon Co. pioneered the scale up efforts by depositing thin films on the internal surface of a cylindrical cavity [1] and over large areas by either scanning the laser or substrate [2-5]. Rapid advancements in switching technology have led to new developments in this technology. Currently, over 1000 Patents on pulsed laser deposition technology exist. The idea of depositing adherent thin films on the inner diameter of a cylindrical cavity has sparked our interest and has led us to investigate the use of pulsed laser deposited SiC films as a potential barrier against corrosive environments. SiC films deposited by conventional techniques require either a high substrate temperature > 1250 C during growth (thermal spray, reactive sputtering [6], radio frequency sputtering [7], and chemical vapor deposition [8-10]) or post deposition annealing (sputtering [11]) to achieve a stoichiometric crystalline structure. So, this lead us to the belief that pulsed laser deposition can deposit stoichiometric SiC films at lower temperature; and this was the driving force for the presented and future works.

5.1.2. Scaled Up Pulsed Laser Deposition

Figure 5.1 shows a schematic of a scaled up pulsed laser deposition system used to deposit thin films on the inner diameter of tubing [12]. The AUTOCAD® designs for facilitating the proposed scaled up PLD system are shown in Figure 5.2. The laboratory prototype of the proposed scaled up pulsed laser deposition set up is shown in Figure 5.3. External to the vacuum chamber; the input parameters are laser type, laser energy, pulse length, pulse rate, and laser scan rate (if employed). When the laser enters the vacuum chamber the following internal input parameters become significant: atmosphere (vacuum condition, inert/ active gas, gas pressure), ablation target surface condition, ablation target rotation speed, fluence (energy/ area), ablation target to cylinder inner surface angle, ablation target to cylinder inner surface distance, nature of plume (transfer of stoichiometry), cylinder inner surface condition, cylinder temperature, cylinder rotation speed (equals ablation target rotation speed in our experimental setup), cylinder translation speed, and deposition time. The external and internal input parameters play a major role in optimizing the output variables: thickness, static deposition width (plume width) and coverage/ adherence.

Near optimal settings for pulsed laser deposition of the tube inner surface processing parameters were determined experimentally (using flat 6.5 mm x 6.5 mm x

1.0 mm coupons) and by using a semi- quantitative controlled random search methodology. Pulsed laser deposition experiments were performed in the Condensed Matter Physics and Materials Science Laboratory at Brookhaven National Laboratory. A Lambda Physik KrF (λ = 248 nm) excimer laser was used to ablate a Hexoloy SA ceramic SiC target and deposit thin films on 25Cr- 20Ni- Fe alloy coupons (removed from tubing supplied by Ultra-cast Inc.). The external input parameters were as follows: laser type, KrF excimer (λ = 248 nm); energy, 500-600 mJ; pulse length, nanosecond; pulse rate, 5-10 Hz; and the scan rate, stationary. The initial laser beam dimensions (v x h, FWHM) were 24 x 6 to 12 mm^2. The pulsed laser deposition system is equipped with optics to scan the laser. Laser scanning is commonly used for larger area deposition [2-5] and to produce composition gradient films to improve adhesion properties [13]. The later is of experiment interest to the authors, but was not employed in this study. [14]

5.1.3. Control Random Search

The parameters of interest for our experiment are shown in Table 5.1 ([15]). In this study; a limited number of thin films were deposited on coupons to obtain data for the semi- quantitative controlled random search procedure. The near optimal conditions for pulsed laser deposition of thin films on the inner surface of a cylinder can be obtained using the experimental data and the semi- quantitative controlled random search methodology. Details of the controlled random search methodology can be found in the literature [16-18].

Chauhan et al. in an earlier work [19] determined that the surface finish had a significant effect on the adhesion properties. Data such as this is very useful in limiting the number of search parameters in the random search procedure. In this initial study, all parameters were fixed except the deposition time and specimen surface condition and the objective function was formulated using the deposition width, thickness and coverage as shown in Figure 5.4.

$$f = (W_d - W)^2 + (T_d - T)^2 + (C_d - C)^2 \qquad \text{(I)}$$

In the object function equation, W_d, T_d, and C_d are the desired values and W, T, and C are the values determined experimentally. In this work, the desired values are W_d= 6.5 mm (coupon dimension), T_d= 0.1 um (roughness dependant), and C_d= 1 (where 0 is no coverage and 1 is complete coverage). The input parameter ranges were deposition time 80 to 540 seconds and specimen surface roughness was 10 nm to 400 nm. A set of 5 candidate solutions were randomly selected from our experiments as shown in the Table 5.2.

Based on the initial candidate solutions and experience of the authors [19], the objective function equation is only dependant on the thickness of the deposited film. From the initial candidate solutions the maximum (f_M) and lowest (f_L) objective functions were found during experiments 3 ($f_M = 0.0049$) and 1 ($f_L = 0.0004$) respectively. The two initial candidate solutions randomly selected to comprise the simplex are 2 and 5 and thus the simplex is composed of 1, 2, and 5. The initial candidate solution 5 becomes the pole of the simplex and the first centroid (deposition time, 258 seconds; surface roughness, 272 nm; and f_P, ~ 0) is calculated from 1 and 2. These solutions produce a thin film with a width of 6.5 mm, thickness of 0.1 um and complete coverage. Since f_P is less that f_M initial candidate solution 3 is eliminated from the solution set and is replaced by the centroid of the simplex. The methodology is continued until the processing conditions (arbitrary *f* value) are optimized.

A semi- quantitative controlled random search methodology is proposed as a method of determining the near- optimal conditions for pulsed laser deposition of a thin film on the inner surface of a cylinder. The objective function was based on the deposited thickness, the width of the deposition and coverage. The input parameters, deposition time and surface condition, were selected because these variables would most likely be controlled during industrial processing. [14]

5.2. Diffusion Modeling

A complete kinetic description of the multicomponent diffusion problem requires mathematical solutions to the generalized Fick's law $[\frac{\partial C_i}{\partial t} = \sum_{k=1}^{n-1} D_{ik} \frac{\partial C_k}{\partial x}]$ and the mass balance equation $[\frac{\partial C_i}{\partial t} + \nabla \bullet J_i = 0]$, where $J_i = -\sum_{k=1}^{n-1} D_{ik} \nabla C_k$. The semi infinite diffusion couple is shown in the schematic Figure 5.5 and Figure 5.6. Figure 5.5 is a five component, single phase semi-infinite diffusion model. The plot is between concentration and distance, where C_s is concentration at the surface and C_o is concentration in the bulk. Five component multi-phase semi infinite diffusion model is shown in Figure 5.6. The number of phases increase going towards the bulk. The x = 0 plane is the free surface and the length of the couple in the diffusing x direction is infinite compare to the diffusion zone. The mathematics can be extended to evaluate multicomponent/ multiphase systems. The general equation for a three component (third component is considered to be the solvent) p- phase system is as follows:

$$(C_n)_p = (\overline{C_n})_p + \sum_{k=1}^{2} (DD_{nk})_p \left\lfloor \frac{erf\left\{\frac{Y}{\sqrt{U_k}}\right\}_p - erf\left\{\frac{\zeta_p}{\sqrt{U_k}}\right\}_p}{erf\left\{\frac{\zeta_{p+1}}{\sqrt{U_k}}\right\}_p - erf\left\{\frac{\zeta_p}{\sqrt{U_k}}\right\}_p} \right\rfloor \qquad \text{(II)}$$

where n= 1, 2 and p= 1, 2, 3, ….., p, and

$$(DD_{11})_p = \left\lfloor (D_{12})_p \left\{ (\overline{C_2})'_p - (\overline{C_2})_p \right\} + 0.5(D_{11} - D_{22} + D)_p \left\{ (\overline{C_1})'_p - (\overline{C_1})_p \right\} \right\rfloor \Big/ (D)_p \ ,$$

$$(DD_{12})_p = \left[(\overline{C_1})'_p - (\overline{C_1})_p - (D_{11})_p \right], \ (DD_{22})_p = \left[(\overline{C_2})'_p - (\overline{C_2})_p - (D_{21})_p \right],$$

$$(DD_{21})_p = \left\lfloor (D_{21})_p \left\{ (\overline{C_1})'_p - (\overline{C_1})_p \right\} + 0.5(D_{22} - D_{11} + D)_p \left\{ (\overline{C_2})'_p - (\overline{C_2})_p \right\} \right\rfloor \Big/ (D)_p \ ,$$

$$(D)_p = \left[(D_{11} - D_{22})^2 + 4 D_{12} D_{21} \right]_p \ , \ (U_1)_p = 0.5(D_{11} + D_{22} + D)_p \, , \ (U_2)_p = 0.5(D_{11} + D_{22} - D)_p \, ,$$

$Y = \frac{x}{2\sqrt{t}}$, and $\zeta = y_p = \frac{x_p}{2\sqrt{t}}$. It is assumed that (1) local equilibrium exist between adjacent phase separated by an interface; (2) the diffusion plane at a particular position moves proportional to the square root of the annealing time; (3) volume changes due to interdiffusion are neglected; (4) sequence of phases appearing during diffusion corresponds to the isothermal phase diagram for the system; and (5) the composition of the phases across a boundary correspond to the equilibrium values in the phase diagram. In the Fe-Ni-Cr-Si-C system, sixteen diffusion coefficients will exist and the interrelationship between them will be described.

If moving interfaces or boundaries exist, the mass balance equation must be considered. The mass balance equation for a three component multiphase system will be provided here and extended for a multicomponent/ multiphase system as part of the proposed work. The mass balance equation at the (r-1)th and rth interface is as follows:

$$\left[\left(\overline{C_n}\right)'_{r-1} - \left(\overline{C_n}\right)_r\right]\sqrt{\pi}\alpha_r = -\sum_{s=r-1}^{r}\left[\sum_{i=1}^{2}\left(D_{ni}\right)_s\left[\sum_{k=1}^{2}\frac{\left(DD_{ik}\right)_s e^{\frac{-\alpha_r^2}{(U_k)_s}}}{\{\sqrt{U_k}\left(erf\left(\frac{\alpha_{s+1}}{\sqrt{U_k}}\right) - erf\left(\frac{\alpha_s}{\sqrt{U_k}}\right)\right)\}_s}\right]\right] \qquad \text{(III)}$$

where k, n= 1, 2 and r = 1, 2, 3, …….., p. This equation is valid for all interfaces including the surface (if the surface is assumed to be stationary and $\zeta_1 = 0$). If chemical reactions occur at the surface (i.e. surface is moving) other factors must be considered in the equation. Once all the interface parameters are known, and the corresponding tie-lines determined, the concentration profiles can be determined. [20]

As shown in Figure 5.7 Fick's first law is

$$J = [D_{ij}] \frac{\partial c}{\partial x_j} \qquad \text{(IV)}$$

Here, flux J is proportional to the concentration gradient and the diffusivity constant is denoted by D_{ij}. As shown in the bottom of Figure 5.7, diffusivity is a 4 X 4 iron (Fe) based matrix for a five component system. The schematic of diffusion of carbon taking place at high temperature 1100 C in Cr-Ni-Fe based alloy (both coated and uncoated) is shown in the center of Figure 5.7. In case of uncoated alloy carbon diffusion is interstitial whereas it is both substitutional and interstitial for coated alloy. Also coating impedes carbon diffusion. The backscattered scanning electron micrograph of the phases formed when the process carbon diffuses in the matrix is shown in Figure 5.8.

5.3. In-Plane Stresses

Comparison of preliminary in-plane stresses of SiC coated HK40 alloy with uncoated HK40 alloy are shown in Figure 5.9. The plot is between $d\phi\psi$ and $\sin^2\psi$ using equation given by Noyan et al [21].

$$\frac{d_{\phi\psi} - d_o}{d_o} = \frac{1+\upsilon}{E}\sigma_\phi \sin^2\psi - \frac{\upsilon}{E}(\sigma_{11} + \sigma_{22}) \qquad \text{(V)}$$

From the plot it can be seen that the uncoated HK40 alloy shows uniaxial and biaxial stresses depicted by the straight lines. The coated HK40 alloy gives textured profile as shown in the plot. More work is suggested for understanding the in-plane stresses on SiC coated films.

5.4. Proposed Design of Coating for Pyrolysis Heaters

Figure 5.10 elaborates on the proposed design of an ideal gradient coating for the cast HP alloy (35 wt% Cr-45 wt% Ni) by stitching a coating of HPM wrought alloy (25 wt% Cr-38 % Ni- Mo- Si). The different geometrical shapes can be easily made by cast HP alloy, not possible by wrought HPM alloy. The wrought HPM alloy has less carbon, so less internal carbon diffusion and thus negligible formation of $Cr_{23}C_6$ ceramic phase resulting in less embrittlement. HPM alloy creeps vigorously at high temperatures so deposited coke in the petrochemical tubing can be easily removed by cycling the temperature (1050 6 50 C) to breakdown the deposited coke.

Figure 5.11 elucidates on the procedure to develop a gradient coating as suggested by Hou et al [13]. So, in order to deposit a coating of wrought HPM alloy over cast HP alloy, a coupon made of cast HP alloy (shown in white color in the schematic) is glued to the target made of wrought HPM alloy (shown as black). The alloys are stitched by starting the ablation of the improvised target with the help of pulsed laser starting from track 1 and gradually move to track 4 in the end. So, on ablation of track 1, only cast HP alloy is deposited on the substrate. On ablating track 2 and track 3, mixture of cast HP alloy and wrought HPM alloy is deposited on the substrate and on ablation of track 4, strictly wrought HPM alloy is deposited as the final layer.

References

[1] J. A. Greer and H. J. Van Hook, "Laser-Ablation of Various Oxide Material Over Large Areas", (1990) p. 171.

[2] J. A. Greer, in "Superconductivity and Applications", edited by H. S. Kwok, Y.-H. Kao and D. T. Shaw (Plenum Press, New York, 1989) p. 117.

[3] J. A. Greer, "High-Quality Ybco Films Grown over Large Areas by Pulsed Laser Deposition", Journal of Vacuum Science & Technology a-Vacuum Surfaces and Films 10 (1992) 1821.

[4] J. A. Greer, "Comparison of Large-Area Pulsed-Laser Deposition Approaches", (Publ by Int Soc for Optical Engineering, Bellingham, WA, USA, Boston, MA, USA, 1993) p. 21.

[5] J. A. Greer and H. J. Van Hook, "Pulsed Laser Deposition of Oxides over Large Areas", (Publ by Int Soc for Optical Engineering, Bellingham, WA, USA, Boston, MA, USA, 1991) p. 79.

[6] A. J. Learn and K. E. Haq, "Low-Temperature Epitaxy of !- SiC by Reactive Deposition", 17 (1970) 26.

[7] T. Tohda, K. Wasa and S. Hayakawa, "Effects of Target Materials on the Structural Properties of Sputtered SiC Films", Journal of the Electrochemical Society 127 (1980) 44.

[8] A. Addamiano and J. A. Sprague, "'Buffer-Layer' Technique for the Growth of Single Crystal SiC on Si", Applied Physics Letters 44 (1984) 525.

[9] M. I. Chaudhry and R. L. Wright, "Epitaxial-Growth of Beta-SiC on Si by Low-Temperature Chemical Vapor-Deposition", Journal of Materials Research 5 (1990) 1595.

[10] J. A. Powell, D. J. Larkin, L. G. Matus, W. J. Choyke, J. L. Bradshaw, L. Henderson, M. Yoganathan, J. Yang and P. Pirouz, "Growth of High-Quality 6h-Sic Epitaxial-Films on Vicinal (0001) 6h-Sic Wafers", Applied Physics Letters 56 (1990) 1442.

[11] I. Berman, R. C. Marshall and C. E. Ryan, (Air Force Cambridge Research Laboratories, 1974).

[12] J. A. Greer, in "Pulsed Laser Deposition of Thin Films", edited by D. B. Chrisey and G. K. Hubler (John Wiley & Sons, Inc., New York, 1994) p. 293.

[13] Q. R. Hou, J. Gao and S. J. Li, "Adherent SiC Coatings on Ni-Cr Alloys with a Composition-Graded Intermediate Layer", Applied Physics A: Materials Science & Processing 67 (1998) 367.

[14] A. Chauhan, M. Anwar, K. Montero, H. White, W. Si and J. Bai, "Scaled up Pulsed Deposition Technology: Carburization Resistant Ablation Coatings for Ethylene Pyrolysis Coils", (Materials Research Society, Warrendale, PA 15086, United States, Boston, MA, United States, 2006) p. 147.

[15] D. W. Bonnell, P. K. Schenck, J. W. Hastie and M. Joseph, "Proceedings of Symposium on High Temperature Chemistry", in Symposium on High Temperature Chemistry (Electrochemical Society, NJ, 1990).

[16] D. Kim, M. Kang and S. Rhee, "Determination of Optimal Welding Conditions with a Controlled Random Search Procedure", Welding Journal (Miami, Fla) 84 (2005) 125.

[17] W. L. Price, "Controlled Random Search Procedure for Global Optimization", Computer Journal 20 (1977) 367.

[18] W. L. Price, "Global Optimization by Controlled Random Search", Journal of Optimization Theory and Applications 40 (1983) 333.

[19] A. Chauhan, W. Moran, S. R. Ge, W. D. Si and H. J. White, "Pulsed laser Deposition of Silicon Carbide on Heat Resistant Materials", Scripta Materialia 52 (2005) 735.

[20] L. L. Seigle, H. Herman and H. J. White, Course Notes, ESM 521 Kinetics I: Diffusion in Solids, (Stony Brook University, Stony Brook, 2006).

[21] I. C. Noyan and J. B. Cohen, Residual Stress: Measurement by Diffraction and Interpretation (Springer- Verlag, 1987).

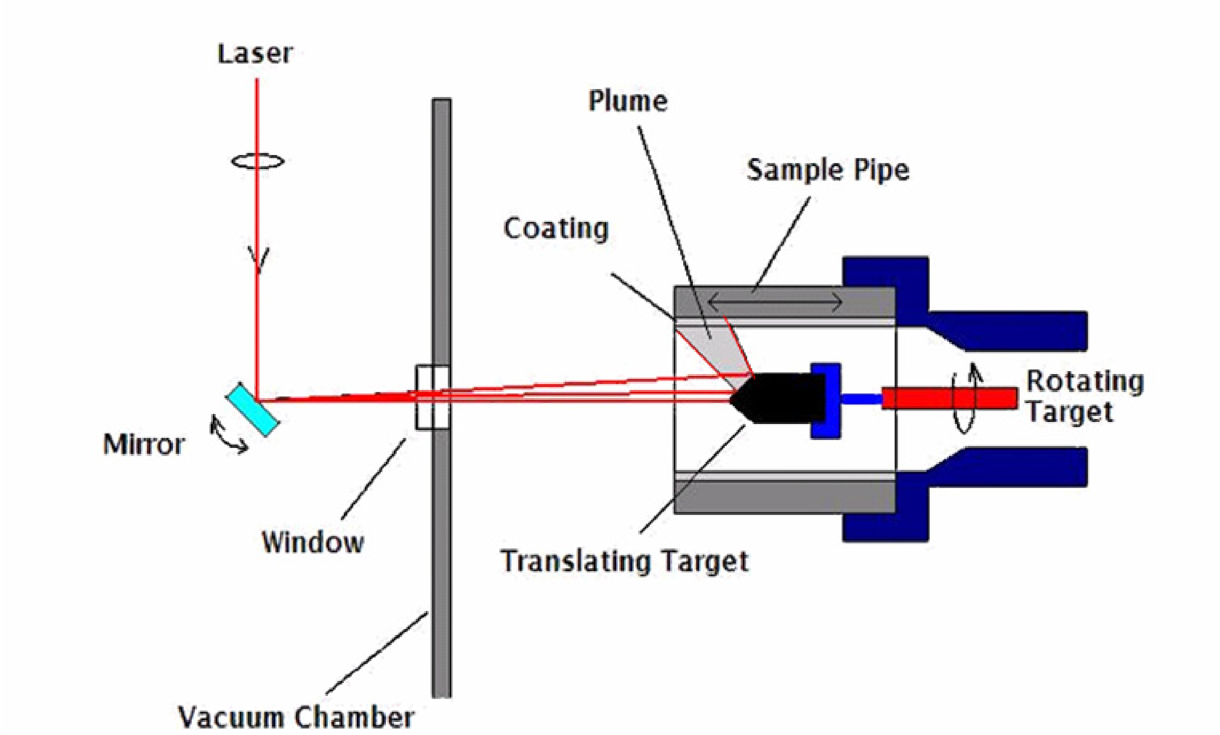

Figure 5.1. Schematic of scaled up pulsed laser deposition system to deposit thin films on the inner surface of a cylinder.

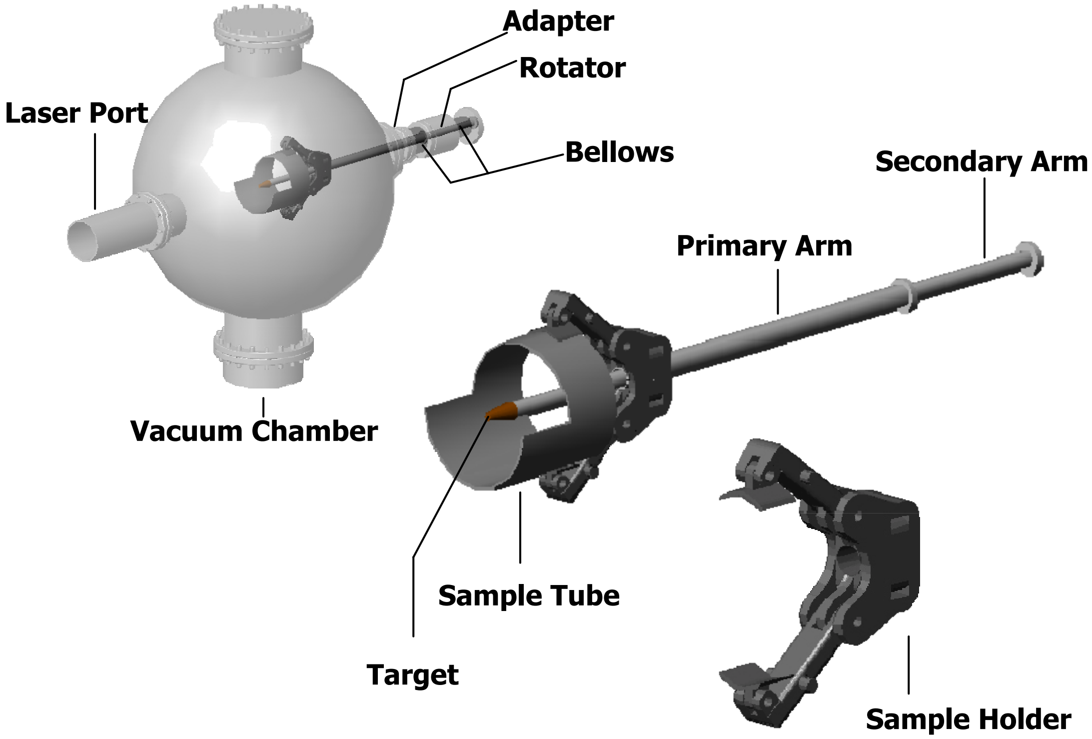

Figure 5.2. AUTOCAD® designs of shaft which holds both the ablation target and the cylinder feeds through the rotation mechanism (hand) and translation bellows. The bellows is attached to the vacuum chamber. The remaining components as shown in the schematic Figure 5.1 are commonly found in most pulsed laser deposition systems.

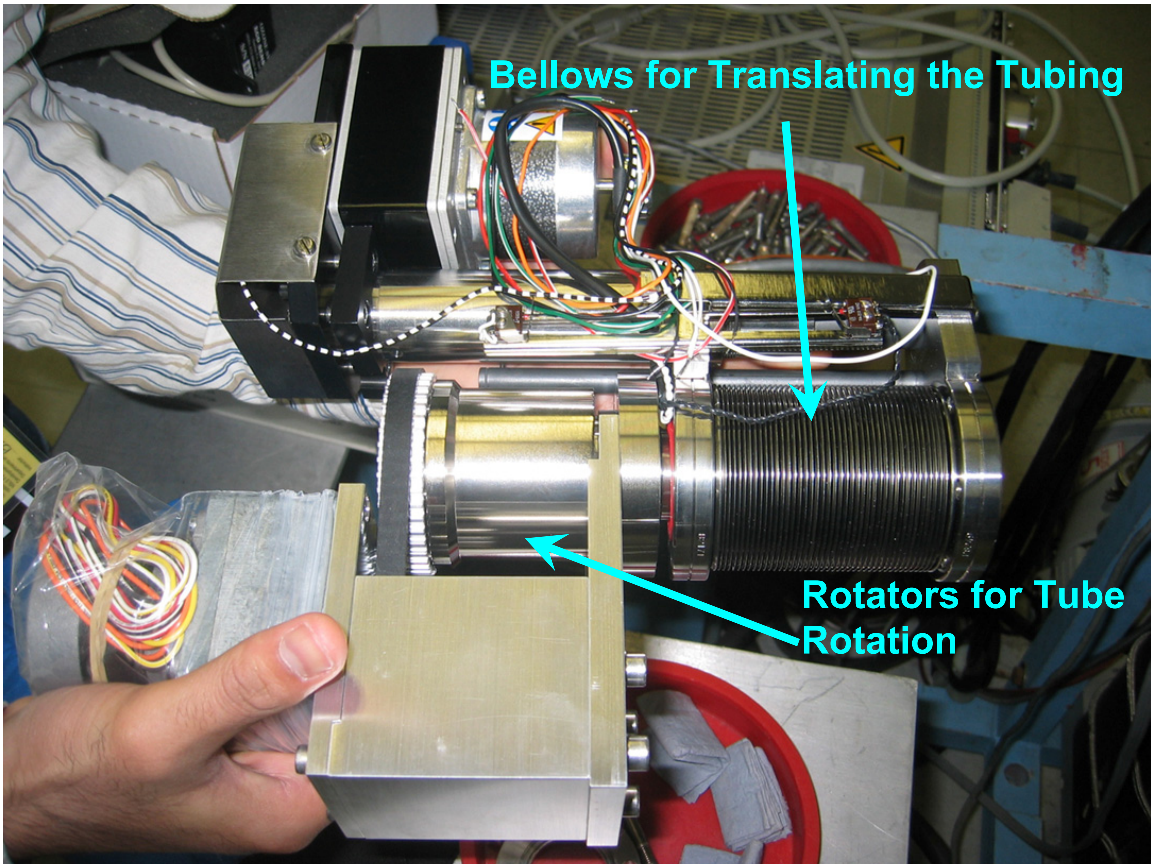

Figure 5.3. Illustration of translation/ rotation stage (as shown in the schematic in Figure 5.1).

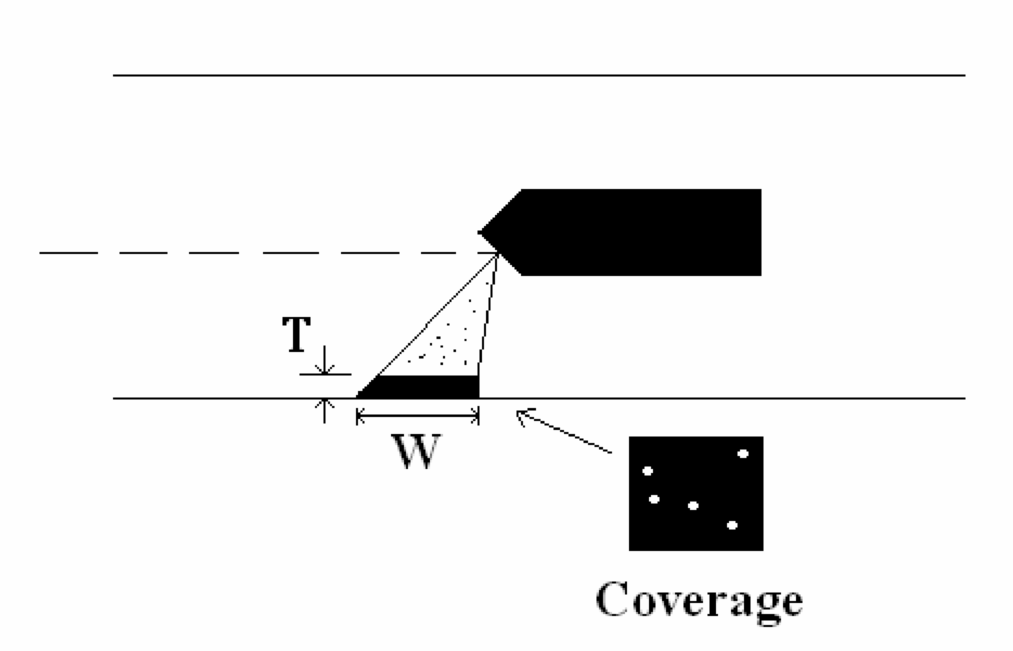

Figure 5.4. Thin film geometry [14].

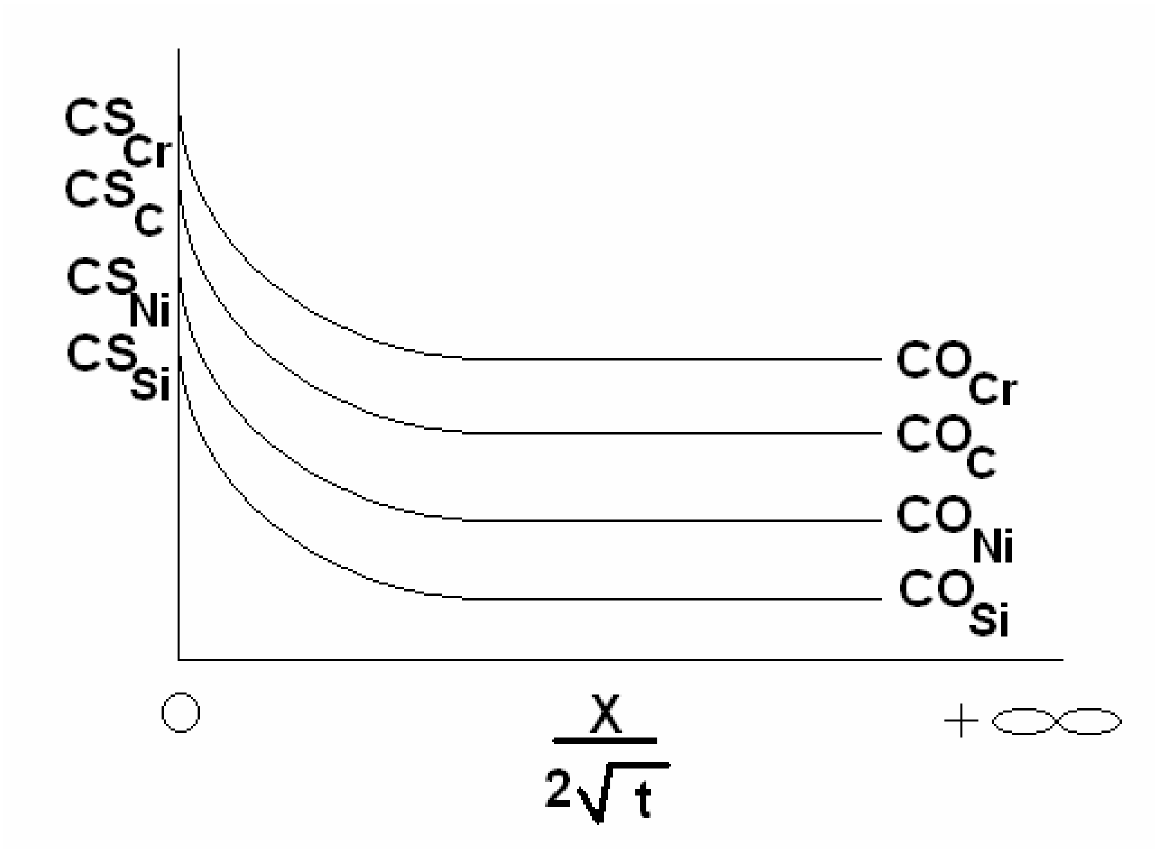

Figure 5.5. Semi Infinite Diffusion Model Case 1: Single Phase.

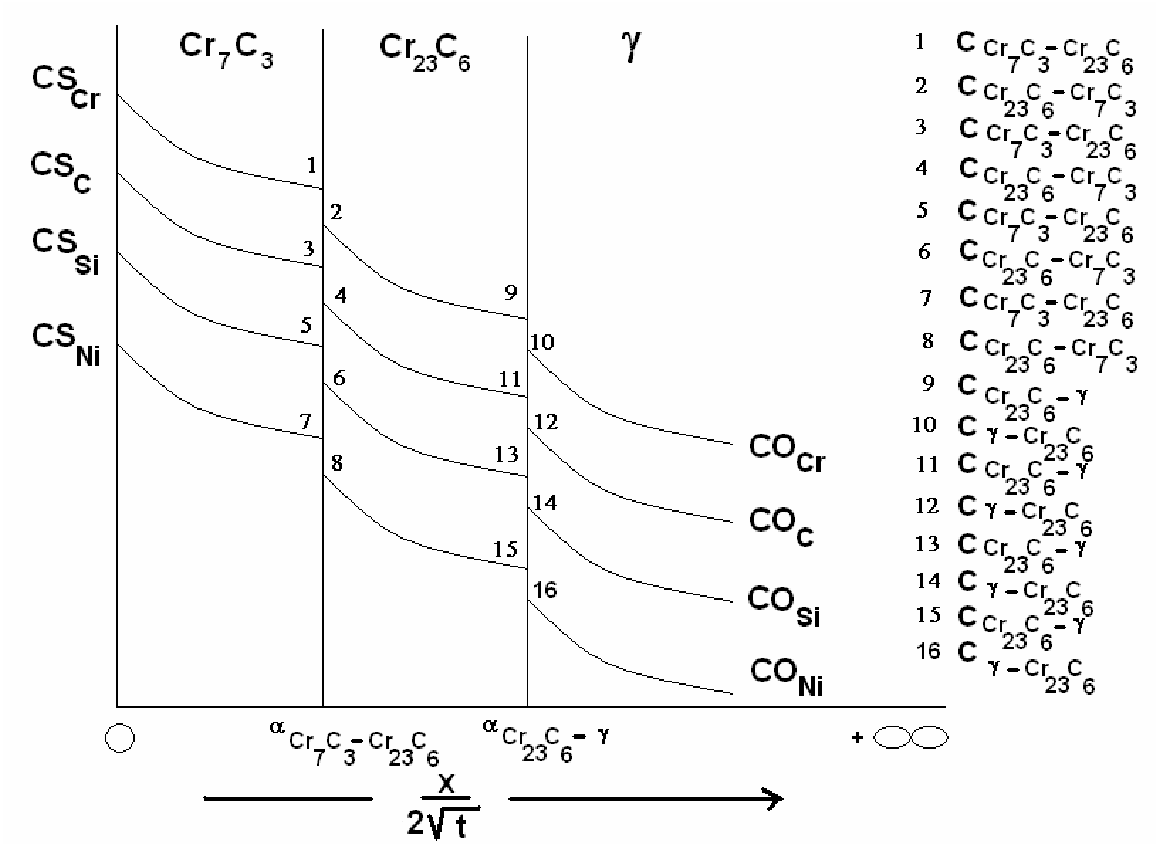

Figure 5.6. Semi Infinite Diffusion Model Case 2: Multi-Phase.

$$J = [D_{ij}] \frac{\partial c}{\partial x_j}$$

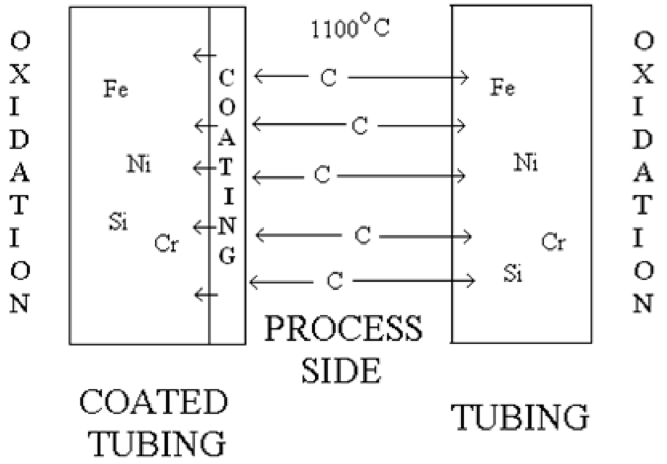

$$[D_{ij}] = \begin{bmatrix} D_{NiNi} & D_{NiCr} & D_{NiSi} & D_{NiC} \\ D_{CrNi} & D_{CrCr} & D_{CrSi} & D_{CrC} \\ D_{SiNi} & D_{SiCr} & D_{SiSi} & D_{SiC} \\ D_{CNi} & D_{CCr} & D_{CSi} & D_{CC} \end{bmatrix}$$

Figure 5.7. Diffusion modeling and schematic of diffusion of carbon taking place in a coated and uncoated Cr-Ni-Fe alloy.

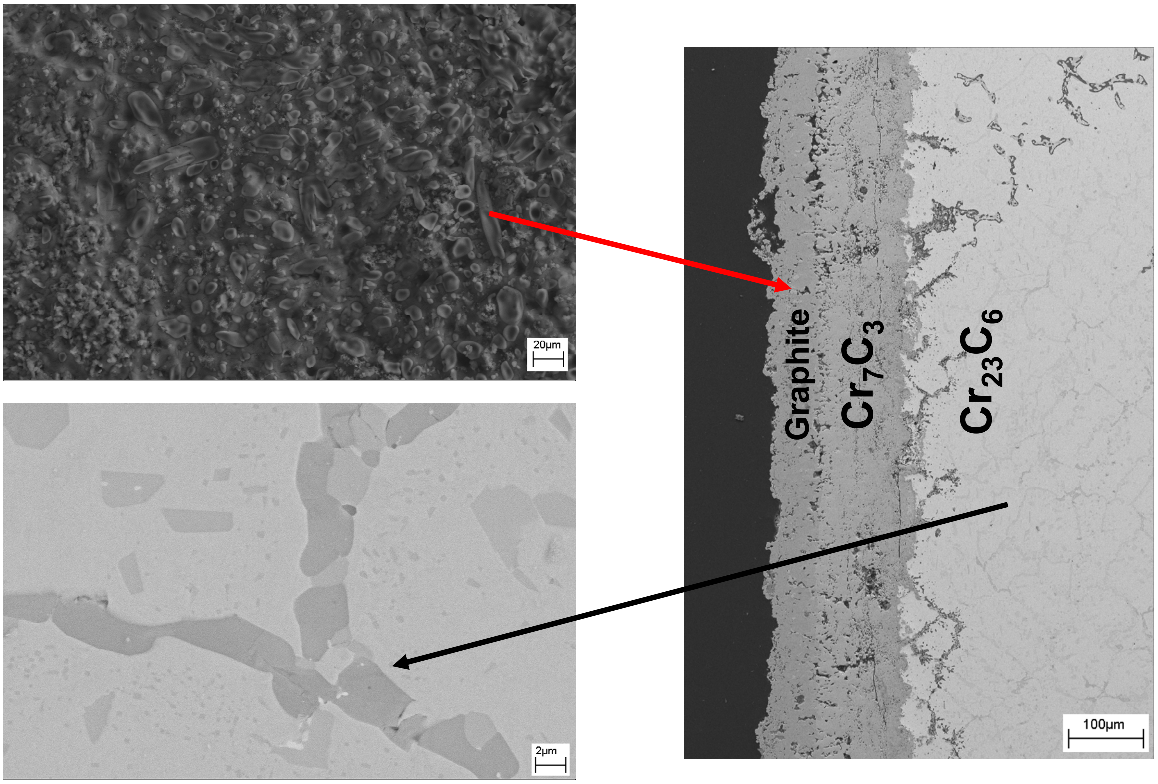

Figure 5.8. Backscattered scanning electron microscopy image. The phase differences are due to z-contrast variation, where higher average atomic number element appears to be lighter. The three layers observed are: outer is carburized layer, second layer is chromium carbides and the rest is the bulk material. In the bottom left inset image $Cr_{23}C_6$ precipitates are observed at the grain boundaries. Black scratches symbolize epoxy which means defect is present in the system.

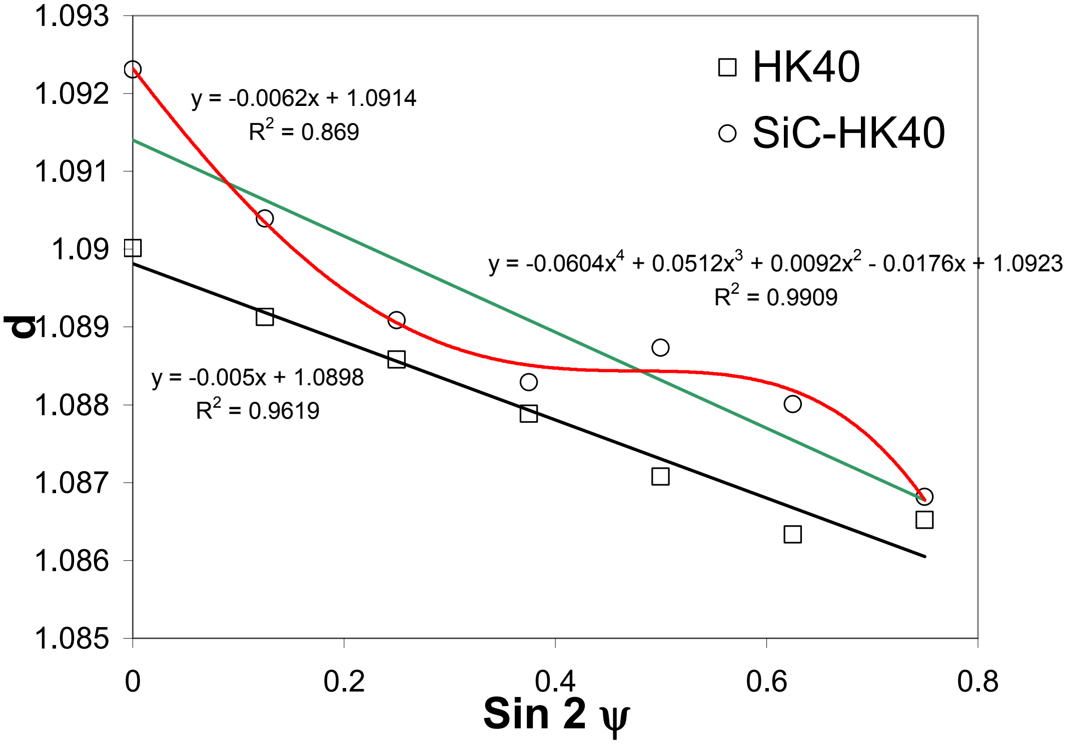

Figure 5.9. Interplanar spacing versus $\sin^2\psi$ plot of uncoated HK40 alloy and SiC coated HK40 alloy.

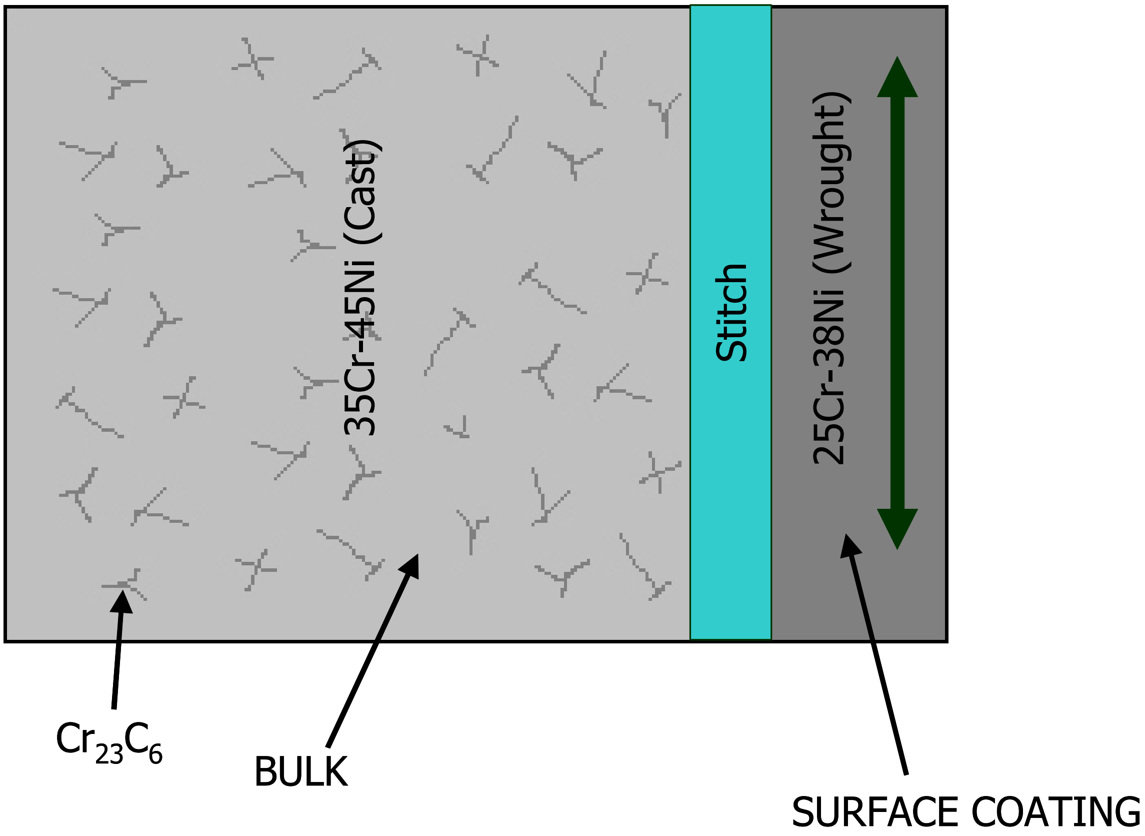

Figure 5.10. Future Work: Proposed Coating Design for Material Used in Ethylene Pyrolysis Plants.

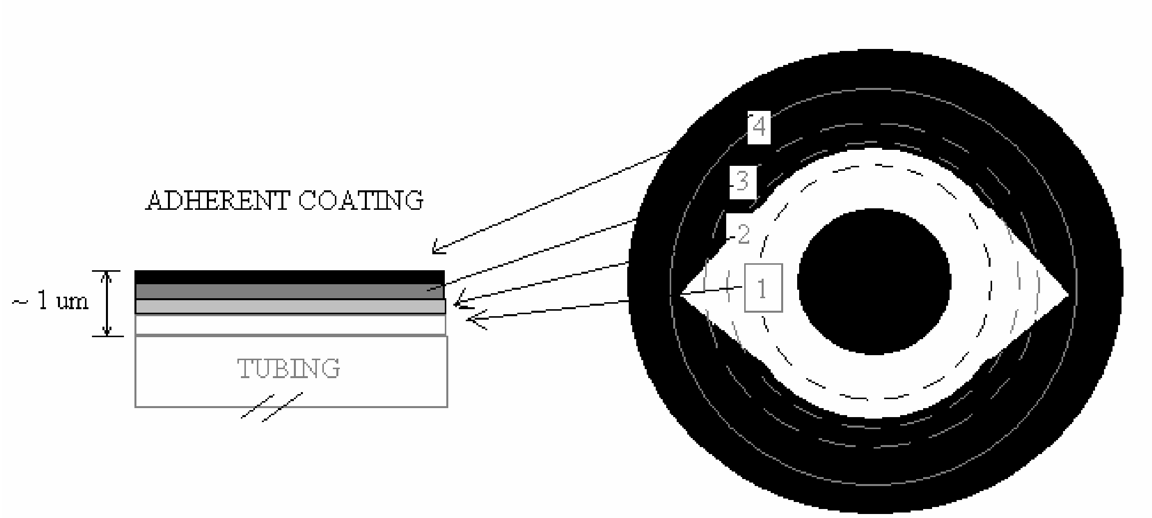

Figure 5.11. Methodology to stitch wrought HPM alloy over cast HP alloy, a coupon made of cast HP alloy (shown in white color in the schematic) is glued to the target made of wrought HPM alloy (shown as black). On ablation of track 1, only cast HP alloy is deposited on the substrate. On ablating track 2 and track 3, mixture of cast HP alloy and wrought HPM alloy is deposited on the substrate and on ablation of track 4, strictly wrought HPM alloy is deposited as the final layer.

Table 5.1. Internal Input Parameters in Pulsed Laser Deposition [14].

Atmosphere (argon)	~ 380 mtorr
Target rotation speed	10 rpm
Target surface condition	sintered SiC (grain size < 10 μm)
Fluence	140 – 170 mJ/mm^2
Target to substrate angle	45^o
Target to specimen distance	40 mm
Nature of plume	molecular transfer [15]
Substrate surface condition	10 – 400 nm rms
Substrate temperature	800^o C
Substrate rotation speed	stationary[*]
Substrate translation speed	stationary[**]
Deposition time	< 1 hour

[*] For deposition on the inner surface of tubing, the target and cylinder rotation speeds are equivalent

[**] For a 4 inch cylinder, the translation speed would be ~1.7 mm/ min

Table 5.2. Initial Candidate Solutions Using Controlled Random Search [14].

Experiment Number	1	2	3	4	5
Deposition Time (sec.)	193	323	433	196	416
Roughness (nm)	146	398	395	123	248
Width (mm)	6.5	6.5	6.5	6.5	6.5
Thickness (μm)	0.08	0.13	0.17	0.08	0.17
Coverage (%)	1	1	1	1	1
f	0.0004	0.0009	0.0049	0.0004	0.0049

Appendix

Plume Analysis

The nature of plume of the Pulsed Laser Deposition unit (Figure 1) was studied prior to film deposition (illustrated in section 4.2). A 5 mm x 5 mm x 25 um polyimide thin film was fastened to a 6 mm x 6 mm x 1.6 mm silicon wafer using a dilute solution (10 mg/ml) of 60,000 MW polystyrene dissolved in toluene. A 3 mm in diameter 600 mesh carbon / formvar supported copper grid was attached on the formvar side to the polyimide film using a drop of the polymer solution mentioned previously. The silicon wafer was fixed to the stage in a manner similar to the substrate (Pyro- Duct paste). The procedure is depicted in Figure 2. [1] The 35Cr- 45Ni target was ablated onto the copper grid for 15 seconds. After ablation, the assembly was removed from the chamber and the copper grid was removed from polyimide film with a razor blade edge (the polyimide film facilitated grid removal). The grid, shown in Figure 3 (c), was examined using a scanning electron microscope (LEO 1550). Atomic, ionic, and molecular transfer can occur when the target material consists of metallic bonds. [2] Clusters of atoms 10-20 nm in size known as nanoparticulates were observed as shown in Figure 3 (a). Similar procedure was followed for SiC target and no nanoparticulates were observed, using scanning electron microscope, in the deposited film as can be seen in Figure 3 (b). Here in SiC, an assortment of atoms and molecules (i.e. Si, SiC, SiC_2, Si_2C, C, C_2, C_3, Si_2, Si_3) are generated instead of ions; due to the breaking down of covalently bonded SiC [3].

References

[1] J. W. Hastie, D. W. Bonnell, A. J. Paul and P. K. Schenck, "Species temporal and spatial distributions in laser ablation plumes", (Publ by Materials Research Society, Pittsburgh, PA, USA, Boston, MA, USA, 1993) p. 39.

[2] A. Chauhan, M. Anwar, K. Montero, H. J. White, R. S. Petrova, J. A. Payne, W. Si and J. Bai, "Slip Plane X-ray Residual Stress Analysis of Pulsed Laser Self Ablated Coatings", Surface and Coatings Technology (2006 (Communicated)).

[3] D. W. Bonnell, P. K. Schenck, J. W. Hastie and M. Joseph, "Ultra-High Temperature Laser Vaporization Mass Spectrometry of SiC and HfO_2", in Symposium on High Temperature Chemistry (Electrochemical Society, NJ, 1990).

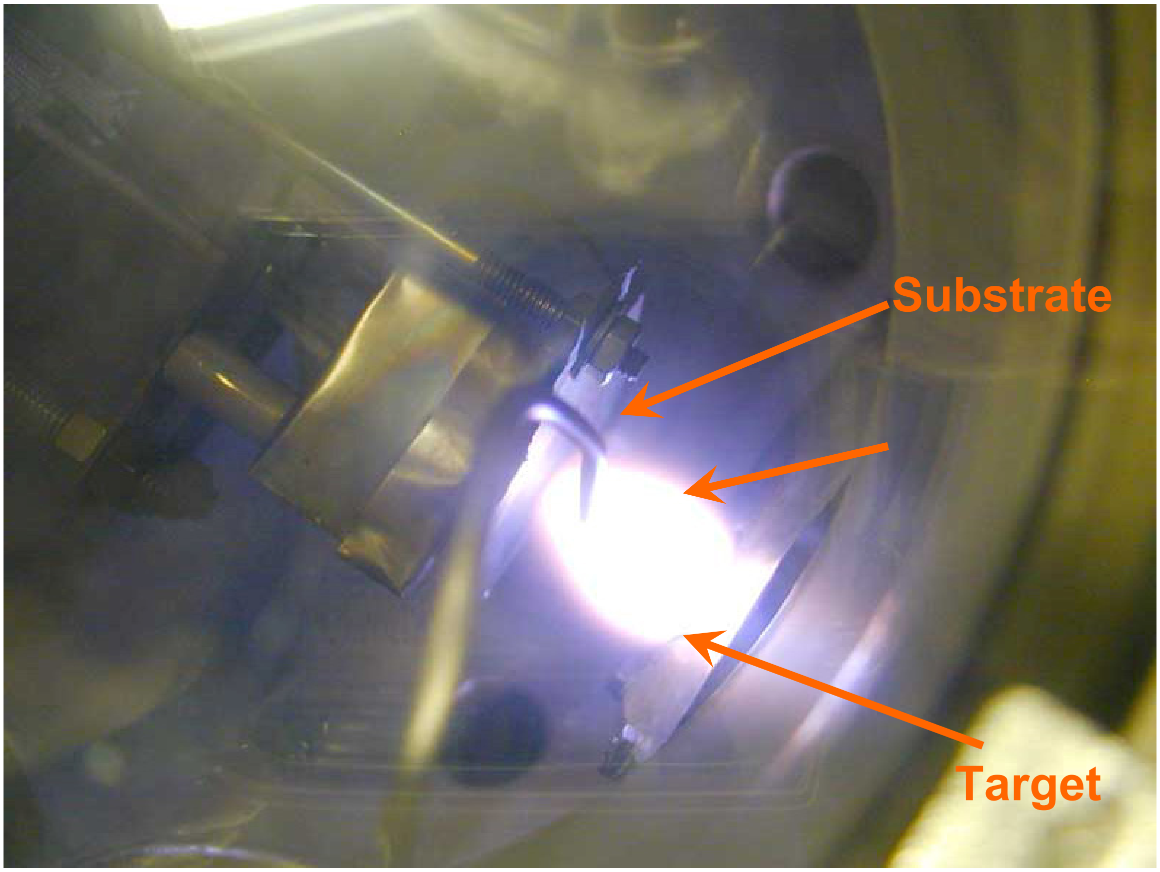

Figure 1. Photograph of plume inside the stainless steel vacuum chamber.

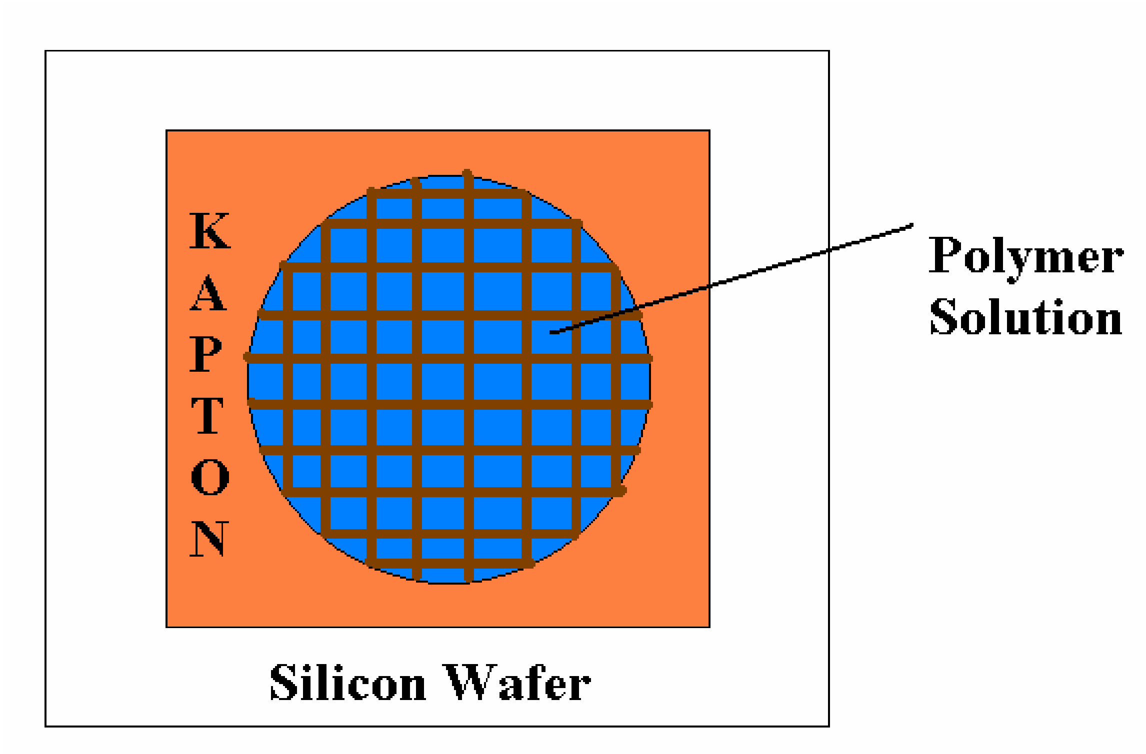

Figure 2. Polyimide thin film (Kaptan) adhered on silicon wafer using a polymer solution. And on the top of the setup copper grid adhered using the same polymer solution.

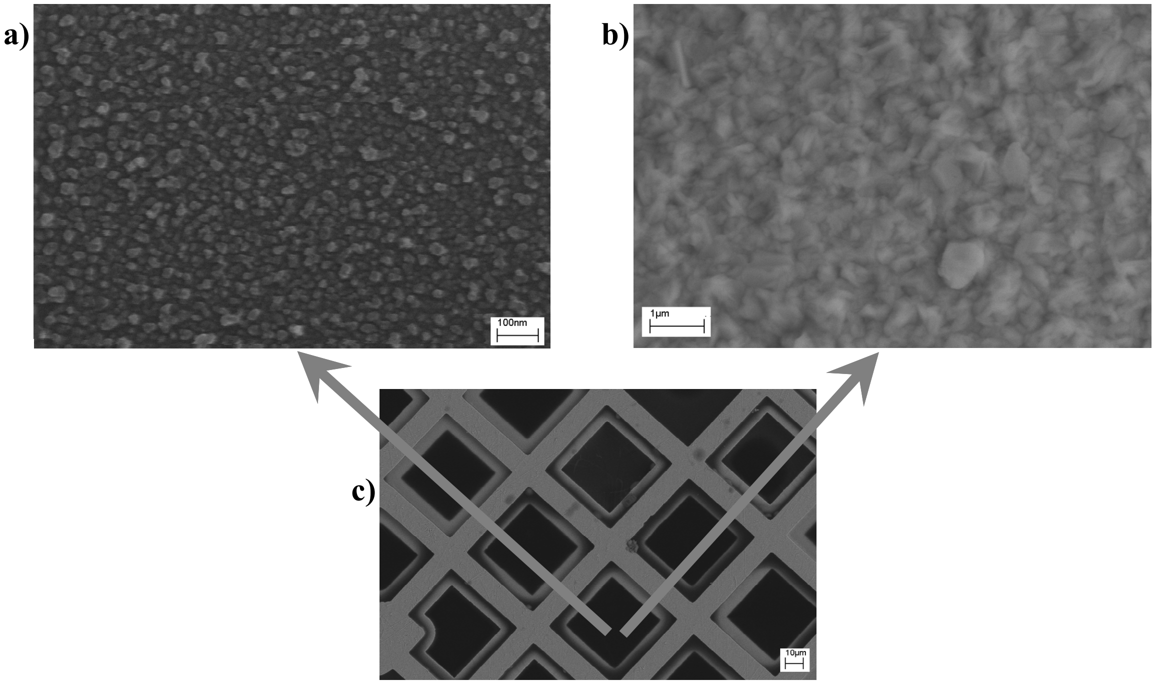

Figure 3. Scanning Electron Microscopy of nanoparticulates in the plume (a), SiC target (b), and copper grid (c). Deposition time 15 seconds [2].